INTERACTIONS BETWEEN OXYGEN MOLECULES, FOR ATMOSPHERIC APPLICATIONS

By

Sasha Caroen Brookhouse North

A DISSERTATION

Submitted to
Michigan State University
in partial fulfillment of the requirements
for the degree of

Chemistry-Doctor of Philosophy

2016

ABSTRACT

INTERACTIONS BETWEEN OXYGEN MOLECULES, FOR ATMOSPHERIC APPLICATIONS

By

Sasha Caroen Brookhouse North

Understanding the energy transfer processes between oxygen molecules is important for the elucidation of the reactions occurring in the Earth's atmosphere[112]. Even though two interacting oxygen molecules is a relatively small system, each diatomic has two unpaired electrons in antibonding, degenerate molecular orbitals, leading to an open shell system that forms a dense manifold of excited electronic states. This type of situation requires a multireference method. For this reason, progress on theoretical calculations for interacting oxygen molecules has been slow, since the discovery of collision-induced absorption in oxygen gas by Crawford, Welsh and Locke[3] in 1949. In this work, interaction energy curves have been generated using the CASPT2[77,78] method, and the aug-cc-pVQZ basis set of Dunning[76]. In addition, electronic properties have been obtained for the oxygen molecule, and are used to obtain the dipole moments using the long-range approximation. Changes in the electric charge distribution during a collision between the oxygen molecules can induce a net dipole and render the molecules infrared active, thus contributing to the absorption and emission in the IR and far-IR spectrum[69]. These dipole moments have also been calculated using *ab initio* methods, for many orientations of the oxygen molecules, and can be used to model the collision-induced spectra.

TABLE OF CONTENTS

LIST OF TABLES

LIST OF FIGURES

CHAPTER 1: Introduction

In order to absorb and emit radiation in the infrared region of the electromagnetic spectrum, a molecule must possess a charge separation in the form of a dipole moment[1].

The oxygen molecule exists as a linear, centrosymmetric molecule, with no dipole moment, and therefore is infrared inactive. However, during collisions between oxygen molecules at high pressures, transition probabilities are enhanced as the transitions can acquire some electric dipole character as a result of breakdown of the symmetry during interactions[2]. This situation is thus useful for investigating intermolecular, as opposed to intramolecular, processes.

These collision-induced interactions were first detected, in fact, in a sample of oxygen, when Crawford, Welsh and Locke[3] observed it while studying the O_2 fundamental rotation-vibrational band with a Perkin-Elmer spectrometer. The absorption varied as the square of the density, suggesting absorption by *pairs* of molecules (since absorption by monomers has a linear dependence on the density of the material). Although occurring in the infrared region of the electromagnetic spectrum, this absorption followed the Raman selection rules of $\Delta J = 0, \pm 2$, leading to a Q, O, and S branch, centered at the O_2 molecule's fundamental frequency of 1556 cm^{-1}. In both Raman scattering and collision-induced absorption an electric dipole is induced; in the case of Raman scattering the dipole is induced by the field of a light wave, while for collision-induced absorption the electric dipole is produced by an intermolecular force field[4]. Further measurements[5] of the infrared absorption of samples of O_2 at high densities showed a local maximum in regions of twice the fundamental frequency of the oxygen molecule. These findings supported the hypothesis that the absorption is caused by distortion of the charge distribution of the absorbing molecule during a two-body collision.

In 1966, Shapiro and Gush[6] also used a Perkin-Elmer spectrometer to make absorption measurements of a sample of oxygen molecules at room temperature, at a pressure of a few atmospheres, where only binary collisions could be observed (ternary collisions are not observed until pressures of 85 atm[7]). The goal of this work was to obtain accurate absorption coefficients for the O_2-O_2 collision-induced infrared bands, including the fundamental. Higher pressures were necessary to obtain the absorption coefficients for the weaker overtone bands. This work reinforced the earlier finding of Welsh and Locke[3]. During a collision, interactions can occur through classical electrostatic effects, dispersion forces (a long-range interaction), exchange/repulsion forces (a short range interaction), and others. Shapiro and Gush noted the broadening of the absorption profile, and the complete "smearing out" of the rotational bands, observed because "collisions occur on the duration of a "fly-by encounter" and thus lead to a broad, continuous spectrum over many wavelengths instead of resolved, sharp peaks"[6]. This is a direct consequence of Heisenberg's uncertainty principle, which says the product of line width and lifetime is never smaller than a number on the order of unity. Typical line widths for collision-induced absorption are roughly $\Delta\nu \approx 10^{13}$ Hz, corresponding to a radiative lifetime of roughly $\Delta t \approx 10^{-12}$ s[1.1].

Shapiro and Gush[6] concluded from their band-profile analysis that the collision-induced dipole moments responsible for the absorption had two sources: overlap induction and quadrupolar induction. The quadrupole-induced dipole moment is orientation-dependent and follows the before-mentioned Raman selection rules, while the overlap-induced dipole moment is less orientation-dependent and therefore contributes mostly to the J=0, or Q branch.

This collision-induced dipole moment has been modeled in early work by Van Kranendonk[8] by the following:

$$\mu = \frac{A}{r^4}\xi \exp\left(-\frac{r}{\rho}\right) \tag{1.1}$$

where r is the intermolecular separation and A, ξ, and ρ are constants. In equation (1.1), the first factor is due to the quadrupolar interaction (long range) and is strongly orientationally dependent, while the second factor is the short range overlap induction factor and is accordingly less orientationally dependent as stated above.

Shapiro and Gush[6] further attribute the quadrupolar induction to two types of molecular transitions. The first is a single transition, where one molecule of the colliding pair makes a vibrational transition of $\Delta\upsilon=1$, accompanied by a rotational transition $\Delta J=0,\pm2$, while the internal energy of the other molecule remains unchanged. The integrated intensity of the absorption due to this transition is proportional to $(Q'\alpha)^2$, where Q' is the rate of change of the quadrupole moment with respect to the internuclear distance and α is the polarizability of the molecule. The second transition type that contributes to the quadrupole-induced absorption spectrum is a double transition, which can occur in two different ways. The first is when one molecule of the colliding pair makes a vibrational transition only, while the other molecule makes a rotational transition according to the Raman selection rules. The intensity of this type of transition is proportional to $(\alpha'Q)^2$, where α' is the rate of change of the polarizability with respect to the internuclear distance, and Q is the quadrupole moment . The second is a double transition during which the first molecule makes a rotation-vibration transition, while the other molecule makes a rotational transition. The spectrum for this case is the most complex, and is proportional to the square of the directionally dependent component of the polarizability.

A year after the work of Shapiro and Gush[6], Rettschnick & Hoytink[9] published a theoretical study of electronic transitions from collision-induced absorption. In this work, they discussed the following very weak magnetic and forbidden electronic transitions that had been found to occur during collisions of oxygen molecules (where for example, the notation $0 \rightarrow 1$ refers to a transition from the ground state to the first accessible excited energy state, $0 \rightarrow 2$ a transition from the ground electronic state to the second accessible energy state, ect.):

$0 \rightarrow 1$, ${}^3\Sigma_g^- \rightarrow {}^1\Delta_g$; weak magnetic dipole transition[9,10,11,12,13,14,15] (the "infrared system") (1.2)

$0 \rightarrow 2$, ${}^3\Sigma_g^- \rightarrow {}^1\Sigma_g^+$; weak magnetic dipole transition[16] (the "red system") (1.3)

$0 \rightarrow 3$, ${}^3\Sigma_g^- \rightarrow {}^3\Delta_g$; weak orbitally forbidden electric dipole transition[17] (1.4)

$0 \rightarrow 4$, ${}^3\Sigma_g^- \rightarrow {}^3\Sigma_u^+$; weak ± forbidden electric dipole transition (Herzberg bands)[18] (1.5)

$0 \rightarrow 5$, ${}^3\Sigma_g^- \rightarrow {}^1\Sigma_u^-$; weak spin-forbidden electric dipole transition[17] (1.6)

Most importantly, they noted that these transitions occur due to exchange interaction between the two oxygen molecules, which leads to these weak transitions borrowing intensity from the Schumann-Runge transition, which is the strongest allowed electronic transition:

$0 \rightarrow 6$, ${}^3\Sigma_g^- \rightarrow {}^3\Sigma_u^-$; strongly allowed electric dipole transition (Schumann-Runge bands)[19] (1.7)

Not long after the theoretical work of Rettschnick & Hoytink[9], Tabisz, Allin, and Welsh[4] also studied the electronic transitions for compressed oxygen using absorption spectra. Their primary goal in doing so was to attempt to gain evidence for bound or at least "quasi -stable" $(O_2)_2$ complexes, separated from the collision-induced or van der Waals spectra. They also studied the

"infrared system"[9-15] and the "red system"[16] described by Rettschnick & Hoytink[9], as well as what are known as the combination systems[20,21]

$$^3\Sigma_g^- + {}^3\Sigma_g^- \rightarrow {}^1\Delta_g + {}^1\Delta_g \quad (1.8)$$

$$^3\Sigma_g^- + {}^3\Sigma_g^- \rightarrow {}^1\Delta_g + {}^1\Sigma_g^+ \quad (1.9)$$

$$^3\Sigma_g^- + {}^3\Sigma_g^- \rightarrow {}^1\Sigma_g^+ + {}^1\Sigma_g^+ \quad (1.10)$$

They concluded from these studies that a bound complex could have a shortening of its lifetime because of predissociation when the rotational energy exceeded the dissociation energy of the pair during a collision. They further stated that their experimental investigation demonstrated that the electronic band systems of oxygen observed in the compressed gas in the near IR and visible regions conform to all known criteria for collision-induced spectra. They assumed a Boltzmann relation known to hold for pressure-induced absorption bands in modeling their spectra, and the fit of their absorption coefficients to this model was their primary evidence for the observed bands being assigned as collision-induced electronic spectra. In the same year, Blickensderfer and Ewing[22] studied just the $^3\Sigma_g^- \rightarrow {}^1\Delta_g$ transition, or "infrared system" at very long path lengths and low pressures, in order to limit their measurements to binary collisions. They also reported finding no evidence of bound $(O_2)_2$ complexes, and found that their absorption coefficients fit the Boltzmann distribution for translationally broadened, or collision-induced, spectra. In 1972, McKellar, Rich and Welsh[23] published their study of the infrared fundamental and the five strongest near-infrared and visible electronic bands of gaseous oxygen (Table 1), using long path lengths as was done by Blickensderfer and Ewing[9], but extending to lower temperatures (90-115K) than the experiments done by Tabisz *et al.*[4] (205-297 K) .

Table 1. Electronic bands of gaseous oxygen studied by McKellar, Rich, and Welsh[23]

TABLE 1. Electronic bands studied

System	Vibrational transition	Location of maximum
$^1\Delta_g \leftarrow {}^3\Sigma_g^-$	0–0	1.26 μ (7890 cm^{-1})
$^1\Delta_g \leftarrow {}^3\Sigma_g^-$	1–0	1.06 μ (9400 cm^{-1})
$^1\Delta_g + {}^1\Delta_g \leftarrow {}^3\Sigma_g^- + {}^3\Sigma_g^-$	0–0	6290 Å (15 870 cm^{-1})
$^1\Delta_g + {}^1\Delta_g \leftarrow {}^3\Sigma_g^- + {}^3\Sigma_g^-$	1–0	5770 Å (17 310 cm^{-1})
$^1\Sigma_g^+ + {}^1\Delta_g \leftarrow {}^3\Sigma_g^- + {}^3\Sigma_g^-$	0–0	4770 Å (20 970 cm^{-1})

Additionally, low temperature experiments were done on the fundamental band in order to supplement the high-temperature observations of Shapiro and Gush[6]. McKellar *et al*[23]. defined the binary absorption coefficient as

$$\tilde{A}(\nu) = (\rho^2 l\nu)^{-1} \ln \frac{I_0(\nu)}{I(\nu)} \tag{1.11}$$

where ρ is the oxygen density in amagat, l is the path length in centimeters, ν is the frequency in cm^{-1}, $I(\nu)$ is the intensity which is transmitted by the gas, and $I_0(\nu)$ is the intensity transmitted by the evacuated cell. The integrated absorption is then defined as

$$\tilde{\alpha} = \int \tilde{A}(\nu)\, d\nu \tag{1.12}$$

They noted a marked narrowing of the fundamental band at the lower temperatures used when compared to the work of Shapiro and Gush[6]. This was attributed to two causes: the higher rotational populations tend towards lower energy levels, and the lower kinetic energies of collision pairs give smaller translation broadening of the individual induced transitions.

McKellar, Rich and Welsh[23] used a computed profile that assumed that only the quadrupole induction is important in producing the collision-induced spectrum for the fundamental band at 6.4 μm. They compared this calculated spectrum to their experimental spectrum obtained at 102 K and found very little difference between the two. They thus concluded that the induction in the fundamental band is due almost entirely to anisotropic interactions operative during collisions (Figure (1)).

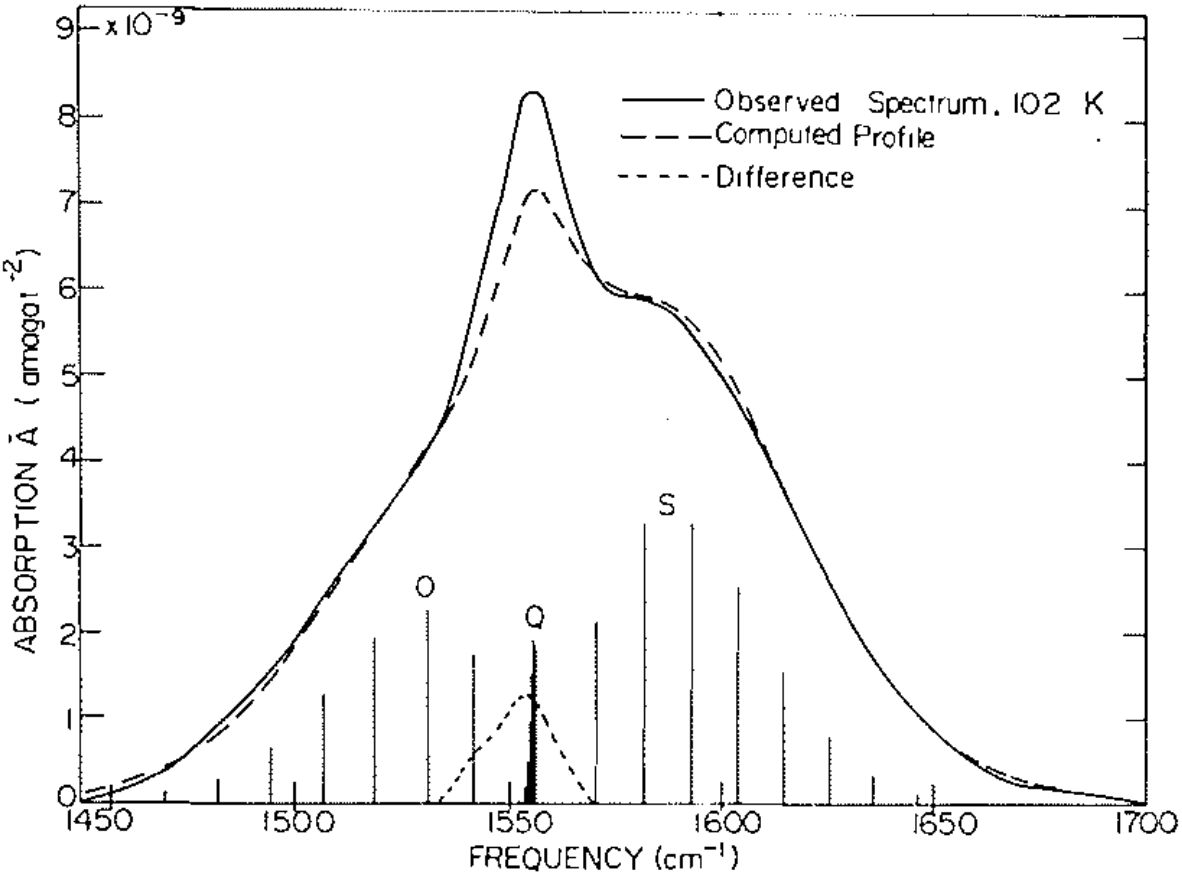

Figure 1. Comparison of the observed and computed O_2-O_2 fundamental band given by McKellar, Rich and Welsh[23]

For the near-IR and visible electronic bands, McKellar, Rich and Welsh[23] fit their data to the following Boltzmann relation:

$$\frac{\tilde{A}(\nu_0+\Delta\nu)}{\tilde{A}(\nu_0-\Delta\nu)} = exp[hc\Delta\nu/kT] \tag{1.13}$$

They noted that the application of this relation to an entire band with an unknown rotational structure rests on the assumption that the translation broadening is much greater than the extent of the structure, as is the case for collision-induced absorption. They found that the bands at 1.26 μ, 6290 Å , and 5770 Å satisfied the relation well. However, they concluded that the low-

temperature profile for the band at 4770 Å did not satisfy the relation satisfactorily, unlike the high-temperature data for this band that did fit the Boltzmann equation used in the work by Tabisz *et al.*[4] The Boltzmann relation could not be applied to the band at 1.06 μm. This band showed two clearly resolved maxima in the low temperature spectra. These were explained by McKellar, Rich and Welsh[23] and in earlier work by Cho[14] *et al*. as arising from two distinct transitions of different energies. In one transition, the vibrational 1-0 transition takes place in the same molecule as the electronic transition. In the second, the vibrational transition takes place in the other of the two colliding molecules.

Perner and Platt[24] carried out the first atmospheric observation of collision-induced absorption of O_2 pairs. They obtained absorption data for the "infrared", "red" and combination systems. Continued atmospheric studies focused on the fundamental vibration-rotation band (see Orlando[25] *et al.* for a review). Thibault[26] *et al*. noted that the first overtone band is approximately 100 times less intense[6], and concluded that the first and therefore sequential overtone bands were thus negligible for modeling the absorption of O_2 in the atmosphere. They studied collision-induced absorption in the fundamental vibration-rotation band with a view to application for atmospheric physics, and thus the acquisition of more accurate absorption coefficients. They performed absorption measurements using an infrared Fourier spectrometer, on gaseous samples of oxygen in the 0-20 atm pressure and 193-293 K temperature ranges. Rinsland *et al*.[27] studied the collision-induced absorption of the fundamental vibration-rotation band by recording high resolution stratospheric absorption spectra from a balloon-borne interferometer. They noted that for spectroscopic experiments of the stratosphere, such as the limb infrared monitor of the stratosphere (LIMS) experiment aboard the Nimbus 7[28], it is important to verify the O_2

laboratory absorption coefficients[3,4,5] by direct comparison to O_2 absorption measured in the atmosphere.

Research on the collision-induced absorption in O_2 pairs has in more recent years focused on its impact in the Earth's global solar short wave (SW) radiation budget. The global average of SW radiation transmitted to the Earth by the Sun has been estimated to be 342 W/m^2. For clear sky conditions, roughly 16% of this radiation is absorbed in the atmosphere by the gases O_2, H_2O, O_3, CO_2, CH_4, and others, with the remaining 84% transmitted to the surface of the Earth[29-31].

Absorption measurements done in both clear[32] and cloudy[29,32] skies using Differential Optical Absorption Spectrometry (DOAS)[33] showed that atmospheric absorption by O_2 collision pairs contribute a minor but non-negligible role for both clear and cloudy sky SW heating, with an estimated 0.57 W/m^2, or about 1% of the globally averaged SW heating. This model took the 1.06 μm and the visible bands into account. Solomon *et al.*[34] extended the work of Pfeilsticker *et al.*[29], showing that the 1.27 μm band of O_2-O_2, and the same band for O_2-N_2 collision pairs, should also be considered in the Earth's radiation budget. To model the collision-induced band at 1.27 μm, Solomon *et al.*[32] stretched the 1.06 μm band shape to fit relationships between the integrated intensity of the two bands taken from older low resolution measurements. As a consequence of using data from different studies[20,23,35], they presented their SW estimates as a range of values. For clear sky conditions alone, they estimated that the absorption in the 1.27 μm band from both complexes is about 0.64-1.55 W/m^2. The corresponding globally averaged, all sky condition values are then 0.93-1.32 W/m^2, which is roughly double of the estimate put forth by Pfeilsticker *et al.*[29] More recent work[36] that used improved data for the band at 1.27 μm

estimated the overall globally averaged impact of collision-induced absorption in mixtures of oxygen and nitrogen to be about 1 W/m^2.

Much work has been done on considerations of O_2-O_2 collisions contributing to the formation/dissociation of ozone, both experimentally (Miller[37], Park and Slanger[38], Stranges[39], Toumi[40]) and theoretically (Hernandez[41], Lauvergnat[42]). Ozone absorbs UV radiation in what is known as the Hartley band[38,43,44]between 200-300 nm. When a photon in this region is absorbed, the ozone molecule dissociates. A mechanism has been proposed in which this dissociation of ozone produces vibrationally excited O_2 ($X^3\Sigma_g^-, \mathrm{v} \geq 26$), which then reacts with a ground state O_2 to produce ozone[45]. This mechanism arose from two observations. The first was a bimodal O(^{3}P) translational energy distribution following photodissociation of ozone at 226 nm, implying the coincident production of triplet O_2, which was identified as O_2 ($X^3\Sigma_g^-$) in very high vibrational levels in subsequent experiments. The second was a large cross section for the reaction of vibrationally excited ground electronic O_2 with O_2 to yield ozone, based on measurements of relaxation rates of vibrationally excited O_2[46,39]. *Miller*[37] *et al.* used photofragment imaging and pump/probe experiments to explore the photodissociation of ozone at 226 nm by the following mechanism:

$$O_3 + h\nu \longrightarrow O_2\left(X^3\Sigma_g^-, \mathrm{v} \geq 26\right) + O \tag{1.14}$$

$$O_2\left(X^3\Sigma_g^-, \mathrm{v} \geq 26\right) + O_2 \longrightarrow O_3 + O \tag{1.15}$$

where *h*υ represents a photon. This was done in hopes of addressing the "ozone deficit problem"[45,46,47,48], or why previously predicted stratospheric ozone concentrations were less than observed. From quantum-yield calculations, *Miller et al.* concluded that highly vibrationally excited $O_2\left(X^3\Sigma_g^-, \mathrm{v} \geq 26\right)$ is in fact produced by the dissociation of ozone in the atmosphere at wavelengths of 226 nm (ultraviolet). They determined the yield of this excited O_2 to be about

1%. Using steady-state calculations, they estimated a 10% upper stratospheric ozone increase as a result of this yield. They therefore concluded that the mechanism in () could help account for the deficit. Later work confirmed the production of $O_2\left(X^3\Sigma_g^-, \mathrm{v} \geq 26\right)$ from the dissociation of ozone following absorption of UV light[49,50,51,52], and additional work done on the photodissociation of ozone by high-resolution photofragment translational spectroscopy by the Stranges group[39] estimated the excited O_2 yield to be even higher, at 7%.

Park and Slanger[38] also addressed the ozone deficit problem. It had been hypothesized that the vibrationally excited oxygen molecules produced in the Hartley band by ozone photodissociation could then undergo subsequent photoexcitation in the Schumann-Runge bands[53].This photoexcitation could lead to predissociation, and subsequent autocatalytic production of ozone, by the following mechanism:

$$O_3 + h\nu \longrightarrow O_2(\upsilon) + O(^3P) \tag{1.16}$$

$$O_2(\upsilon = 7) + h\nu \rightarrow O(^3P) + O(^3P) \tag{1.17}$$

$$3[O(^3P) + O_2 \rightarrow O_3] \tag{1.18}$$

In (1.17), the vibrationally excited oxygen molecule is in the υ=7 vibrational state because absorption at that step must occur at the photolysis wavelength of 248 nm, which is the location of the (2,7) band in the Schumann-Runge system.

This new source of ozone could then help alleviate the discrepancies between modeled and observed ozone profiles. In order for this mechanism to generate enough ozone to help account for the discrepancy, the lifetime of the vibrationally excited oxygen molecules in (1.17) would have to be long enough to then absorb a photon in the Schumann-Runge band. Toumi[54]

previously modeled atmospheric ozone production by the autocatalytic mechanism in (1.16)-(1.18), assuming that O_2 would be the only important quencher of the excited oxygen molecules produced in the Hartley bands. In this model, the quenching was slow enough to allow the autocatalytic mechanism to generate significant amounts of ozone. In order to evaluate this possibility, Park and Slanger[38] studied the nascent distribution of vibrationally excited oxygen at 248 nm, near the peak of the Hartley band. They also obtained their rate coefficients for relaxation by O_2 and N_2. Their results were similar to that of Toumi[54] for O_2 as a quencher of the excited O_2 molecules. However, Park and Slanger also considered N_2 as a quencher. They found that O_2 collisions with N_2 quenched the excited O_2 molecules five times faster than when O_2 was the collisional partner. They concluded that this precludes a significant role for the vibrationally excited oxygen photodissociation as a source of stratospheric ozone.

Geiser[55] *et al*. later used resonance-enhanced multiphoton ionization techniques, coupled with time-of-flight product imaging to determine the yield of $O_2\left(X^3\Sigma_g^-, \mathrm{v} \geq 26\right)$ from photodissociation of ozone between 226 and 240 and at 260 nm. The yields at these wavelengths were between 0.6±0.1% and 11.8±1.9%. They additionally stated that it now seemed unlikely that the production of ozone from (1.14) and (1.15) occurs, given that there had been no direct evidence found for step (1.15). Specifically, theoretical work[41,42,56-66] involving this reaction using *ab initio* surfaces[60,62] and semi-empirical potentials[57,59,60,62-65] found no evidence to support the proposed mechanism.

As mentioned at the beginning of this chapter, it is through the induced dipoles that collision-induced absorption is able to occur between otherwise spectroscopically inactive molecules. If the induced dipole moment and the interaction potential are known as functions of the intermolecular separation and molecular orientation, an absorption spectrum can be

obtained[1]. For the purpose of computing spectral line shapes and spectral moments, the induced dipole moment μ is best expressed in spherical coordinates[1,67,68,69] as follows:

$$\mu_M(r_A, r_B, R) =$$

$$\frac{(4\pi)^{\frac{3}{2}}}{\sqrt{3}} \sum_{\substack{\lambda_A,\lambda_B,\lambda,L \\ m_A,m_B}} D_{\lambda_A,\lambda_B,\lambda,L}(r_A, r_B, R) Y_{\lambda_A}^{m_A}(\hat{r}_A) Y_{\lambda_B}^{m_B}(\hat{r}_B) Y_L^{M-m}(\hat{R}) \times \langle \lambda_A \lambda_B m_A m_B | \lambda m \rangle \langle \lambda\ L\ m\ M-m | 1M \rangle \tag{1.19}$$

In (1.19), $\hat{r}_A$and $\hat{r}_B$ are unit vectors along the symmetry axes of molecules A and B, $\hat{R}$ is a unit vector along the intermolecular axis **R**, and $\langle \lambda_A \lambda_B m_A m_B | \lambda m \rangle$ is a Clebsch-Gordan coefficient. The functions $D_{\lambda_A,\lambda_B,\lambda,L}(r_A, r_B, R)$ are expansion coefficients.

To model the collision-induced spectra of binary or pure mixtures of diatomic gases, we first define an absorption coefficient[66,70] as a function of wavenumber ω as follows:

$$\alpha(\omega) = \omega\left(1 - e^{-\beta\hbar\omega}\right) A(\omega) \tag{1.20}$$

where $\beta = \frac{1}{kT}$. By considering only binary collisions, we can then write the function $A(\omega)$ as

$$A(\omega) = \rho^2 G(\omega)/2 \tag{1.21}$$

for a pure gas such as O_2-O_2. The function $G(\omega)$ consists of a linear superposition of individual components $G_n(\omega)$. For pure rotational-translational spectra, vibrational quantum numbers are zero, and therefore *n* is specified by the set of integers:

$$n \equiv \{J_1, J_1', J_2, J_2', \lambda_1, \lambda_2, \Lambda, L\} \tag{1.22}$$

where J_i and J_i' are the initial and final rotational quantum numbers, and the other four integers characterize the induced dipole mechanism, as in the expansions coefficients in (1.19).

Therefore, the primary goal of this work will be to calculate the expansion coefficients $D_{\lambda_A,\lambda_B,\lambda,L}(r_A, r_B, R)$ in (1.19), and subsequently the collision-induced dipole moments, for use in spectroscopic line shape analysis.

CHAPTER 2: The Interaction Energy of O_2-O_2 Collisional Complexes

2.1 Introduction

Knowledge of the interaction potential energy for colliding oxygen molecules is relevant for atmospheric chemistry and physics[71,72] (including the airglow phenomenon), in the chemical oxygen iodine laser (COIL)[73], in ultracold collisions[74], and in condensed phase studies [75,82]. Diatomic oxygen has an unusual ground electronic state of $^3\Sigma_g^-$. This electron configuration has two unpaired electrons in antibonding, degenerate molecular orbitals, and therefore the oxygen molecule is paramagnetic. Interaction between these two open-shelled molecules leads to non-dynamical correlation effects and requires a multireference method for calculation of the energies involved. In general, non-dynamical or static electron correlation effects arise when the wavefunction of an electronic state is well described only with more than one Slater determinant. This effect is dominant in bond cleavage cases, such as at the long O-O distances of the stretched O2 molecule. Therefore the inclusion of the static correlation via the multi-reference self-consistent field (MCSCF) is essential. MCSCF allows the simultaneous optimization of the coefficients and the molecular orbitals pertaining to the contributing determinants.

When two diatomic oxygen molecules in their ground states interact through a collision, three asymptotic states can be formed, leading to a quintet, triplet, and singlet spin state. The potential energy curves for these states have been investigated in the current work with an aug-cc-PVQZ basis set[76], using the CASPT2[77,78] method. The CASPT2 method was chosen because the singlet and triplet asymptotic states require a multireference method. For each oxygen monomer, we correlate 16 electrons to 12 orbitals at the MCSCF level, namely the 2p orbitals of all oxygens, and then we allow excitations out of the 2s orbitals at the CASPT2, and so we correlate 24

electrons to 16 orbitals. All calculations have been done using the MOLPRO package[79], unless otherwise noted.

Four main geometries for the O_2-O_2 collisional complex were examined. These are the H-shape geometry, the T-shape geometry, the X-shape geometry, and the linear geometry. These are represented in Figure (2)[80], in Jacobi coordinates.

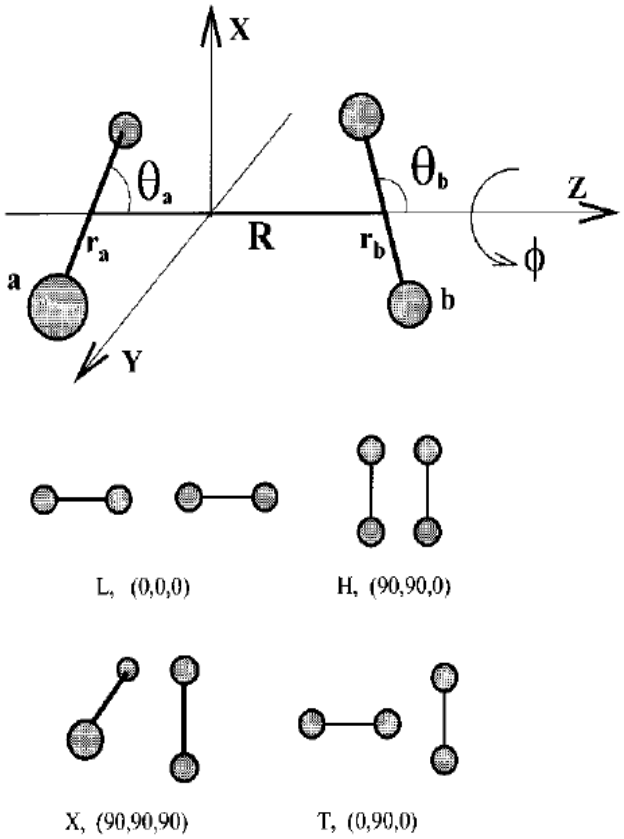

Figure 2. Four main geometries studied, as a function of three angles (θ_A, θ_B, and $\varphi = \varphi_A - \varphi_B$), bond distance r_A and r_B, and the intermolecular separation R[80]

The linear and H-shape geometries possess D_{2h} point group symmetry, while the X-shape and T-shape geometries possess C_{2v} symmetry.

2.2 Basis Set Superposition Error (BSSE)

The supermolecular method is used to calculate the interaction energy by the following equation:

$$\Delta E(R) = E^{AB}(R) - E^{A}(R) - E^{B}(R) \tag{2.1}$$

where E^{AB} is the energy of the complex, and E^{A}, E^{B} are the energies of the isolated molecules A and B, respectively (all as a function of the intermolecular distance R). One of the problems this method suffers from is Basis Set Superposition Error (BSSE), which is an artificial lowering of the energy of the pair relative to the monomers, caused by the overlapping basis sets of the monomers in the complex**.** In order to correct this error, the Counterpoise Method, as proposed by Boys and Bernardi[81], has been used. The BSSE for each of the monomers A, B in the complex is given by:

$$E_{BSSE}(A) = E_A^{AB} - E_A^{A} \tag{2.2}$$

$$E_{BSSE}(B) = E_B^{AB} - E_B^{B} \tag{2.3}$$

where E_A^{AB} and E_B^{AB} are the energies of molecule A and B, respectively, using the basis set of the complex AB. Subtracting these equations from equation (2.1), we obtain

$$\Delta E^{CP}(R) = E_{AB}^{AB}(R) - E_A^{AB}(R) - E_B^{AB}(R) \tag{2.4}$$

There has been some disagreement as to the merits of using this correction, as discussed by A. J. Stone[82] in his book "*Theory of Intermolecular Forces*".

Looking at Tables (1)-(3), it is apparent that the BSSE is largest for the smallest intermolecular distances (R) between monomers, because the artifiial reduction of the dimer energy is largest when each molecule can take advantage of the basis functions of the other

molecule. This is true regardless of the geometry formed by the interacting monomers. One point worth mentioning is that the BSSE has the same values regardless of whether we are discussing the singlet, triplet, or quintet spin state within a particular geometry. However, we can compare the magnitude of the BSSE between different geometries.

Out of the four main geometries, the linear geometry shows the largest magnitude of BSSE, with a value of 1.87 mHar (10000 mHar=1 Hartree) at a intermolecular separation of 5 bohr (Tables 4-6). The second largest error is in the T-shaped geometry, with an error of 0.815 mHar at the same intermolecular distance. Next is the X-shaped geometry, with an error of 0.557 mHar at 5 bohr, and finally, the H-shape geometry has the smallest error at 5 bohr of 0.393 mHar.

Table 2. BSSE and interaction energy for the triplet spin state of the T-shape geometry

Intermolecular Distance (bohr)	Uncorrected Interaction Energy (mHar)	BSSE (mHar)	Corrected Interaction Energy (mHar)
5	19.306	0.8154	20.121
6	-1.329	0.3919	-0.937
8	-3.092	0.1026	-0.299
10	-2.808	0.0365	-2.771
12	-2.738	0.0204	-2.718
15	-2.714	0.0131	-2.701
20	-2.708	0.0118	-2.696

Table 3. BSSE and interaction energy for the singlet spin state of the T-shape geometry

Intermolecular Distance (bohr)	Uncorrected Interaction Energy (mHar)	BSSE(mHar)	Corrected Interaction Energy (mHar)
5	16.777	0.8154	17.592
6	-1.840	0.3919	-1.448
8	-3.167	0.1026	-3.064
10	-2.872	0.0365	-2.836
12	-2.803	0.0204	-2.783
15	-2.778	0.0131	-2.765
20	-2.772	0.0118	-2.761

Table 4. BSSE and interaction energy for the quintet spin state of the T-shape geometry

Intermolecular Distance (bohr)	Uncorrected Interaction Energy (mHar)	BSSE (mHar)	Corrected Interaction Energy (mHar)
5	26.232	0.8154	27.048
6	-0.651	0.3919	-0.259
8	-3.123	0.1026	-3.020
10	-2.851	0.0365	-2.814
12	-2.782	0.0204	-2.761
15	-2.757	0.0131	-2.744
20	-2.751	0.0118	-2.739

Table 5. BSSE and interaction energy for the triplet spin state of the linear geometry

Intermolecular Distance (bohr)	Uncorrected Interaction Energy (mHar)	BSSE (mHar)	Corrected Interaction Energy (mHar)
5	195.639	1.8710	197.510
6	20.640	0.8181	21.458
8	-3.254	0.1904	-3.064
10	-2.927	0.0593	-2.868
12	-2.800	0.0163	-2.780
15	-2.757	0.0038	-2.754
20	-2.748	0.0002	-2.747

Table 6. BSSE and interaction energy for the quintet spin state of the linear geometry

Intermolecular Distance (bohr)	Uncorrected Interaction Energy (mHar)	BSSE (mHar)	Corrected Interaction Energy (mHar)
5	230.225	1.8710	232.097
6	24.365	0.8181	25.183
8	-3.202	0.1904	-3.011
10	-2.928	0.0593	-2.869
12	-2.799	0.0163	-2.782
15	-2.760	0.0038	-2.756
20	-2.750	0.0002	-2.750

Table 7. BSSE and interaction energy for the singlet spin state of the linear geometry

Intermolecular Distance (bohr)	Uncorrected Interaction Energy (mHar)	BSSE (mHar)	Corrected Interaction Energy (mHar)
5	166.721	1.8710	168.592
6	18.452	0.8181	19.270
8	-3.306	0.1904	-3.115
10	-2.951	0.0593	-2.892
12	-2.820	0.0163	-2.803
15	-2.781	0.0038	-2.777
20	-2.486	0.0002	-2.486

Table 8. BSSE and interaction energy for the singlet spin state of the X-shape geometry

Intermolecular Distance (bohr)	Uncorrected Interaction Energy (mHar)	BSSE (mHar)	Corrected Interaction Energy (mHar)
5	-0.614	0.5574	-0.057
6	-3.353	0.2648	-3.088
8	-3.003	0.0578	-2.945
10	-2.520	0.0176	-2.502
12	-2.476	0.0058	-2.470
15	-2.461	0.0008	-2.460
20	-2.457	0.0002	-2.457

Table 9. BSSE and interaction energy for the quintet spin state of the X-shape geometry

Intermolecular Distance (bohr)	Uncorrected Interaction Energy (mHar)	BSSE (mHar)	Corrected Interaction Energy (mHar)
5	-0.677	0.5574	-0.120
6	-3.324	0.2648	-3.060
8	-2.981	0.0578	-2.923
10	-2.814	0.0176	-2.797
12	-2.771	0.0058	-2.765
15	-2.756	0.0008	-2.755
20	-2.752	0.0002	-2.752

Table 10. BSSE and interaction energy for the triplet spin state of the X-shape geometry

Intermolecular Distance (bohr)	Uncorrected Interaction Energy (mHar)	BSSE (mHar)	Corrected Interaction Energy (mHar)
5	-33.873	0.5574	-33.316
6	-36.694	0.2648	-36.430
8	-36.359	0.0578	-36.301
10	-36.180	0.0176	-36.162
12	-36.132	0.0058	-36.127
15	-36.115	0.0008	-36.115
20	-36.111	0.0002	-36.111

Table 11. BSSE and interaction energy for the triplet spin state of the H-shape geometry

Intermolecular Distance (bohr)	Uncorrected Interaction Energy (mHar)	BSSE (mHar)	Corrected Interaction Energy (mHar)
5	-1.767	0.3928	-1.374
6	-3.500	0.1941	-3.305
8	-2.985	0.0402	-2.945
10	-2.811	0.0128	-2.798
12	-2.770	0.0035	-2.763
15	-2.752	0.0004	-2.751
20	-2.748	0.0002	-2.748

Table 12. BSSE and interaction energy for the singlet spin state of the H-shape geometry

Intermolecular Distance (bohr)	Uncorrected Interaction Energy (mHar)	BSSE (mHar)	Corrected Interaction Energy (mHar)
5	-3.178	0.3928	-2.785
6	-3.726	0.1941	-3.532
8	-3.013	0.0402	-2.973
10	-2.834	0.0128	-2.821
12	-2.790	0.0035	-2.787
15	-2.775	0.0004	-2.775
20	-2.771	0.0002	-2.771

Table 13. BSSE and interaction energy for the quintet spin state of the H-shape geometry

Intermolecular Distance (bohr)	Uncorrected Interaction Energy (mHar)	BSSE (mHar)	Corrected Interaction Energy (mHar)
5	1.457	0.3928	1.850
6	-3.087	0.1941	-2.893
8	-2.978	0.0402	-2.938
10	-2.811	0.0128	-2.799
12	-2.768	0.0035	-2.765
15	-2.753	0.0004	-2.752
20	-2.749	0.0002	-2.749

By looking at the uncorrected energies at the minimum of the potential energy curves for all four geometries, and comparing them to the energies at the minimum of the BSSE corrected curves, we can determine if the BSSE affects the position of the minimum of the potential energy wells.

From Table (13), we can see that the singlet, uncorrected T-shaped potential energy curve minimum occurs at an intermolecular separation of 7 bohr. After applying the correction for BSSE, the minimum occurs at an intermolecular separation of 7.1 bohr . Table (14) shows the corresponding data for the triplet spin state in the same geometry. The uncorrected minimum occurs at an intermolecular separation of 7.1 bohr. The corrected minimum occurs at an intermolecular separation of 7.2 bohr. Finally, Table (15) shows the data acquired for the quintet spin state in the T-shape geometry. The minimum in the uncorrected PEC occurs at 7.2 bohr. This spin state experiences the largest displacement of the minimum with BSSE correction for the T-shape, with a corrected minimum position of 7.4 bohr.

Table (16) contains the data for the singlet spin state within the linear geometry. For the uncorrected PEC, the minimum occurs at 8 bohr. After correcting for the BSSE, the minimum occurs at 8.1 bohr. Table (17) shows the corresponding data for the triplet spin state in the linear

geometry. The minimum for the triplet PEC occurs at 8.1 bohr while the corrected well depth minimum occurs at 8.2 bohr. Finally, for the quintet spin state of the linear geometry, Table (18), the PEC minimum occurs at an intermolecular distance of 8.2 bohr . The minimum of the corrected PEC occurs at 8.3 bohr.

Table (19) contains the data for the singlet spin state of the H-shape geometry. The minimum for the uncorrected PEC occurs at 5.6 bohr. After applying the correction for the BSSE, the minimum is located at 5.8 bohr. The corresponding data for the triplet spin state is in Table (20). The uncorrected minimum in the PEC occurs at 6 bohr. The corrected minimum is located at 6.1 bohr. Lastly, the data for the quintet spin state of the H-shape geometry is in Table (21). The location of the uncorrected minimum is at 6.5 bohr. After the BSSE correction, the minimum is located at 6.6 bohr.

Table (22) shows the data acquired for the singlet spin state of the X-shape geometry. The minimum for the uncorrected PEC occurs at 6.2 bohr and has a well depth of -3.204 mHar. After correction of the BSSE, the minimum of the PEC occurs at 6.3 bohr. Table (23) shows the data for the triplet spin state of the X-shape geometry. The uncorrected PEC minimum is at 6.2 bohr and the corrected minimum is located at 6.3 bohr. Finally, the uncorrected PEC for the quintet spin state is located at 6.3 bohr, and the corrected PEC has a minimum at 6.4 bohr.

Table 14. Position of the PEC minimum for the singlet state and T-shape geometry

Intermolecular Distance (bohr)	Uncorrected Interaction Energy (mHar)	BSSE (mHar)	Corrected Interaction Energy (mHar)
6.5	-3.169	0.2662	-2.903
6.6	-3.264	0.2484	-3.015
6.7	-3.327	0.2319	-3.095
6.8	-3.366	0.2166	-3.149
6.9	-3.385	0.2022	-3.183
7.0	-3.391	0.1888	-3.202
7.1	-3.385	0.1762	-3.209
7.2	-3.372	0.1643	-3.208
7.3	-3.353	0.1531	-3.200
7.4	-3.330	0.1425	-3.187
7.5	-3.304	0.1325	-3.171

Table 15. Position of the PEC minimum for the triplet state and T-shape geometry

Intermolecular Distance (bohr)	Uncorrected Interaction Energy (mHar)	BSSE (mHar)	Corrected Interaction Energy (mHar)
6.5	-3.004	0.2662	-2.738
6.6	-3.124	0.2484	-2.876
6.7	-3.208	0.2319	-2.976
6.8	-3.264	0.2166	-3.047
6.9	-3.298	0.2022	-3.095
7.0	-3.314	0.1888	-3.126
7.1	-3.318	0.1762	-3.142
7.2	-3.313	0.1643	-3.148
7.3	-3.300	0.1531	-3.147
7.4	-3.282	0.1425	-3.140
7.5	-3.261	0.1325	-3.128

Table 16. Position of the PEC minimum for the quintet state and T-shape geometry

Intermolecular Distance (bohr)	Uncorrected Interaction Energy (mHar)	BSSE (mHar)	Corrected Interaction Energy (mHar)
6.5	-2.721	0.2662	-2.454
6.6	-2.892	0.2484	-2.644
6.7	-3.019	0.2319	-2.787
6.8	-3.109	0.2166	-2.892
6.9	-3.171	0.2022	-2.969
7.0	-3.211	0.1888	-3.022
7.1	-3.234	0.1762	-3.058
7.2	-3.244	0.1643	-3.079
7.3	-3.243	0.1531	-3.090
7.4	-3.236	0.1425	-3.093
7.5	-3.223	0.1325	-3.091

Table 17. Position of the PEC minimum for the singlet state and linear geometry

Intermolecular Distance (bohr)	Uncorrected Interaction Energy (mHar)	BSSE (mHar)	Corrected Interaction Energy (mHar)
7.7	-3.246	0.2320	-3.014
7.8	-3.282	0.2172	-3.065
7.9	-3.300	0.2034	-3.097
8.0	-3.306	0.1904	-3.115
8.1	-3.301	0.1783	-3.123
8.2	-3.289	0.1669	-3.122
8.3	-3.272	0.1564	-3.116
8.4	-3.252	0.1465	-3.106
8.5	-3.230	0.1374	-3.093
8.6	-3.207	0.1290	-3.078
8.7	-3.183	0.1211	-3.062

Table 18. Position of the PEC minimum for the triplet state and linear geometry

Intermolecular Distance (bohr)	Uncorrected Interaction Energy(mHar)	BSSE (mHar)	Corrected Interaction Energy(mHar)
7.7	-3.171	0.2320	-2.939
7.8	-3.217	0.2172	-3.000
7.9	-3.243	0.2034	-3.040
8.0	-3.254	0.1904	-3.064
8.1	-3.255	0.1783	-3.076
8.2	-3.247	0.1669	-3.080
8.3	-3.234	0.1564	-3.077
8.4	-3.216	0.1465	-3.070
8.5	-3.196	0.1374	-3.059
8.6	-3.175	0.1290	-3.046
8.7	-3.153	0.1211	-3.032

Table 19. Position of the PEC minimum for the quintet state and linear geometry

Intermolecular Distance (bohr)	Uncorrected Interaction Energy(mHar)	BSSE (mHar)	Corrected Interaction Energy(mHar)
7.7	-3.071	0.2320	-2.839
7.8	-3.136	0.2172	-2.919
7.9	-3.178	0.2034	-2.974
8.0	-3.202	0.1904	-3.011
8.1	-3.212	0.1783	-3.034
8.2	-3.213	0.1669	-3.046
8.3	-3.206	0.1564	-3.050
8.4	-3.194	0.1465	-3.048
8.5	-3.179	0.1374	-3.042
8.6	-3.161	0.1290	-3.032
8.7	-3.142	0.1211	-3.021

Table 20. Position of the PEC minimum for the singlet state and H-shape geometry

Intermolecular Distance (bohr)	Uncorrected Interaction Energy(mHar)	BSSE (mHar)	Corrected Interaction Energy(mHar)
5.2	-3.554	0.3380	-3.216
5.3	-3.666	0.3141	-3.352
5.4	-3.740	0.2924	-3.447
5.5	-3.783	0.2726	-3.510
5.6	-3.801	0.2546	-3.547
5.7	-3.801	0.2380	-3.563
5.8	-3.786	0.2225	-3.564
5.9	-3.760	0.2080	-3.552
6.0	-3.726	0.1941	-3.532
6.1	-3.686	0.1809	-3.505
6.2	-3.642	0.1682	-3.474

Table 21. Position of the PEC minimum for the triplet state and H-shape geometry

Intermolecular Distance (bohr)	Uncorrected Interaction Energy(mHar)	BSSE (mHar)	Corrected Interaction Energy(mHar)
5.5	-3.223	0.2726	-2.950
5.6	-3.336	0.2546	-3.082
5.7	-3.414	0.2380	-3.176
5.8	-3.463	0.2225	-3.241
5.9	-3.490	0.2080	-3.282
6.0	-3.500	0.1941	-3.305
6.1	-3.495	0.1809	-3.315
6.2	-3.481	0.1682	-3.313
6.3	-3.459	0.1559	-3.303
6.4	-3.431	0.1441	-3.287
6.5	-3.400	0.1328	-3.268

Table 22. Position of the PEC minimum for the quintet state and H-shape geometry

Intermolecular Distance (bohr)	Uncorrected Interaction Energy(mHar)	BSSE (mHar)	Corrected Interaction Energy(mHar)
6.0	-3.087	0.1941	-2.893
6.1	-3.157	0.1809	-2.977
6.2	-3.204	0.1682	-3.036
6.3	-3.232	0.1559	-3.076
6.4	-3.245	0.1441	-3.101
6.5	-3.247	0.1328	-3.115
6.6	-3.241	0.1220	-3.119
6.7	-3.230	0.1118	-3.118
6.8	-3.213	0.1023	-3.111
6.9	-3.194	0.0936	-3.101
7.0	-3.173	0.0856	-3.088

Table 23. Position of the PEC minimum for the singlet state and X-shape geometry

Intermolecular Distance (bohr)	Uncorrected Interaction Energy(mHar)	BSSE (mHar)	Corrected Interaction Energy(mHar)
5.7	-36.537	0.1808	-36.357
5.8	-36.642	0.1684	-36.473
5.9	-36.714	0.1569	-36.557
6.0	-36.760	0.1463	-36.614
6.1	-36.787	0.1366	-36.650
6.2	-36.797	0.1277	-36.669
6.3	-36.796	0.1196	-36.676
6.4	-36.785	0.1120	-36.673
6.5	-36.768	0.1050	-36.663
6.6	-36.746	0.0984	-36.648
6.7	-36.721	0.0922	-36.629

Table 24. Position of the PEC minimum for the triplet state and X-shape geometry

Intermolecular Distance (bohr)	Uncorrected Interaction Energy(mHar)	BSSE (mHar)	Corrected Interaction Energy(mHar)
5.7	-36.469	0.1808	-36.289
5.8	-36.574	0.1684	-36.406
5.9	-36.647	0.1569	-36.490
6.0	-36.695	0.1463	-36.548
6.1	-36.722	0.1366	-36.585
6.2	-36.733	0.1277	-36.606
6.3	-36.733	0.1196	-36.614
6.4	-36.724	0.1120	-36.612
6.5	-36.708	0.1050	-36.603
6.6	-36.687	0.0984	-36.589
6.7	-36.663	0.0922	-36.571

Table 25. Position of the PEC minimum for the quintet state and X-shape geometry

Intermolecular Distance (bohr)	Uncorrected Interaction Energy(mHar)	BSSE (mHar)	Corrected Interaction Energy(mHar)
5.7	-36.433	0.1808	-36.252
5.8	-36.539	0.1684	-36.371
5.9	-36.614	0.1569	-36.457
6.0	-36.663	0.1463	-36.517
6.1	-36.693	0.1366	-36.556
6.2	-36.707	0.1277	-36.579
6.3	-36.709	0.1196	-36.589
6.4	-36.702	0.1120	-36.590
6.5	-36.688	0.1050	-36.583
6.6	-36.670	0.0984	-36.571
6.7	36.648	0.0922	-36.555

Table 26. Positions of BSSE corrected minima for the four main geometries studied

	H-shape	X-shape	T-shape	Linear
singlet	5.8 bohr	6.3 bohr	7.1 bohr	8.1 bohr
triplet	6.1 bohr	6.3 bohr	7.2 bohr	8.2 bohr
quintet	6.6 bohr	6.4 bohr	7.4 bohr	8.3 bohr

2.3 Comparison of Interaction Energy to Literature

Much work has been done to determine the interaction energy of the O_2-O_2 collisional complex.[73,76-96,60,66] In this section, we therefore compare our interaction energy curves to literature values that were determined both theoretically [73,86,92,60,94,95] and experimentally[75,78,99] in order to validate their accuracy.

The first reliable potential energy surface for the exchange-interaction driven singlet, triplet, and quintet splittings of the $O_2(^3\Sigma_g^-)$-$O_2(^3\Sigma_g^-)$ interaction surface was obtained by Bussery and Wormer[92]. The PESs were built by combining *ab initio* calculations by Wormer and van der Avoird[13a] using first order exchange perturbation theory at the Hartree–Fock level and a second-order polarization energy evaluated semiempirically, circumventing in this way the difficulty inherent to an *ab initio* determination of the dispersion terms[93,96].

Tables (26)-(28) shows our results for the position and depth of the attractive interaction potential curves. Bussery and Wormer[92] studied the same four geometries that we have investigated, and paid special attention to the H-shape geometry, noting that it is the structure found in the solid oxygen crystal[104], and appeared from their PES to be the most stable geometry. They also discussed the coupling given by a Heisenberg spin Hamiltonian described by a single parameter, J_{AB} for the $O_2^A - O_2^B$ pair. This anisotropic term is used to determine if the interaction is ferro-magnetic or antiferromagnetic. The sign of this term is dictated by the overlap between the π_g^* orbitals. Their H-shape geometry yields an antiferromagnetic coupling, with a negative value of J_{AB}. Their X-shape potential gives a ferromagnetic coupling, with a positive value for J_{AB}. This is used to explain the stabilization of the H-shape geometry relative to the X-shape geometry for their singlet and triplet states. While we can see from Tables (28) and (29) that our H-shape singlet spin state is indeed more stable, both in position and well depth, than the X-

shape singlet state, we find that the triplet state for the X-shape has a slightly deeper potential well (ϵ). However, the position of the H-shape is slightly more favorable for the triplet state (6.1 bohr) than that of the X-shape triplet (6.3 bohr). Their data shows that the most favorable geometry of the two for the quintet splitting is the X-shape, and our data shows this as well, both for the position and depth of the potential minimum. Their T-shape and linear geometries are more repulsive and less favored than the H-shape and X-shape, and our data agrees. Their conclusion of the H-shape as the most stable geometry helped validate the experiments done by Goodman *et al.* [105], in which electronic spectra in the visible region was used to make the same conclusion.

We next compare our data for the position and depth of the interaction energy curves to the experimental work of Aquilanti *et al.*[80] They explored they nature of the bond in the O_2-O_2 "dimer" using molecular beam experiments for collisions between oxygen molecules. The resulting cross sections were used to extract information on the position and energy of the minima of the singlet, triplet, and quintet splittings. This work is significant as it allowed the first complete experimental characterization of the interaction in such a system. Experiments of this type must be carried out with sufficiently high angular and energy resolution in order to allow the measurement of quantum interference effects for an accurate description of the interaction potential. Earlier attempts[106] made with hot effusive beams of fast rotating molecules emerging from a microwave discharge source had yielded the interaction potential that was averaged over all molecular orientations. Considerable progress in the production and characterization of beams emerging from supersonic sources[107] in work done by R.B. Bernstein and T.J.P. O'Brien allowed for collisional studies of cold molecules, with slow rotations and more control over

molecular alignment, in order to more fully understand the anisotropy of the collisions. From the "glory pattern" produced by quantum interference, it is possible to extract information on the potential well features[100] while the absolute value of the cross section contains information about the long-range attraction.[101]

In generating their potential energy surface, Aquilanti[10] *et al*. considered oxygen molecule A and oxygen molecule B in the pair $O_2^A - O_2^B$ to be at their fixed equilibrium bond distances, and therefore behaving as rigid rotors. They separate the interaction potential into the radial and angular components as follows:

$$V(R,\theta_A,\theta_B,\phi) = 4\pi \sum_{L_aL_b,L} V^{L_aL_bL}(R) Y^{L0}_{L_aL_b}(\theta_A,\theta_B,\phi) \tag{2.5}$$

with L_a, L_b=0,1,2...*and* $|L_a\text{-}L_b| \leq L \leq L_a+L_b$. The functions $Y^{L0}_{L_aL_b}(\theta_A,\theta_B,\phi)$ are coupled spherical harmonics. The radial components contain the interaction information, whether from induction, dispersion, electrostatic repulsion, etcetera. Because the oxygen molecule is a homonuclear diatomic, only even moments contribute to the sum in equation (2.5). After inserting the proper values into equation (2.5) for the three angles θ_A, θ_B, and ϕ, the interaction potentials (truncated after the first four terms) for the four basic configurations H,X,T, and linear are given by:

$$V^H(R) = V^{000}(R) - \sqrt{5}V^{202}(R) + \sqrt{5}V^{220}(R) + \frac{5}{\sqrt{14}}V^{222}(R) \tag{2.6}$$

$$V^X(R) = V^{000}(R) - \sqrt{5}V^{202}(R) - \frac{\sqrt{5}}{2}V^{220}(R) - 2\frac{5}{\sqrt{14}}V^{222}(R) \tag{2.7}$$

$$V^T(R) = V^{000}(R) + \frac{\sqrt{5}}{2}V^{202}(R) - \frac{\sqrt{5}}{2}V^{220}(R) + \frac{5}{\sqrt{14}}V^{222}(R) \tag{2.8}$$

$$V^L(R) = V^{000}(R) + 2\sqrt{5}V^{202}(R) + \sqrt{5}V^{220}(R) - 2\frac{5}{\sqrt{14}}V^{222}(R) \tag{2.9}$$

Aquilanti[80] *et al.* compared their experimental potential and glory pattern to that of the semi *ab initio* potential and subsequent glory pattern in [16] and found they were dephased with

respect to each other, and had a different frequency. They concluded that the marked difference suggests that the isotropic term for the potential $V^{000}(R)$ needs to be much larger (more negative than) that calculated in [Ref. 16]. When comparing their potential energy curves to that of Bussery[21] *et al.*, they concur that the lowest energy minimum for the singlet state occurs when the oxygen molecules are in the planar parallel (H-shape) geometry. Indeed, this is the same result we have found in the present work, and our *ab initio* curves estimate an even deeper singlet well depth for the minimum in the H-shape geometry, at 23.5 eV, compared to 19.0 eV from Bussery[92] and 17 eV from the work of Aquilanti[80] and coworkers (Table (28)). In addition, both Bussery and Aquilanti find that the lowest potential energy for the quintet state occurs for the X-shape geometry, and again, our results confirm this (Table (29)).

We next compare our work to the *ab initio* study done by Minaev *et al.*[89]. They performed *ab initio* complete active space configuration interaction (CASCI) calculations on the singlet, triplet, and quintet state of $O_2^A - O_2^B$, using a 6-31G* basis set[108]. They performed calculations only for the parallel planar (H-shape) geometry. In addition, they used restricted open-shell Hartree Fock quintet state orbitals in all of their calculations. This was presumably done because the quintet splitting is a single reference state, while the singlet and triplet state contain multireference character. Though the dependence on the intermolecular distance R and subsequent positions of the van der Waals minima are similar in value to our work and that of all other literature values in Table (28), the well depths are significantly smaller.

Hernández[60] and coworkers have performed *ab initio* calculations of the singlet splitting for all four main geometries, at the CASSCF level. With the exception of the linear geometry, where we have calculated a deeper potential well for the singlet state, their results match ours almost exactly, both in position and magnitude of the interaction potential minima.

Dayou[98] and coworkers used the CASPT2 method, as we have, to obtain their two-dimensional potential energy curves, with an atomic natural orbital basis set with *s,p,d* and *f* functions. They calculated the van der Waals minima for the singlet state of the H-shape geometry, and is in good agreement with our results, with our potential giving a slightly deeper interaction well.

More recently, Bartolomei[100] *et al*. performed a detailed study on the intermolecular potentials for the three lowest multiplet states. They used the CASPT2 method and an ANO basis set to obtain the quintet state's minima and well depth for all four main geometries. In addition they obtained the potential energy curve for the quintet state using the CCSD(T) method[109]. Because the triplet and singlet multiplet states are multireference, CCSD(T) is not an appropriate method to use in calculating their potential energy curves. Therefore, the potential energy for these states was obtained as follows:

$$V^{S=0} = V_{CCSD(T)} + \Delta^{\mathrm{s-q}}_{\mathrm{multi}} \tag{2.9}$$

$$V^{S=1} = V_{CCSD(T)} + \Delta^{\mathrm{t-q}}_{\mathrm{multi}} \tag{2.10}$$

where $V^{S=0}$ and $V^{S=1}$ are the potentials for the singlet state and triplet state, respectively. The quintet energy obtained using the CCSD(T) method is given by $V_{CCSD(T)}$, and $\Delta^{\mathrm{s-q}}_{\mathrm{multi}}$, $\Delta^{\mathrm{t-q}}_{\mathrm{multi}}$ are the singlet-quintet and triplet-quintet energy differences obtained using the CASPT2 method. In this way they obtained a lower and upper limit to the position of the singlet and triplet states. These are given in the CCSD(T) column in Tables (26)-(29). Comparing to our data, we can see that our results reproduce theirs for the quintet at the CASPT2 level well. Our T,X, and H-shape results are slightly more attractive in the van der Waals well, perhaps because of the use of additional functions in our basis set. Examining their CCSD(T) results for the linear geometry in Table (26), we see that our singlet state is more attractive than that found by Bartolomei[100] at the

CCSD(T) level. Our data for the triplet state shows a well depth that is exactly the same as the lower limit calculated by Bartolomei[100] at the CCSD(T) level. Finally, our quintet state for the linear geometry is somewhat more repulsive than the CCSD(T) one.

The same analysis is applied to Table (27), corresponding to our data for the T-shape geometry. Our singlet state is more repulsive than that obtained by Bartolomei[29] *et al.* using the CCSD(T) method, with a minimum that is about 4 meV more shallow than the CCSD(T) lower limit. Our triplet state is 2.6 meV shallower than the CCSD(T) lower limit, and our quintet state is 3.4 meV shallower than the corresponding CCSD(T) quintet state.

Now turning to Table (28), we see that our singlet state is near the CCSD(T) upper limit of the curve obtained by Bartolomei[100] *et al*. for the H-shape geometry. Our triplet state is about 4 meV shallower than the upper limit of the CCSD(T) curve. Finally, our quintet state is 3.6 meV shallower than the CCSD(T) value. All of the positions of these minima are comsistent between methods.

Finally we compare our position and depth of our X-shape minima to that obtained by Bartolomei[100] *et al*. using the CCSD(T) method. Our singlet state is only 0.6 meV from their upper limit of the CCSD(T) results. The same is true for the triplet state. It is worth noting that while previous works[80,92] determined the quintet state to be more attractive than either the singlet or triplet for the X-shape, our results agree with that of Bartolomei that this is not necessarily the case.

In conclusion, from comparison with the results in the literature, we find that our choice of method and basis set give reliable results for the interaction of the $O_2^A - O_2^B$ system for the four main geometries. These methods will therefore be employed, with changes as appropriate, in subsequent chapters, particularly when calculating the *ab initio* dipole moments.

Table 27. The position and depth of the interaction potential energy curve for the linear geometry of O_2-O_2

Linear (D_{2h})		**$X\ ^1A_g$**		**$^3B_{1u}$**		**^5A_g**	
Reference	Method/Basis	$R_e(a_0)$	ϵ(meV)	$R_e(a_0)$	ϵ(meV)	$R_e(a_0)$	ϵ(meV)
present work	CASPT2/ aug-cc-pVQZ	8.1	17.4	8.2	9.1	8.3	8.2
Bussery *et al.*[92]	SCF/ GTO[5s3p2d]	8.6	5.8	8.6	5.7	8.8	5.6
Aquilanti *et al.*[80]	Experiment	8.0	9.1±0.8	8.1	8.6±0.8	8.3	7.7±0.8
Hernández *et al.*[60]	CASSCF/ 5s3p2d	8.3	8.5	-	-	-	-
Bartolomei[100]	CCSD(T)/ 5s4p3d2f	8.01/7.97	14.0/14.6	8.05/8.06	9.1/13.4	8.16	12.3
Bartolomei[100]	CASPT2/5s4p3d2f	-	-	-	-	8.25	8.59

Table 28. The position and depth of the interaction potential energy curve for the T-shape geometry of O_2-O_2

T-shape (C_{2v})		**$X\ ^1B_1$**		**$^3B_1$**		**$^5B_1$**	
Reference	Method/Basis	$R_e(a_0)$	ϵ(meV)	$R_e(a_0)$	ϵ(meV)	$R_e(a_0)$	ϵ(meV)
present work	CASPT2/ aug-cc-pVQZ(6s5p4d3f2g)	7.1	12.2	7.2	12.2	7.4	9.7
Bussery *et al.*[92]	SCF/GTO[5s3p2d]	7.6	8.0	7.6	7.9	7.6	7.6
Aquilanti *et al.*[80]	Experiment	7.1	16.0±0.8	7.2	14.7±0.8	7.3	12.9 ±0.8
Hernández *et al.*[60]	CASSCF/5s3p2d	7.2	10.9	-	-	-	-
Bartolomei[100]	CCSD(T)/5s4p3d2f	7.02/6.95	16.0/17.2	7.12/7.07	14.8/15.5	7.26	13.1
Bartolomei[100]	CASPT2/5s4p3d2f	-	-	-	-	7.5	9.08

Table 29. The position and depth of the interaction potential energy curve for the H-shape geometry of O_2-O_2

H-shape (D_{2h})		$X\ ^1A_g$		$^3B_{1u}$		^5A_g	
Reference	Method/Basis	$R_e(a_0)$	ϵ(meV)	$R_e(a_0)$	ϵ(meV)	$R_e(a_0)$	ϵ(meV)
present work	CASPT2/ aug-cc-pVQZ (6s5p4d3f2g)	5.8	23.5	6.1	15.4	6.6	10.1
Bussery *et al.*[92]	SCF/GTO[5s3p2d]	6.1	19.0	6.2	17.3	6.4	14.8
Aquilanti *et al.*[2]	Experimental	6.71	17.0 ±0.8	6.82	15.9 ±0.8	6.95	14.3 ±0.8
Minaev *et al.*[3]	CASCI/6-31G*	6.33	6.96	6.46	5.67	6.69	3.81
Dayou *et al.*[98]	CASPT2/ 5s4p3d2f (ANO)	5.85	19.9				
Hernández *et al.*[60]	CASSCF/5s3p2d	5.8	24.4	-	-	-	-
Bartolomei[100]	CCSD(T)/ 5s4p3d2f	5.77/5.56	25.4/32.3	6.07/5.94	19.5/22.2	6.48	13.7
Bartolomei[100]	CASPT2/5s4p3d2f	-	-	-	-	6.5	8.72

Table 30. The position and depth of the interaction potential energy curve for the X-shape geometry of O_2-O_2

X-Shape (C_{2v})		**$X\,^1A_2$**		**$^3A_2$**		**$^5A_2$**	
Reference	Method/Basis	$R_e(a_0)$	ϵ(meV)	$R_e(a_0)$	ϵ(meV)	$R_e(a_0)$	ϵ(meV)
Present work **spin-averaged*	CASPT2/ aug-cc-pVQZ(6s5p4d3f2g)	6.3	15.6	6.3	15.6	6.4	13.7
Bussery *et al.*[92] **spin-averaged*	SCF/GTO[5s3p2d]	6.2	14.7	5.8	15.0	6.8	15.6
Hernández *et al.*[60]	CASSCF/5s3p2d	6.2	15.7	-	-	-	-
Aquilanti *et al.*[80]	Experimental	6.86	15.3±0.8	6.84	15.5 ±0.8	6.8	16 ±0.8
Bartolomei[100]	CCSD(T)/5s4p3d2f	6.24/6.18	16.2/17.3	6.23/6.19	16.2/17.0	6.22	16.3
Bartolomei[100]	CASPT2/5s4p3d2f	-	-	-	-	6.5	10.67

CHAPTER 3: Multipole Moments and (hyper)polarizabilites of the O_2 Molecule

3.1 Introduction

The elucidation of the energy transfer processes between oxygen molecules can provide a better understanding of the energy balance occurring in the Earth's atmosphere.[112] Although the oxygen molecule does not possess a permanent dipole moment, collision-induced electric dipoles (in addition to the magnetic dipole) facilitate the absorption of radiation in the roto-translational region. This effect can potentially change the role of the molecular oxygen in the atmospheric thermodynamics. It is therefore crucial to understand the underlying physics of the O_2-O_2 interaction and how each molecule is polarized in the electric field of its neighbor.

The collision-induced dipole moment is dependent on the dipole polarizability ($\alpha_{\alpha\beta}$), dipole-octupole ($E_{\alpha,\beta\gamma\delta}$), quadrupole-quadrupole ($C_{\alpha\beta,\gamma\delta}$), and second hyperpolarizabilities ($\gamma_{\alpha\beta\gamma\delta}$), as well as the quadrupole (Θ_{zz}) and hexadecapole (Φ_{zzzz}) moments. These properties have been reported in the literature for the O_2 molecule at its equilibrium bond length[113-118,120-126]. In particular, we focus on comparing our data to that of Y. N. Kalugina and V. N. Cherepanov[113], who have calculated the dipole polarizabilities, quadrupole moment, hexadecapole moment, dipole-octupole polarizabilities, and quadrupole-quadrupole polarizabilities using finite field techniques and the R-CCSD(T) method, with an aug-cc-pVQZ basis set. We also compare our data to that of Bartolomei[114] *et al.*, who has calculated these same properties using again the aug-cc-pVQZ basis set but the MRCI method. In particular, we compare our data to their value obtained using what they label as the "CAS1" active space, as it is identical to ours. In this active space, they distribute 12 electrons in 8 orbitals, keeping the fully occupied $1\sigma_{u,g}$ orbitals closed,

but allowing excitations out of the (2,3) $\sigma_{u,g}$ and $\pi_{u,g}$ orbitals. However, there are few available values for these properties at non-equilibrium internuclear bond distances. In addition, there are no values in the literature for the dipole-dipole-quadrupole polarizability, as far as we are aware.

We have calculated these properties at several bond distances, for use in the calculation of average rovibrational properties for the υ=0-5, J=0 energy levels. In order to calculate energies at bond distances that are shorter or longer than the equilibrium bond distance, we require a multireference method. This is because as the bond distance is shortened/stretched, the occupied orbitals and the nearest unoccupied orbitals can become quasi-degenerate (near each other in energy). This is especially important for the oxygen molecule, because its open shell nature leads to many low-lying excited electronic energy states[128,129]. One of the methods we will therefore employ is the Complete Active Space Second Order Perturbation Theory method (CASPT2). In the CASPT2 method, a multi-configurational CASSCF wave function is used to obtain the dynamic electron correlation, which allows the construction of appropriate molecular orbitals at distances longer than the equilibrium bond length. Single, double, and all higher excitations to virtual orbitals (non-dynamic correlation) are considered through the second order perturbation theory scheme. Our second method used to calculate the electronic properties is the MRCI method, also starting from a CASSCF wavefunction. In this method, excitations into the quasi-degenerate orbitals encountered away from equilibrium are explicitly included in the reference wavefunction. We have considered only double and single excitations in our MRCI calculations. There are advantages and diadvantages inherent in both methods. The MRCI method is variational, which means that we approach the true energy for our system from above; that is, the energy obtained using this method will always be larger than the exact energy. However, the CASPT2 method is not variational, and therefore can give an energy that is lower than the exact

energy. In this way the CASPT2 method can be seen as somewhat less trustworthy than the MRCI method. The advantage of the CASPT2 method is that it is faster and less computationally demanding than the MRCI method, because the coefficients in the wavefunction are obtained through the second order perturbation theory formulas (instead of variationally).

In addition to the use in calculating the vibrational averages, these properties have been used to obtain the long-range approximate collision-induced dipole moments (chapter 4).

This chapter is organized as follows: in Section 3.2 we will explain our methodology and computational details. Section 3.3 begins our results & discussion, beginning with the electronic properties obtained at the equilibrium bond distance, and using the singly augmented basis sets aug-cc-pVXZ. Section 3.4 continues our results with the properties obtained at the equilibrium bond distance with the doubly augmented basis sets d-aug-cc-pVXZ. These sections also include a comparison to selected literature values. Section 3.5 contains our results for properties obtained away from the equilibrium internuclear distance. Section 3.6 gives our results for the estimate of the complete basis set (CBS) limit. Section 3.7 gives our results for the rovibrational averages of the properties obtained using the Numerov-Cooley Method[128,129]. Finally, we give our conclusions in Section 3.8.

3.2 Methodology

Dipole, quadrupole, octopole, and hexadecapole fields must be applied in order to obtain the multipole moments and polarizabilities. Our Hamiltonian includes the dipole ($\hat{\mu}$), quadrupole ($\widehat{\Theta}$), octopole ($\widehat{\Omega}$), and hexadecapole ($\widehat{\Phi}$) moment operators:

$$\widehat{H} = \widehat{H}_0 - F_\alpha \hat{\mu}_\alpha - \frac{1}{3} F_{\alpha\beta} \widehat{\Theta}_{\alpha\beta} - \frac{1}{15} F_{\alpha\beta\gamma} \widehat{\Omega}_{\alpha\beta\gamma} - \frac{1}{105} F_{\alpha\beta\gamma\delta} \widehat{\Phi}_{\alpha\beta\gamma\delta} \quad (3.1)$$

In equation (3.1), $\widehat{H}_0$ is the unperturbed electronic Hamiltonian, and the Greek subscripts run through the x,y,z coordinates. The Einstein convention of summation over Greek indices is being followed throughout this study. The F_α, $F_{\alpha\beta}$, $F_{\alpha\beta\gamma}$, $F_{\alpha\beta\gamma\delta}$ amplitudes define the strength of the corresponding fields (and field gradients).

Applying perturbation theory, the most important terms of the energy expansion are:

$$E = E_0 - \frac{1}{3}\Theta_{\alpha\beta}F_{\alpha\beta} - \frac{1}{105}\Phi_{\alpha\beta\gamma\delta}F_{\alpha\beta\gamma\delta} - \frac{1}{2}\alpha_{\alpha\beta}F_\alpha F_\beta - \frac{1}{6}C_{\alpha\beta,\gamma\delta}F_{\alpha\beta}F_{\gamma\delta} - \frac{1}{15}E_{\alpha,\beta\gamma\delta}F_\alpha F_{\beta\gamma\delta} - \frac{1}{6}B_{\alpha,\beta,\gamma\delta}F_\alpha F_\beta F_{\gamma\delta} - \frac{1}{24}\gamma_{\alpha\beta\gamma\delta}F_\alpha F_\beta F_\gamma F_\delta \quad (3.2)$$

In equation (3.2), E_0 is the energy of the unperturbed system, and $\Theta_{\alpha\beta}$ and $\Phi_{\alpha\beta\gamma\delta}$ are the quadrupole and hexadecapole moments. The dipole moment and octopole moment, μ_α and $\Omega_{\alpha\beta\gamma}$, respectively, vanish for linear centrosymmetric molecules. This is also true for the dipole-quadrupole polarizability ($A_{\alpha\beta\gamma}$) and the dipole hyperpolarizability $\beta_{\alpha\beta\gamma}$[130]. If we place O_2 molecule along the z-axis, then by symmetry, and using equation(3.2), we require the following tensors only:

$$\alpha_{\tau\tau} = -\frac{\partial^2 E}{\partial F_\tau^2}, \tau = x \; or \; z \quad (3.3)$$

$$\Theta_{zz} \equiv \Theta = -3\frac{\partial E}{\partial F_{zz}} \quad (3.4)$$

$$\Phi_{zzzz} \equiv \Phi = -105\frac{\partial E}{\partial F_{zzzz}} \quad (3.5)$$

$$C_{\sigma\tau,\sigma\tau} = -3\frac{\partial^2 E}{\partial F_{\sigma\tau}^2}, \sigma\tau = xx, zz, or \; xz \quad (3.6)$$

$$E_{\tau,\tau\tau\tau} = -15\frac{\partial^2 E}{\partial F_\tau \partial F_{\tau\tau\tau}}, \tau = x \; or \; z \quad (3.7)$$

$$B_{\sigma,\tau,\kappa\lambda} = -3\frac{\partial^3 E}{\partial F_\sigma \partial F_\tau \partial F_{\kappa\lambda}}, (\sigma,\tau,\kappa\lambda) = (x,x,xx),(z,z,zz),(x,x,zz) or\ (x,z,xz) \quad (3.8)$$

$$\gamma_{\alpha\beta\gamma\delta} = -24\frac{\partial^4 E}{\partial F_\alpha \partial F_\beta \partial F_\gamma \partial F_\delta}, (\alpha\beta\gamma\delta) = (xxxx),(zzzz), or\ (xxzz)$$

(3.9)

Practically, the derivatives in equations 3-9 are calculated via the central differences formulae as follows:

$$\frac{\partial E(F)}{\partial F} = \frac{1}{2f}[E(f) - E(-f)] \quad (3.10)$$

$$\frac{\partial^2 E(F)}{\partial F^2} = \frac{1}{f^2}[E(f) + E(-f) - 2E(0)] \quad (3.11)$$

$$\frac{\partial^2 E(F,G)}{\partial F \partial G} = \frac{1}{4fg}[E(f,g) + E(-f,-g) - E(f,-g) - E(-f,g)] \quad (3.12)$$

$$\frac{\partial^3 E(F,G)}{\partial F^2 \partial G} = \frac{1}{2f^2 g}[E(f,g) - E(-f,-g) - E(f,-g) + E(-f,g) + 2E(0,-g) - 2E(0,g)]$$

(3.13)

$$\frac{\partial^3 E(F,G,H)}{\partial F \partial G \partial H} =$$

$$\frac{1}{8fgh}[E(f,g,h) + E(-f,-g,h) + E(-f,g,-h) + E(f,-g,-h) - E(-f,-g,-h) -$$

$$E(-f,g,h) - E(f,-g,h) - E(f,g,-h)] \quad (3.14)$$

$$\frac{\partial^4 E(F,G)}{\partial F^2 \partial G^2} = \frac{1}{f^2 g^2}[(E(f,g) + E(-f,-g) + E(-f,g) + E(f,-g) - 2\big(E(f) + E(-f) + E(g) + E(-g)\big) + 4E(0)] \quad (3.15)$$

The field amplitudes *f*, *g*, and *h* have to be selected wisely. They should be big enough to generate numerically significant energy differences but not too big to render the above equations invalid. In addition, using different field strengths will yield slightly different results, and this is still under investigation. We finally chose $f = 10^{-3}$ a.u, $g = 10^{-3}$ a.u., and $h = 10^{-4}$ a.u. The above equations yield errors on the order of the second power of *f*, *g*, or *h*. Thirty-four energy calculations were performed for each internuclear distance to fulfill the above calculations. It was necessary to impose symmetry constraints on the wavefunction according to the symmetry of the fields applied to obtain accurate values. For example, we considered the D_{2h} point group for zero field and quadrupole field calculations. The C_{2v} and C_s symmetry was also applied for various other combinations of fields required. All computational work was performed using the MOLPRO[79] package.

3.3. Properties at the Equilibrium Bond Length, Obtained using the Singly Augmented Basis Sets

All electronic properties calculated for the oxygen molecule that are discussed in this section and the following sections are given in atomic units. The units for the quadrupole moment are ea_0^2, where *e* is the charge on the electron, and a_0 is the bohr radius. The units for the hexadecapole moment are ea_0^4, and the units of the dipole-octupole polarizability E are $e^2a_0^4/E_h$, where E_h is the energy in atomic units (Hartrees). The dipole-dipole-quadrupole polarizability B has units of $e^3a_0^4/E_h^2$, and the units of the quadrupole-quadrupole polarizability C are $e^2a_0^4/E_h$. Finally, the units of the second hyperpolarizability γ are $e^4a_0^4/E_h^3$. Referring to Table (31), we examine the

MRCI and CASPT2 values of the dipole polarizability ($\alpha_{\alpha\beta}$), dipole-octupole ($E_{\alpha,\beta\gamma\delta}$), quadrupole-quadrupole ($C_{\alpha\beta,\gamma\delta}$), and dipole-dipole-quadrupole ($B_{\alpha,\beta,\gamma\delta}$) polarizabilities and second hyperpolarizabilities ($\gamma_{\alpha\beta\gamma\delta}$), as well as the quadrupole (Θ_{zz}) and hexadecapole (Φ_{zzzz}) moments, at the equilibrium bond distance of r=2.28187 bohr. We compare these values with some in the literature[113-115], and also examine the effect of change in the cardinal number X in the singly augmented correlation consistent polarized valence (aug-cc-pVXZ) basis sets of Dunning[76] . The numbers in these tables are replicable numbers, as opposed to significant digits. That is, they are numbers the method will reliably generate on different machines, as opposed to being numbers that are correct to these many digits. In Table (32), we will discuss the same values obtained using the doubly augmented (d-aug-cc-pVXZ) basis sets. This analysis of basis set sensitivity is useful for determining what basis set to use when trying to balance the accuracy of the result using that basis set with the basis set cost. In general, the addition of more functions of angular momentum *l* to a given basis set increases it's cost and is more computationally demanding. However, in some cases, a certain number of functions is necessary in order to obtain accurate results. Increasing the cardinal number increases the number of functions in the basis set, as does adding one (in the aug-cc-PVXZ case) or two (d-aug-cc-pVXZ) diffuse functions for every angular momentum present in the basis. Diffuse functions allow greater flexibility in the wavefunction by allowing the electrons to be held further away from the nucleus. These functions are known to be necessary for weakly bound systems, especially when obtaining the polarization for a system.

Looking first at the x-component of the polarizability (α_{xx}), we see that using the MRCI method and our largest basis set ((5Z)=aug-cc-pV5Z), there is about a 5% difference between our value and that calculated by Yu N. Kalugina and V. N. Cherepanov[113], who used a slightly smaller

aug-cc-pVQZ basis set and the R-CCSD(T) method . Our value of (α_{xx}) obtained using the CASPT2 method is closer, with a 2.6% difference. Our value for the z-component of the polarizability (α_{zz}) using the MRCI method is only just over 1% different from that of Kalugina and Cherepanov, and again the CASPT2 value is even closer, with only a 0.6% difference from the literature. As far as basis set sensitivity, the x-component of the polarizability (α_{xx}) is relatively insensitive to the cardinal number X, with an 8.5% difference in going from the aug-cc-pVDZ to the aug-cc-pV5Z basis set for the CASPT2 method, and a 6.5% difference between the same levels for the MRCI method. The z-component of the polarizability (α_{zz}) is even more insensitive to the choice of the cardinal number X, with only a 1.5 % difference in between the value obtained at the X=D level and the value obtained at the X=5 level for CASPT2, and only about 0.8% difference between the same values for MRCI.

Table 31. Electronic properties (in a.u.) of O_2 at the equilibrium bond length, r(O-O)=2.28187 bohr, using the MRCI and CASPT2/aug-cc-pVXZ levels of theory.

Method	MRCI	MRCI	MRCI	MRCI	CASPT2	CASPT2	CASPT2	CASPT2	Literature
Basis set	X = D	X = T	X = Q	X = 5	X = D	X = T	X = Q	X = 5	
$-E_0$	150.0007	150.111	150.146	150.1575	149.9954	150.1135	150.1535	150.1683	-
α_{xx}	7.303	7.729	7.825	7.797	7.332	7.853	7.987	7.99	8.20[a]
α_{zz}	14.788	14.888	14.897	14.906	14.95	15.143	15.182	15.178	15.09[a]
Θ_{zz}	-0.1589	-0.2393	-0.2508	-0.2597	-0.1594	-0.2331	-0.2422	-0.25	-0.21[b], -0.22[d],-0.24[c]
Φ_{zzzz}	5.3889	4.5787	4.5058	4.3609	5.3273	4.5794	4.5162	4.3703	4.67[b], 4.70[d],4.48[c]
$E_{x,xxx}$	-15.9879	-17.0159	-17.1905	-17.1309	-16.0291	-17.31	-17.5451	-17.5232	20.95[a],18.81[e]
$E_{z,zzz}$	14.532	18.6798	19.7699	20.2751	14.3343	18.5936	19.8435	20.3474	-17.93[b],-18.06[e]
$B_{x,z,xz}$	-70.8515	-85.3055	-95.1795	-98.73	-72.0735	-90.854	-102.702	-107.307	-
$B_{x,x,zz}$	12.556	6.246	23.480	30.88	24.470	32.157	38.685	42.836	-
$B_{x,x,xx}$	-34.831	-42.927	-60.291	-68.536	-42.229	-58.444	-71.814	-79.270	-
$B_{z,z,zz}$	-77.566	-101.017	-118.399	-124.483	-71.68	-98.349	-115.116	-122.036	-
$C_{xx,xx}$	8.699	10.863	12.073	12.798	8.722	11.069	12.373	13.162	12.84[b],13.64[e]
$C_{zz,zz}$	17.902	20.320	21.159	21.709	17.974	20.698	21.660	22.277	22.30[b],23.00[e]
$C_{xz,xz}$	16.575	18.000	18.648	18.935	18.006	19.737	20.501	20.833	19.75[b],20.48[e]
γ_{xxxx}	187.977	272.1	374.406	439.931	190.68	286.435	402.458	471.133	490[f]
γ_{xxzz}	198.926	243.534	290.740	312.823	219.849	285.485	350.420	-	358[f]
γ_{zzzz}	431.872	500.444	612.824	652.564	367.111	461.353	602.010	663.836	776[f]

a. Yu N. Kalugina and V. N. Cherepanov[113]

b Yu N. Kalugina and V. N. Cherepanov[113], using R-CCSD(T), with an aug-cc-pVQZ basis set

c Bartolomei *et al.*[114], using aug-cc-pVQZ basis set and MRCI method, and active space CAS1

d Bartolomei *et al.*[114], using aug-cc-pVQZ basis set and MRCI method, and active space CAS2

e Values taken from Bartolomei *et al.*[114], as cited in Yu N. Kalugina and V. N. Cherepanov[113]

f Neogrády *et al.*[118], using the CCSD Method and aug-cc-pV5Z basis set

Now moving to the quadrupole moment (Θ_{zz}), we see that our value calculated using our largest basis set (5Z), and using the MRCI method, is about 8% different from the nearest literature value, that is, that of Bartolomei *et al.*[114], who have also used the MRCI method, with a similar active space to ours (labeled CAS1). For our value calculated with the (5Z) basis set but with the CASPT2 method, the nearest literature value is again that of Bartolomei *et al.*[114] also with the CAS1 active space, with only a 4% difference. Examining now the dependence of the quadrupole moment on basis set cardinal number X, we see that the quadrupole moment is much more sensitive than the polarizabilities. For the MRCI method, there is a 48% difference in going from the DZ to 5Z level. The majority of the difference is found in going from the DZ to TZ levels (40%). The situation is similar for the CASPT2 method values; there is a 44% difference in values from the DZ to 5Z levels, with 37% of that difference occurring between the DZ and TZ levels.

If we now examine the hexadecapole moment (Φ_{zzzz}), we find that our value at the highest singly augmented basis set we considered (5Z), is again closest to that of Bartolomei *et al.*[114], for both our MRCI and CASPT2 value, with about a 2.5% difference. Looking at the basis set dependence, we find that increasing the basis set from the DZ to 5Z in the singly augmented correlation consistent series decreases the value of the MRCI hexadecapole by 21%; 16% of that difference is between the DZ and TZ levels. The CASPT2 value decreases by almost 20% in going from the DZ to 5Z levels, with 15% of that difference between the DZ and TZ levels.

We now turn to the higher-order polarizabilities. Our value of the $E_{x,xxx}$ tensor (dipole-octopole polarizability) using the MRCI method and aug-cc-pV5Z basis set is of opposite sign to that found in the literature[113]. We find that this is true also for the $E_{z,zzz}$ tensor. For comparison, we have found that their values for these tensors are also opposite in sign from others we have

calculated for H_2[131]. We have reexamined the formulas we have used and found them to be correct. If we assume that the indices were somehow switched, then our $E_{x,xxx}$= their $E_{z,zzz}$ and vice versa. In this case, our value for $E_{x,xxx}$ using the aug-cc-pV5Z basis and MRCI method is -17.1309 au, which is 4.55% different from their value of $E_{z,zzz}$. Our CASPT2 values for $E_{x,xxx}$ is just over 2% different from their value for $E_{z,zzz}$. Using the same analysis for our $E_{z,zzz}$ values, both the MRCI and CASPT2 values with the 5Z basis set are around 3% different from their reported values for $E_{x,xxx}$. Looking at basis set sensitivity, our MRCI value of $E_{x,xxx}$ is less sensitive to the choice of cardinal number X than the quadrupole and hexadecapole moments, with only a 7% decrease when increasing the basis set size from the DZ to 5Z level, with 6% of the decrease occurring from the DZ to TZ levels. Our CASPT2 value is slightly more sensitive, with a total decrease of almost 9% when increasing the basis set from the DZ to the 5Z level, with almost 8% of that difference again occurring between the DZ and TZ levels. Our $E_{z,zzz}$ values are more sensitive: there is a 33% difference in increasing the cardinal number from X=D to X=5 for our MRCI value, with 25% percent difference occurring between the DZ and TZ levels, and a 35% difference in going from the DZ level to the 5Z level for our CASPT2 values, with a 26% difference occurring between the DZ and TZ levels.

We now examine the dipole-dipole quadrupole polarizabilities $B_{x,z,xz}$. We are unable to find literature values to compare to, but we can do a basis set sensitivity analysis. In going from the DZ to 5Z basis set level using the MRCI method, there is an almost 33% decrease. A large portion of that difference is between the DZ and TZ levels (almost 19%). However, there is also an appreciable difference when increasing the basis set size from the TZ to QZ levels (over 10%). Therefore, the remaining percent difference in going from the QZ to 5Z levels makes up the smallest difference, of only about 4%. The situation is similar for the corresponding CASPT2

values, with a 23% difference between the DZ and TZ levels, an appreciable difference of about 12% between the TZ and QZ levels, and again a small difference of 4% between the QZ and 5Z levels. Applying the same analysis to the $B_{x,x,zz}$ values of the polarizability, we observe some strange behavior with respect to basis set size. In increasing the basis set size from the DZ to TZ levels, there is a 67% decrease in the value of the polarizability. However, when we increase the basis set size from the TZ to QZ levels, there is a 115% *increase* in the value of the polarizability. Finally, when going from the QZ to 5Z levels, there is a 27% increase in the value of the dipole-dipole-quadrupole polarizability. Thus, we notice two main things from this analysis. The first is that we cannot consider the value of this polarizability to be monotonic with the increase in basis set size. Second, there is a large difference between basis sets for all cardinal numbers X considered. Though the difference between the QZ and 5Z levels is still the smallest, it is larger than previous cases considered. In addition, we do not observe this non-monotonic behavior for the same values obtained at the CASPT2 level. Instead, the dipole-dipole-quadrupole polarizability $B_{x,x,zz}$ increases in a monotonic manner, with a total of almost 55% difference in increasing the basis set size from the DZ to 5Z levels. About half of this difference is found between the DZ and TZ levels. There is a large difference between the TZ and QZ levels as well (about 18%), and the smallest difference is again found between the QZ and 5Z levels, with about a 10% increase in going from the QZ to 5Z level. Because these values increases as we increase the basis set size, they are probably more accurate than those obtained using the MRCI method, at least for the singly augmented basis set series.

If we now examine the MRCI values for the dipole-dipole-quadrupole polarizability $B_{x,x,xx}$, we see that in going from the DZ to 5Z levels, there is a decrease of 65%. While there is an almost

21% difference between the DZ and TZ levels, the bulk of the percent difference is seen when increasing the basis set from the TZ to QZ levels, with a difference of almost 33%. There is only a 12% difference when increasing the basis set from the QZ to 5Z level. In contrast, for the $B_{x,x,xx}$ polarizability obtained using the CASPT2 method, the largest difference occurs between the DZ and TZ levels (32%), with almost 20% difference between the TZ and QZ levels, and finally an additional 9% difference between the QZ and 5Z levels. This gives a total of nearly 61% difference when increasing the basis set size from the DZ to 5Z level.

For the fourth and final component of the dipole-dipole-quadrupole polarizability, $B_{z,z,zz}$, we see a 46% decrease when increasing the basis set from the DZ to 5Z level using the MRCI method. Most of this difference is found between the DZ and TZ levels (26%), with almost 16% difference between the TZ and QZ levels, and less than 5% difference between the QZ and 5Z levels. For the same values obtained using the CASPT2 method, there is a 52% decrease when increasing the basis set from the DZ to 5Z level. Again, most of this difference is between the DZ and TZ levels (31%), with about 15% of the difference between the TZ and QZ levels, and less than 6% difference between the QZ and 5Z levels.

From Table (31), we see that there are literature values[113] to compare to our values of the quadrupole-quadrupole polarizability ($C_{\alpha\beta,\gamma\delta}$). We first discuss the quadrupole-quadrupole polarizability $C_{xx,xx}$. Our value obtained using the MRCI method, and the aug-cc-pV5Z basis set, is only 0.33% different from the value of Kalugina and Cherepanov[113], who used a QZ basis. Our CASPT2 value is farther from their value, but is still less than 3% different. Examining basis set sensitivity, we see that there is a 38% increase in the MRCI value of $C_{xx,xx}$ when increasing

the basis set from the DZ to 5Z levels. Over 22% of this difference is found between the DZ and TZ levels, with a 10% difference between the TZ and QZ levels, and only about 6% difference between the QZ and 5Z levels. The situation with the CASPT2 values is essentially the same, with almost a 41% increase in the value of $C_{xx,xx}$ when increasing the basis set size from the DZ to 5Z levels; the large portion of the difference (~24%) again occurring between the DZ and TZ levels, about 11% difference between the TZ and QZ, and finally only about 6% difference between the QZ and 5Z levels. The next component of the quadrupole-quadrupole polarizability in Table (31), $C_{zz,zz}$, is less sensitive to the choice of cardinal number X in the aug-cc-pVXZ series. The total difference found when increasing the basis set size from the DZ to 5Z level for the MRCI method is about 19%, with 12% of that difference occurring between the DZ and TZ levels, and only 3-4% difference between additional levels. The values obtained using CASPT2 have a total of a 21% increase between the DZ and 5Z levels, with 14% of the increase occurring between the DZ and TZ levels, with again only 3-4% of an increase for additional increases in the cardinal number. Comparing to the available literature data, we see that there is very good agreement between our values and that of Kalugina and Cherepanov[113], with less than 3% of a difference between our MRCI value and their value, and our CASPT2 value is identical with their value to the first decimal place. Our best (5Z level) MRCI value for the third component of the quadrupole-quadrupole polarizability in Table (26), $C_{xz,xz}$, is about 4% smaller than that of Kalugina and Cherepanov[113]. Our CASPT2 value at the same level is about 5% *larger* than the value calculated by Kalugina and Cherepanov[113], but less than 2% larger than the value calculated by Bartolomei *et al.*[114], who used a QZ basis set, and the MRCI method. This tensor is the least sensitive of the three quadrupole-quadrupole polarizabilities to cardinal number with

between 13% and 15% total difference in going from the DZ to 5Z basis sets, for the MRCI and CASPT2 methods, respectively.

Our final quantities to be discussed are the second hyperpolarizabilities ($\gamma_{\alpha\beta\gamma\delta}$). We begin by examining the component γ_{xxxx}. Our value obtained using the MRCI method and aug-cc-pV5Z basis set, is about 11% smaller than the value reported by P. Neogràdy *et al.*[118] (who used the CCSD[119] method and aug-cc-pVQZ basis set). The same quantity obtained with the CASPT2 method is less than 4% smaller than the literature value. However, in both cases, this quantity shows extreme sensitivity to the choice of cardinal number X in the basis set. The MRCI value at the 5Z level is more than 80% larger than the value obtained at the DZ level. Nearly 37% of this difference occurs between the DZ and TZ levels, but there is almost as much difference between the TZ and QZ levels (~30%). The difference between the QZ and 5Z levels is not insignificant either, at 14%. There is an even larger difference between basis set levels for the values obtained using the CASPT2 method, with an increase of almost 85% between the DZ and 5Z levels. Over 40% of this difference is between the DZ and TZ levels, with over 31% difference between the TZ and QZ levels, and an appreciable 13% difference between the QZ and 5Z levels.

The next second hyperpolarizability we examine is γ_{xxzz}. Though less so than the previous quantity, it is still quite sensitive to the choice of basis set. For our value using the MRCI method, there is an almost 45% increase in the value when increasing the basis set from the DZ to 5Z levels. A large portion of this increase happens between the DZ to TZ levels (20%), but there is almost as much difference between the TZ and QZ levels (17%). The difference is even more pronounced for the CASPT2 values, with almost a 26% increase in the quantity when

increasing the basis set from the DZ to TZ level, and about 20% difference between the TZ and QZ levels. Comparing to the literature value for this quantity, our value using the MRCI method and aug-cc-pV5Z basis set is less than 14% smaller than that of the literature. Since we do not have a value at the same basis set level for our CASPT2 series, we compare our value using the aug-cc-pVQZ basis set to the literature value, and find they are in good agreement, with a difference of about 2%.

Finally we examine the second hyperpolarizability γ_{zzzz}. Our value using the MRCI method and our largest basis set is about 17% smaller than that of P. Neogràdy *et al.*[118]. Our CASPT2 value using our largest basis set is about 16% smaller than the literature value. As far as basis set sensitivity, the MRCI value increases by 40% when we increase the basis set from the DZ to TZ level, with the largest part of the difference (~20%) occurring between the TZ and QZ levels, as opposed to the largest portion of the difference usually being found between the DZ and TZ levels. This is also true for the CASPT2 values, where about 26% of the nearly 58% total difference being found between the TZ and QZ levels. The difference between the DZ and TZ levels are nearly as large for both the MRCI and CASPT2 values, at ~15% and ~23% respectively.

3.4 Properties at the Equilibrium Bond Length, Obtained using the Doubly Augmented Basis Sets

Table (32) shows the same quantities as Table (31), but now using the *doubly* augmented correlation-consistent polarized valence double-, triple-, quadruple- and quintuple-zeta basis sets. We abbreviate these basis sets in the following discussions and figures as "d-DZ", "d-TZ", "d-QZ, and "d-5Z", respectively. We first discuss the dipole polarizability α_{xx}. Within the values

obtained using the MRCI method there is only about a 2% decrease in the value of the polarizability when the basis set is increased from the d-DZ to d-5Z levels. Most of the difference is between the d- DZ and d-TZ levels (1.4%), with only about 0.4% difference between subsequent levels. Our values calculated using the CASPT2 method are even more stable amongst basis sets considered, with only a 0.5% decrease in the value when increasing the basis set size from the d-DZ to d-5Z levels. This is significant, because calculations done with a lower cardinal number X in the d-aug-ccpVXZ series can be performed, at least for this polarizability, without much loss in accuracy. These calculations take significantly less computational time. We know that this stabilization across cardinal number comes from the addition of the second set of diffuse functions in the basis set. We know this because when we compare to the values obtained using the singly augmented series in Table (31), we see that there was a much higher % difference between values when the basis set was increased from the double-zeta to quintuple-zeta levels for both the MRCI and CASPT2 methods (~7% and ~9%, respectively). The values calculated using the d-5Z basis sets and the MRCI and CASPT2 methods are ~5% and ~2% smaller than the value given by Kalugina and Cherepanov[113], respectively. This is about the same difference we saw for the same values obtained using our 5Z basis set and MRCI and CASPT2 methods (about 5% and 3%, respectively).

Table 32. Electronic properties (in a.u.) of O_2 at the equilibrium bond length, r(O-O)=2.28187 bohr, using the MRCI and CASPT2/d-aug-cc-pVXZ levels of theory.

Method	MRCI	MRCI	MRCI	MRCI	CASPT2	CASPT2	CASPT2	CASPT2	Literature
Basis set	X = D	X = T	X = Q	X = 5	X = D	X = T	X = Q	X = 5	
$-E_0$	150.002067	150.112012	150.146552	150.157681	149.996735	150.114578	150.154184	150.168632	-
α_{xx}	7.998	7.887	7.849	7.826	8.041	8.034	8.020	8.003	8.20[a]
α_{zz}	15.367	15.056	14.948	14.920	15.390	15.309	15.227	15.197	15.09[a]
Θ_{zz}	-0.1899	-0.2641	-0.2602	-0.2617	-0.1903	-0.2570	-0.2512	-0.2520	-0.21[b], -0.22[d],-0.24[c]
Φ_{zzzz}	5.4824	4.1968	4.2921	4.2895	5.4831	4.2134	4.3019	4.2947	4.67[b], 4.70[d],4.48[c]
$E_{x,xxx}$	-18.3036	-17.6089	-17.2863	-17.2669	-18.4462	-17.9592	-17.6627	-17.6392	20.95[a],18.81[d]
$E_{z,zzz}$	19.2409	21.2591	20.7043	20.8193	18.9992	21.2922	20.8353	20.9305	-17.93[b],-18.06[e]
$B_{x,z,xz}$	-110.2305	-112.8545	-107.0655	-105.5565	-112.5295	-114.7905	-114.3285	-113.8950	-
$B_{x,x,zz}$	36.4501	45.2970	44.7550	67.4910	42.1400	44.4930	45.6490	45.4370	-
$B_{x,x,xx}$	-67.9500	-79.8010	-79.4530	-84.9220	-72.8190	-85.3200	-87.4300	-87.4390	-
$B_{z,z,zz}$	-115.8030	-150.0030	-143.8510	-125.1810	-118.2050	-130.9940	-129.2510	-129.228	-
$C_{xx,xx}$	9.6903	13.3216	13.3907	13.3873	10.1833	13.6528	13.8109	13.8259	12.84[b],13.64[e]
$C_{zz,zz}$	20.5033	22.2236	22.0262	21.9659	21.0910	22.7200	22.6312	22.5809	22.30[b],23.00[e]
$C_{xz,xz}$	18.9835	19.4538	19.3547	19.3038	20.4782	21.2897	21.2808	21.2444	19.75[b],20.48[e]
γ_{xxxx}	518.962	526.344	526.528	517.456	526.479	567.99	582.53	580.125	651[f]
γ_{xxzz}	396.679	370.176	362.012	-	481.705	481.447	486.052	500.751	434[g]
γ_{zzzz}	1006.78	773.587	771.715	763.38	734.93	781.737	775.59	768.883	906[f]

a Yu N. Kalugina and V. N. Cherepanov[113], using CCSD(T), with an aug-cc-pVQZ basis set
b Yu N. Kalugina and V. N. Cherepanov[113], using R-CCSD(T), with an aug-cc-pVQZ basis set
c Bartolomei *et al.*[114], using aug-cc-pVQZ basis set and MRCI method, and active space CAS1
d Bartolomei *et al.*[114], using aug-cc-pVQZ basis set and MRCI method, and active space CAS2
e Values taken from Bartolomei *et al.*[114], as cited in Yu N. Kalugina and V. N. Cherepanov[113]
f P. Neogràdy, M. Medved, I. Černusak, and M. Urban[118], using the CCSD method and d- aug-cc-pV5Z basis set
g P. Neogràdy, M. Medved, I. Černusak, and M. Urban[118], using the CCSD method and d- aug-cc-pQ5Z basis set

Examining now the dipole polarizability α_{zz}, we see that there is about a 3% decrease in the MRCI value when increasing the basis set from the d-DZ to the d-5Z level. Again, the CASPT2 series is more stable, with only about a 1% decrease in the value when the basis set size is increased the same way. This difference for the CASPT2 levels is about the same as was seen for the singly augmented series (1.5%), while the 3% decrease for the MRCI values is actually about three times larger of a difference than was seen for the singly augmented series. However, the differences are still small, especially when compared to the other moments and polarizabilities we have calculated. The difference between the value reported by Kalugina and Cherepanov[113] and our MRCI and CASPT2 values obtained with the d-5Z basis set are around 1% in both cases. As with the xx-component of the polarizability, this difference is about the same as that observed between the values of Kalugina and Cherepanov[113] and our 5Z MRCI/CASPT2 values.

We will now discuss the quadrupole moment, Θ_{zz}. The values obtained using the MRCI method do not show a monotonic decrease. There is first a substantial decrease of almost 33% when we increase the basis set size from the d-DZ to d-TZ level. There is then about 1.5% *increase* in the value when we increase the basis set from the d-TZ to d-QZ level, and then finally 0.3% decrease between the d-QZ and d-5Z levels. Therefore, when compared to the large difference between the d-DZ and d-TZ levels, there is essentially no change in the value with a subsequent increase of the basis set size. The same is true for the CASPT2 values. There is a large decrease between the d-DZ and d-TZ levels (almost 30%), then an increase of ~2% when we increase the basis set from the d-TZ to d-QZ levels, and only about 0.3% decrease between the d-QZ and d-5Z levels. There is a stabilization between cardinal numbers compared to the singly augmented

series here as well. The singly augmented values had a difference of about 40% and 38% between the DZ/TZ levels for the MRCI and CASPT2 values, respectively. Therefore, there is almost a 10% reduction in this difference when adding a second set of diffuse functions. The difference between the triple -zeta/quadruple zeta and quadruple-zeta/quintuple-zeta basis sets is reduced when adding a second set of diffuse functions as well, from 7-8% to 1.5% at most. Both our MRCI and CASPT2 d-5Z values for the quadrupole moment are closest to the literature value of Bartolomei *et al*[114]., with about 4% and 5% difference, respectively.

Moving to the hexadecapole moment, (Φ_{zzzz}), calculated with the "d-XZ" series, we find that it follows the same non-monotonic behavior as the quadrupole moment just discussed. Focusing on the MRCI values, there is first a nearly 27% decrease when the basis set size is increased from the d-DZ to d-TZ level. Subsequent increases of the basis set, from d-TZ to d-QZ and from d-QZ to d-5Z, result in about a 2% *increase* in the value of the hexadecapole, and then a 0.06% decrease in the value, respectively. Therefore the value is very stable after the initial 27% decrease. The CASPT2 values follow the same trend, including the large difference in the value between the d-DZ and d-TZ basis sets, which in this case is 26%. The values obtained with subsequent increases of the cardinal number X are even closer to each other than those at the MRCI level, with only a 0.21% increase in increasing the basis set from the d-TZ level to the d-QZ level, and only a 0.17% decrease when increasing the basis set size further to the d-5Z level. When we compare these differences to the differences between values obtained in the "XZ" (singly-augmented) series, we see there is about a 10% larger separation between the doubly augmented double-zeta and doubly augmented triplet-zeta basis sets than between the singly augmented double-zeta and triplet-zeta values. The difference between the TZ/QZ and d-TZ/d-

QZ MRCI values are about the same. However, the difference between the TZ/QZ for the CASPT2 values is an order magnitude larger than between the d-TZ/d-QZ values. The differences between the QZ/5Z levels are significantly larger for both the MRCI and CASPT2 values than between the values obtained using the d-QZ/d-5Z levels. Therefore there is altogether a stabilization in values when using the doubly augmented series as opposed to the singly augmented one. The values of the hexadecapole obtained using the d-5Z basis set and both the MRCI and CASPT2 methods are about 4% smaller than the literature value from Bartolomei *et al*.[114]

The next set of values in Table (32) are the dipole-octupole polarizabilities $E_{x,xxx}$. These values *do* follow a monotonic trend, a decrease in absolute magnitude, when increasing the basis set size. As with most of the properties we have examined, the largest difference is seen between the d-DZ and d-TZ levels. There is a nearly 4% difference between these values obtained using the MRCI method. The difference between the d-TZ and d-QZ is of the same magnitude, at almost 2%. The difference between the d-QZ and d-5Z levels is an order smaller in magnitude, at only about 0.3%. The separations are about the same in the CASPT2 case (same magnitude), but even smaller. Therefore this property is rather insensitive altogether to a change in cardinal number. Both the MRCI and CASPT2 values obtained using the d-5Z basis set are closest to the literature value of Kalugina and Cherepanov[113], at only about a 4% and 2% difference, respectively.

When we now examine the dipole-quadrupole polarizability $E_{z,zzz}$, we see that this property once again deviates from monotonic behavior. Looking at the MRCI(CASPT2) values, we see there is about a 10% (12%) increase in the dipole-octopole polarizability when we increase the basis set

from the d-DZ to d-TZ level. This is followed by a 3% (2%) decrease, when increasing the basis set size from the d-TZ to d-QZ levels, and then a less than 1% (for both MRCI and CASPT2) increase in the value. The MRCI value using the d-5Z basis set is only 0.63% smaller than the value reported by Kalugina and Cherepanov[113], and the CASPT2 value is only ~0.1% different, nearly identical to their value.

We now move on to the dipole-dipole-quadrupole polarizability $B_{x,z,xz}$ that was obtained using the doubly augmented basis sets. This tensor does not show monotonic behavior with the size of the basis set. However, the differences between the values obtained at the different cardinal numbers X are an order of magnitude smaller than the differences between the singly augmented basis set levels. There is a ~2% decrease in the MRCI value of $B_{x,z,xz}$ when the basis set is increased from the d-DZ to d-TZ levels. When the basis set is increased from the d-TZ to d-QZ levels, there is over a 5% increase. So in this case the largest difference is between the d-TZ/d-QZ levels (this was not true for $B_{x,z,xz}$ when we considered the singly augmented series, where the largest difference was between the DZ and TZ levels). An additional increase of the cardinal number to the d-5Z level causes an almost 1.5% increase in the value. Looking at the CASPT2 values, we see that there is also about a 2% decrease when we increase the basis set from the d-DZ to d-TZ level, as there was between the same MRCI values. However, in the CASPT2 case, there is a much smaller difference in between the d-TZ and d-QZ levels (0.4%). So in the CASPT2 the largest difference is between the d-DZ and d-TZ levels. The difference between the d-QZ and d-5Z levels is 0.4% as well.

The next dipole-dipole-quadrupole polarizability in Table (32) is $B_{x,x,zz}$. Again this tensor does not increase monotonically with the basis set. When the basis set is increased from the d-DZ to the d-TZ level using the MRCI method, there is an almost 22% increase in the value of the polarizability. There is then about a 1% decrease when the basis set is further enlarged from the d-TZ to d-QZ level. From the d-QZ to d-5Z level, there is over a 40% increase in the value of the polarizability. Comparing these values to the CASPT2 situation, we see a 5% increase in the value of the polarizability when we increase the basis set from the d-DZ to the d-TZ level. There is then about a 3% increase when the basis set is increased in size from the d-TZ to the d-QZ level, and then finally about a 0.5% difference between the values at the d-QZ and d-5Z level. Given the stability in the CASPT2 values, especially the very small difference between the two largest basis sets, it is likely that the CASPT2 values are the more accurate between the two methods.

We know turn to an examination of the dipole-dipole-quadrupole polarizability $B_{x,x,xx}$ calculated using the doubly augmented basis sets. Not surprisingly at this point, these values also do not follow a monotonic pattern. There is a 16% decrease in the MRCI value when the basis set size is increased from the d-DZ to d-TZ level. There is then a ~0.5% increase between the d-TZ and d-QZ values (so these two values for the polarizability are essentially the same). Finally, there is a ~7% decrease in the value of the dipole-dipole polarizability when the basis set is further increased to the d-5Z level. The situation for the CASPT2 values is similar. There is about a 16% decrease in the value of the polarizability when the basis set is increased from the d-DZ to d-TZ level. There is a larger difference between the d-TZ and d-QZ values obtained with the CASPT2

method than those obtained with the MRCI method (about 2% instead of 0.5%). However, the values at the d-QZ and d-5Z are the same to the second decimal place in the CASPT2 case.

The fourth and final non-redundant component of the dipole-dipole-quadrupole polarizability is $B_{z,z,zz}$. There is the same decrease seen in the MRCI value of this polarizability when increasing the basis set size from the d-DZ to d-TZ levels as was seen in the last three components of the B-tensor. This decrease is a difference of ~26%. There is then an increase of about 4% when the basis set is increased to the d-QZ level, and then finally an increase of about 13% between the d-QZ and d-5Z levels. The CASPT2 values for this tensor also display non-monotonic behavior, but as seen previously, the values display greater stability against a change in the cardinal number than the MRCI values. There is only a 10% decrease in between the d-DZ and d-TZ levels, and only about a 1% and 0.01% increase between the d-TZ/d-QZ and d-QZ/d-5Z levels, respectively.

We will now discuss the quadrupole-quadrupole polarizabilities ($C_{\alpha\beta,\gamma\delta}$). The first in Table (32) is $C_{xx,xx}$. The MRCI values of this tensor increase with basis set size until the d-5Z basis set. There is a 32% difference between the d-DZ and d-TZ levels, and the values at the d-TZ and d-QZ levels are nearly identical, with only about a 0.5% difference. The difference between the d-QZ and d-5Z levels is an extremely slight decrease, with only a 0.03% difference between values. The CASPT2 values increase in value with an increase in basis set size. There is a total of a 30% increase in going from the d-DZ to d-5Z basis set, and a whopping 29% of this difference occurs between the d-DZ and d-TZ levels. Comparing to the literature values, our MRCI and

CASPT2 values are nearest to that of Bartolomei *et al*[114]., with only between 1-2% difference in both cases.

The next quadrupole-quadrupole polarizability is $C_{zz,zz}$. These values do not vary monotonically with the basis set size. We instead observe that there is first an increase of 8% in the MRCI value of the polarizability when we increase the basis set size from the d-DZ to the d-TZ level, but then the value decreases when the basis set is increased to the d-QZ level. However, the decrease is only by less than 1%. There is then an additional decrease in the polarizability when the basis set size is increased to the d-5Z level. However, this difference is even smaller. Therefore, the value of $C_{zz,zz}$ is essentially constant after the increase from the d-DZ to the d-TZ basis set size. The same is seen for the CASPT2 values. There is an initial increase of around 7%, but then the differences in increasing the cardinal number any further are far under 1%. Altogether this is a significant stabilization for both methods compared to the singly augmented series, in which the total percent difference in increasing the basis set size from double-zeta to quintuple-zeta was around 20%. Comparing to the literature values, our values are consistent with the value calculated by Kalugina and Cherepanov[113], with a difference of less than 2% for both our MRCI and CASPT2 values. Our values are near that of Bartolomei *et al.*[114] as well, with less than 5% difference between them for both methods.

The third and final component of the quadrupole-quadrupole polarizability is $C_{xz,xz}$. For both the MRCI and CASPT2 values, the largest difference is between the d-DZ and d-TZ basis set levels, at less than 3% and less than 4%, respectively. Any additional increase in the cardinal number produces a value of the polarizability that is under 1% different than the d-TZ level value (and in

most cases far under even 0.5%). The MRCI value obtained using our best basis set is closest to the value of Kalugina and Cherepanov[113], with only about a 2% difference, but it is still less than 6% different than the Bartolomei *et al*.[114] value. Our CASPT2 value however, is closer to the value calculated by Bartolomei *et al*.[114], with a difference of about 4%, and over 7% different from the value calculated by Kalugina and Cherepanov[113].

We now discuss our last set of values, the second (hyper)polarizabilities ($\gamma_{\alpha\beta\gamma\delta}$). We first look at the values for γ_{xxxx}. The MRCI values increase with increased basis set size until the d-5Z level, where there is a *very* slight decrease (around 0.02 %). In fact, the value for the hyperpolarizability at the d-5Z level is only about 0.3% different than that obtained at the d-DZ level. There is more separation in the CASPT2 levels, with about a 10% difference between the smallest (d-DZ) and largest (d-5Z) basis sets. These differences are dramatically smaller than those between the basis set sizes for the singly augmented series, where the total difference between the DZ/5Z levels was over 80% for both methods. Comparison with the literature value shows that our MRCI value at the d-5Z level is about 22% different than that provided by P. Neogràdy *et al.*[118] and our CASPT2 value is about 12% different.

The second hyper-polarizability in table (2) is γ_{xxzz}. We were able to obtain values at the d-DZ, d-TZ, and d-QZ level with the MRCI method. There is about a 9% reduction in the value of this hyper-polarizability when we increase the basis set from the d-DZ to the d-5Z level. The CASPT2 values are not monotonic with the increase in basis set size. However, our value at the d-5Z level is the farthest from that at the d-DZ level, and the difference is still less than 4%.

P. Neogràdy *et al.*[118] did not obtain a value using the d-aug-cc-pV5Z basis set, but they did obtain a value using the d-aug-cc-pVQZ basis set that we can use to compare to our values using the same basis set. Our value at the d-QZ level and using the MRCI method is about 18% different from the literature value, while our CASPT2 value using the d-5Z basis set is about 11% different from the literature value.

Finally, our last hyperpolarizability to discuss is γ_{zzzz}. The MRCI values for this quantity decrease monotonically with an increase in basis set size. The separation between basis set levels is larger than for the previous hyperpolarizabilities discussed. There is a 27.5% reduction in the MRCI value of this tensor when we increase the basis set size to the d-5Z level. Over 26% of this difference is between the d-DZ and d-TZ levels, however, so subsequent increases of the cardinal number only cause small decreases. The CASPT2 values, in contrast, do not decrease monotonically with the basis set size, and in fact the value of γ_{zzzz} is larger at our highest basis set level than at our smallest. However, the difference between the d-DZ and d-5Z levels is only 4.5%, with differences of less than 1% between the d-TZ/d-QZ and d-QZ/d-5Z levels. So in general the CASPT2 values show less change with basis set size in this case than the MRCI values. Our MRCI value using the d-5Z basis set is less than 6% different from the literature value in Table (32), and our CASPT2 value is less than 7% different.

3.5 Properties Obtained at non-Equilibrium Bond Lengths

In order to calculate vibrational averages of the multipole moments and (hyper)polarizabilities discussed, we must have values of these quantities away from equilibrium. In particular, we wish to obtain these quantities for the first six vibrational levels. In order to decide what bond distances we wish to obtain these properties at, two things were done. First, a calculation done at the MCSCF level that included all nine triplet states formed from two triplet oxygen atoms showed that the ground state is well separated from the other eight excited states for O-O bond lengths under about 3.78 bohr. Most calculations have unphysical results at bond lengths over 3.6 bohr however, so this was used as the upper limit of the bond length. Indeed, a majority of the calculations attempted for bond lengths larger than this either did not converge or gave unphysical results, blowing up to extremely large numbers. Secondly, using our potential energy curve obtained with the MRCI method and the d-aug-cc-pVQZ basis set, we used the Numerov-Cooley[129,130] technique to numerically solve the rovibrational Schrödinger equation. The vibrational wavefunctions in Figure (3) were thus obtained. This figure shows that the vibrational wavefunctions are well embedded in the region of O-O=1.8-3 bohr. Therefore, the lower limit for our calculations was a bond distance of 1.8 bohr.

Figure 3. Wavefunctions for the first six vibrational levels (υ=0-5) for the ground rotational state (J=0) of the O_2 molecule

Figure (4) shows the dipole polarizability (α_{zz}) using the "d-XZ" basis sets, using both the MRCI and CASPT2 methods, as a function of the O-O bond length. The MRCI and CASPT2 values agree within 2% for the d-DZ levels, within 3% for the d-TZ levels, and within about 7% for the d-QZ levels. Once we reach the d-5Z basis set level, differences are again within 3% for all bond distances considered. For all levels, the greatest difference between the MRCI and CASPT2 values occurs at the bond distances of 2.646 bohr and 2.929 bohr.

We now observe the basis set sensitivity of the dipole polarizability (α_{zz}) within the CASPT2 method for the bond distances studied (Figure (5)). Although the figure shows all levels of the cardinal number considered, we will restrict our discussions within a particular method to the effect of adding a second set of diffuse functions to our largest basis set, that is, X=5. For this component of the dipole polarizability, the effect of adding a second set of these functions is negligible, with the largest difference between the 5Z and d-5Z basis sets occurring at the shortest bond distance (1.8 bohr), where it is only 0.5%. Figure (6) shows the same quantity and basis sets for the MRCI method. From this figure, we can see that the DZ/d-DZ basis sets are separated from the values calculated using higher order basis sets. As with the CASPT2 values, the differences between the singly and doubly augmented basis sets 5Z/d-5Z are very small, at 0.4% or less.

Our next figure shows the dipole polarizability (α_{xx}) using the "d-XZ" basis sets and the MRCI and CASPT2 methods versus the O-O bond length. There is improved agreement between methods for the d-DZ basis set, with less than 1% difference between methods. The largest differences between the methods using the d-TZ basis set is around 2%, and then there is a

difference of almost 9% between methods at a bond distance of 2.9 bohr when using the d-QZ basis set. As with the polarizability (α_{zz}), the difference between methods using the d-5Z basis set is within 3%.

Figure (8) shows the dipole polarizability (α_{xx}) obtained with the CASPT2 method and all basis sets. The difference between the singly and doubly augmented basis sets is over 13% at some points between the DZ/d-DZ basis sets, but this difference grows smaller between sets as the cardinal number is increased, until it is under 1% between the 5Z/d-5Z basis sets. This is also the case for the values obtained using the MRCI method and the singly and doubly augmented basis sets (Figure (9)).

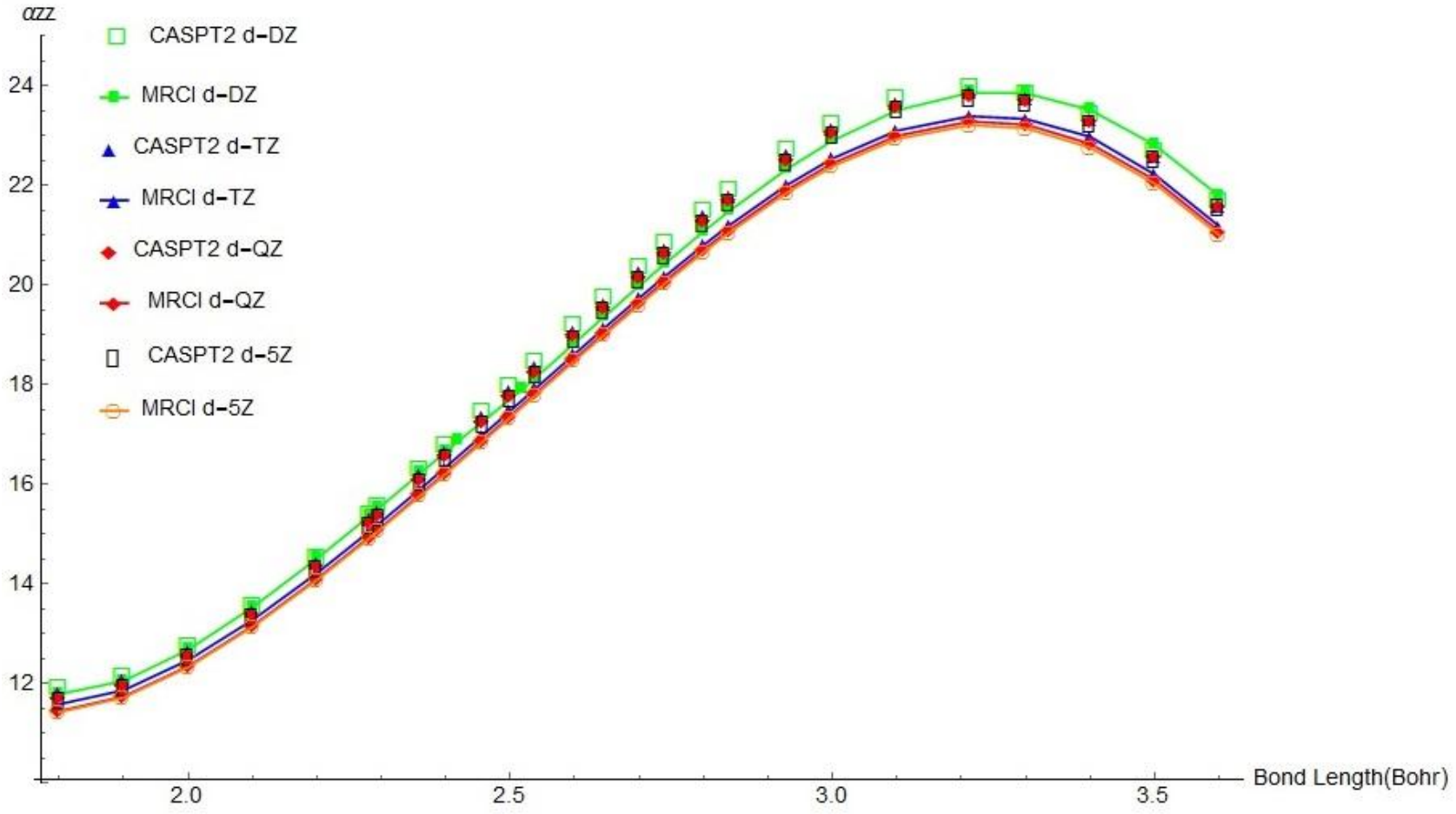

Figure 4. The dipole polarizability (α_{zz}) in atomic units versus bond length for the CASPT2 and MRCI methods, using the doubly augmented basis sets.

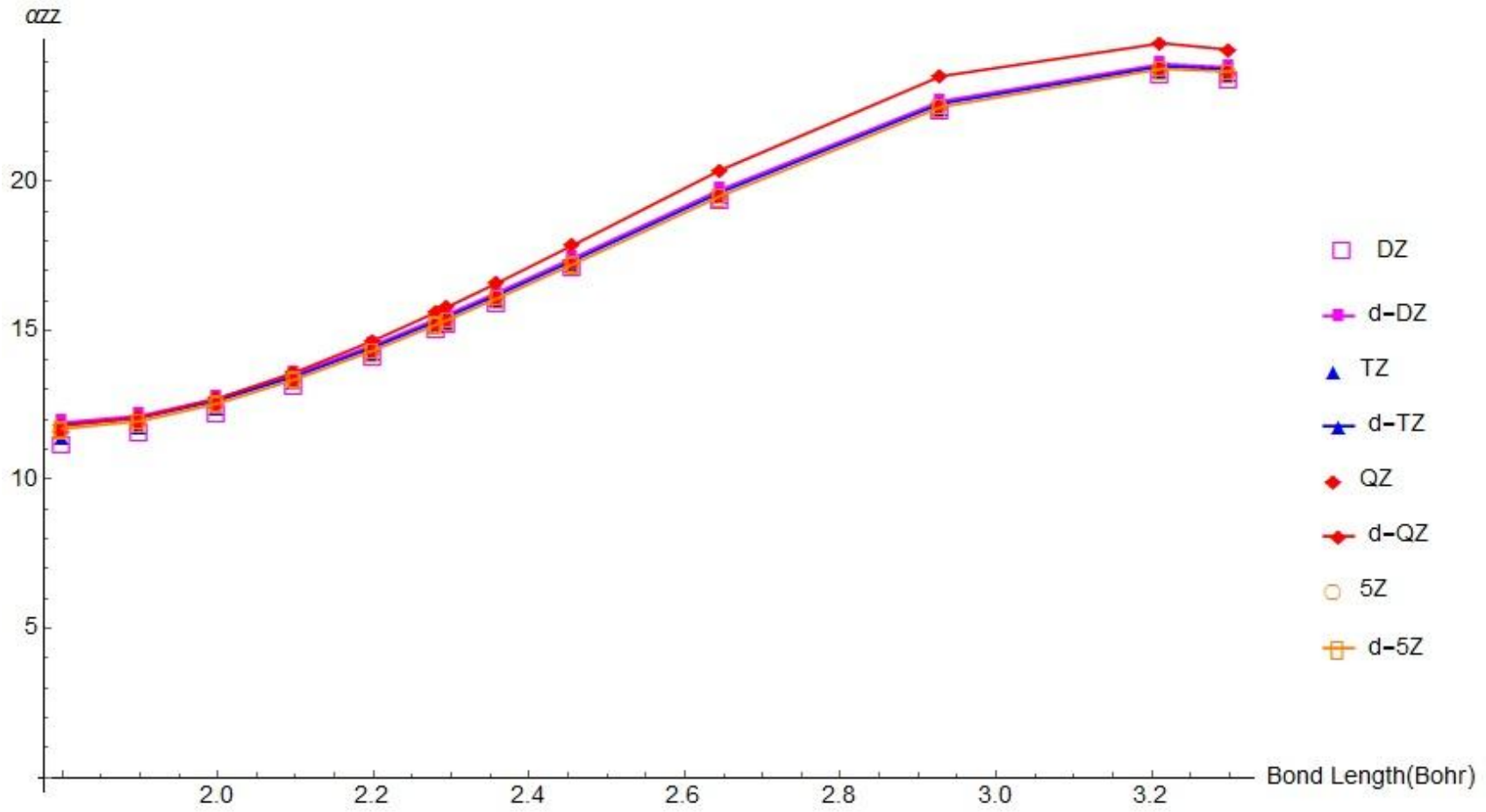

Figure 5. The dipole polarizability (α_{zz}) in atomic units versus bond length obtained with the CASPT2 method, using the singly and doubly augmented basis sets.

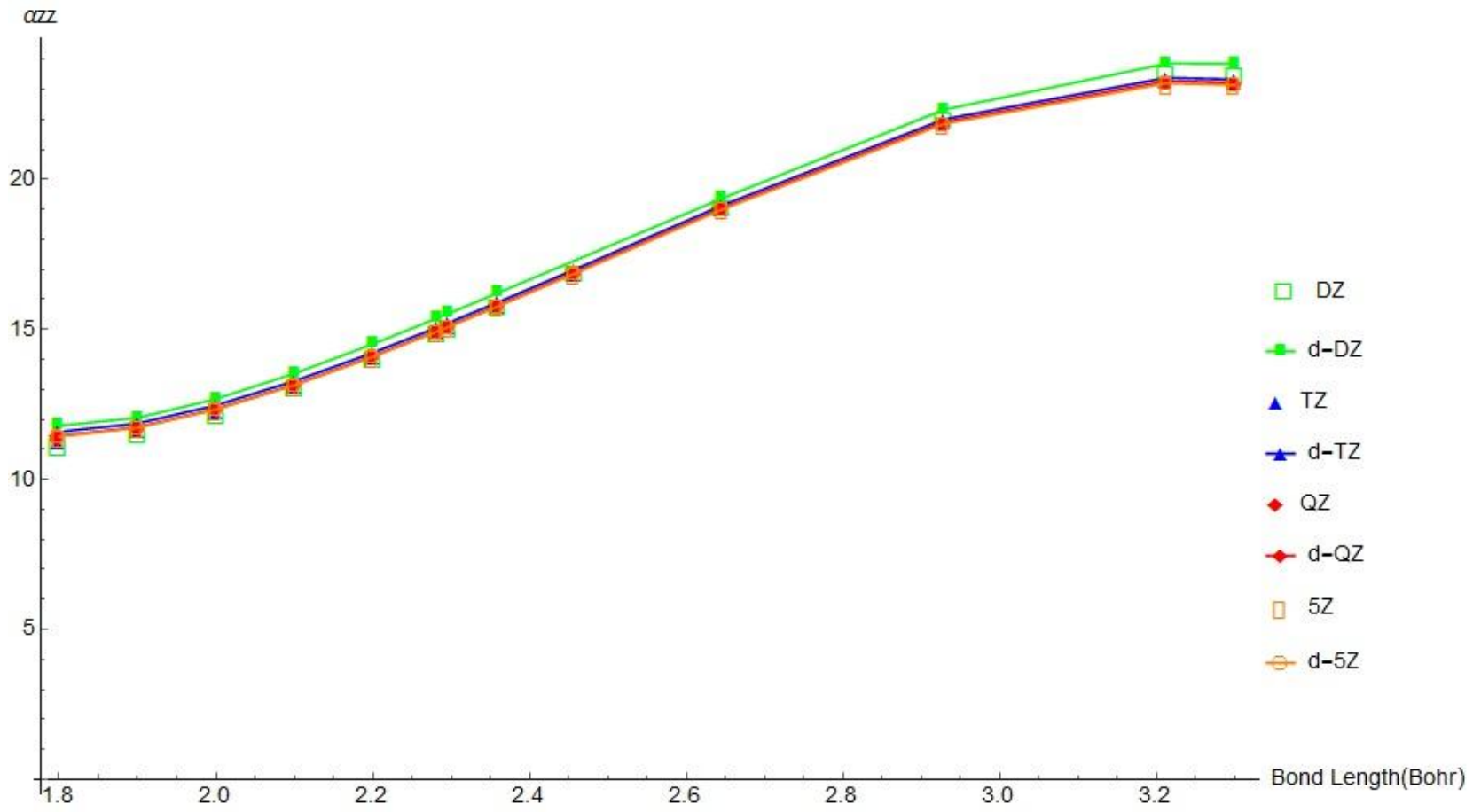

Figure 6. The dipole polarizability (α_{zz}) in atomic units versus bond length, obtained using the MRCI method and the singly and doubly augmented basis sets.

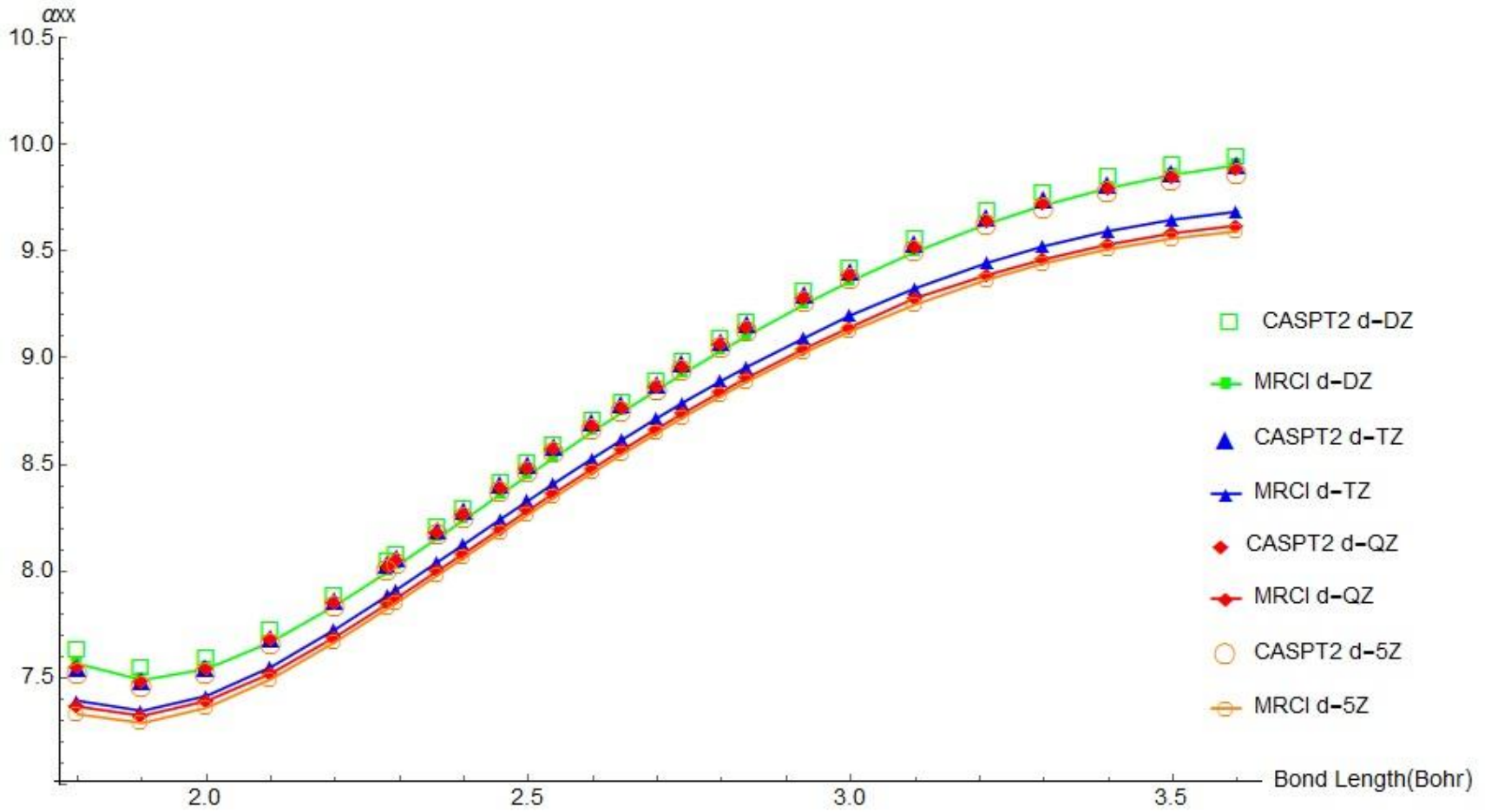

Figure 7. The dipole polarizability (α_{xx}) in atomic units versus bond length, obtained with the MRCI and CASPT2 methods and the doubly augmented basis sets.

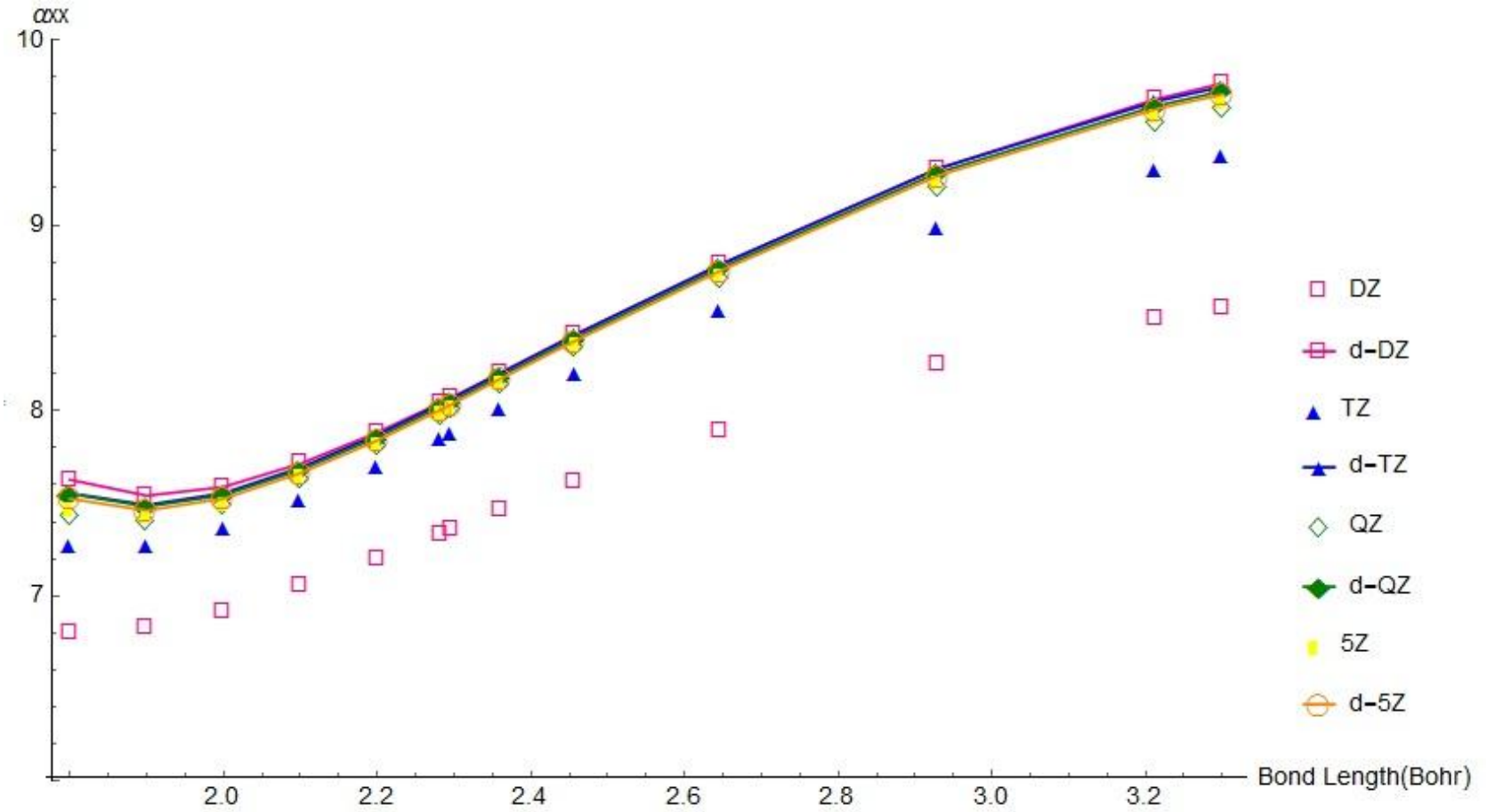

Figure 8. The dipole polarizability (α_{xx}) in atomic units versus bond length, obtained with the CASPT2 method and the singly and doubly augmented basis sets.

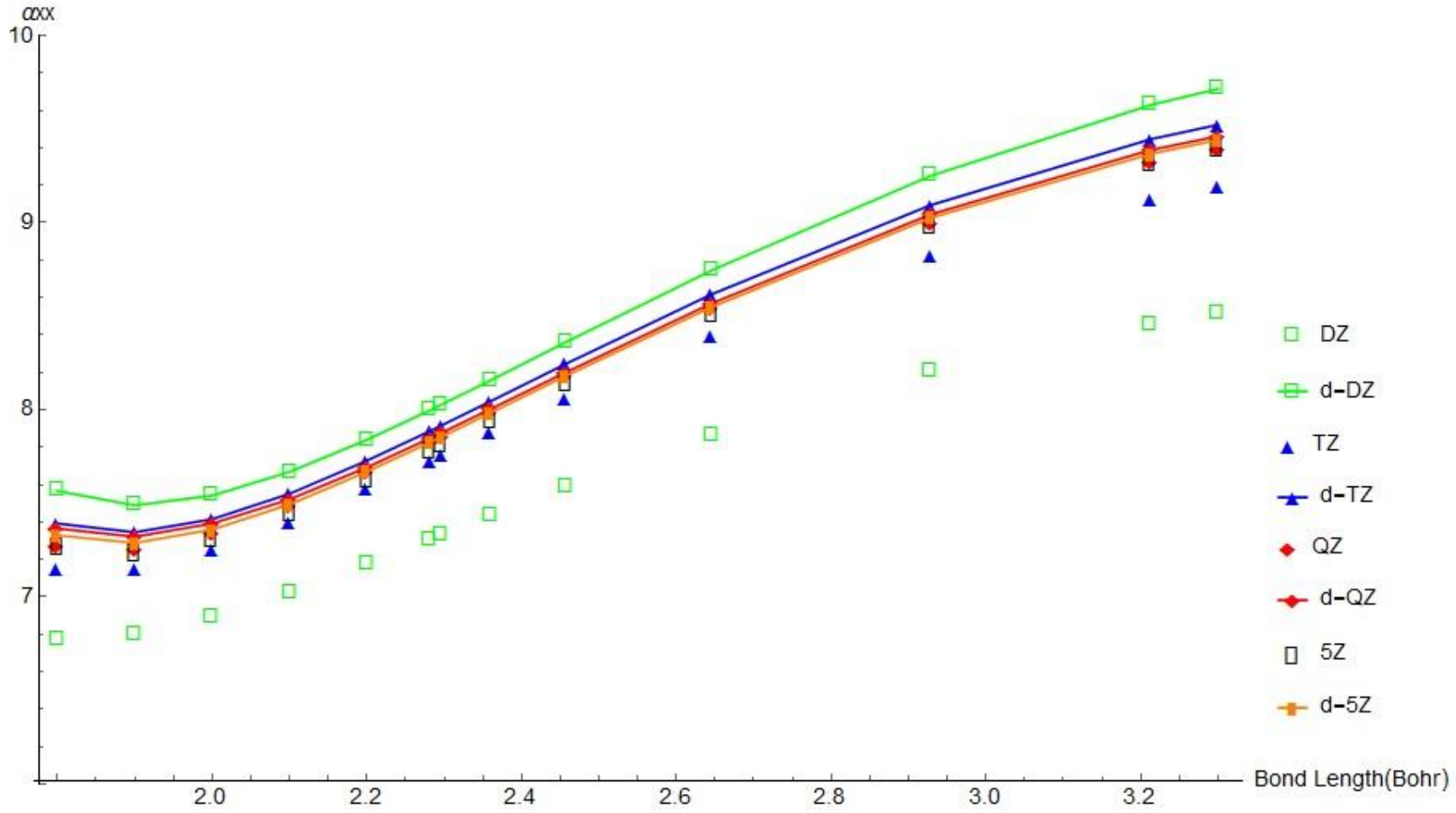

Figure 9. The dipole polarizability (α_{xx}) in atomic units versus bond length, obtained with the MRCI method and the singly and doubly augmented basis sets.

The next property we examine as a function of bond length is the quadrupole moment Θ_{zz}, shown in Figure (10). Because the quadrupole moment is very small and positive for the CASPT2 method and very small and negative for the MRCI method at 2.457 bohr, the difference between them blows up to 407% at this point when looking at the d-5Z basis set values. All other bond distances have differences of 0.01-9%, with the higher end of the difference again occurring for bond distances longer than equilibrium, as was seen for the dipole polarizabilities. Also seen clearly is the separation of the d-DZ basis set from all other basis sets, as was seen for many of the properties we examined at equilibrium. It is interesting to note the sign change of the quadrupole moment, that occurs as the bond distance is increased past equilibrium. Figure (11) shows a schematic diagram for why this occurs[82]. The quadrupole moment behaves as a $\cos^2(\theta)$ function. Therefore, when the bond distance is lengthened in the O_2 molecule, the electron density is shifted from a region where the cosine squared function is negative to one that is positive.

Figure (12) shows the quadrupole moment Θ_{zz} versus bond distance for the singly and doubly augmented basis sets within the CASPT2 method. The DZ/d-DZ levels are again clearly separated from the larger basis set. The values have a large difference when they are very small, near the point where the quadrupole moment changes sign, as was seen in the previous figure (here observed in the region between 2.36-2.46 bohr). Otherwise, the effect of adding a second diffuse function is very small (less than 1% between the 5Z/d-5Z basis sets). Figure (13) shows the quadrupole moment versus both length obtained using the MRCI method. The difference between the singly and doubly augmented basis set values at the point 2.46 bohr are even larger

for the MRCI method, as the value of the quadrupole at this point is even smaller, on the order of 10^{-2} a.u. Otherwise, the differences are again very small.

We now discuss the hexadecapole moment(Φ_{zzzz}) for both methods as a function of bond distance, as shown in Figure (14). Right away we can see the separation of the d-DZ level values from all other basis set values. The two methods are in good agreement for this property as well, with around 1% difference at most between the d-DZ values, less than 3% difference between the values using the d-TZ basis set, around 3% difference at most between the d-QZ values, and finally around 3% at most difference between the methods when using the d-5Z basis set. Unlike the previous properties we examined, the largest differences occur for the *shortest* bond distance in this case, of 1.8 bohr.

The next figure shows the hexadecapole moment obtained using the CASPT2 method, and all basis sets. We can see that in this case both the singly and doubly augmented double zeta basis sets are separated from all other basis sets. As with the quadrupole moment, adding a second diffuse function has little effect at the quintuple zeta level, with less than a 2% difference. Figure (16) shows the same quantities for MRCI, which show the same behavior as those obtained using the CASPT2 method.

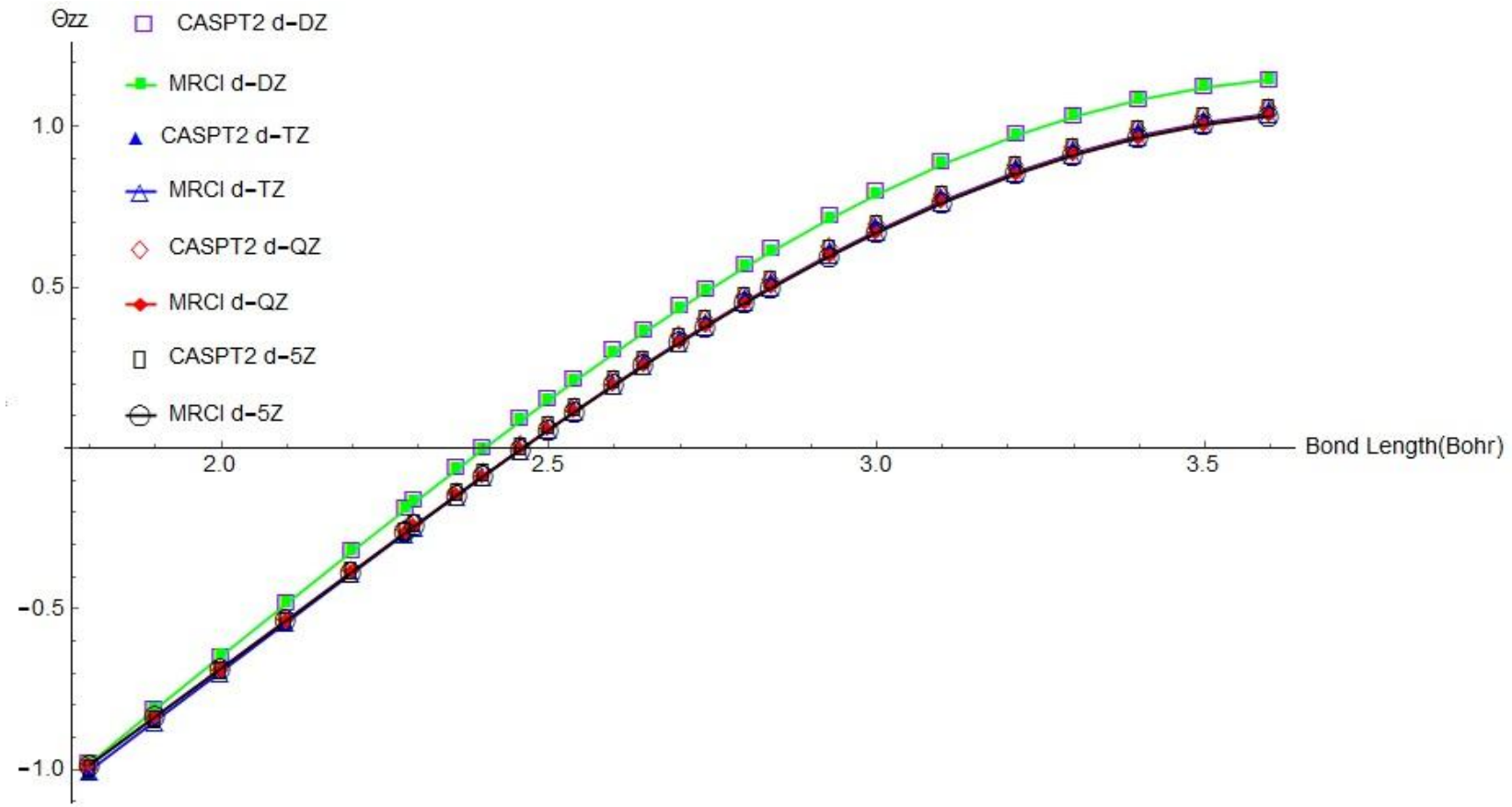

Figure 10. The quadrupole moment (Θ_{zz}) in atomic units versus bond length obtained with the MRCI and CASPT2 methods and the doubly augmented basis sets.

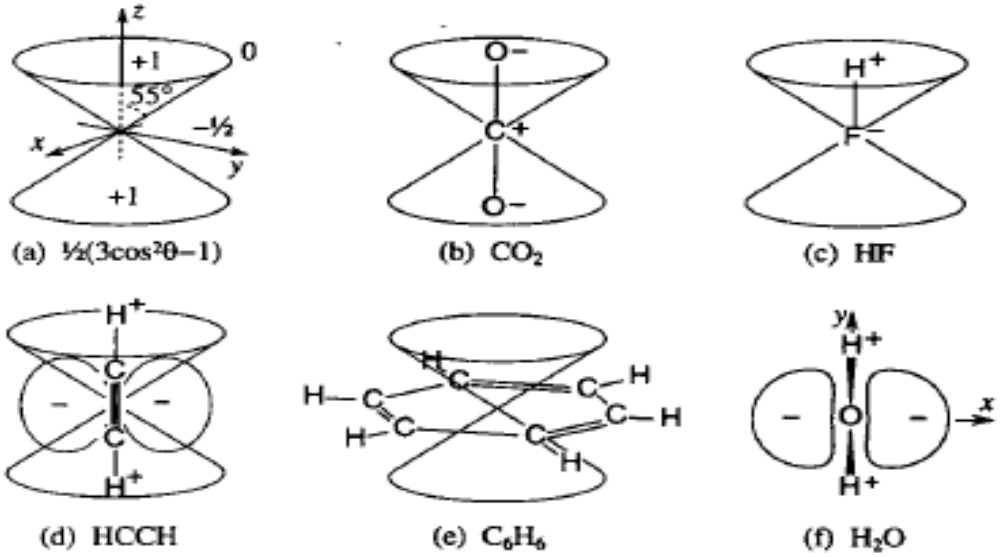

FIG. 2.1. Quadrupole moments.

$$\Theta_{zz} = \int \rho(\mathbf{r}) r^2 \left(\tfrac{3}{2}\cos^2\theta - \tfrac{1}{2}\right) \mathrm{d}^3\mathbf{r}, \qquad (2.1.2)$$

Figure 11. The shape of the quadrupole moment as determined by the $\cos^2(\theta)$ function[82]

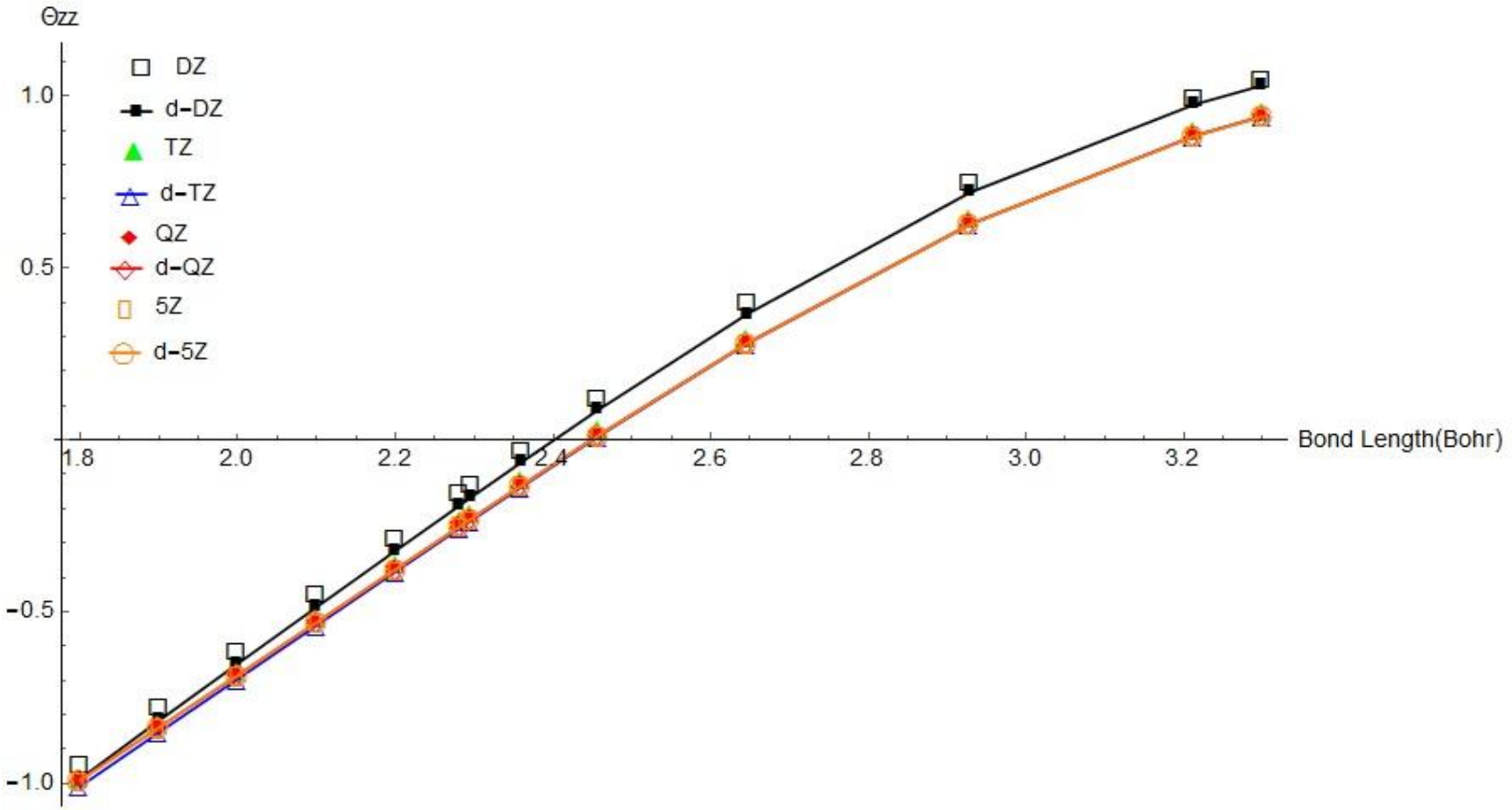

Figure 12. The quadrupole moment (Θ_{zz}) in atomic units versus bond length obtained using the CASPT2 method and the doubly and singly augmented basis sets.

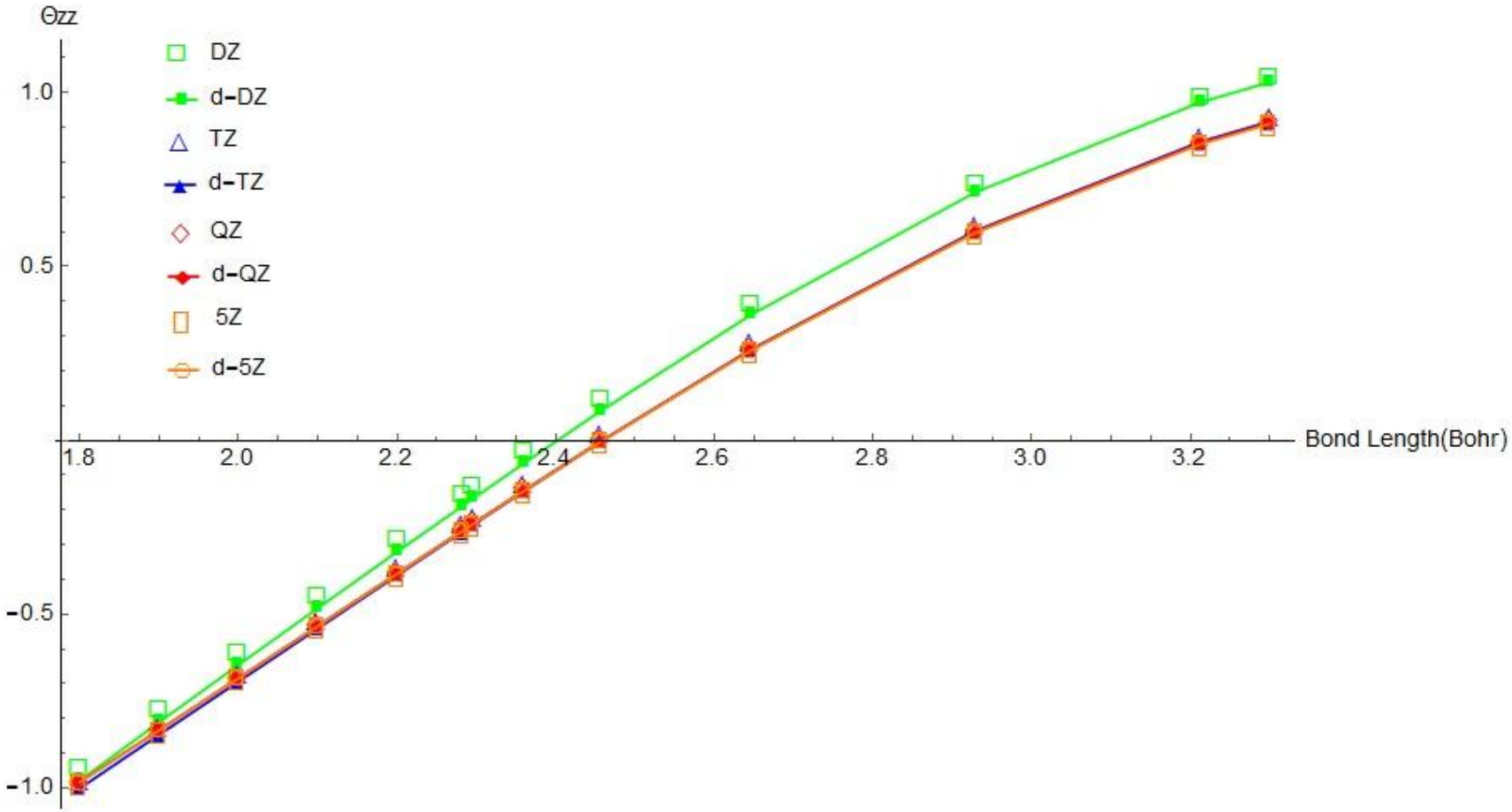

Figure 13. The quadrupole moment (Θ_{zz}) in atomic units versus bond length obtained using the MRCI method and the doubly and singly augmented basis sets.

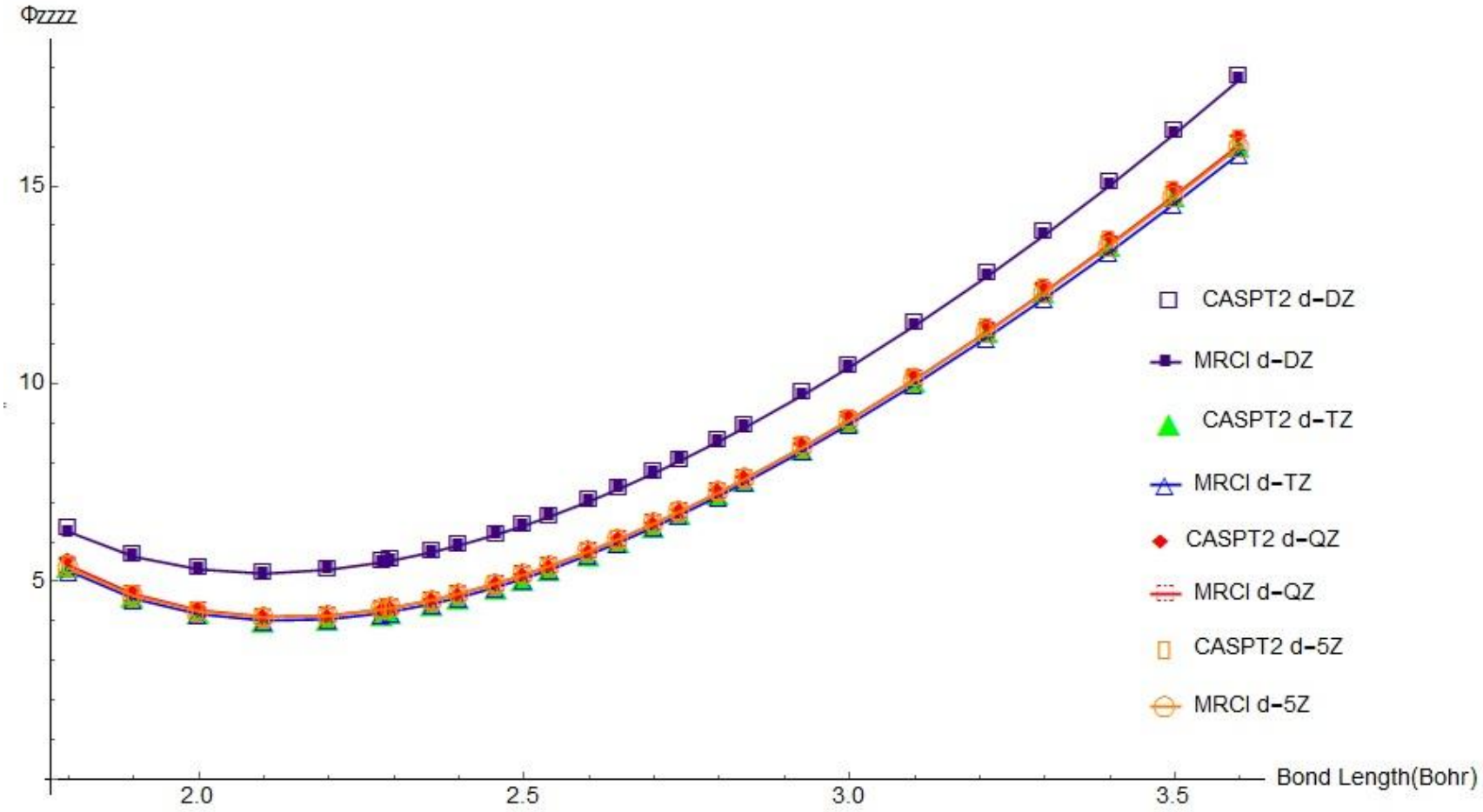

Figure 14. The hexadecapole moment (Φ_{zzzz}) in atomic units versus bond length obtained using the MRCI and CASPT2 methods, and the doubly augmented basis sets.

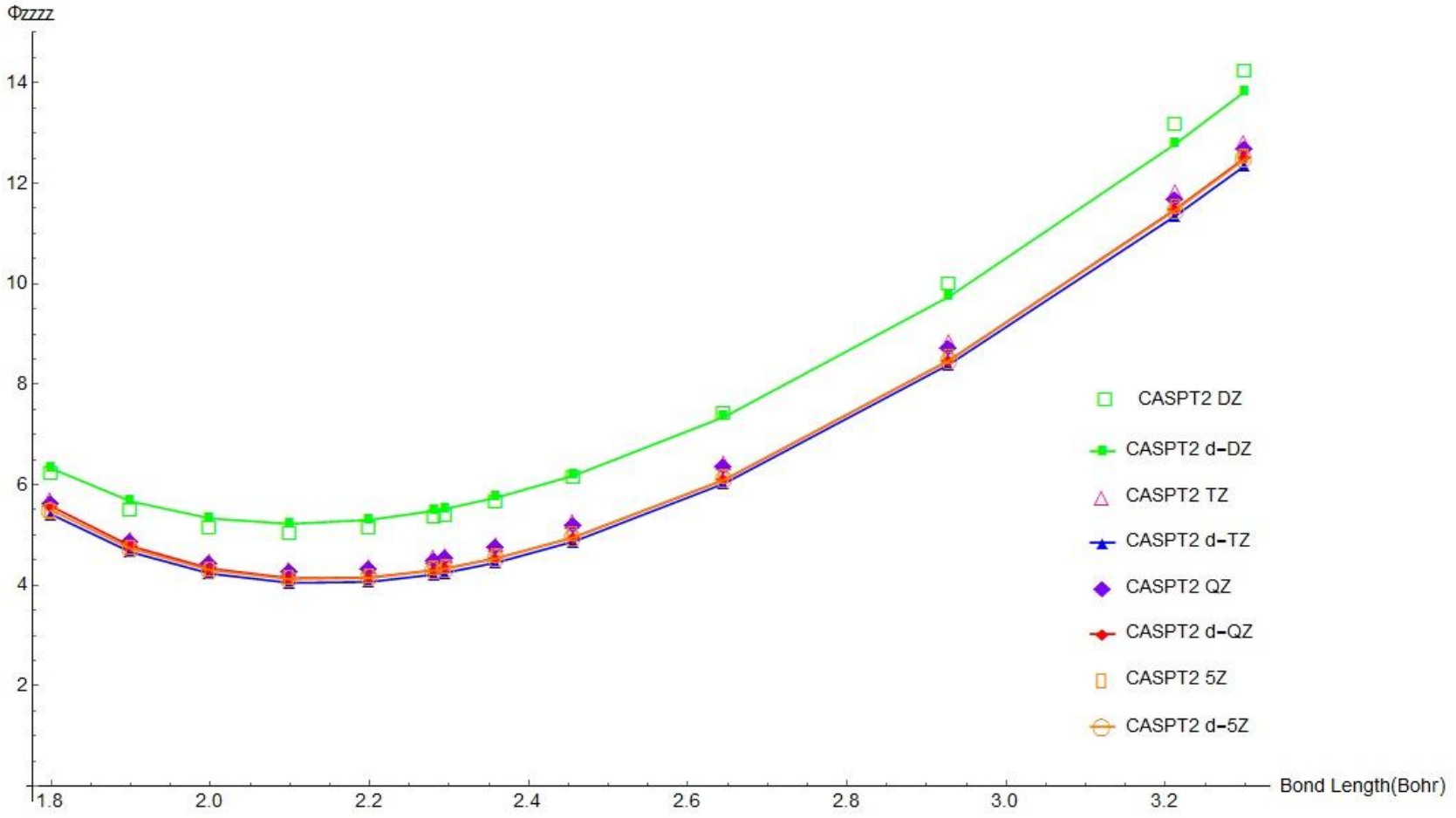

Figure 15. The hexadecapole moment (Φ_{zzzz}) in atomic units versus bond length obtained using the CASPT2 method and the singly and doubly augmented basis sets.

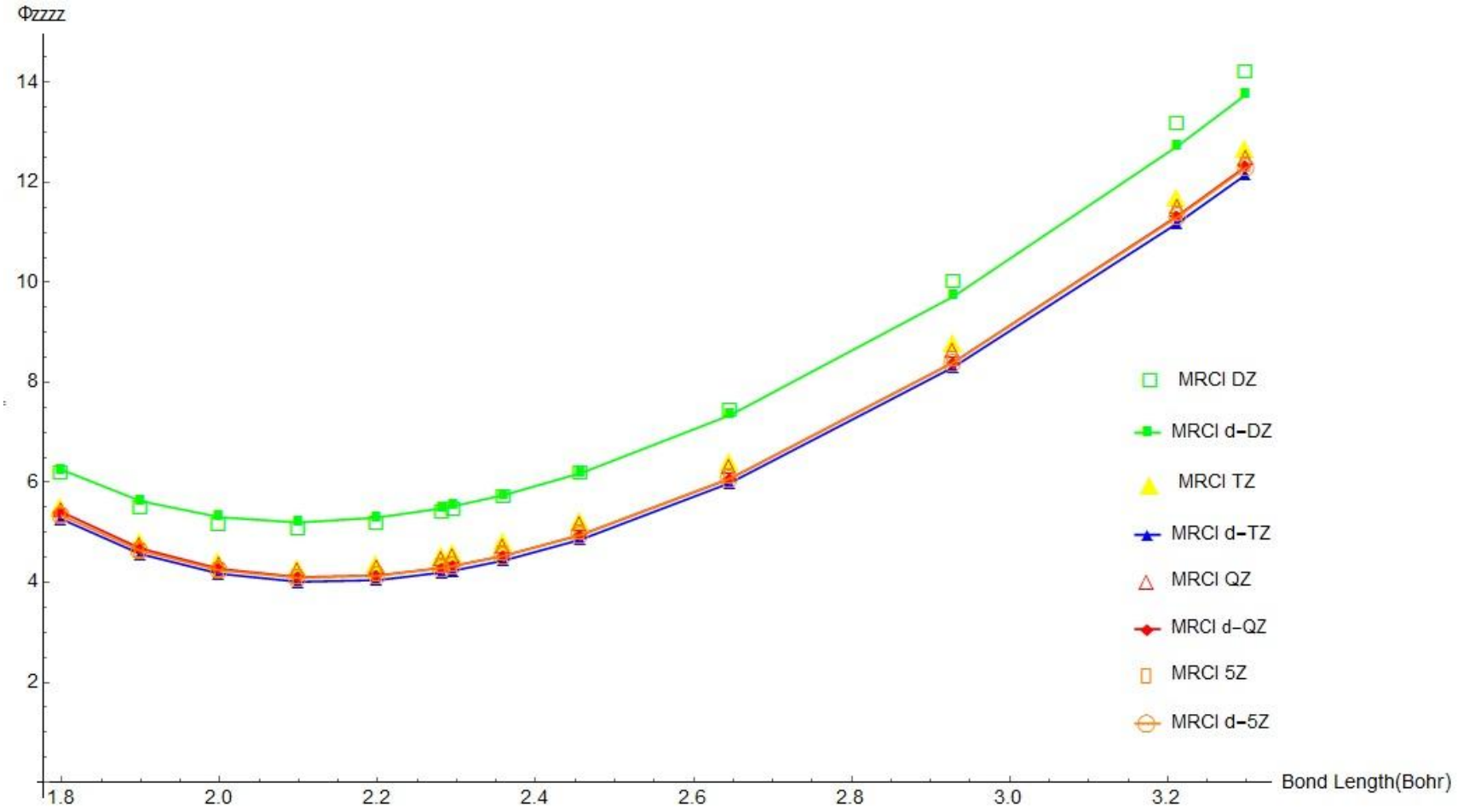

Figure 16. The hexadecapole moment (Φ_{zzzz}) in atomic units versus bond length obtained using the MRCI method and the singly and doubly augmented basis sets.

We will now discuss the dipole-octopole polarizability, $E_{x,xxx}$. As was the case for the hexadecapole moment, the largest differences occur at the shortest distance and grow smaller as the bond is lengthened. This is seen clearly in Figure (17). There is good agreement between methods however, with even the largest differences being under 5%.

We now look at the dipole-octopole polarizability $E_{x,xxx}$ as obtained within the CASPT2 method. Figure (18) shows these values. We can see clearly that as the cardinal number is increased, the difference between the singly and doubly augmented curves grows smaller. At the shortest distance of 1.8 bohr, the difference between the 5Z/d-5Z basis sets is almost 4%, but the difference quickly drops off as the bond is lengthened, and is under 1% for most bond distances. The same is true for the values obtained using the MRCI method (Figure (19)).

Figure (20) shows a comparison of methods for the dipole-octopole polarizability $E_{z,zzz}$. Again, the largest difference occurs at the shortest bond distance, and in this case is as much as 13% (between the d-QZ levels). However, the differences between methods at all other bond lengths considered are smaller than those for $E_{x,xxx}$.

Figure (21) shows the values for this tensor obtained using the CASPT2 method, and all singly and doubly augmented basis sets studied. As observed for the dipole-octopole polarizability $E_{x,xxx}$, the difference between the singly and doubly augmented basis sets decreases with increasing cardinal number. At a bond distance of 1.8 bohr, the largest difference occurs, at 33%, with a values of 3.05 a.u. at the 5Z level and a value of 4.30 at the d-5Z level. This difference quickly drops off with increasing bond length and is between 1-3% for most bond lengths. Figure (22) shows the MRCI values for this tensor, which behaves very similarly to the CASPT2 values, with the largest difference occurring for 1.8 bohr, at 27%.

Figure (23) shows the dipole-dipole-quadrupole polarizability, $B_{x,z,xz}$ versus the bond length. The differences between methods grow larger with the basis set size for this tensor, growing from around 2% between the d-DZ values to around 9% for the d-5Z values. The points at 1.8 bohr show this trend well, as this is where the largest differences are found. For the d-QZ levels, there is also around an 8% difference after 3 bohr, which occurs because the MRCI values have some unreliability in that region.

Figure (24) shows the values of $B_{x,z,xz}$ obtained using just the CASPT2 method, and all singly and doubly augmented basis sets. Like previous properties discussed, the differences between the singly and doubly augmented basis sets do grow smaller with increased cardinal number. However, even between the 5Z/d-5Z basis sets, there is an appreciable difference between values. The largest difference is at shorter distances of the bond length, with ~17% difference at 1.8 bohr, but there is at least 4% difference at all bond lengths studied. The situation is the same for the MRCI values (Figure (25)).

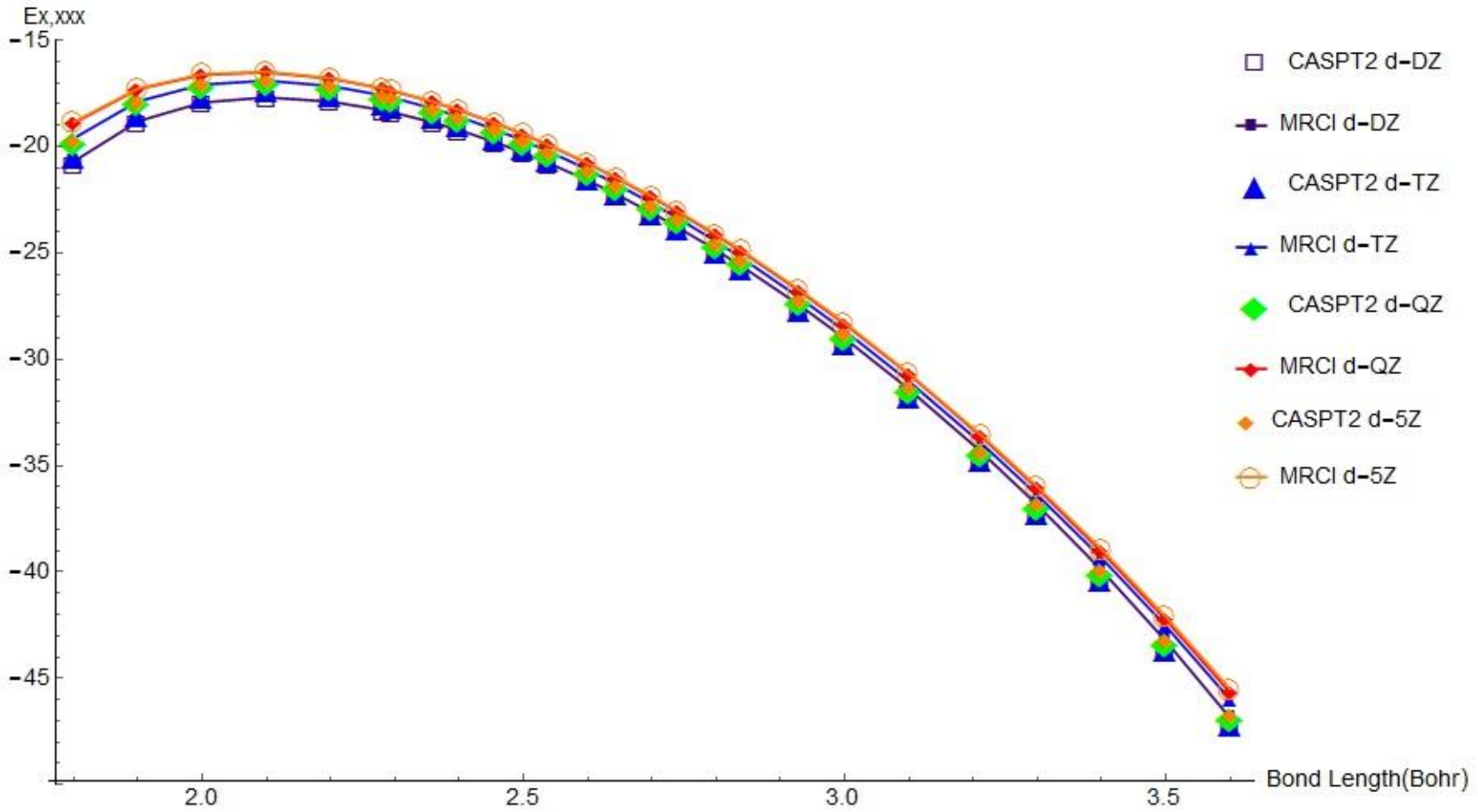

Figure 17. The dipole-octopole polarizability ($E_{x,xxx}$) in atomic units versus the bond length obtained using the MRCI and CASPT2 methods, with the doubly augmented basis sets.

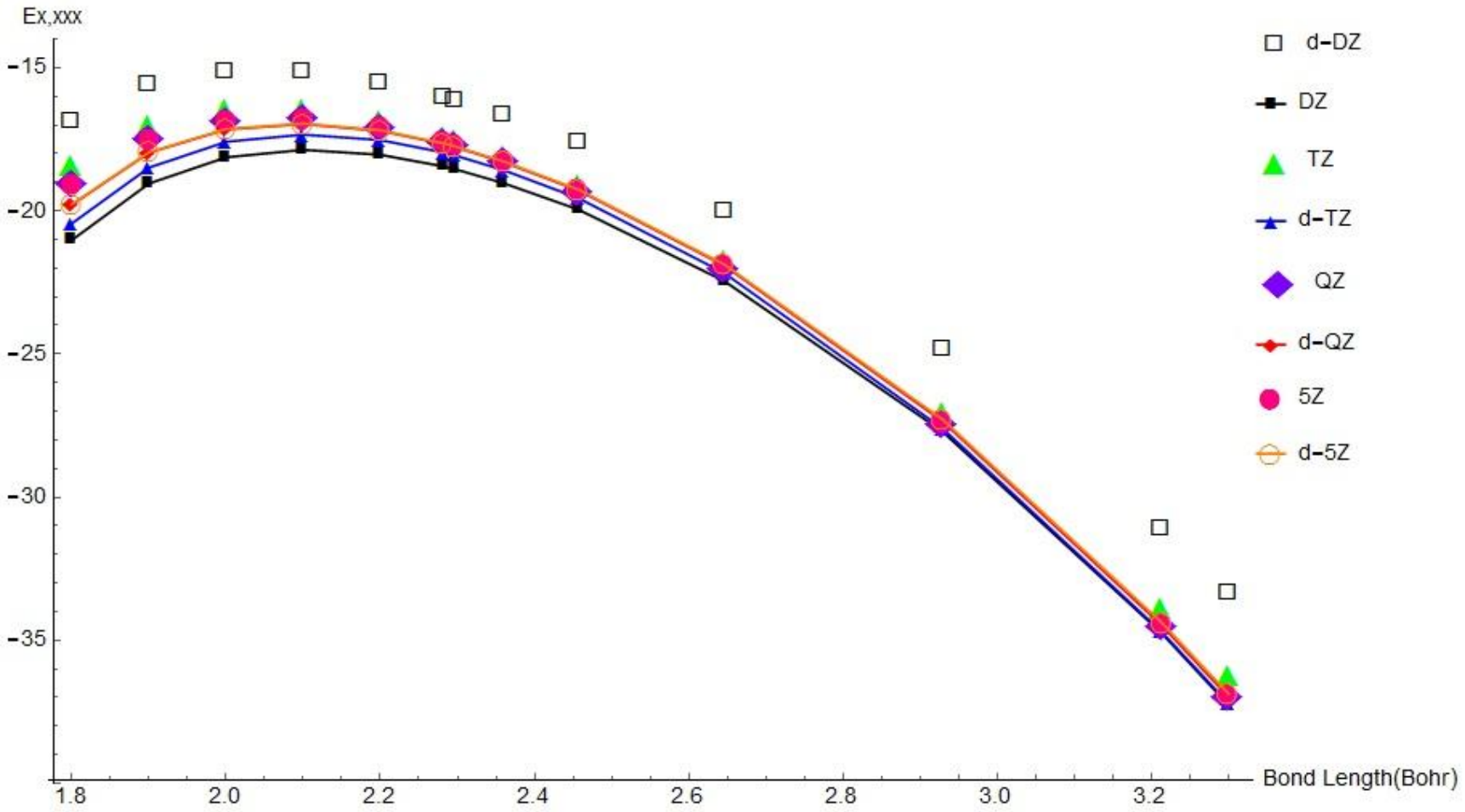

Figure 18. The dipole-octopole polarizability ($E_{x,xxx}$) in atomic units obtained using the CASPT2 method and the singly and doubly augmented basis sets

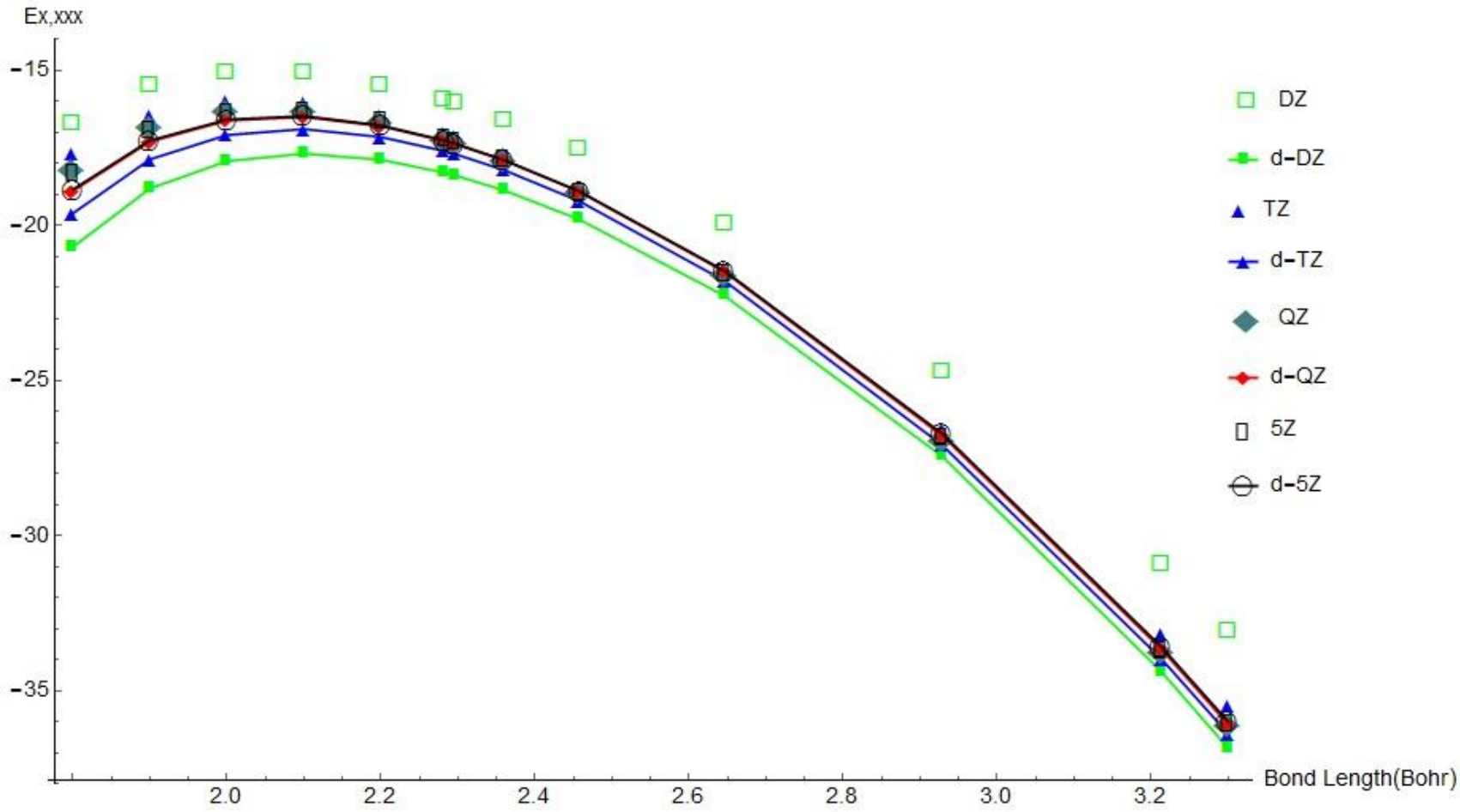

Figure 19. The dipole-octopole polarizability ($E_{x,xxx}$) in atomic units obtained using the MRCI method and the singly and doubly augmented basis sets

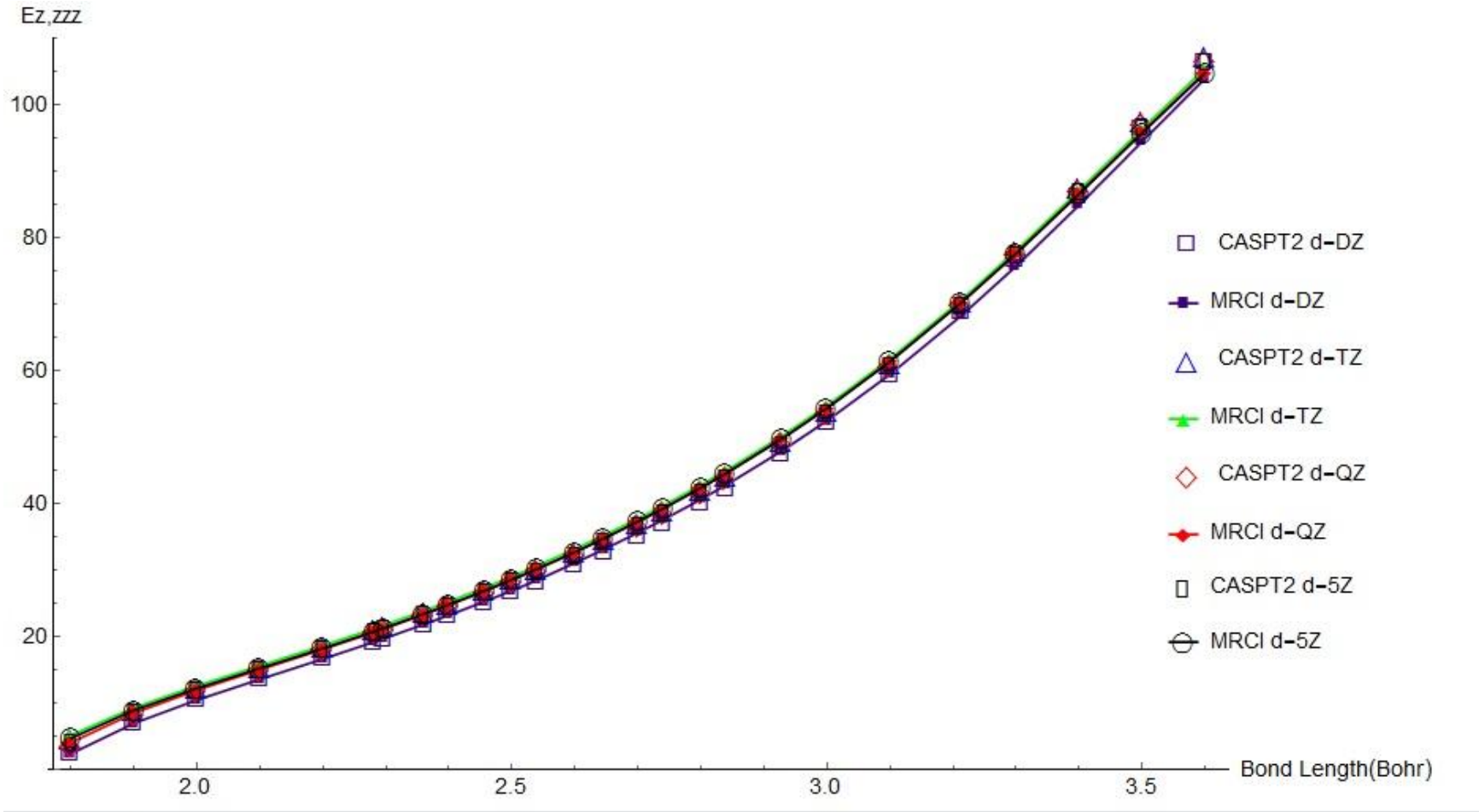

Figure 20. The dipole-octopole polarizability ($E_{z,zzz}$) in atomic units obtained using the MRCI and CASPT2 methods, and the doubly augmented basis sets

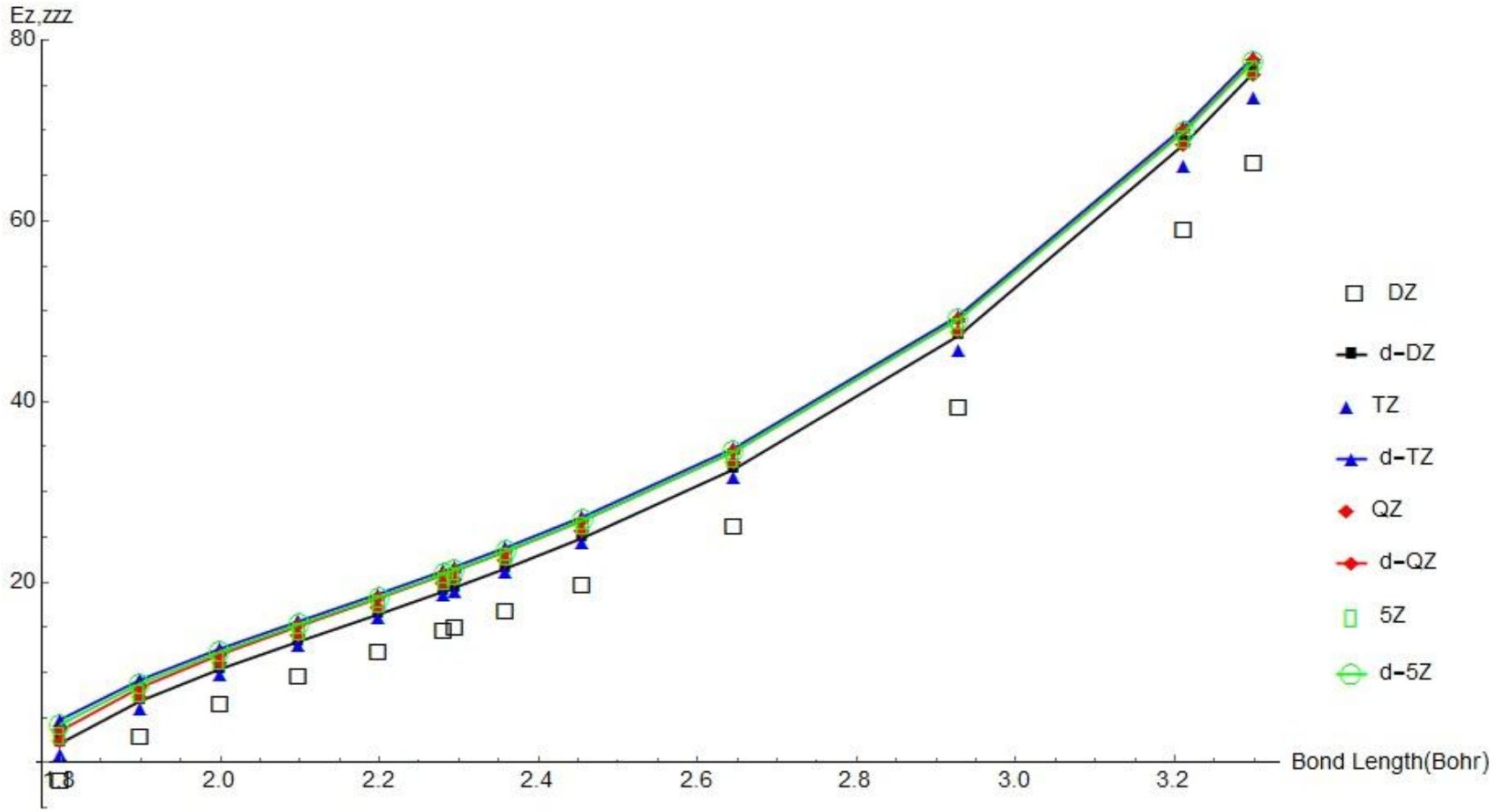

Figure 21. The dipole-octopole polarizability ($E_{z,zzz}$) in atomic units obtained using the CASPT2 method and the singly and doubly augmented basis sets.

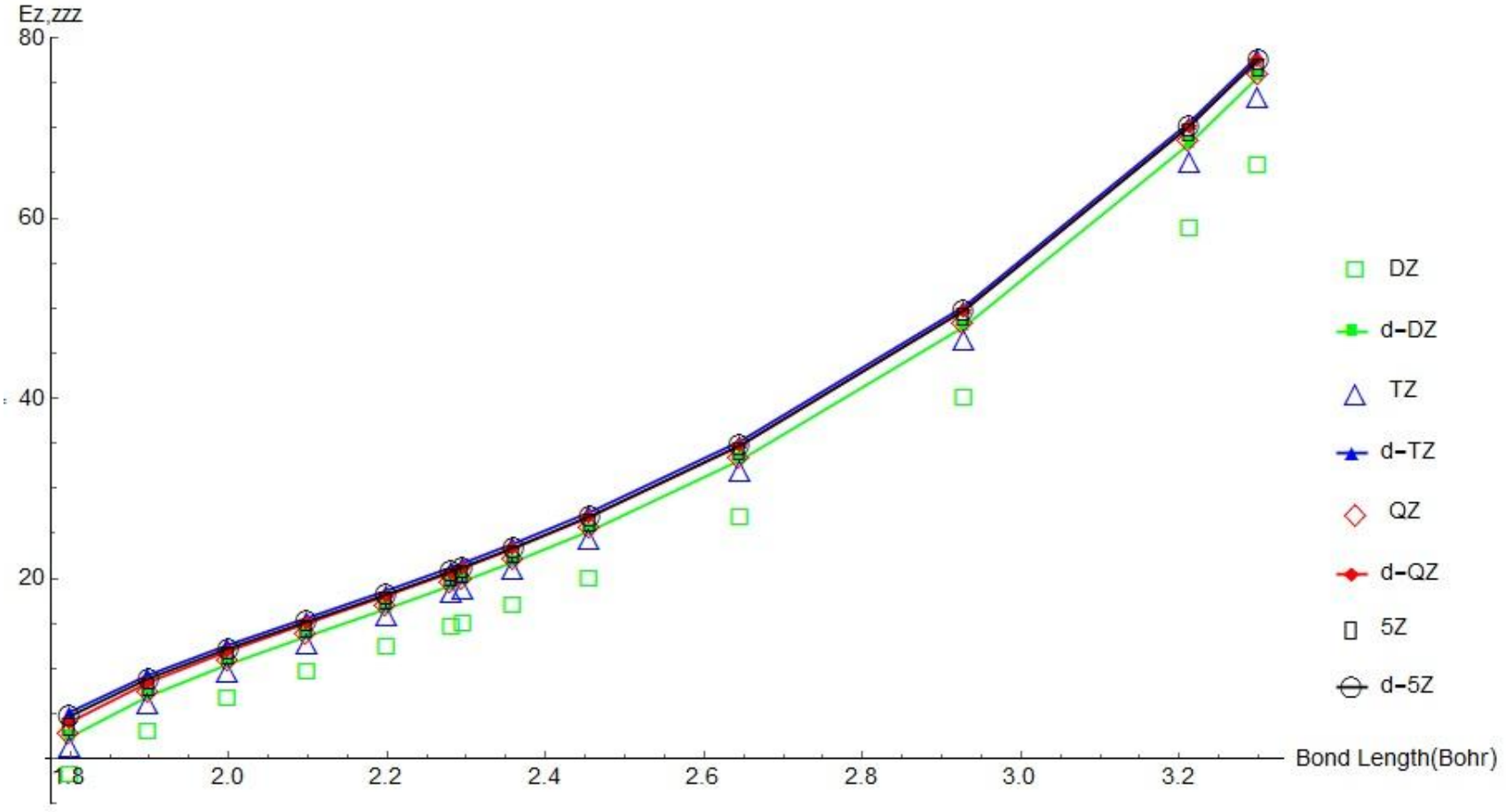

Figure 22. The dipole-octopole polarizability ($E_{z,zzz}$) in atomic units obtained using the MRCI method and the singly and doubly augmented basis sets.

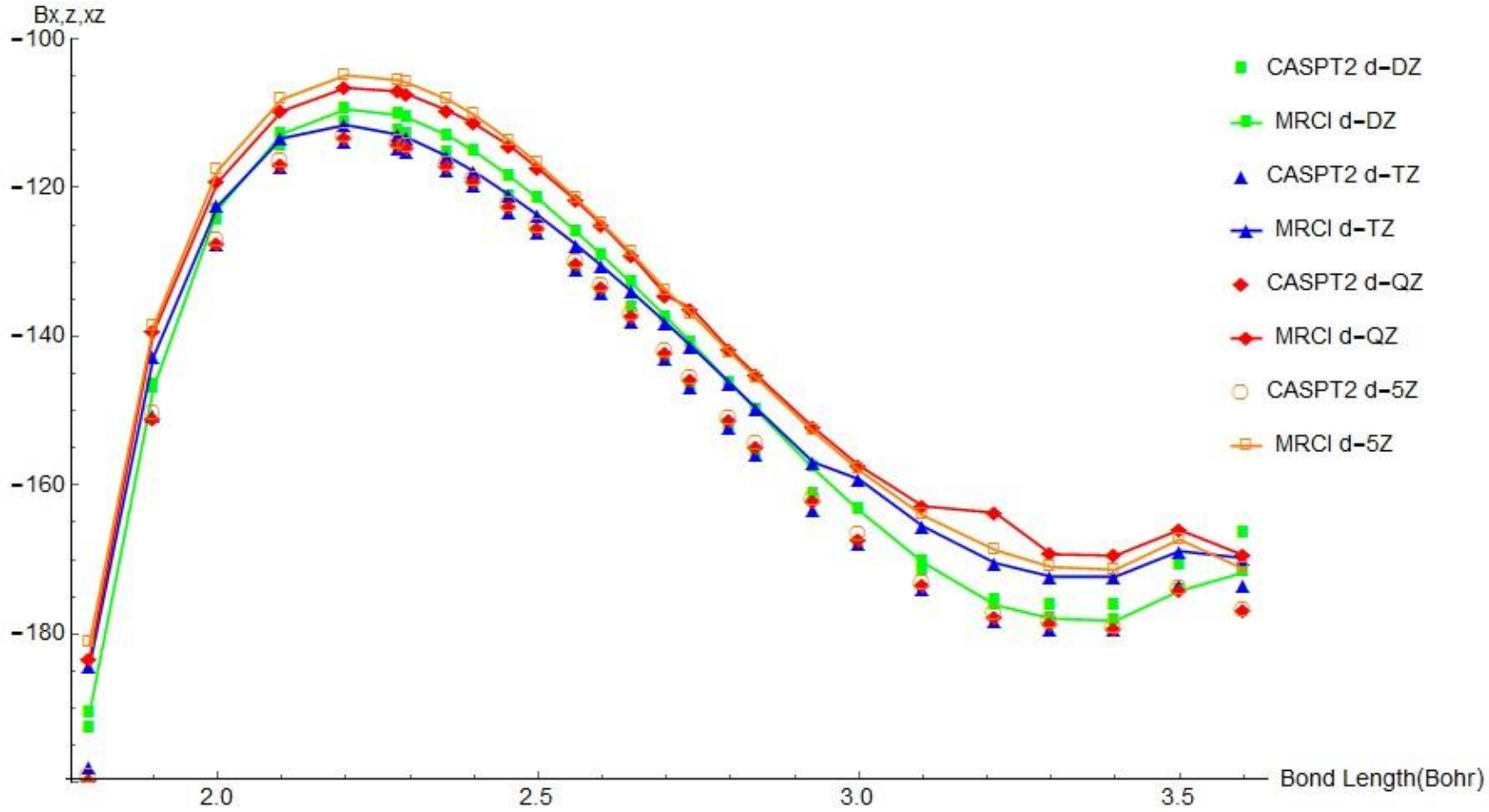

Figure 23. The dipole-dipole-quadrupole polarizability ($B_{x,z,xz}$) in atomic units versus bond length obtained using the MRCI and CASPT2 methods and the doubly augmented basis sets

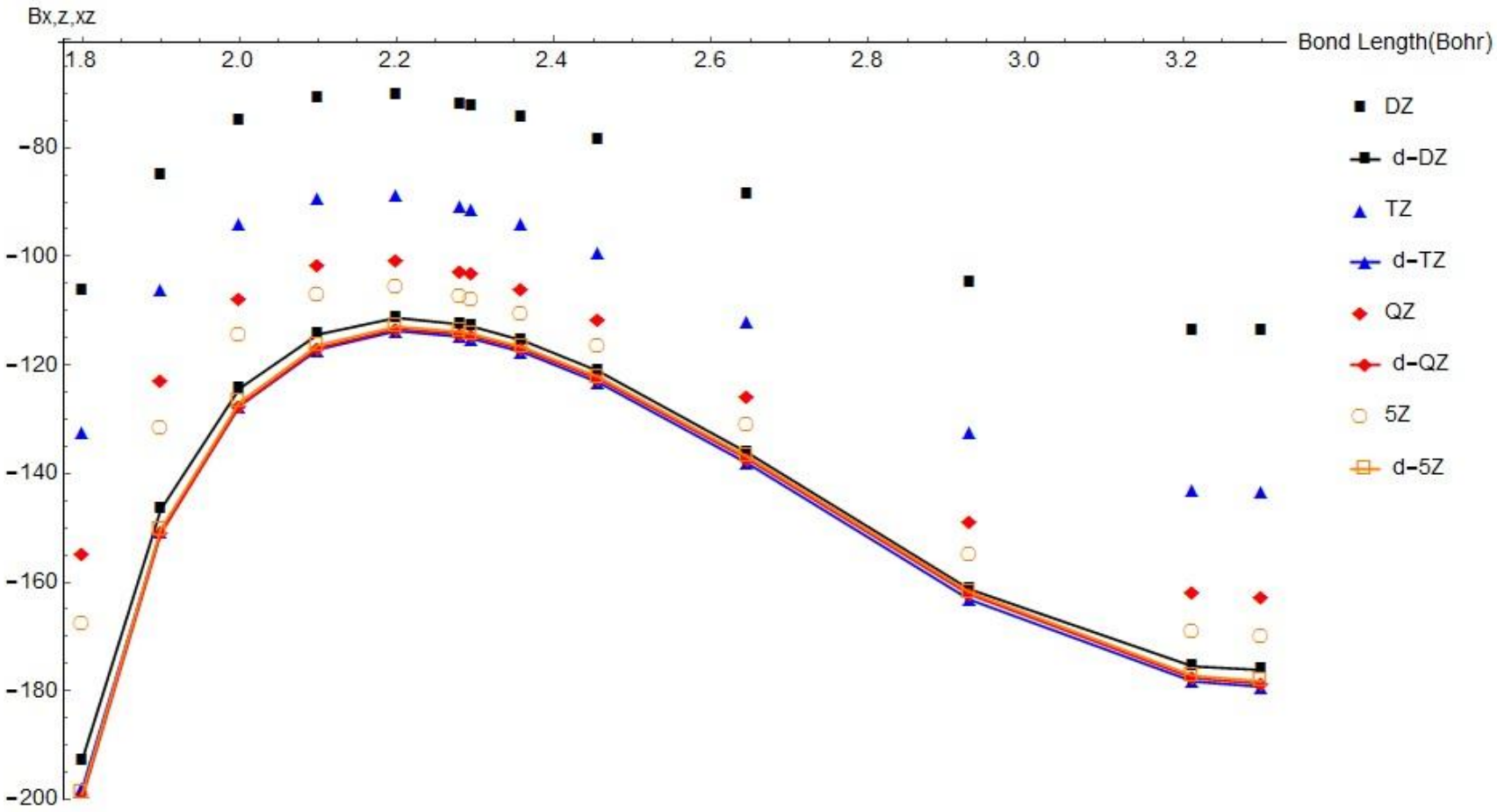

Figure 24. The dipole-dipole-quadrupole polarizability ($B_{x,z,xz}$) in atomic units versus bond length obtained using the CASPT2 method and the singly and doubly augmented basis sets

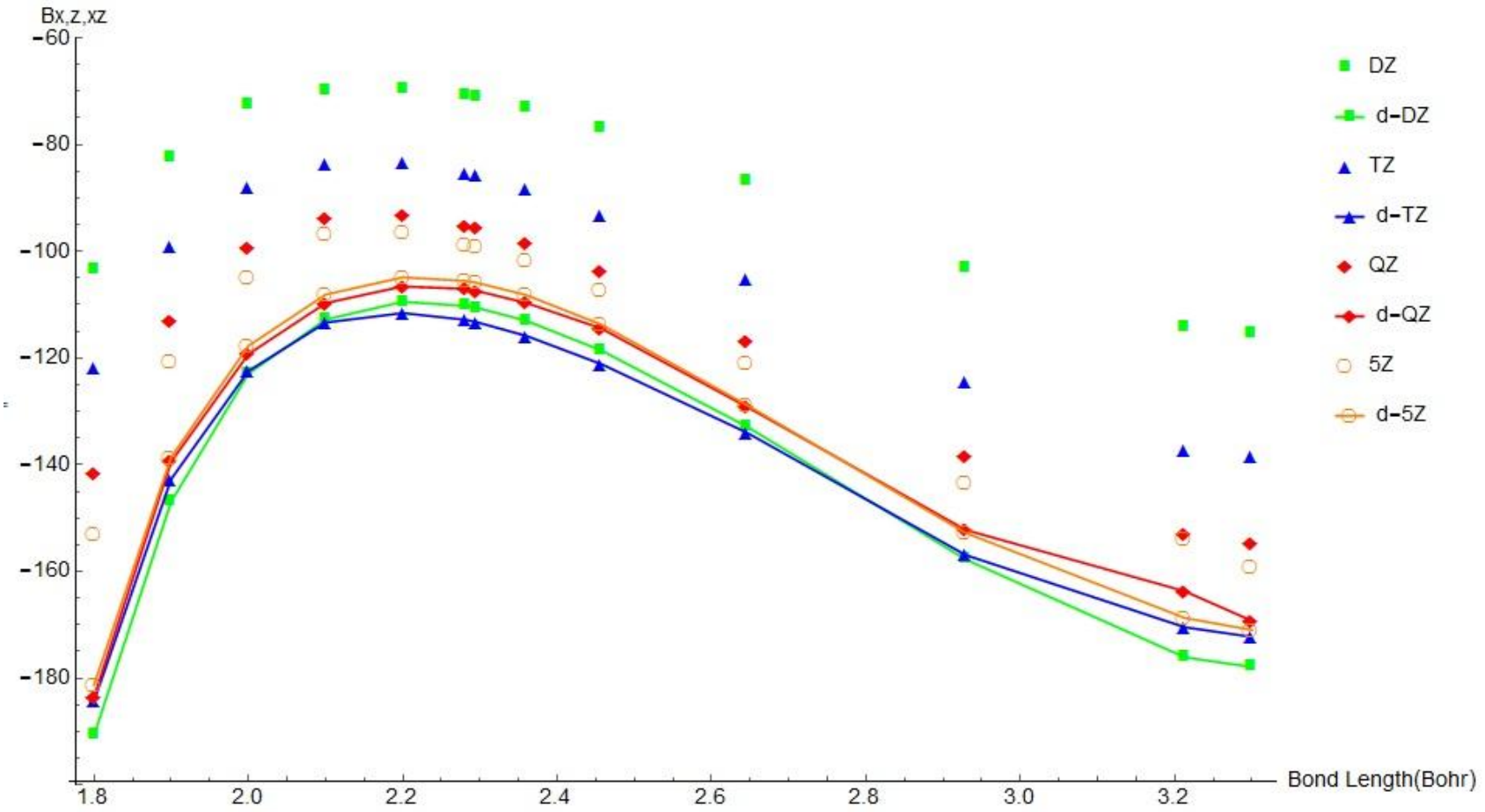

Figure 25. The dipole-dipole-quadrupole polarizability ($B_{x,z,xz}$) in atomic units versus bond length obtained using the MRCI method and the singly and doubly augmented basis sets.

The next property we examine as a function of the bond length is the dipole-dipole-quadrupole polarizability $B_{x,x,zz}$, Figure (26). As with the last property, we see that the MRCI values do not converge smoothly. This results in some very large differences between methods. The points at a bond distance of 1.8 bohr show this separation well. At this point, there is a 54% difference between the MRCI and CASPT2 values here for the d-DZ basis set, a 49% difference between values for the d-TZ basis set, a 40% difference in values for the d-QZ basis set, and an 83% difference in values for the d-5Z basis set. Around a bond distance of 3 bohr, these differences become much smaller, and are on the order of 1% in some cases.

We now look at the values of $B_{x,x,zz}$ obtained using just the CASPT2 method. As we can see in Figure (27), there is an appreciable difference between even the 5Z/d-5Z basis sets. At the shortest distance of 1.8 bohr, the difference is largest, at ~28%. But even at the longest bond lengths studied, there is a difference of 10-12%. The difference is even larger for the values obtained using the MRCI method (Figure (28)). This is partially because the doubly augmented curves are not smooth, and probably contain some convergence errors. For the 5Z/d-5Z basis sets, the difference at the shortest distance of 1.8 bohr is 160%. As the bond length is lengthened, the difference slowly decreases, until it reaches a minimum at the longest distance of 3.3 bohr, with a difference between basis sets of 11.4%.

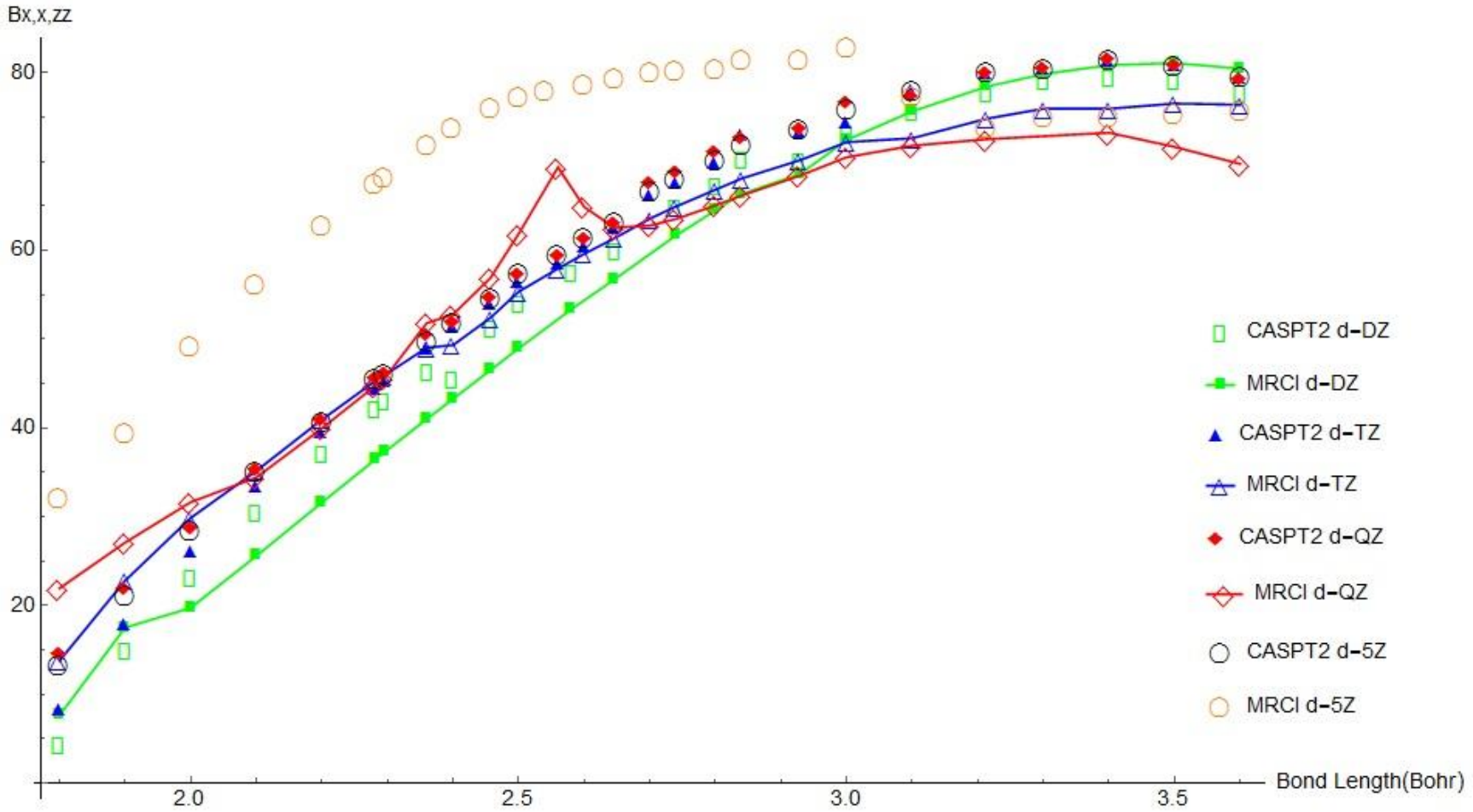

Figure 26. The dipole-dipole-quadrupole polarizability ($B_{x,x,zz}$)in atomic units versus bond length obtained using MRCI and CASPT2 methods using the doubly augmented basis sets

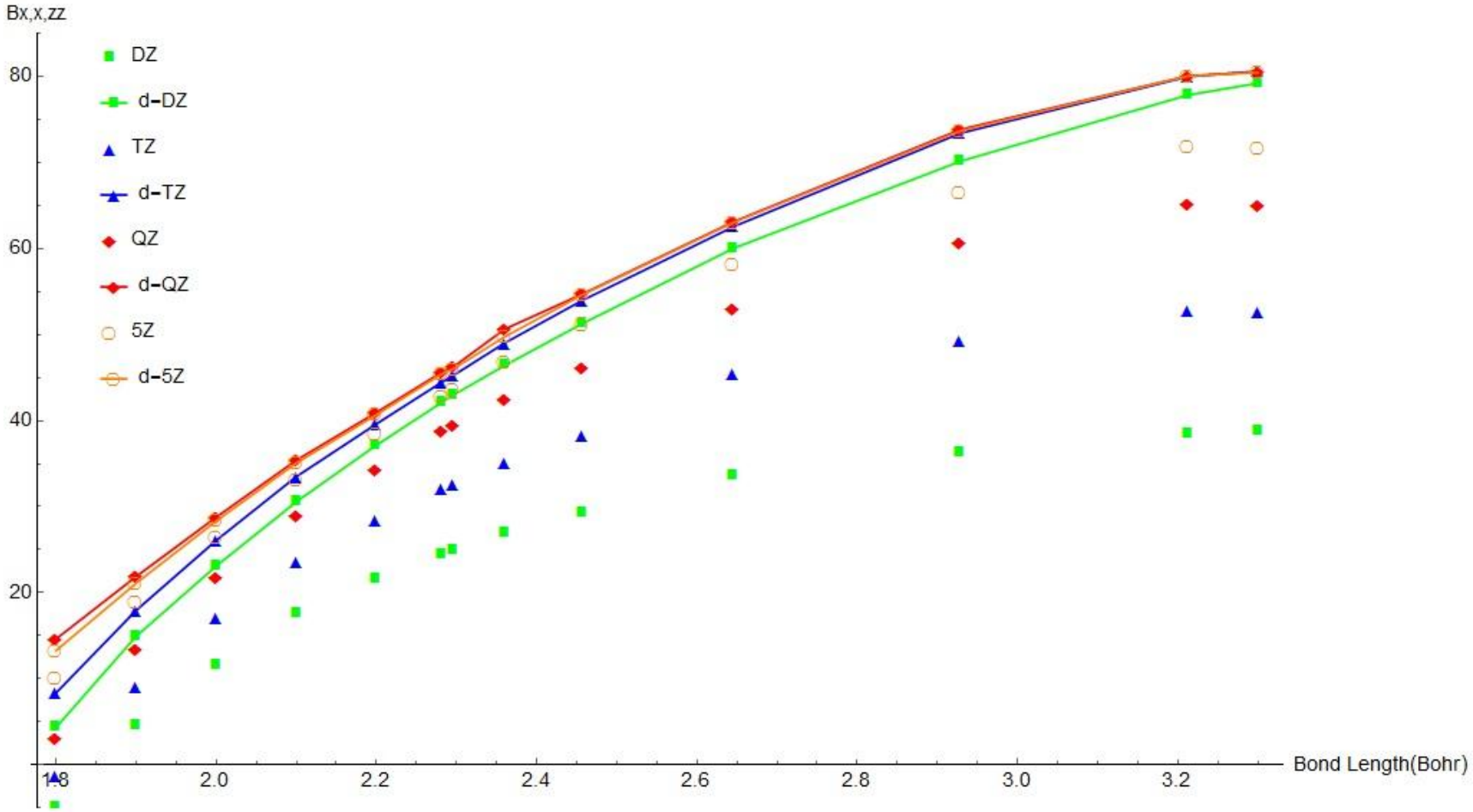

Figure 27. The dipole-dipole-quadrupole polarizability ($B_{x,x,z,z}$) in atomic units obtained using the CASPT2 method and the singly and doubly augmented basis sets

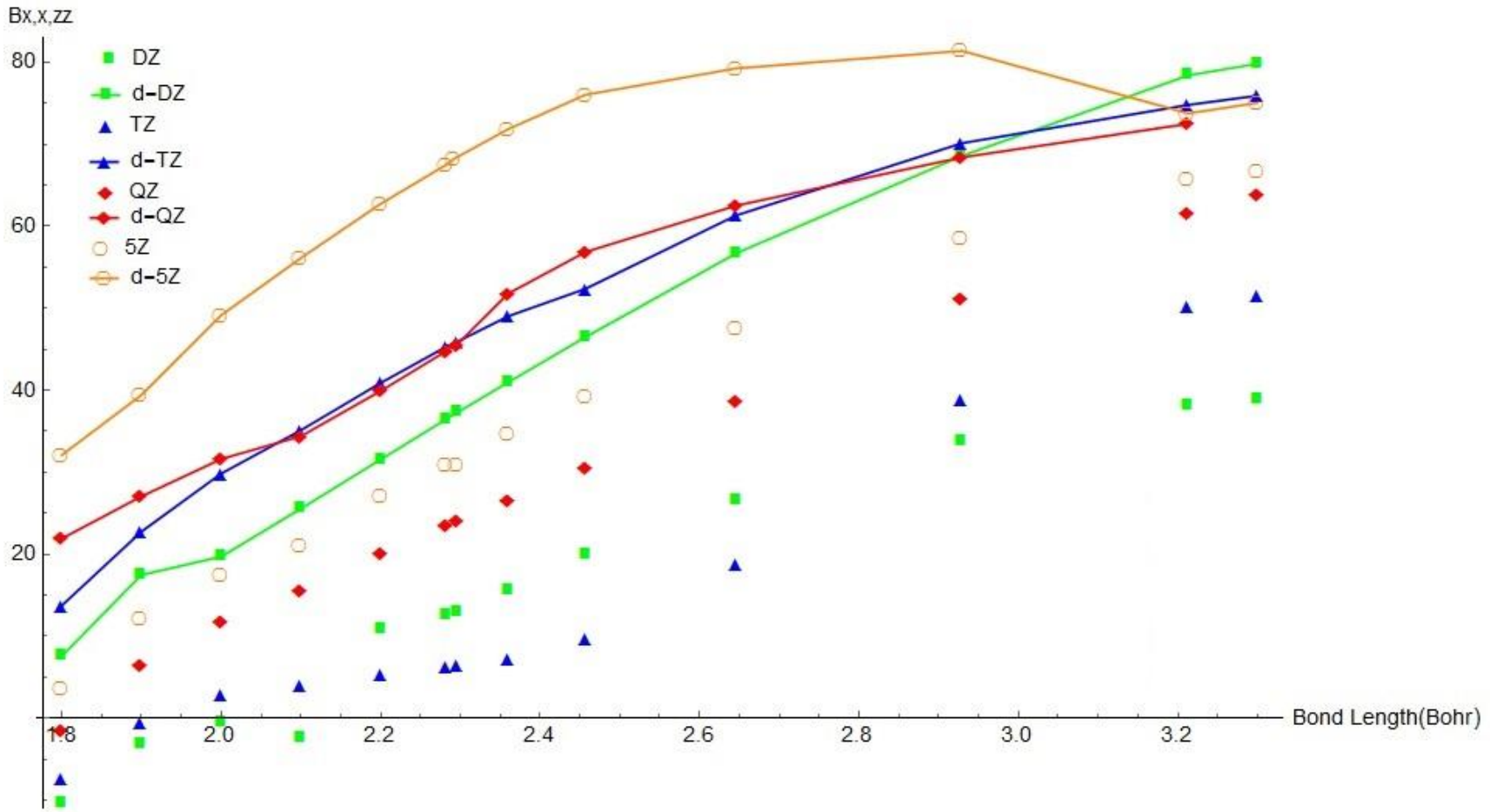

Figure 28. The dipole-dipole-quadrupole polarizability($B_{x,x,z,z}$) in atomic units obtained using the MRCI method and the singly and doubly augmented basis sets

Figure (29) shows the third dipole-dipole-quadrupole polarizability, $B_{x,x,xx}$, versus the bond length. We can see that the MRCI values again do not converge smoothly, especially for the d-QZ and d-5Z levels. Because of this, the largest differences between the two methods occur for the longer distances of the bond length, at up to 17%.

We now examine $B_{x,x,xx}$ within the CASPT2 method (Figure (30)). These curves converged smoothly, and it is apparent that there is a basis set sensitivity even at the 5Z/d-5Z levels, with a difference between 10-19% for all bond lengths. Figure (31) shows the same MRCI values, and as the curves are not as smooth as the CASPT2 curves, the difference between the singly and doubly augmented values is larger, between 11-33%.

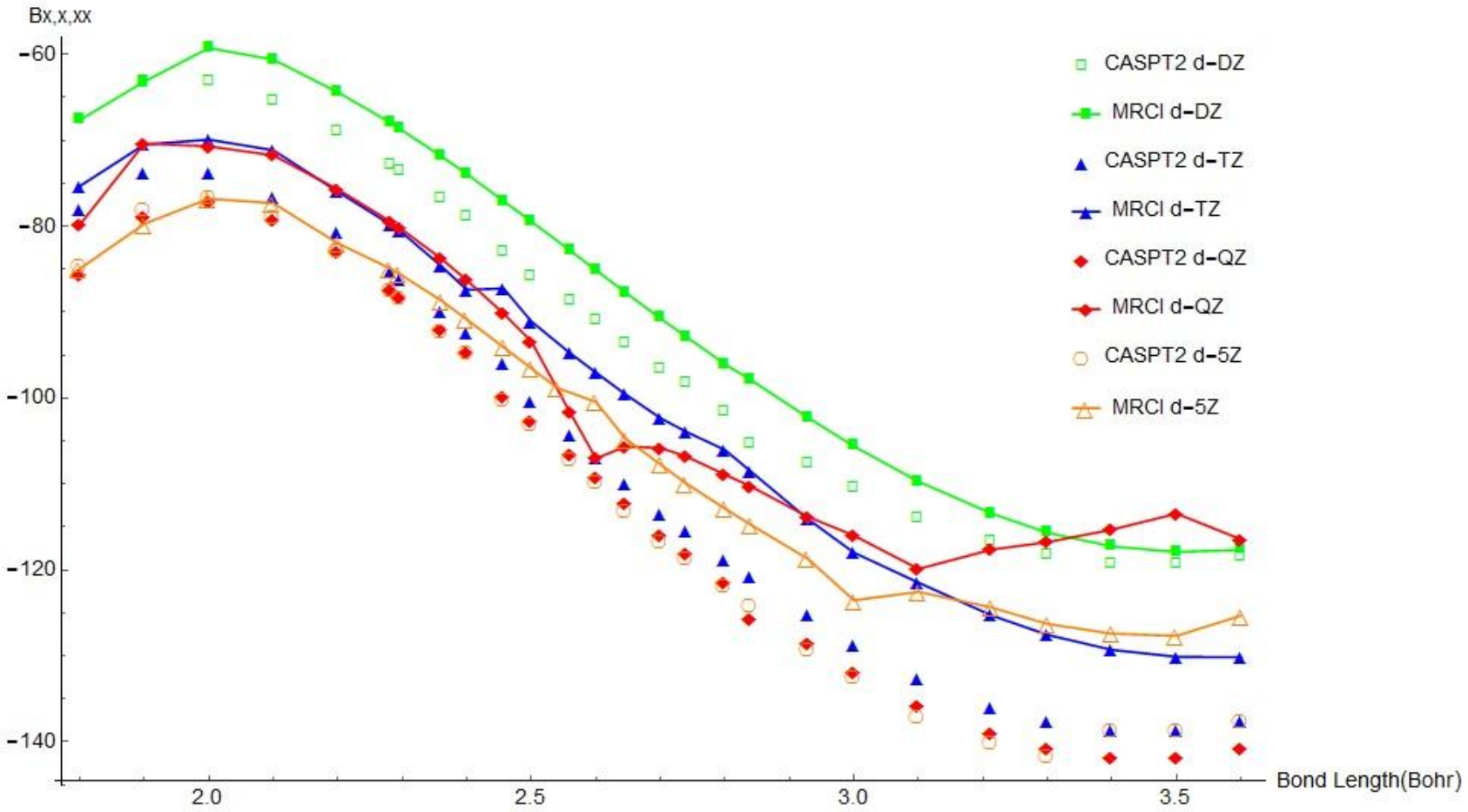

Figure 29. The dipole-dipole-quadrupole polarizability ($B_{x,x,xx}$) in atomic units versus bond length, obtained using the MRCI and CASPT2 methods, and the doubly augmented basis sets.

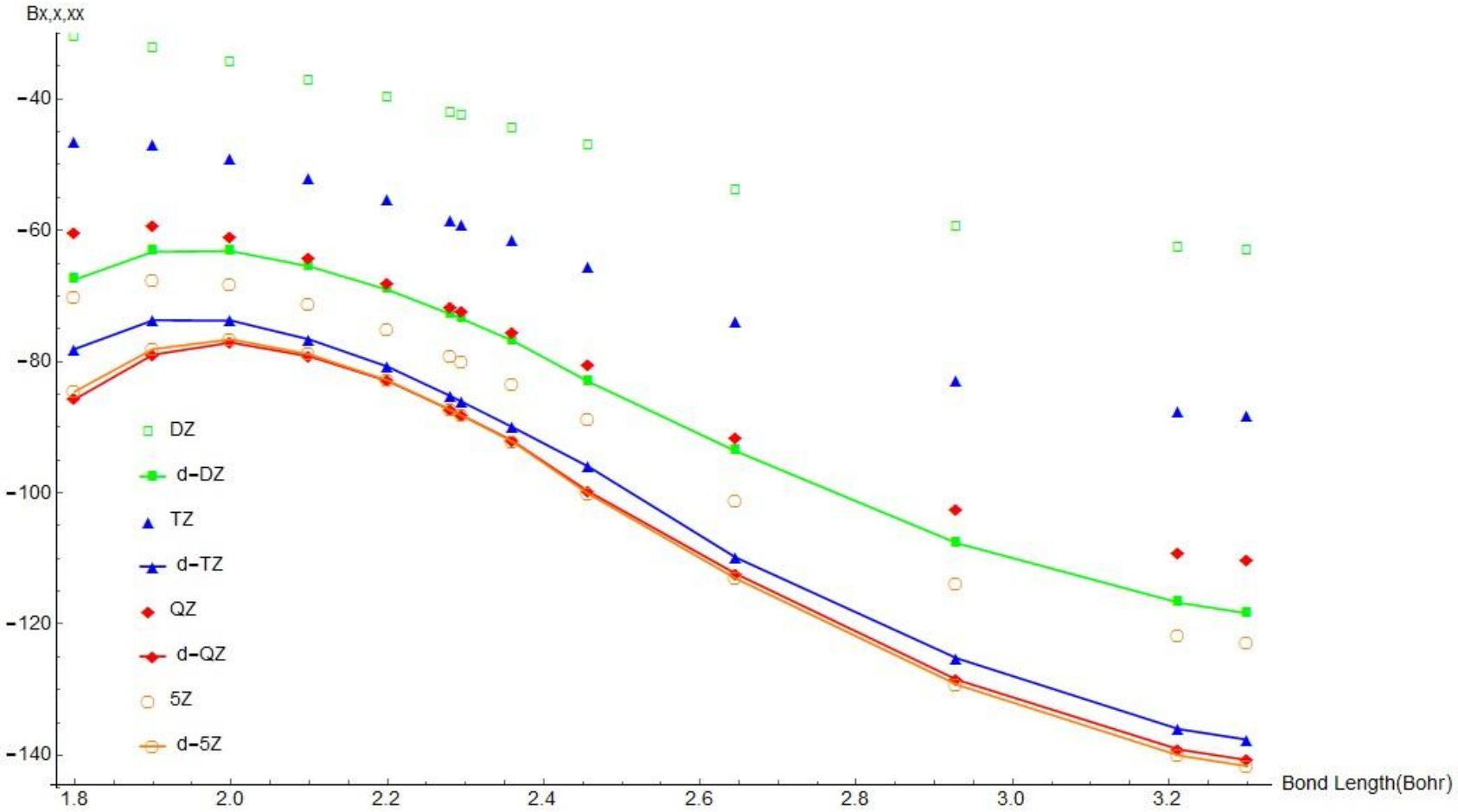

Figure 30. The dipole-dipole-quadrupole polarizability ($B_{x,x,xx}$) in atomic units versus bond length, obtained using the CASPT2 method and the singly and doubly augmented basis sets

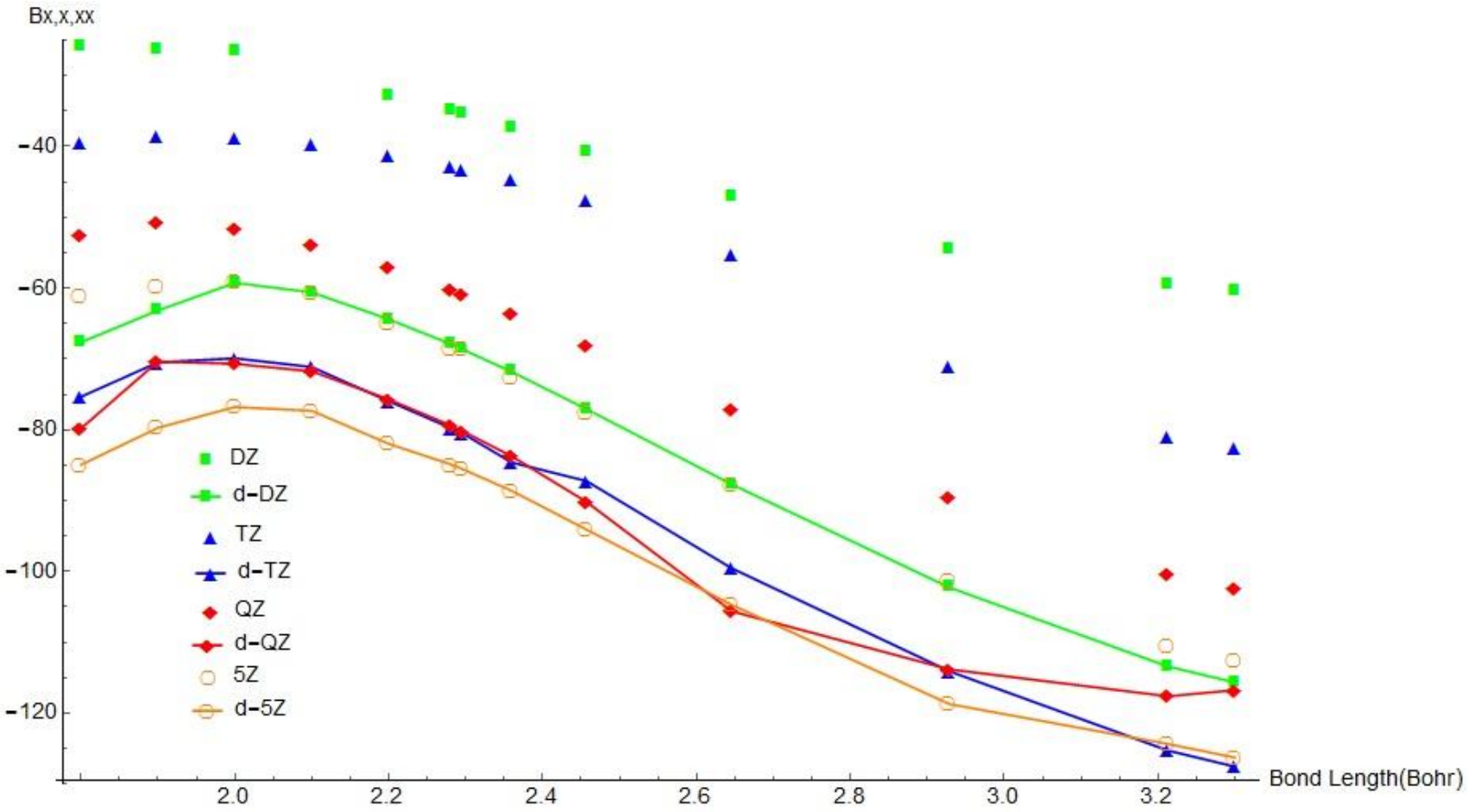

Figure 31. The dipole-dipole-quadrupole polarizability($B_{x,x,xx}$) in atomic units versus bond length, obtained with the MRCI method and the singly and doubly augmented basis sets

Figure (32) shows the fourth and final dipole-dipole-quadrupole polarizability, $B_{z,z,zz}$. In the region from 2.5 to 3 bohr, there is good agreement between the MRCI and CASPT2 methods for all four doubly augmented basis sets, on the order of 1%. The agreement at shorter distances is the worst, with differences as large as 14%.

The next graph, Figure (33), shows $B_{z,z,zz}$ versus bond length obtained using the CASPT2 method and all singly and doubly augmented basis sets. There is almost a 20% difference between the 5Z/d-5Z basis sets for the shortest bond length, and at least 5% difference for all bond lengths studied. The same quantities obtained using the MRCI method (Figure (34)) show much smaller differences between the 5Z/d-5Z basis set, with only a 2.7% difference at the shortest bond length, and less than one percent difference in the region between 2.1-2.3 bohr. The largest difference between these basis sets for the MRCI values actually occurs at the longest bond distance (3.3 bohr) with an 8% difference at this point.

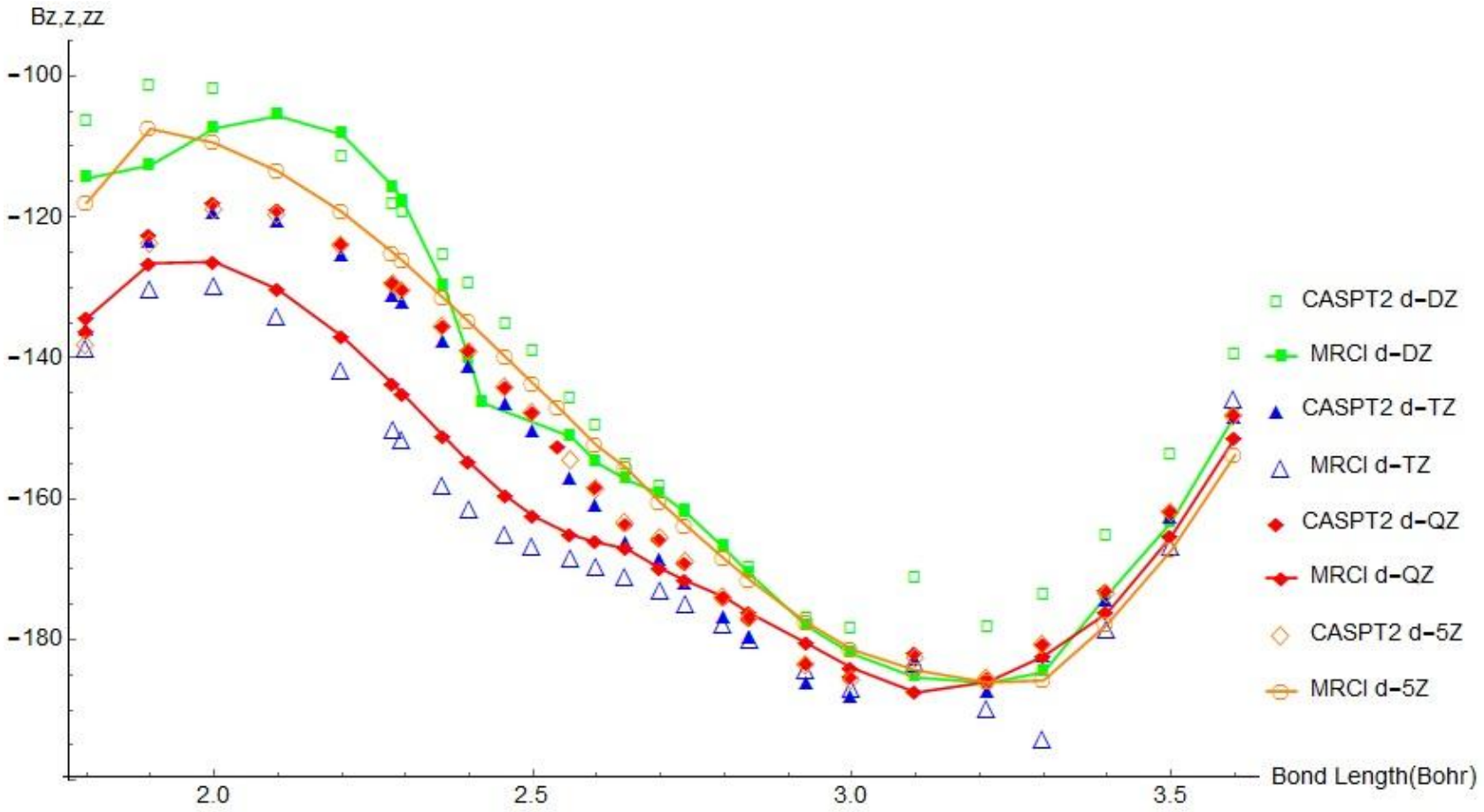

Figure 32. The dipole-dipole-quadrupole polarizability ($B_{z,z,zz}$) in atomic units versus bond length obtained using the MRCI and CASPT2 methods, with the doubly augmented basis sets

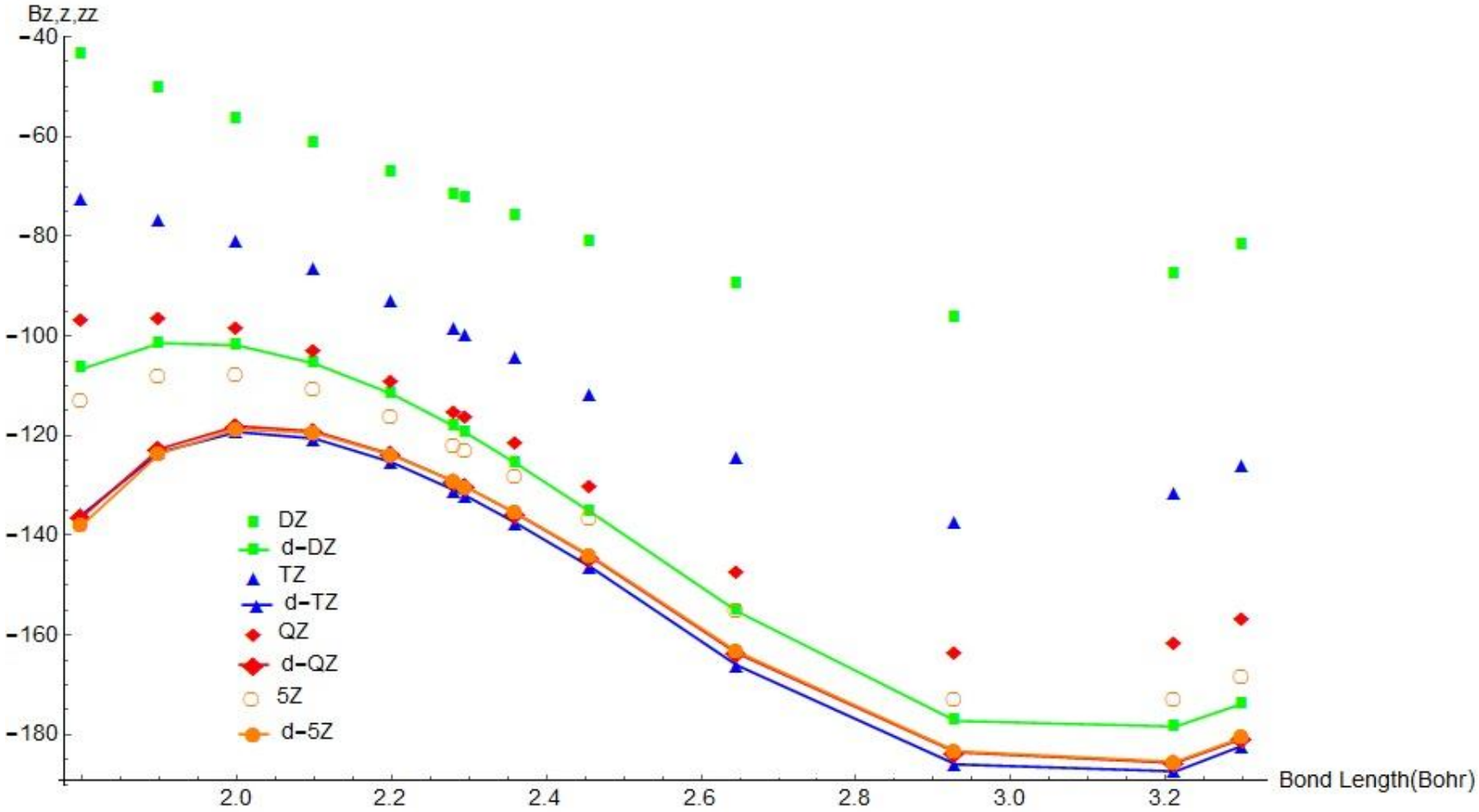

Figure 33. The dipole-dipole-quadrupole polarizability ($B_{z,z,zz}$) in atomic units versus bond length obtained using the CASPT2 method and the singly and doubly augmented basis sets

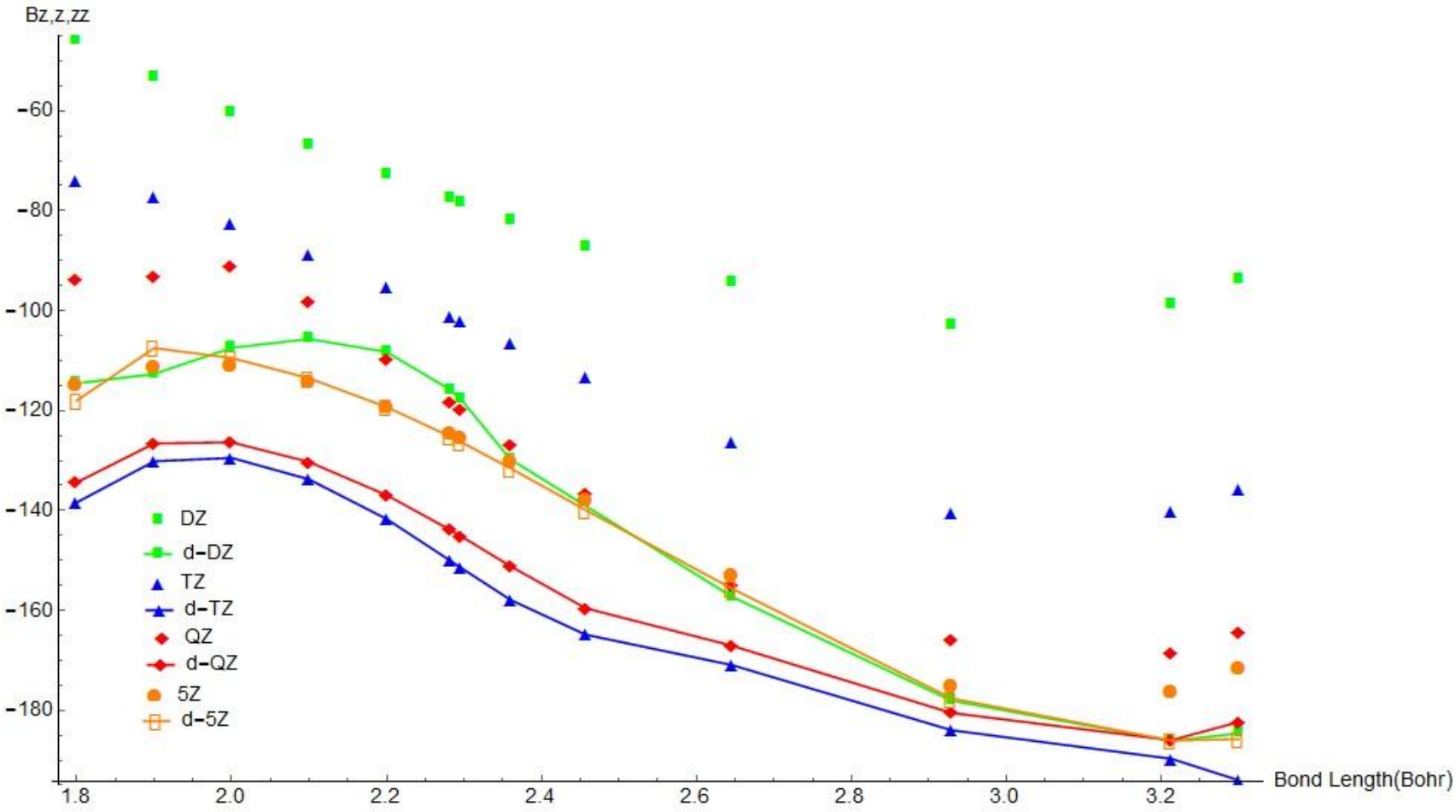

Figure 34. The dipole-dipole-quadrupole polarizability ($B_{z,z,zz}$) in atomic units versus bond length obtained using the MRCI method and the singly and doubly augmented basis sets

We now turn to the quadrupole-quadrupole polarizabilities, starting with $C_{xx,xx}$ (Figure (35)). For this property it is easily seen again that the d-DZ values of both methods are well separated from the values obtained with the larger basis sets. It is easy to see where the differences are between methods using that basis set as well. The points in the region from 2.2-2.5 bohr show the largest differences between methods, with around 5% difference, while all other points obtained with the d-DZ basis set show less than a 1% difference. For the values obtained using the d-TZ basis set, the difference between methods is fairly uniform for all distances considered, with a difference between 2-3%. For the d-QZ basis set, we again see the largest difference between methods in the values from 2.2-2.5 bohr, where the difference is as much as 11%. Finally, for the d-5Z values the differences are once again uniform, and between 3-4%.

In Figure (36), we consider just the values of $C_{xx,xx}$ obtained within the CASPT2 method with the singly and doubly augmented basis sets. The difference between the 5Z/d-5Z basis sets is pretty uniform throughout, between about 5-6%. This is also true for the MRCI values (Figure (37)).

The second quadrupole-quadrupole polarizability we have calculated values for is $C_{zz,zz}$ (Figure (38)). For the values obtained using the d-DZ basis set, there is again the same increased difference between values obtained with the two methods from 2.2-2.5 bohr, with the largest difference being about 5% at 2.2 bohr. For all other basis sets, the difference is uniformly between 2-3% for all distances. When we view just the values obtained using the CASPT2 method (Figure (39)), we see that there is a very small difference between the values obtained at the 5Z and d-5Z level. amounting to between 1-2% for all bond lengths. The same is true for the values obtained with the singly and doubly augmented basis sets within the MRCI method (Figure (40)).

The third and last quadrupole-quadrupole polarizability is $C_{xz,xz}$ (Figure (41)). This component of the quadrupole-quadrupole polarizability exhibits larger differences between the methods in general, though the curves are qualitatively similar in behavior. For the d-DZ basis set, there again is the largest differences between methods in the region from 2.2-2.5 bohr, though the increase in difference in this region is not as large as in the previous two components examined. The largest difference between methods at this level of basis set is between 8-9%. For the d-TZ basis set, the difference between methods increases with the bond length, and is almost 10% at 2.6 bohr. The same is true for the d-5Z basis set. Note that for the MRCI values, there is no point at 3.6, as the finite field calculations done for this quantity gave unphysical results after 3.5 bohr. The singly and doubly augmented basis sets for just the CASPT2 method (Figure (42)) show a 7% difference between the 5Z/d-5Z basis sets at the shortest distance, but the difference drops off quickly as the bond is lengthened and is between 1-3% for most bond lengths. Once again, the MRCI values are very similar (Figure (43)).

The last property to compare for the performance of the two methods is the second hyperpolarizability. The first component we will discuss is γ_{xxxx} (Figure (44)). The separation between the values obtained using both methods at the d-DZ basis set level from the larger basis sets is apparent in this figure. The MRCI and CASPT2 values at this level show good agreement, with the largest difference being about 3% and most differences under 2%. For the d-TZ values, there is a clear outlier at 2.9 bohr in the MRCI values. Other than this point, the d-TZ values are within 10% of each other between methods. The largest difference is found between methods at the d-QZ level, where the difference reaches 16% at 3.3 bohr. The values at the d-5Z level have their largest difference at 2.2 bohr, where there is a 12.4% difference.

Looking now at just the CASPT2 values for γ_{xxxx} in Figure (45), we can see that even at the 5Z/d-5Z level, there is a 20-27% difference between the singly and doubly augmented levels (the DZ/d-DZ values for this property using the CASPT2 method are nearly 100% different for all bond distances). The MRCI singly and doubly augmented values at the 5Z/d-5Z level are slightly closer together (Figure (44)), but still 16-25% different for all bond lengths.

The next component of the second hyperpolarizability is γ_{xxzz}. Figure (47) shows the MRCI and CASPT2 values versus bond distance for the d-DZ, d-TZ, and d-QZ basis sets. The calculations for this quantity attempted with the d-aug-cc-pv5Z basis set did not converge. As far as this property is concerned, the MRCI method seems to do better, and we were able to obtain more values and a smoother curve with this method than with the CASPT2 method. However, for the curves we do have, we note that there are large differences between the two methods. At the d-DZ basis set level, the differences range between 19-45%. There is as much as a 70% difference between methods at the d-TZ basis set level, and 58% between values at the d-QZ level.

Figure (48) shows just the CASPT2 values for γ_{xxzz}. Because we do not have values at the X=5 level, we will examine the singly and doubly augmented values at the QZ/d-QZ level. This tensor shows sensitivity to the addition of a second diffuse function, as the difference between the QZ/d-QZ basis set values are 23-33% for all bond distances considered. The MRCI values show similar differences between the QZ and d-QZ levels, with differences ranging from 14-41% (Figure (49)).

The last component of the second hyperpolarizability is γ_{zzzz} . At the d-DZ level, Figure (50) shows that the MRCI value deviates sharply from that obtained using the same basis set and the CASPT2 method at 2.46 bohr. Therefore the difference at this point between methods at this basis set level is 80%. Many of the points are vary at anywhere from 10-32% difference at this basis set level, but at a distance of 2.65 bohr the difference is only about 2.5%. The values at the d-TZ level differ by up to 15% for some of the distances considered, but the difference is very small again at 2.65 bohr, at only 0.2%. Very similar behavior in the differences between methods are observed for the two larger basis sets.

Figure (51) shows the CASPT2 values of γ_{zzzz} for all basis sets. This tensor is sensitive to the addition of a second set of diffuse functions. The difference is largest for shorter distances, with a difference of nearly 32% between the 5Z and d-5Z basis sets at this point. Even at the longest distances of the bond length, we see a 14-17% difference between the singly and doubly augmented quintuple zeta basis sets. The MRCI values (Figure (52)) are similar, starting with a 23% difference at the shortest bond length, but the difference drops off with increased bond length and is only 2-4% at the longer bond lengths.

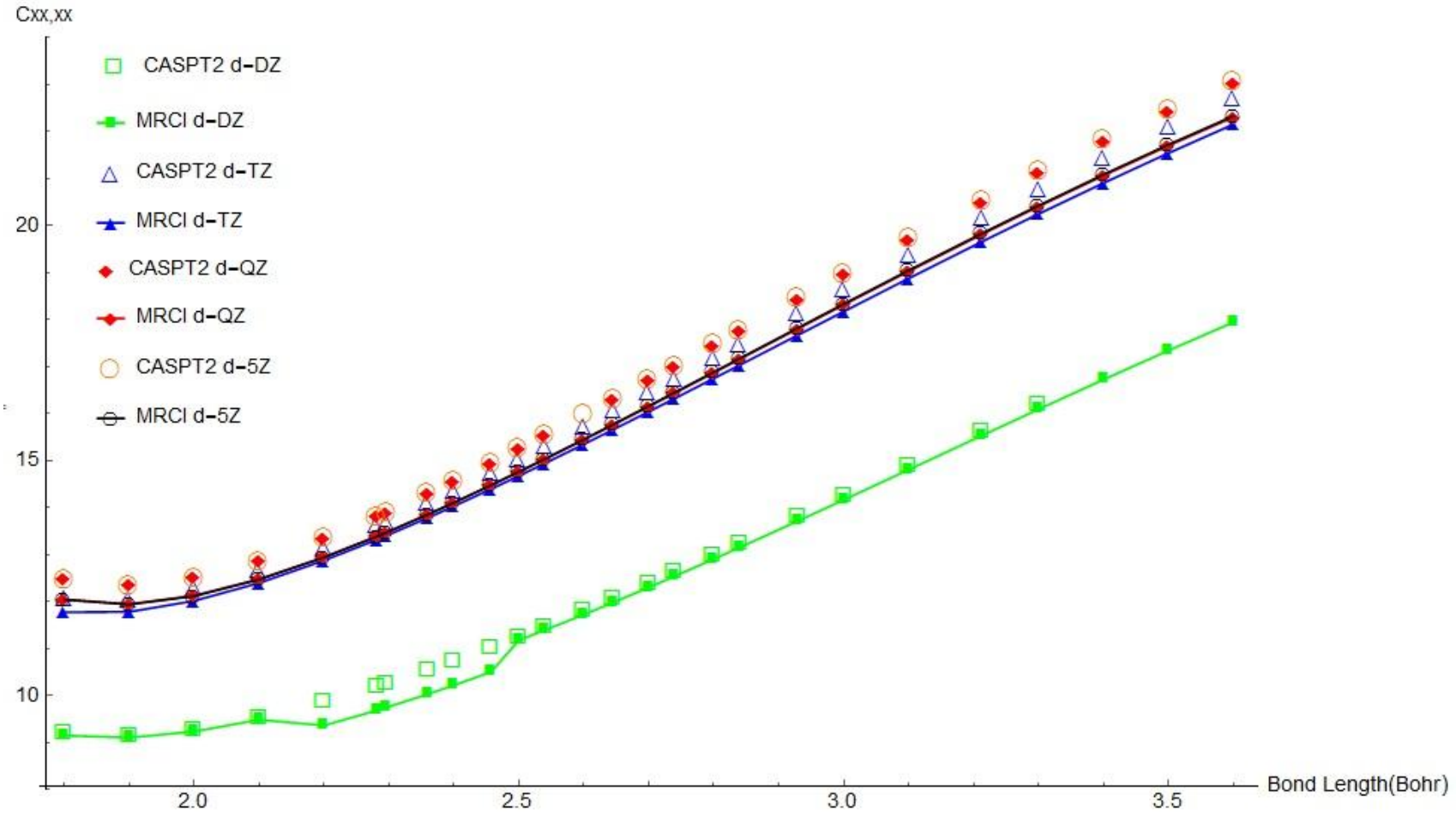

Figure 35. The quadrupole-quadrupole polarizability ($C_{xx,xx}$) in atomic units versus bond distance obtained using the MRCI and CASPT2 methods and the doubly augmented basis sets

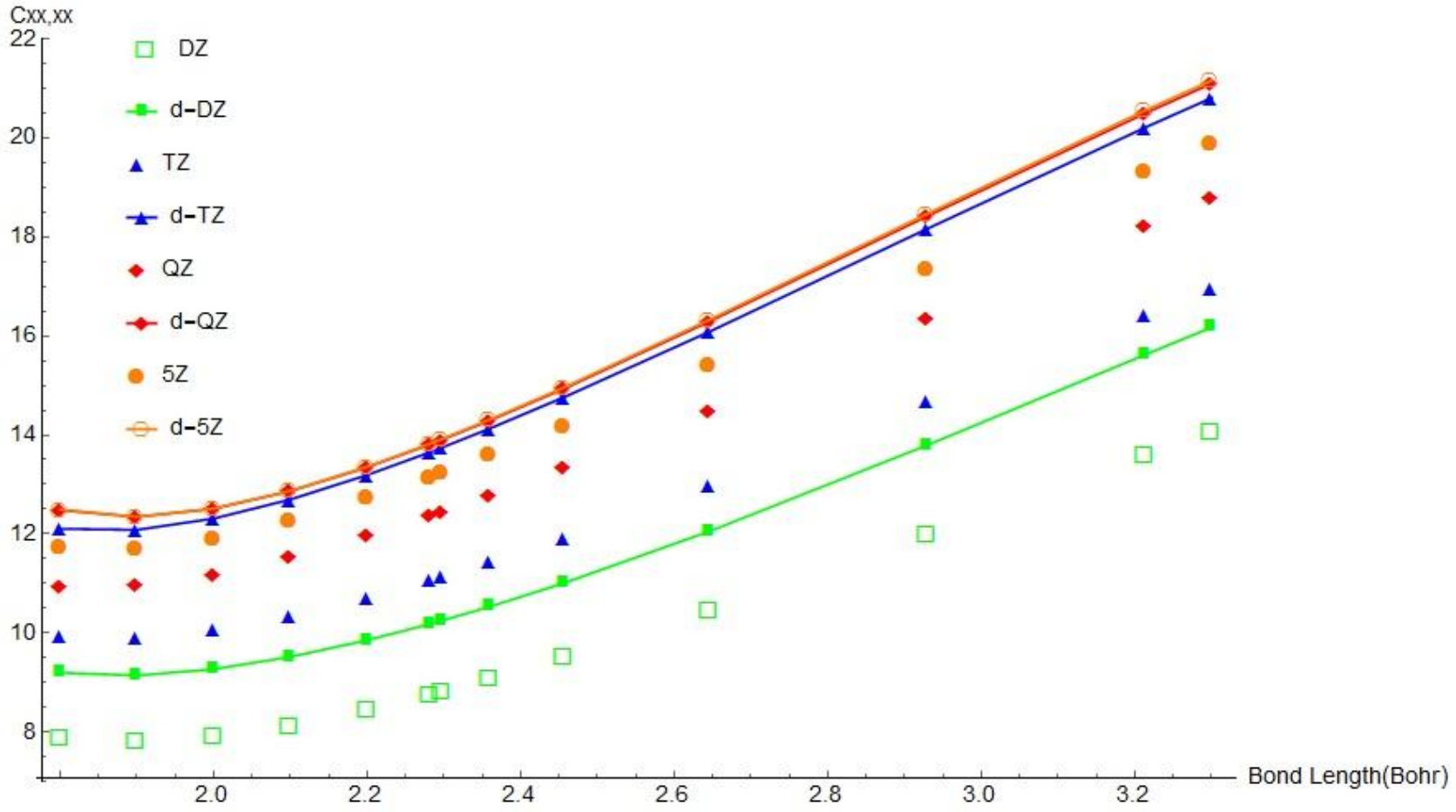

Figure 36. The quadrupole-quadrupole polarizability ($C_{xx,xx}$) in atomic units versus bond length obtained using the CASPT2 method and the singly and doubly augmented basis sets

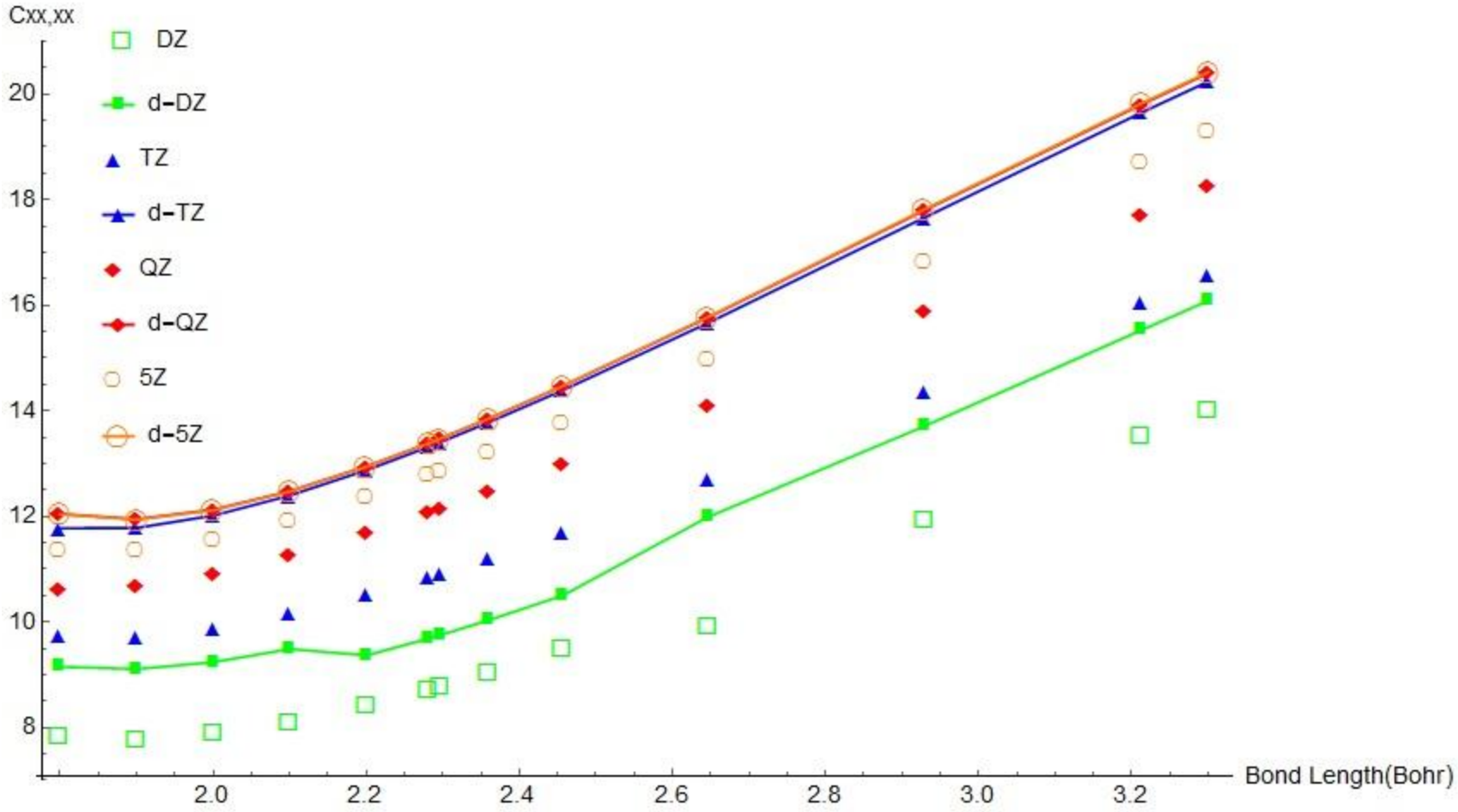

Figure 37. The quadrupole-quadrupole polarizability ($C_{xx,xx}$) in atomic units obtained using the MRCI method and the singly and doubly augmented basis sets

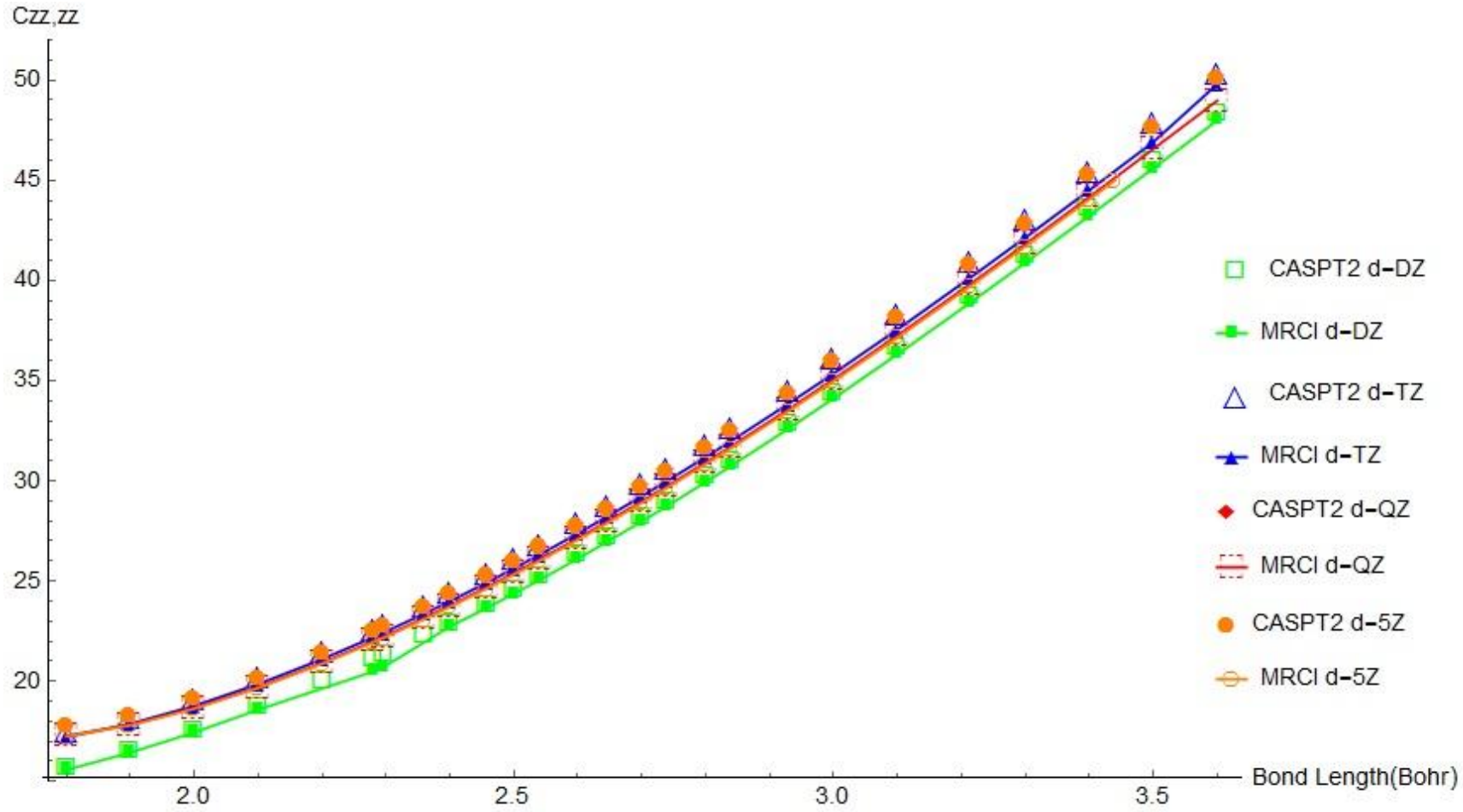

Figure 38. The quadrupole-quadrupole polarizability ($C_{zz,zz}$) in atomic units versus bond length obtained using the MRCI and CASPT2 methods and the doubly augmented basis sets

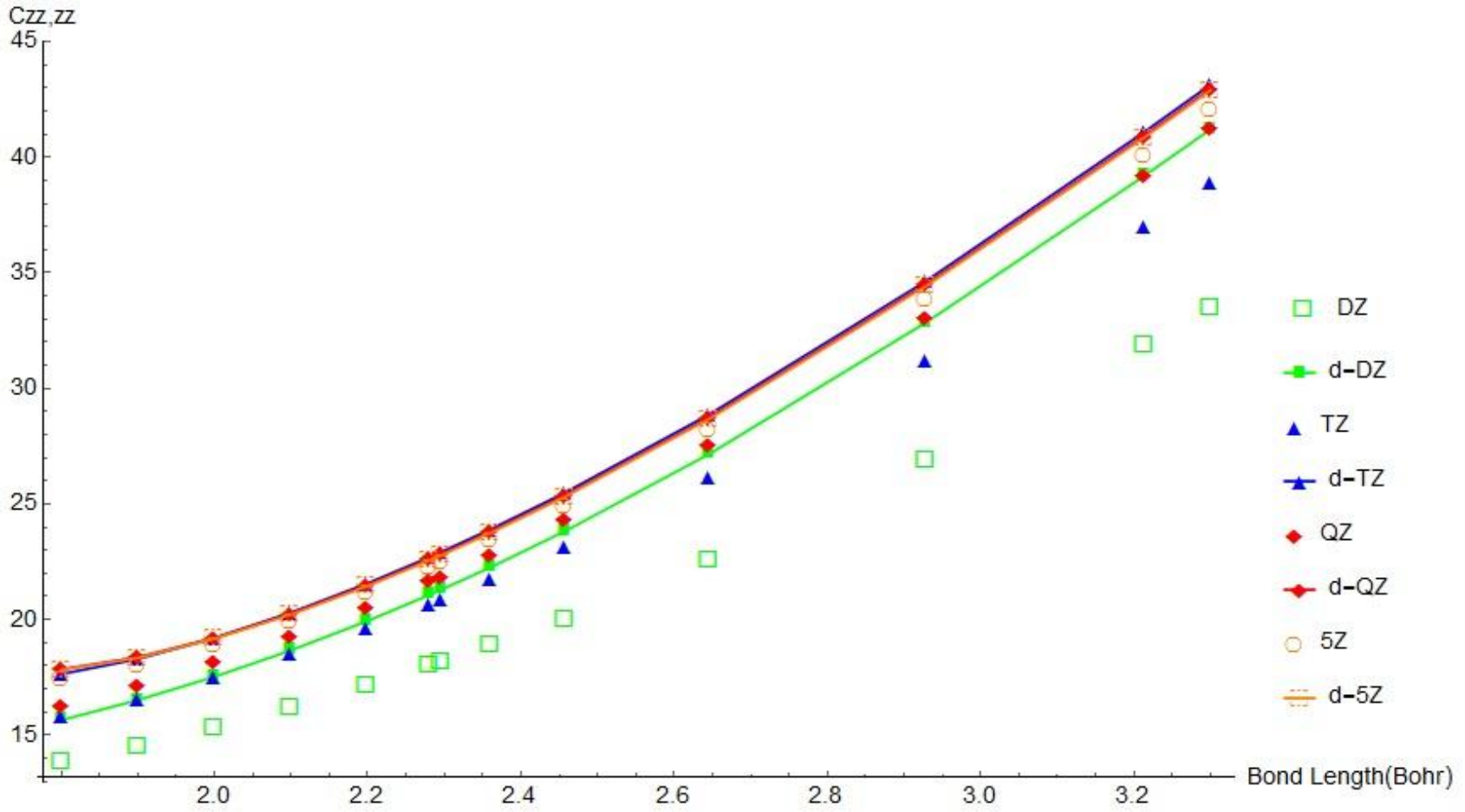

Figure 39. The quadrupole-quadrupole polarizability ($C_{zz,zz}$) in atomic units versus bond length obtained using the CASPT2 method and the singly and doubly augmented basis sets

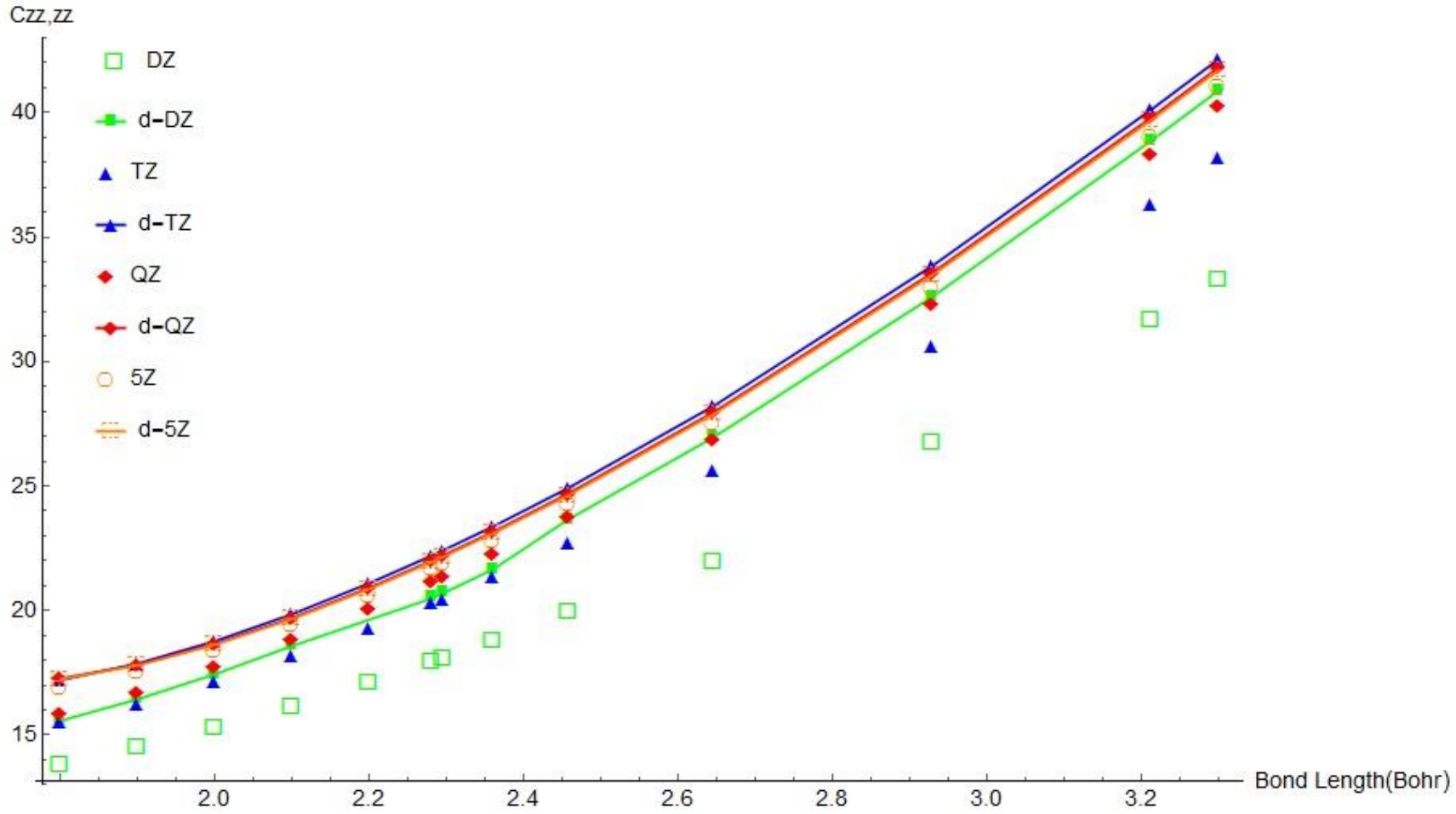

Figure 40. The quadrupole-quadrupole polarizability ($C_{zz,zz}$) in atomic units versus bond length obtained using the CASPT2 method and the singly and doubly augmented basis sets

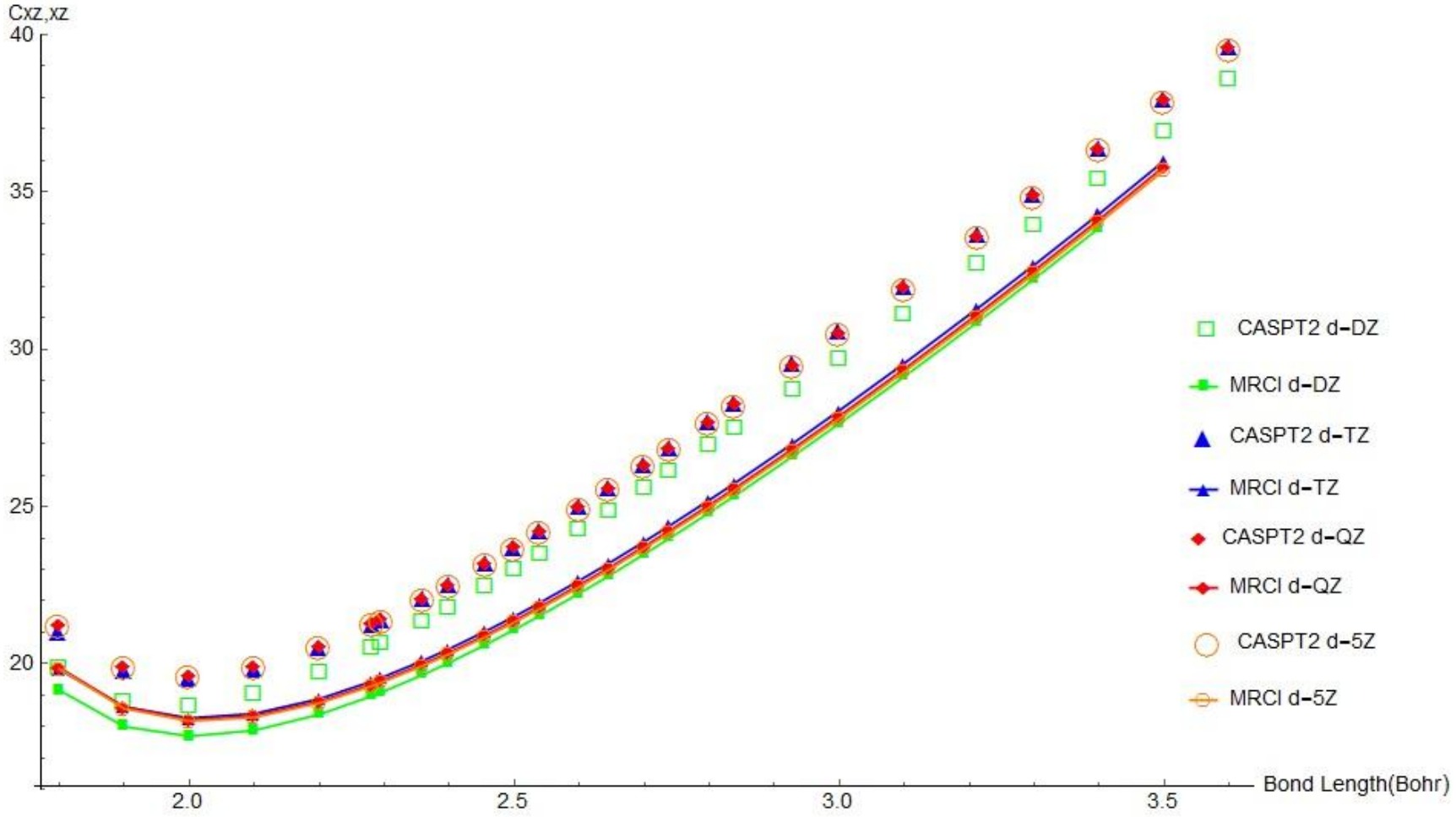

Figure 41. The quadrupole-quadrupole polarizability ($C_{xz,xz}$) in atomic units versus bond distance obtained using the MRCI and CASPT2 basis sets and the doubly augmented basis sets

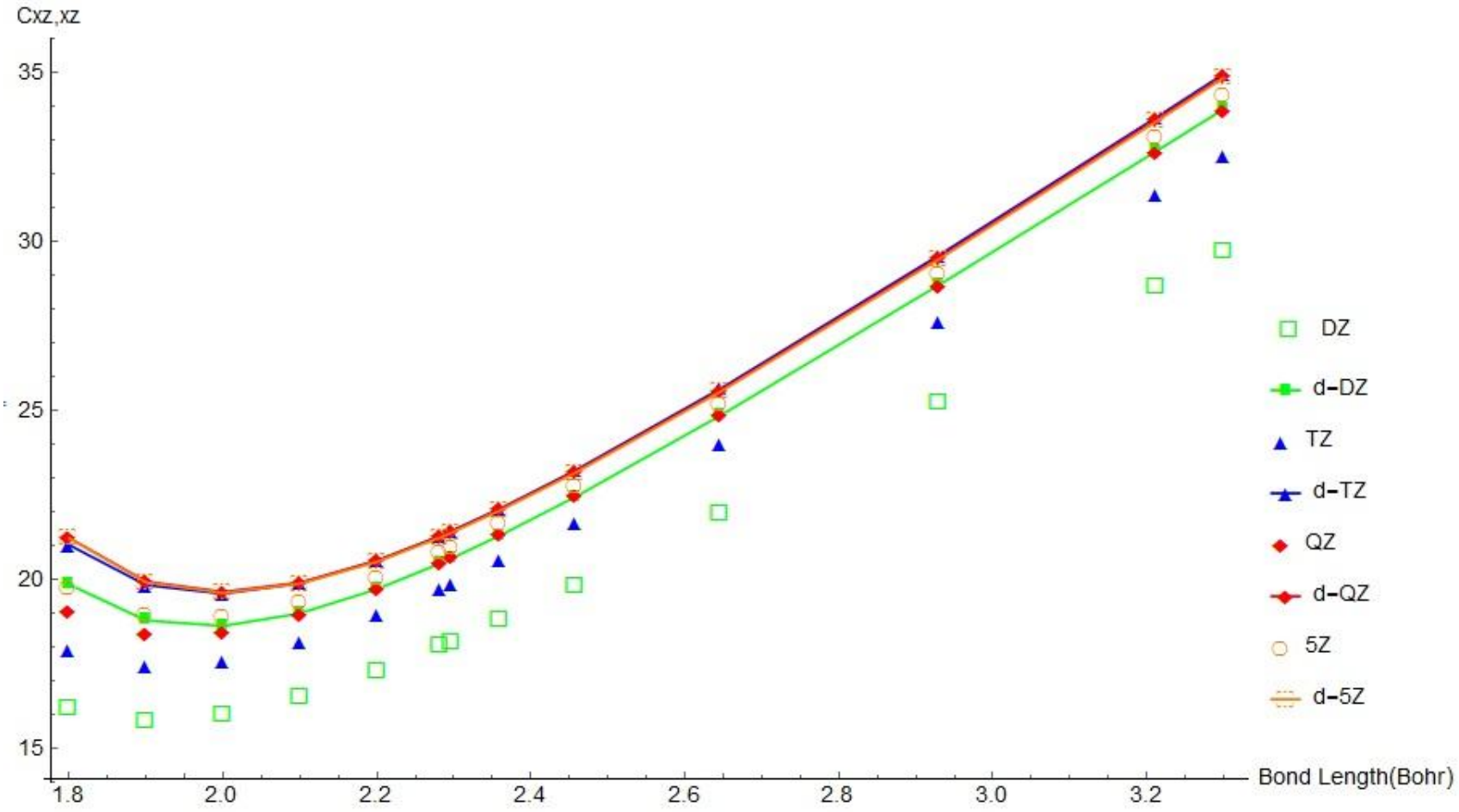

Figure 42. The quadrupole-quadrupole polarizability ($C_{xz,xz}$) in atomic units versus bond distance obtained using the CASPT2 basis set and the singly and doubly augmented basis sets

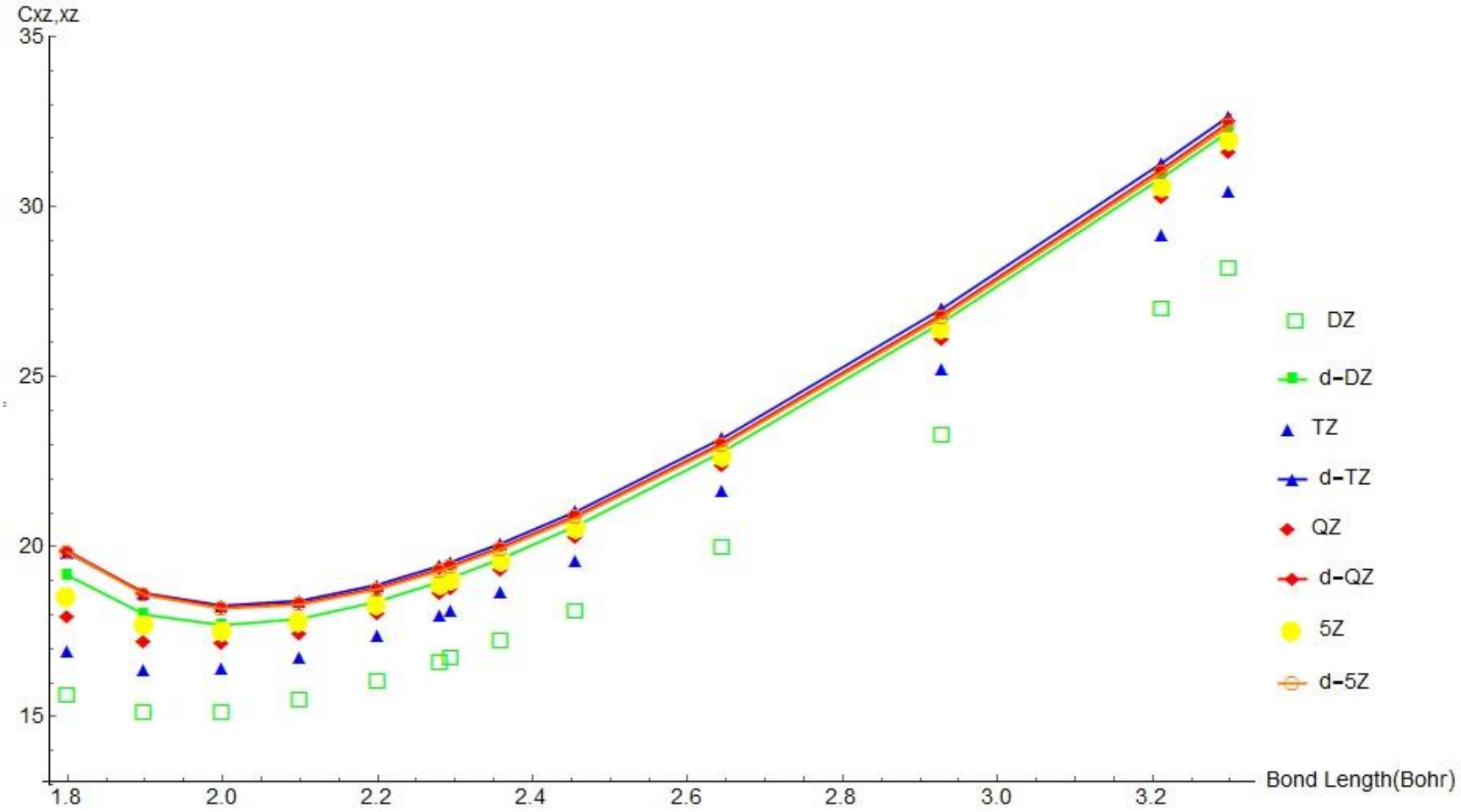

Figure 43. The quadrupole-quadrupole polarizability ($C_{xz,xz}$) in atomic units versus bond distance obtained using the MRCI method and the singly and doubly augmented basis sets

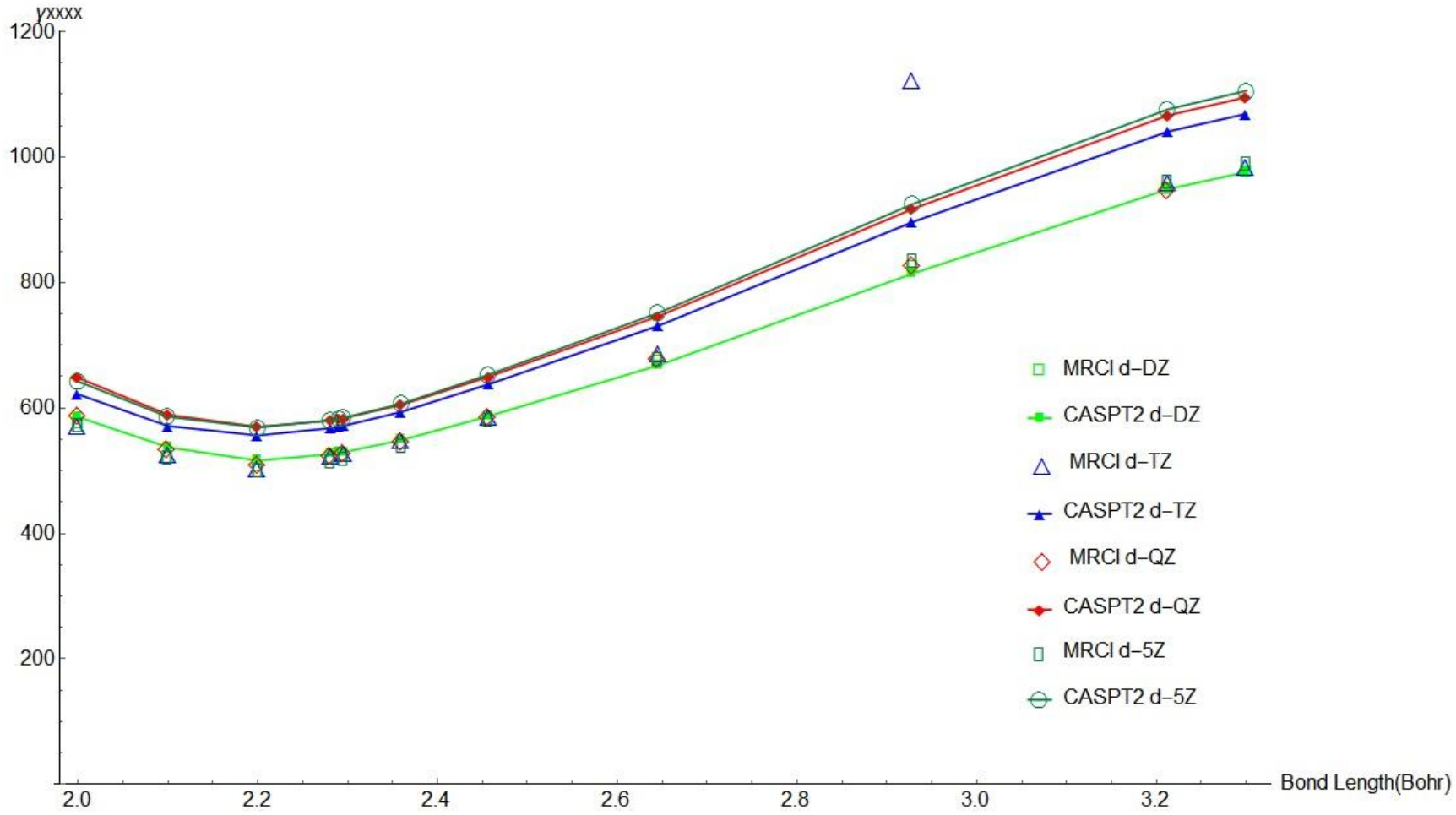

Figure 44. The second hyperpolarizability (γ_{xxxx}) in atomic units versus bond distance obtained using the MRCI and CASPT2 methods and the doubly augmented basis sets

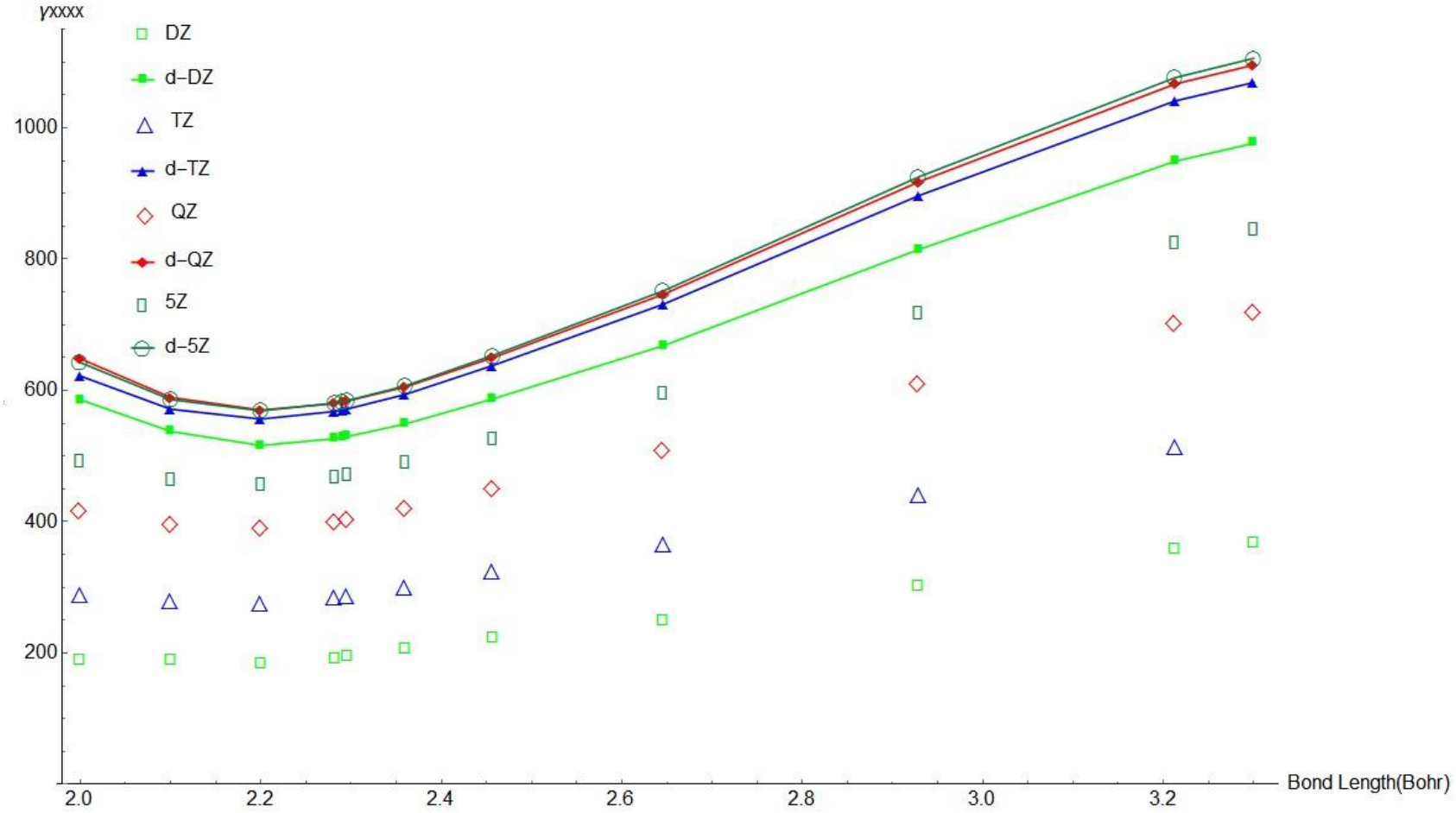

Figure 45. The second hyperpolarizability (γ_{xxxx}) in atomic units versus bond distance obtained using the CASPT2 method and the singly and doubly augmented basis sets

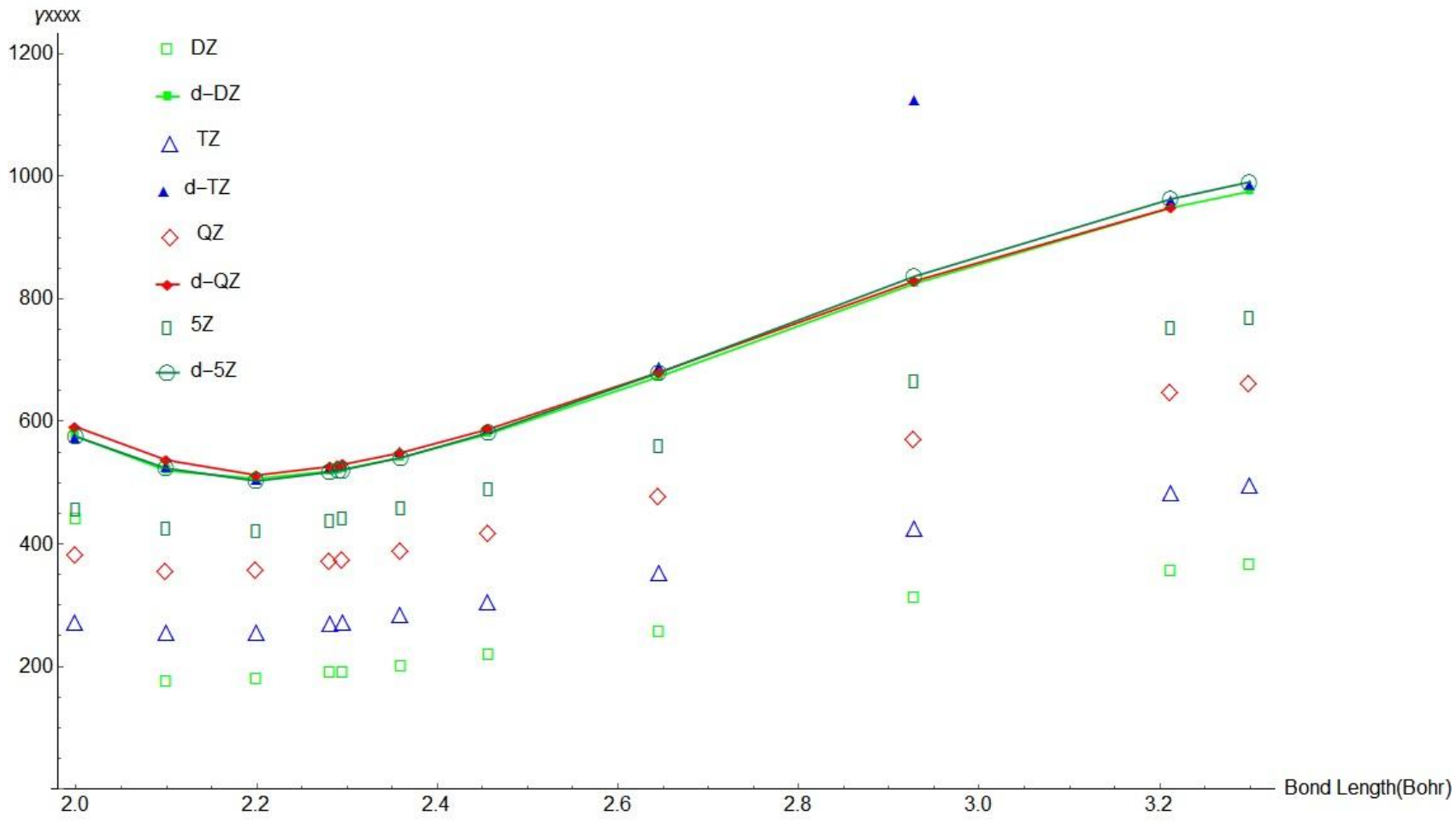

Figure 46. The second hyperpolarizability (γ_{xxxx}) in atomic units versus bond distance obtained using the MRCI method and the singly and doubly augmented basis sets

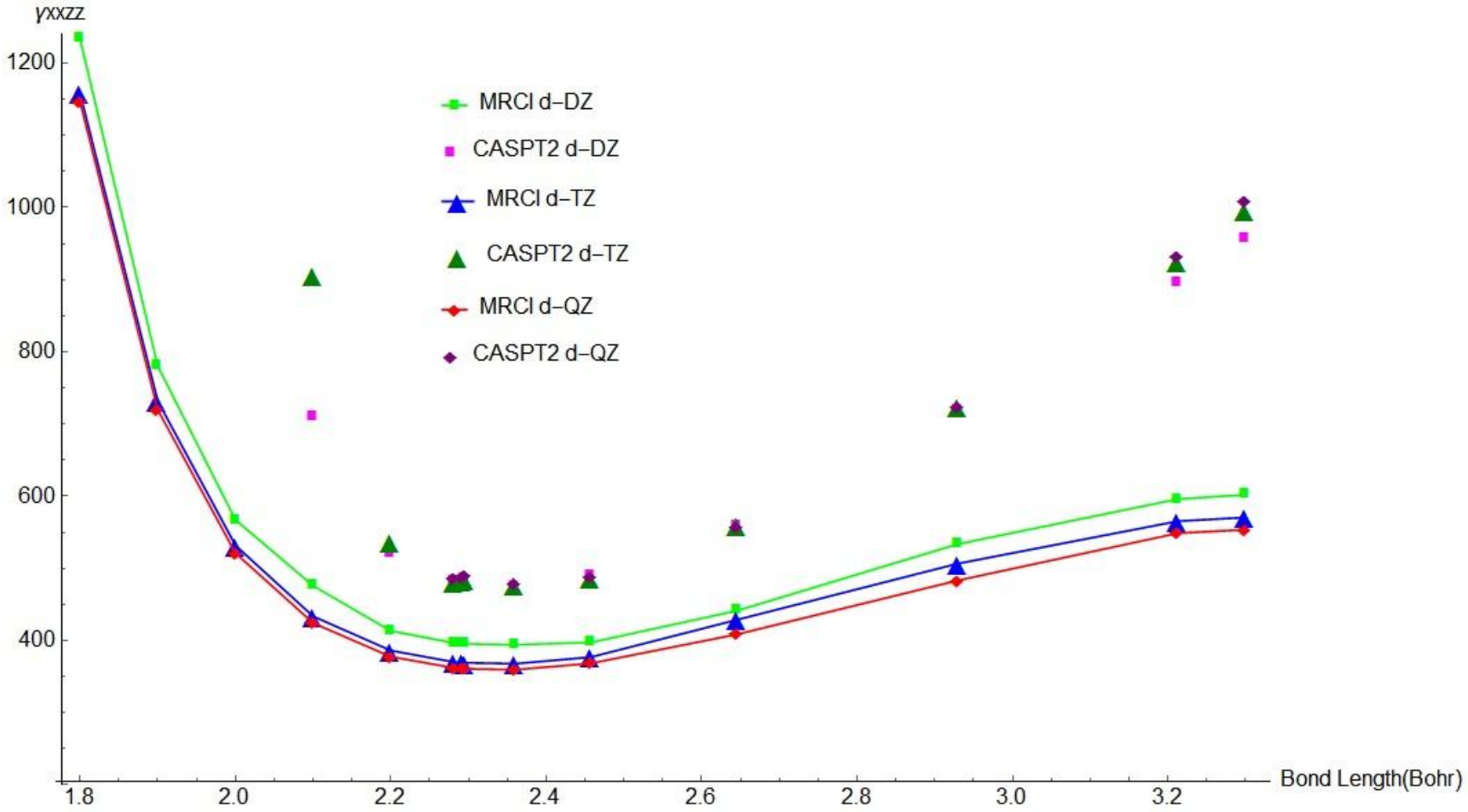

Figure 47. The second hyperpolarizability (γ_{xxzz}) in atomic units versus bond distance obtained using the MRCI and CASPT2 methods and the doubly augmented basis sets

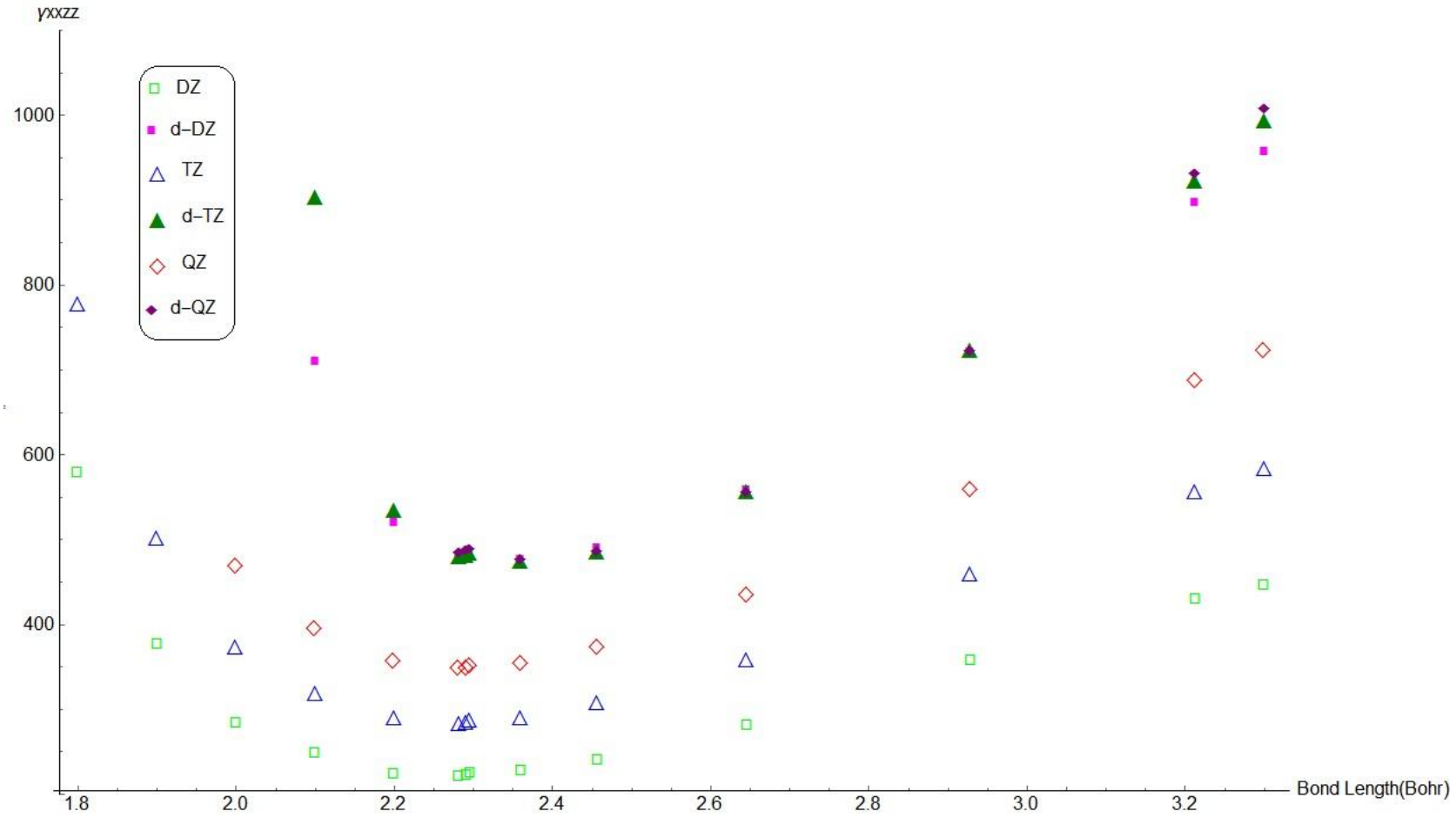

Figure 48. The second hyperpolarizability (γ_{xxzz}) in atomic units versus bond distance obtained using the CASPT2 method and the singly and doubly augmented basis sets

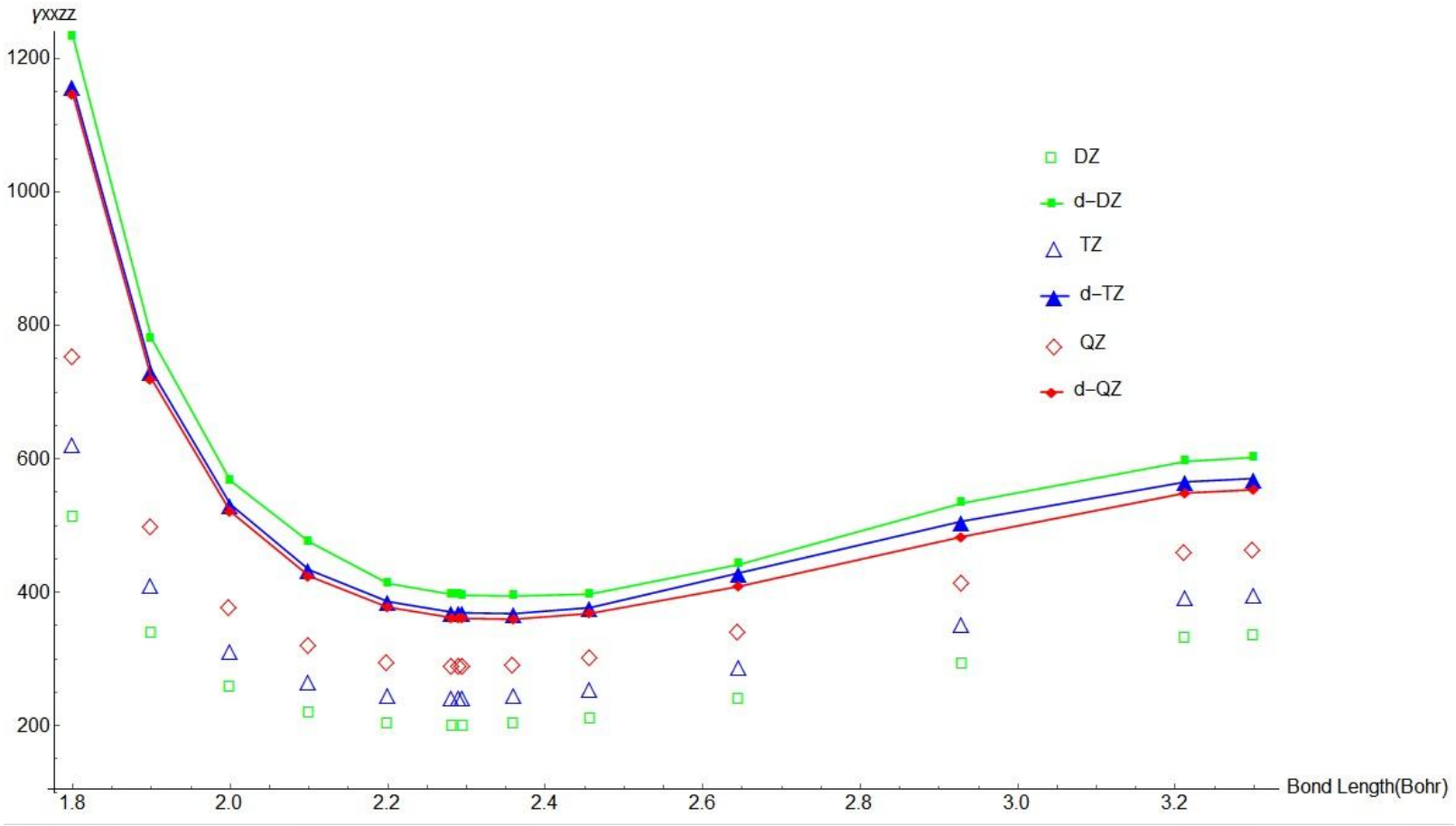

Figure 49. The second hyperpolarizability (γ_{xxzz}) in atomic units versus bond distance obtained using the MRCI method and the singly and doubly augmented basis sets

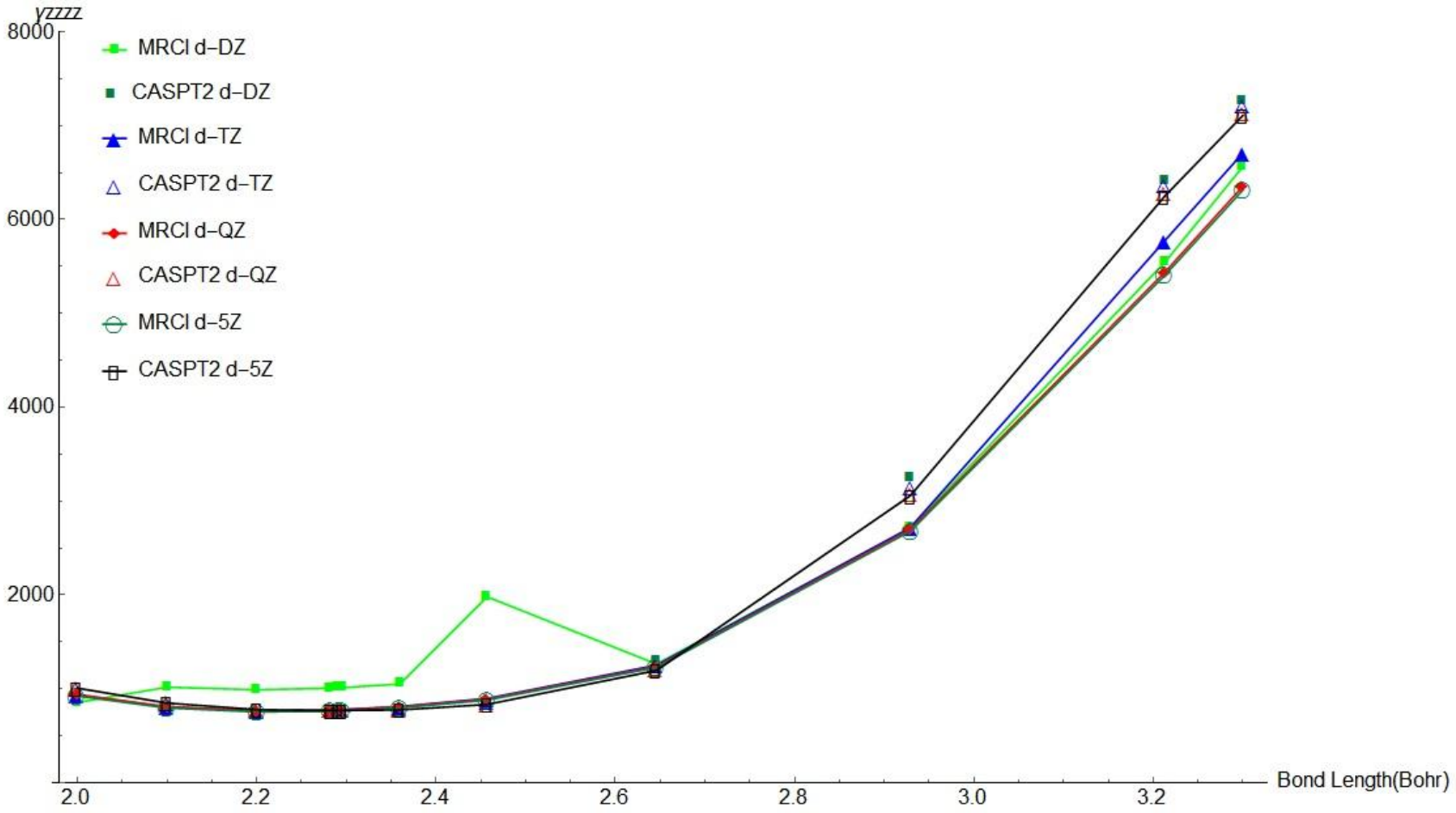

Figure 50. The second hyperpolarizability (γ_{zzzz}) in atomic units versus bond distance obtained using the MRCI and CASPT2 methods and the doubly augmented basis sets

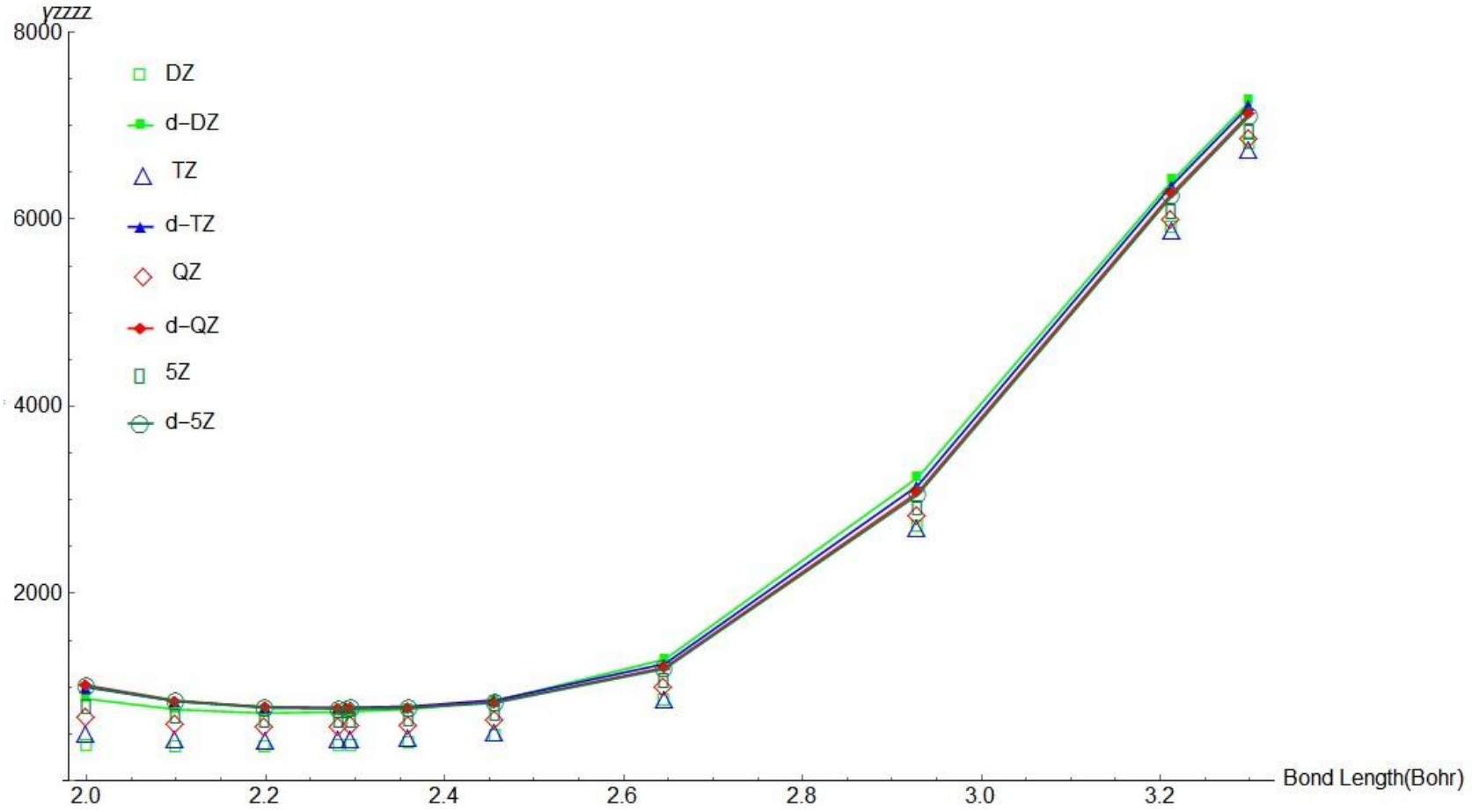

Figure 51. The second hyperpolarizability (γ_{zzzz}) in atomic units versus bond distance obtained using the CASPT2 method and the singly and doubly augmented basis sets

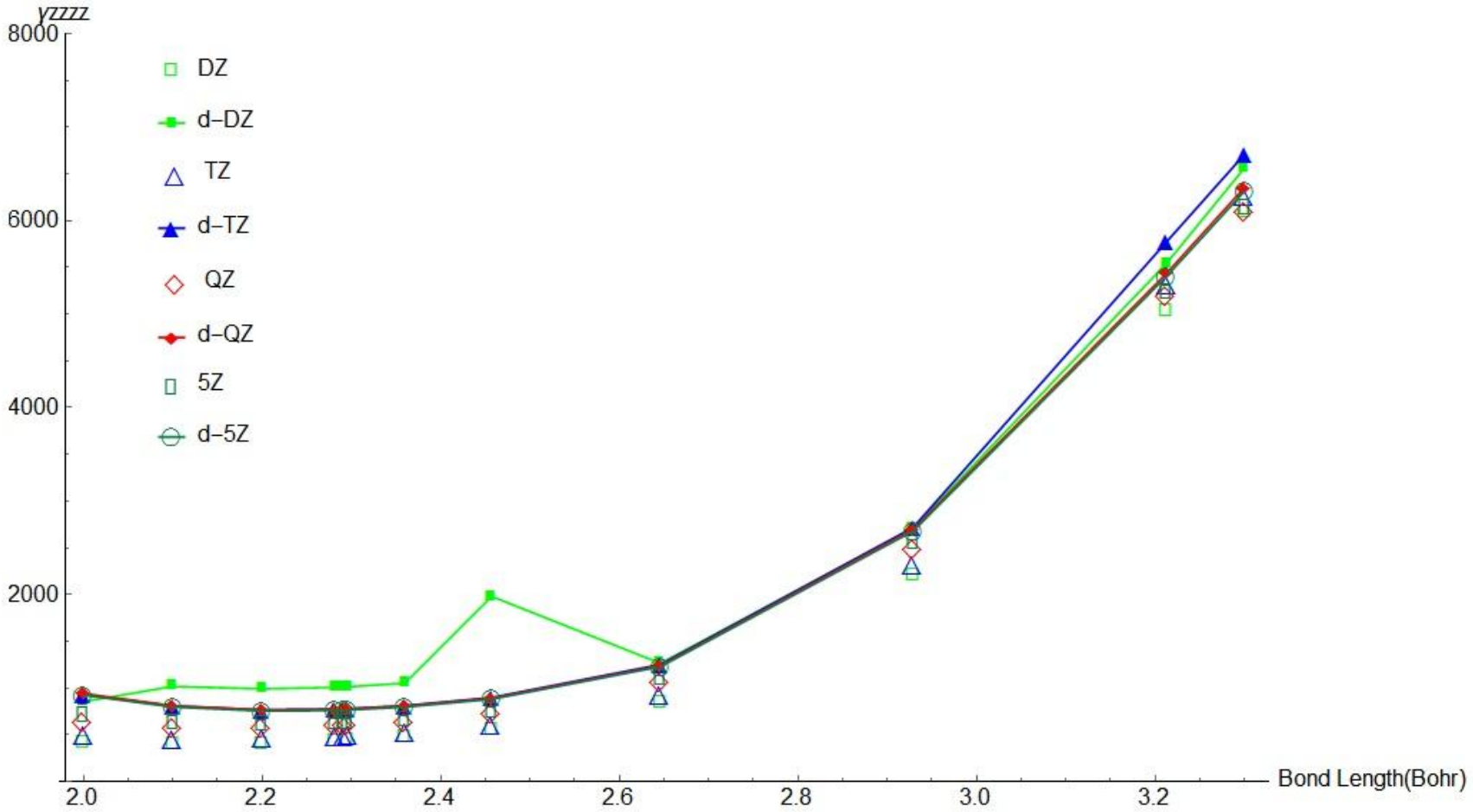

Figure 52. The second hyperpolarizability (γ_{zzzz}) in atomic units versus bond distance obtained using the MRCI method and the singly and doubly augmented basis sets

3.6 Estimate of Complete Basis Set Limit

From the data gathered for each electronic property, we have estimated the CBS limit as follows:

$$CBS = 0.5\big(value(5Z) + value(d5Z)\big) \pm 0.5\big(value(5Z) - value(d5Z)\big) \quad (3.16)$$

In this equation, we have found the average of the property calculated with the aug-cc-pV5Z basis set and the corresponding value calculated with the d-aug-cc-pV5Z basis set within a given method. We then find the difference between the values in order to assign an error to this value. This method of calculating the CBS limit operates on the assumption that the two basis sets should theoretically give the same limit within a given method. Therefore, the CBS limit should lie somewhere between the two values calculated with each basis set. Figure (53) shows the values calculated for the CBS limit for the $B_{x,z,xz}$ tensor, using the MRCI method. For points where the error between the two basis sets is larger, such as for the value at the bond length of 1.8 bohr in Figure (53), the value calculated using the d-aug-ccc-pV5Z basis set is probably the better one. We base this assumption on the behavior of these basis sets given in Figure (54).

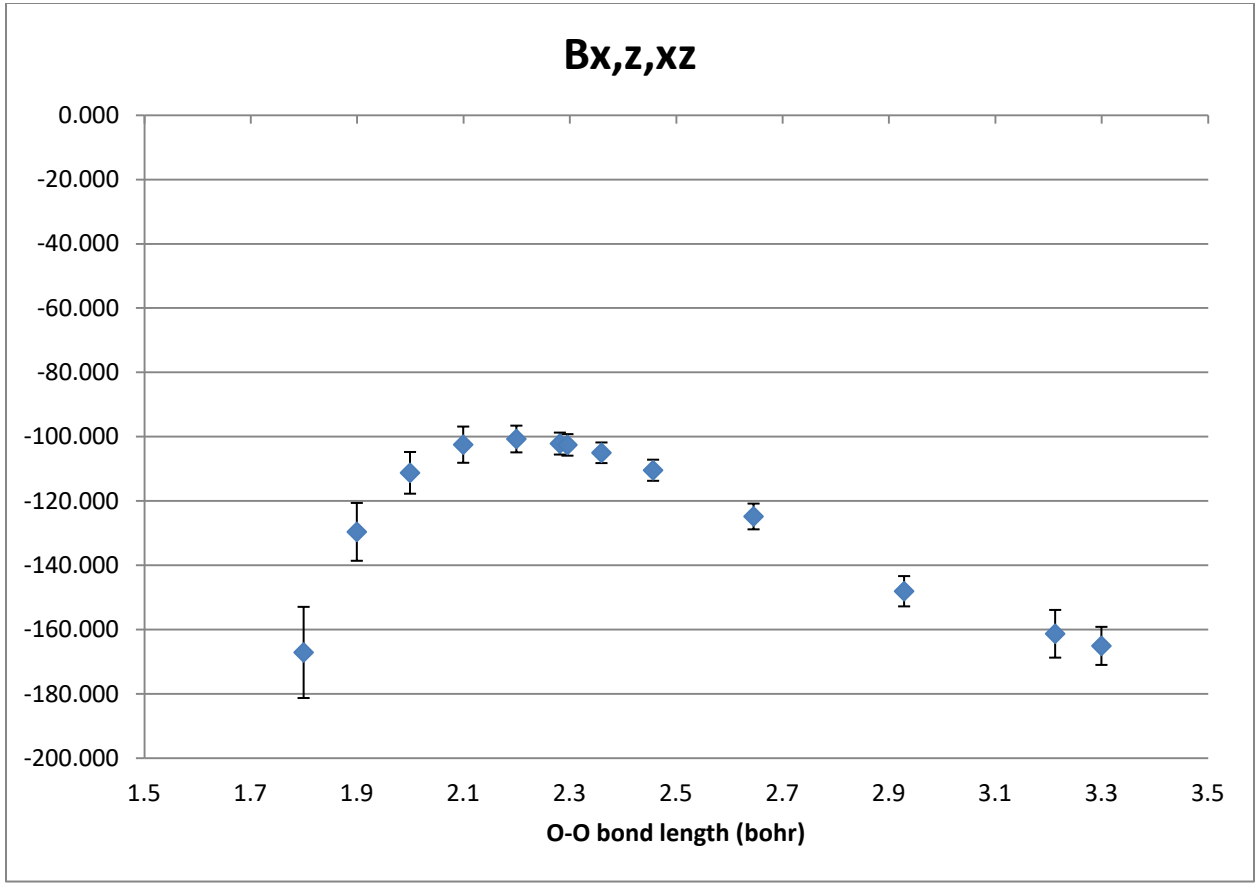

Figure 53. CBS limit for the dipole-dipole-quadrupole tensor ($B_{x,z,xz}$), with assigned error

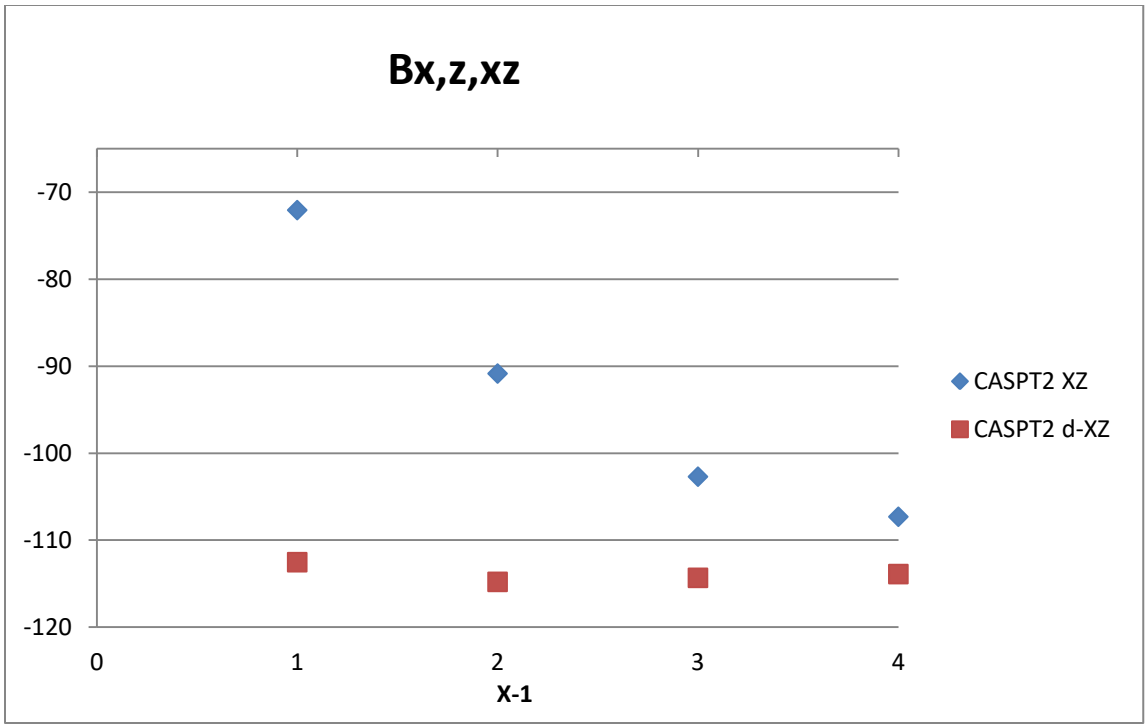

Figure 54. Convergence behavior of aug-cc-pVXZ and d-aug-cc-pVXZ basis sets, as illustrated for values of the dipole-dipole-quadrupole tensor, Bx,z,xz at the equilibrium O_2 bond distance. The x-axis has values of the cardinal number (X), given by X-1.

In Figure (54), it is apparent that the d-aug-cc-pVXZ basis set series converges to the X=5 level much more quickly than the aug-cc-pVXZ basis set. Indeed, there is very little change between the d-aug-cc-pVDZ and the d-aug-cc-pV5Z basis sets. Therefore, the value calculated with the d-aug-cc-pV5Z basis set should be used whenever larger differences are observed between the singly and doubly augmented basis sets.

Tables (33) and (34) give the CBS limit estimated values for the MRCI method, along with their calculated errors. Tables (35) and (36) give the same, calculated using the CASPT2 values.

Table 33. CBS Limit Estimated Values (B-tensors and C-tensors) Obtained with the MRCI Method

O-O (bohr)	$-B_{x,z,xz}$	$B_{x,x,zz}$	$-B_{x,x,xx}$	$-B_{z,z,zz}$	$C_{xx,xx}$	$C_{zz,zz}$	$C_{xz,xz}$
1.8	167.109±14.174	17.880±14.219	73.075±11.856	116.452±1.552	11.700±0.342	17.078±0.169	19.195±0.646
1.9	129.605±8.993	25.801±13.637	69.693±10.026	109.354±1.859	11.650±0.289	17.665±0.132	18.142±0.435
2.0	111.245±6.487	33.265±15.890	67.976±8.801	110.171±0.691	11.849±0.268	18.510±0.118	17.863±0.319
2.1	102.483±5.631	38.645±17.490	69.021±8.294	113.829±0.292	12.203±0.267	19.549±0.115	18.051±0.249
2.2	100.719±4.159	44.910±17.832	73.444±8.535	119.256±0.030	12.661±0.279	20.748±0.120	18.547±0.206
2.28187	102.143±3.413	49.185±18.305	76.729±8.193	124.832±0.349	13.093±0.294	21.837±0.129	19.119±0.184
2.296	102.552±3.353	49.536±18.682	77.010±8.537	125.882±0.410	13.171±0.298	22.035±0.130	19.231±0.181
2.36	105.002±3.203	53.309±18.545	80.568±8.052	130.844±0.705	13.541±0.314	22.960±0.139	19.775±0.171
2.457	110.439±3.287	57.664±18.376	85.861±8.217	138.820±1.099	14.135±0.340	24.461±0.155	20.711±0.161
2.646	124.812±4.006	63.424±15.831	96.206±8.522	154.219±1.421	15.376±0.399	27.696±0.194	22.842±0.158
2.929	148.070±4.711	69.972±11.427	109.991±8.732	176.311±1.285	17.332±0.484	33.207±0.261	26.592±0.175
3.213	161.305±7.418	69.756±4.008	117.431±6.919	181.094±4.973	19.281±0.549	39.377±0.320	30.822±0.208
3.3	165.074±5.917	70.929±4.126	119.439±6.836	178.633±7.143	19.858±0.562	41.365±0.337	32.187±0.218

Table 34. CBS Limit Estimated Values (polarizabilities, quadrupole moments, hexadecapole moments and E-tensors) obtained with the MRCI method

O-O (bohr)	α_{xx}	α_{zz}	Θ_{zz}	Φ_{zzzz}	$-E_{x,xxx}$	$E_{z,zzz}$
1.8	7.302±0.027	11.399±0.025	-0.983±0.001	5.345±0.013	18.541±0.307	4.178±0.560
1.9	7.266±0.022	11.706±0.014	-0.834±0.001	4.649±0.018	17.068±0.204	8.526±0.420
2.0	7.340±0.019	12.316±0.011	-0.684±0.001	4.265±0.024	16.448±0.149	11.909±0.346
2.1	7.477±0.017	13.126±0.008	-0.534±0.001	4.118±0.029	16.367±0.117	14.949±0.305
2.2	7.654±0.014	14.070±0.007	-0.384±0.001	4.164±0.033	16.687±0.100	17.966±0.282
2.28187	7.812±0.015	14.913±0.007	-0.261±0.001	4.325±0.036	17.199±0.068	20.547±0.272
2.296	7.840±0.015	15.063±0.007	-0.240±0.001	4.363±0.036	17.306±0.063	21.008±0.271
2.36	7.970±0.014	15.757±0.007	-0.145±0.001	4.572±0.038	17.858±0.044	23.164±0.267
2.457	8.167±0.013	16.842±0.007	0.003±0.001	4.991±0.040	18.879±0.020	26.675±0.265
2.646	8.537±0.013	18.989±0.007	0.259±0.001	6.122±0.044	21.476±0.008	34.526±0.271
2.929	9.010±0.016	21.837±0.009	0.598±0.001	8.447±0.047	26.749±0.031	49.529±0.289
3.213	9.350±0.018	23.189±0.016	0.853±0.001	11.360±0.046	33.594±0.019	69.923±0.314
3.3	9.425±0.018	23.140±0.004	0.911±0.001	12.346±0.045	35.996±0.008	77.267±0.355

Table 35. CBS Limit Estimated Values (B-tensors and C-tensors) obtained with the CASPT2 method

O-O (bohr)	$-B_{x,z,xz}$	$B_{x,x,zz}$	$-B_{x,x,xx}$	$-B_{z,z,zz}$	$C_{xx,xx}$	$C_{zz,zz}$	$C_{xz,xz}$
1.8	183.195±15.756	11.664±1.680	77.356±7.178	125.469±12.397	12.112±0.382	17.633±0.194	20.486±0.735
1.9	140.849±9.400	19.973±1.131	72.853±5.235	115.827±7.772	12.027±0.323	18.192±0.153	19.428±0.491
2.0	120.579±6.316	27.346±0.989	72.512±4.094	113.153±5.525	12.215±0.300	19.035±0.137	19.250±0.355
2.1	111.691±4.662	34.067±0.997	75.119±3.776	115.050±4.379	12.573±0.300	20.087±0.135	19.602±0.277
2.2	109.176±3.735	39.543±1.145	79.047±3.796	120.102±3.812	13.046±0.314	21.312±0.142	20.296±0.229
2.28187	110.601±3.294	44.137±1.301	83.355±4.085	125.643±3.607	13.494±0.332	22.429±0.152	21.039±0.206
2.296	111.028±3.245	44.823±1.196	84.161±4.137	126.698±3.584	13.576±0.336	22.631±0.154	21.179±0.202
2.36	113.624±3.061	48.254±1.484	87.901±4.288	131.855±3.581	13.961±0.354	23.583±0.165	21.853±0.192
2.457	119.279±2.921	52.850±1.774	94.491±5.658	140.374±3.682	14.582±0.384	25.127±0.184	22.971±0.182
2.646	133.903±2.974	60.566±2.471	107.164±5.905	159.213±4.047	15.879±0.451	28.460±0.229	25.374±0.181
2.929	158.381±3.460	70.103±3.564	121.561±7.676	178.153±5.104	17.917±0.548	34.131±0.307	29.260±0.204
3.213	173.121±4.095	75.920±4.130	130.935±9.083	179.067±6.324	19.933±0.620	40.463±0.380	33.319±0.242
3.3	174.079±4.165	76.022±4.433	132.262±9.381	174.362±6.114	20.526±0.635	42.499±0.400	34.587±0.256

Table 36. CBS Limit Estimated Values (polarizabilities, quadrupole moments, hexadecapole moments and E-tensors) obtained with the CASPT2 method

O-O (bohr)	α_{xx}	α_{zz}	Θ_{zz}	Φ_{zzzz}	$-E_{x,xxx}$	$E_{z,zzz}$
1.8	7.500±0.025	11.664±0.033	-0.990±0.001	5.509±0.015	19.406±0.363	3.677±0.624
1.9	7.446±0.015	11.929±0.021	-0.837±0.001	4.750±0.020	17.713±0.237	8.349±0.464
2.0	7.515±0.010	12.527±0.015	-0.684±0.001	4.325±0.026	16.976±0.161	11.908±0.377
2.1	7.655±0.008	13.345±0.012	-0.531±0.001	4.151±0.031	16.838±0.112	15.035±0.329
2.2	7.832±0.007	14.314±0.010	-0.377±0.001	4.179±0.035	17.107±0.078	18.076±0.303
2.28187	7.996±0.006	15.188±0.010	-0.251±0.001	4.333±0.038	17.581±0.058	20.639±0.292
2.296	8.026±0.006	15.344±0.010	-0.229±0.001	4.370±0.038	17.684±0.055	21.093±0.290
2.36	8.163±0.007	16.072±0.010	-0.132±0.001	4.576±0.040	18.229±0.042	23.208±0.287
2.457	8.368±0.007	17.215±0.009	0.013±0.001	4.997±0.042	19.230±0.027	26.621±0.286
2.646	8.743±0.010	19.495±0.009	0.282±0.001	6.146±0.046	21.865±0.004	34.173±0.297
2.929	9.251±0.015	22.480±0.010	0.627±0.001	8.527±0.049	27.297±0.015	48.832±0.328
3.213	9.607±0.018	23.768±0.010	0.884±0.001	11.515±0.047	34.384±0.012	69.616±0.363
3.3	9.686±0.019	23.672±0.010	0.941±0.001	12.525±0.046	36.880±0.007	77.327±0.374

3.7 Rovibrational Averages

As we stated at the beginning of the last section, the purpose of obtaining the electric properties of the O_2 molecule at non-equilibrium values is for the use in calculating the averages of the properties at the first six vibrational levels(υ=0-5), in the rotational ground state (J=0). We used our MRCI potential energy curve and the Numerov-Cooley[129,130] method to first obtain the rovibrational wavefunction, $\chi_\upsilon(R)$. Our grid spanned the region of 1.5 to 5.5 bohr and contained 3000 points. We then integrated numerically over the internuclear distance R to obtain each property P as $\langle \chi_\upsilon(R) |P(R)| \chi_\upsilon(R) \rangle$. The averages thus obtained are shown in the following tables.

Table 37. Vibrational averages obtained for the MRCI properties, at the d-aug-cc-pV5Z basis set level, unless otherwise noted.

υ	α_{xx}	α_{zz}	$-\Theta_{zz}$	Φ_{zzzz}	$-E_{x,xxx}$	$E_{z,zzz}$	γ_{xxzz}*	γ_{xxxx}	γ_{zzzz}
$r=r_0$	7.8451	15.0188	0.2478	4.3140	17.3338	21.1222	361.1860	519.8290	763.3750
0	7.8473	15.0335	0.2483	4.3494	17.4011	21.1820	365.5860	523.8240	774.8550
1	7.8885	15.2640	0.2211	4.4721	17.6725	21.9396	373.6440	538.5700	804.6570
2	7.9295	15.4958	0.1940	4.5998	17.9557	22.7229	381.7650	552.8010	838.4130
3	7.9704	15.7288	0.1669	4.7327	18.2513	23.5354	389.6740	566.5900	877.0130
4	8.0113	15.9639	0.1397	4.8713	18.5604	24.3831	397.1410	580.0360	921.4350
5	8.0522	16.2009	0.1122	5.0156	18.8835	25.2692	404.0280	593.2320	972.6930

*Using properties obtained with the d-aug-cc-pVQZ basis set

Table 38. Vibrational averages obtained for the MRCI properties, at the d-aug-cc-pV5Z basis set level

υ	$B_{x,z,xz}$	$B_{x,x,zz}$	$B_{x,x,xx}$	$B_{z,z,zz}$	$C_{xx,xx}$	$C_{zz,zz}$	$C_{xz,xz}$
$r=r_0$	-105.7740	68.0230	-85.7960	-125.9130	13.4413	22.0970	19.3750
0	-106.5965	68.0267	-85.4824	-126.3420	13.4563	22.1296	19.4201
1	-108.5077	68.4101	-86.7799	-128.0340	13.5951	22.4641	19.6518
2	-110.5015	68.7584	-88.0485	-129.7910	13.7360	22.8066	19.8898
3	-112.5631	69.0784	-89.2946	-131.6020	13.8792	23.1578	20.1344
4	-114.6779	69.3803	-90.5280	-133.4630	14.0253	23.5196	20.3863
5	-116.8290	69.6675	-91.7536	-135.3590	14.1743	23.8925	20.6458

Table 39. Vibrational averages obtained for the CASPT2 properties, at the d-aug-cc-pV5Z basis set level, unless otherwise noted.

υ	α_{xx}	α_{zz}	Θ_{zz}	Φ_{zzzz}	$E_{x,xxx}$	$E_{z,zzz}$	γ_{xxzz}*	γ_{xxxx}	γ_{zzzz}
$r=r_0$	7.6278	15.4064	-0.2232	4.3444	-17.7727	21.5352	-351.760	-585.777	-769.817
0	8.0265	15.3188	-0.2382	4.3558	-17.7796	21.2784	-356.507	-588.686	-777.03
1	8.0692	15.5649	-0.2103	4.4807	-18.0554	22.0029	-366.168	-604.538	-800.22
2	8.1117	15.8124	-0.1824	4.6110	-18.3442	22.7516	-375.824	-619.604	-829.849
3	8.1540	16.0612	-0.1546	4.7466	-18.6463	23.5282	-385.481	-634.017	-867.172
4	8.1965	16.3121	-0.1267	4.8881	-18.9627	24.3394	-395.148	-647.944	-913.489
5	8.2390	16.5646	-0.0986	5.0357	-19.2941	25.1888	-404.847	-661.55	-970.149

*Obtained using the aug-cc-pVQZ basis set

Table 40. Vibrational averages obtained for the CASPT2 properties, at the d-aug-cc-pV5Z basis set level

υ	$B_{x,z,xz}$	$B_{x,x,zz}$	$B_{x,x,xx}$	$B_{z,z,zz}$	$C_{xx,xx}$	$C_{zz,zz}$	$C_{xz,xz}$
$r=r_0$	-114.3830	46.5130	-88.5480	-130.6210	13.9404	22.8544	21.4273
0	-114.9325	45.8690	-88.3302	-130.2810	13.8987	22.7504	21.3782
1	-116.8292	46.7178	-89.9921	-132.5340	14.0450	23.0961	21.6446
2	-118.8062	47.5639	-91.6356	-134.7980	14.1934	23.4501	21.9156
3	-120.8533	48.4096	-93.2589	-137.0600	14.3441	23.8129	22.1913
4	-122.9601	49.2609	-94.8642	-139.3110	14.4978	24.1867	22.4728
5	-125.1133	50.1181	-96.4479	-141.5370	14.6546	24.5720	22.7602

Often, the vibrationally averaged bond distance (r_0) is used in *ab initio* calculations to obtain the expectation value of a given property at the υ=0 vibrational energy level. The Numerov-Cooley method is a good method for evaluating how good of an approximation this procedure is. We have calculated the properties in the above tables *ab initio* at the vibrationally averaged bond distance ($r=r_0$)for each method, and compared them with the averages at υ=0 obtained with the Numerov-Cooley method. The average properties for the MRCI method at υ=0 (Tables 3 and 4) are less than 1% different from the *ab initio* properties obtained at r_0=2.2912 bohr. The properties for the CASPT2 method at υ=0 (tables 5 and 6) are less than 1.4% different than the properties obtained at r_0=2.3007 bohr. Therefore, at least for the O_2 molecule and the first five vibrational levels, using the vibrationally averaged bond distance to obtain these properties is an excellent approximation.

3.8 Conclusion

We have obtained values for the dipole polarizability ($\alpha_{\alpha\beta}$), quadrupole moment (Θ_{zz}), hexadecapole (Φ_{zzzz}) moment, dipole-octopole ($E_{\alpha,\beta\gamma\delta}$), quadrupole-quadrupole ($C_{\alpha\beta,\gamma\delta}$), and dipole-dipole-quadrupole ($B_{\alpha,\beta,\gamma\delta}$) polarizabilities and second hyper-polarizabilities ($\gamma_{\alpha\beta\gamma\delta}$) for the oxygen molecule O_2 using both the MRCI and CASPT2 methods. We have examined the effect on these properties of changing the cardinal number (X) in the aug-cc-PVXZ basis set, with X=D,T,Q and 5. We have also examined the effect of adding a second diffuse function to the aug-cc-pVXZ basis sets to result in the d-aug-cc-pVXZ basis sets.

We have also compared our properties at the equilibrium bond length with properties in the literature, and find good agreement. We have been unable to find values for comparison to our dipole-dipole-quadrupole ($B_{\alpha,\beta,\gamma\delta}$) polarizabilities in the literature.

We have exhaustively examined the properties for their basis set sensitivity, and find that for the singly augmented basis set aug-cc-pVXZ, the components of the dipole polarizability ($\alpha_{\alpha\beta}$) are quite insensitive to the choice of cardinal number X. However, the quadrupole moment (Θ_{zz}), hexadecapole (Φ_{zzzz}) moment, dipole-octopole ($E_{\alpha,\beta\gamma\delta}$), quadrupole-quadrupole ($C_{\alpha\beta,\gamma\delta}$), and dipole-dipole-quadrupole ($B_{\alpha,\beta,\gamma\delta}$) polarizabilities and second hyper-polarizabilities ($\gamma_{\alpha\beta\gamma\delta}$) all displayed sensitivity to a change in cardinal number, with the second hyper-polarizability showing the greatest change in value when increasing the basis set size from the aug-cc-pVDZ to aug-cc-PV5Z level.

For the properties obtained with the doubly augmented basis set d-aug-cc-pVXZ we find that there is a large stabilization in values amongst cardinal number; that is, many of the properties do not vary much when the cardinal number is increased. Notably, although the second hyperpolarizability γ_{xxxx} was amongst the most sensitive to a change in cardinal number for the singly augmented series, for the doubly augmented series we see virtually no change in this property when the cardinal number is increased from X=D to X=5. We therefore agree with Bartolomei *et al.*[114] when they state that "the use of polarized functions of high zeta order in the basis sets is important to describe accurately multipole moments especially those of high order..".

The quadrupole moment, hexadecapole moment, dipole-dipole-quadrupole polarizability, and some components of the quadrupole-quadrupole polarizability and second hyperpolarizability still show sensitivity to the cardinal number chosen for the doubly augmented basis set. Most often, the majority of the difference is found when the basis set is increased from the d-aug-cc-pVDZ to the d-aug-cc-pVTZ level. This separation was seen in many of the singly augmented properties as well. This strong effect of f functions in the basis set has been attributed to the fact

that the Φ orbitals can be accessed during two successive dipole allowed transitions if the Π orbitals are occupied in the reference state[133].

We also compared the properties obtained at the MRCI and CASPT2 methods and examined them for any differences. We found that the dipole polarizabilities, quadrupole-quadrupole polarizabilities, quadrupole moment, and hexadecapole moment were in excellent agreement. Larger differences between methods were found for the dipole-dipole-quadrupole and dipole-octopole polarizabilities, and for the second hyperpolarizabilities.

In addition, we examined the properties for sensitivity to adding a second set of diffuse functions to the aug-cc-pV5Z basis set to form the d-aug-cc-pV5Z basis set. We conclude that the dipole polarizabilities, quadrupole-quadrupole polarizabilities, quadrupole moment and hexadecapole moment are essentially unchanged when adding a diffuse function. The largest changes are seen in the dipole-dipole-quadrupole polarizabilities, dipole-octupole polarizabilities, and second hyperpolarizabilities.

CHAPTER 4: Long-Range Approximation for the Interaction Dipole Moments of the O_2-O_2 Supermolecule, for Collision-Induced Absorption Applications

4.1 Introduction: The Use of Electric Properties in the Long-Range Approximation

In order to be useful for spectroscopic rototranslational line-shape analysis[134-136], it is customary to cast collision-induced dipole moments into a symmetry-adapted spherical harmonic expansion as follows[137-139,68,69]:

$$\mu_M(r_A, r_B, R) = \frac{(4\pi)^{3/2}}{\sqrt{3}} \sum_{\substack{\lambda_A,\lambda_B,\lambda \\ L,m_A,m_B}} D_{\lambda_A,\lambda_B,\lambda,L}(r_A, r_B, R) Y_{\lambda_A}^{m_A}(\hat{r}_A) \times Y_{\lambda_B}^{m_B}(\hat{r}_B) Y_L^{M-m}(\hat{R}) \langle \lambda_A \lambda_B m_A m_B | \lambda m \rangle \langle \lambda L m M - m | 1 M \rangle \quad (4.1)$$

where $\hat{r}_A$ and $\hat{r}_B$ are unit vectors along the symmetry axes of molecules A and B, $\hat{R}$ is a unit vector along the intermolecular vector **R** between molecules A and B and $\langle \lambda_A \lambda_B m_A m_B | \lambda m \rangle$ is a Clebsch-Gordan coefficient. The first step in calculating the dipole moments using the expansion is to determine the expansion coefficients $D_{\lambda_A,\lambda_B,\lambda,L}$. To calculate these expansion coefficients we first assume that the diatomic oxygen molecules are interacting at a sufficiently long distance apart as to consider overlap, exchange, and charge transfer effects to be negligible; therefore this model is only valid at long-range distances of the intermolecular separation R. The equations used include induction by permanent multipolar fields and their gradients[137,138,140-143], dispersion[144-147], and back-induction[148] and are complete through order R^{-7} in the intermolecular separation R.

To calculate the expansion coefficients for the direct induction contribution to the collision-induced dipole moment, we have used the following expressions[69,146,149]:

$$D_{2023}^{i} = -\sqrt{3}\bar{\alpha}^{B}\Theta^{A}R^{-4} \quad (4.2)$$

$$D^i_{4045} = -\sqrt{5}\bar{\alpha}^B \Phi^A R^{-6} \tag{4.3}$$

$$D^i_{22\lambda L} = \left[1 + (-1)^{\lambda+1} \wp_{AB}\right] \times \left[a^i_{\lambda L}(\alpha^A_{||} - \alpha^A_{-|-})\Theta^B R^{-4} + b^i_{\lambda L}(3E^A_{z,zzz} - 8E^A_{x,xxx})\Theta^B R^{-6}\right] \tag{4.4}$$

$$D^i_{42\lambda L} = \left[c^i_{\lambda L}(\alpha^B_{||} - \alpha^B_{-|-})\Phi^A + d^i_{\lambda L}(E^A_{z,zzz} + 2E^A_{x,xxx})\Theta^B\right] R^{-6} \tag{4.5}$$

$$D^i_{0\lambda\lambda L} = -\wp_{AB} D^i_{\lambda 0 \lambda L} \tag{4.6}$$

$$D^i_{24\lambda L} = (-1)^{\lambda+1} \wp_{AB} D^i_{42\lambda L} \tag{4.7}$$

where $\bar{\alpha}^B$ is the isotropic dipole polarizability of molecule B in the A-B collision pair, given by

$$\bar{\alpha} = \frac{1}{3}(\alpha_{\parallel} + 2\alpha_{\perp}) \tag{4.8}$$

and $\alpha_{\parallel} \equiv \alpha_{zz}, \alpha_{\perp} \equiv \alpha_{xx} = \alpha_{yy}$. The coefficient D^i_{2023} contains additionally the permanent quadrupole moment (Θ^A) and thus describes the quadrupolar induction through order R^{-4}; and the coefficient D^i_{4045} contains the permanent hexadecapole moment Φ^A and therefore describes the hexadecapolar induction through order R^{-6}. Equation (4.4) contains the permanent quadrupole moment, and also the dipole-octopole polarizability E. Similarly, equation (4.5) contains the permanent hexadecapole moment and again the dipole-octopole polarizability E.

The coefficients $a^i_{\lambda L}$, $b^i_{\lambda L}$, $c^i_{\lambda L}$, and $d^i_{\lambda L}$ are given in the Ref. [69]. In this work, the superscripts *A* and *B* refer to molecules *A* and *B*, which in this work are an oxygen molecule at its equilibrium bond length, and an oxygen molecule with a bond length of 2-3.3 bohr, respectively. In equations (4.6) and (4.7), the operator $\wp_{AB}$ interchanges molecules A and B, but does not change the direction of the intermolecular vector **R**.

Back-induction effects appear at order R^{-7}. This is a classical effect that occurs when the quadrupolar field of molecule A polarizes its neighbor (molecule B), setting up a static reaction

field that acts back onto molecule A, producing a dipole[69,150]. The back-induction expansion coefficients for the collision-induced dipole with λ_B=0 are calculated using the following:

$$D^b_{0001} = (1 - \wp_{AB})\frac{6}{5}(\alpha^B_{||} - \alpha^B_{\_|\_})\bar{\alpha}^A\Theta^B R^{-7} \tag{4.9}$$

$$D^b_{2021} = \frac{3\sqrt{2}}{5}(2\alpha^A_{||} - \alpha^A_{\_|\_})\bar{\alpha}^B\Theta^A R^{-7} - \frac{\sqrt{2}}{25}(\alpha^B_{||} - \alpha^B_{\_|\_})(\alpha^A_{||} - \alpha^A_{\_|\_})\Theta^B R^{-7} \tag{4.10}$$

$$D^b_{2023} = \frac{8}{25}\sqrt{\frac{1}{3}}(\alpha^B_{||} - \alpha^B_{\_|\_})(\alpha^A_{||} - \alpha^A_{\_|\_})\Theta^B R^{-7} - \frac{4\sqrt{3}}{35}(3\alpha^A_{||} - 4\alpha^A_{\_|\_})\bar{\alpha}^B\Theta^A R^{-7} \tag{4.11}$$

$$D^b_{4043} = \frac{24}{35}(\alpha^A_{||} - \alpha^A_{\_|\_})\bar{\alpha}^B\Theta^A R^{-7} \tag{4.12}$$

Terms with λ_A=0 are given by the analog of equation (4.6).

All remaining back-induction terms can be obtained using the following general formula:

$$D^b_{\lambda_A 2\lambda L} = \left[1 + \delta_{\lambda_A 2}(-1)^{\lambda+1}\wp_{AB}\right]\left[a^b_{\lambda_A\lambda L}\bar{\alpha}^A + b^b_{\lambda_A\lambda L}(\alpha^A_{||} - \alpha^A_{\_|\_})\right](\alpha^B_{||} - \alpha^B_{\_|\_})\Theta^A R^{-7} \tag{4.13}$$

Coefficients *a* and *b* are given in Ref. [69].

Dispersion is the last effect that contributes to the collision-induced dipole at long range. This effect is purely quantum mechanical, and arises from the constantly fluctuating charge distributions of the interacting molecules[82]. To evaluate the dispersion contribution to the dipole, the dipole-quadrupole hyperpolarizabilites ($B_{\alpha\beta,\gamma\delta}$) are required. as functions of the imaginary frequency. However, the dispersion coefficients can be evaluated using static response tensors and dispersion energy coefficients $C_n^{L_A L_B M}$, as demonstrated by Bohr and Hunt[69], using the Constant Ratio approximation. The isotropic dispersion coefficient is given by:

$$D_{0001}^{d} \cong 2C_6^{000}R^{-7}\left[\frac{B_0^A}{\bar{\alpha}^A} - \frac{B_0^B}{\bar{\alpha}^B}\right] \tag{4.14}$$

where

$$B_0^{A,B} = \frac{2}{15}B_{z,z,zz} + \frac{8}{15}B_{x,z,xz} + \frac{2}{15}B_{x,x,zz} + \frac{8}{15}B_{x,x,xx} \tag{4.15}$$

The anisotropic dispersion coefficients are given approximately by

$$D_{2021}^{d} \cong -\frac{\sqrt{2}}{5}C_6^{200}\left[\frac{4(3B_{2b}^A + B_{2c}^A + 10B_{2d}^A)}{(\alpha_{||}^A - \alpha_{\_|\_}^A)} - \frac{B_0^B}{\bar{\alpha}^B}\right]R^{-7} \tag{4.16}$$

$$D_{2023}^{d} \cong -\frac{8}{5\sqrt{3}}C_6^{200}\left[\frac{B_0^B}{\bar{\alpha}^B} - 2\frac{(B_{2b}^A + 2B_{2c}^A)}{\alpha_{||}^A - \alpha_{\_|\_}^A}\right]R^{-7} \tag{4.17}$$

$$D_{4043}^{d} \cong -\frac{8}{15}C_8^{400}B_4^A R^{-7}/(3C_4^A + 2E_4^A) \tag{4.18}$$

$$D_{22\lambda L}^{d} \cong -\frac{2}{3}\left[1 + (-1)^{\lambda+1}\wp_{AB}\right]C_6^{220} \times \left[\frac{a_{\lambda L}^d B_{2b}^A + b_{\lambda L}^d B_{2c}^A + c_{\lambda L}^d B_{2d}^A}{\alpha_{||}^A - \alpha_{\_|\_}^A}\right]R^{-7} \tag{4.19}$$

$$D_{42\lambda L}^{d} \cong -\frac{1}{4}C_8^{420}d_{\lambda L}^d B_4^A R^{-7}/(33C_4^A + 19E_4^A) \tag{4.20}$$

The formulas for B_{2b}^A, B_{2c}^A, B_{2d}^A, B_4^A, C_4^A,and E_4^A are calculated using components of the dipole-dipole-quadrupole, quadrupole-quadrupole, and dipole-octopole polarizabilities and are given explicitly in Ref [69]. The dispersion coefficients of Bartolomei *et al* [114] have been used in these expressions: $C_6^{000} = 62.394$, $C_6^{200} = 22.293$, $C_6^{220} = 0.8$, $C_8^{400} = -219.169$, and $C_8^{420} = -6.336$. These coefficients were calculated by use of static properties obtained using the MRCI method[111] with a CASSCF[151,152] reference wavefunction and formulas contained within reference [150]. Our results for the direct multipolar induction, back induction, and dispersion terms in the

collision-induced dipole coefficients $D_{\lambda_A\lambda_B\lambda L}$ for O_2-O_2 are shown in Tables (41)-(52). We take molecule A to be an oxygen molecule with an equilibrium bond length of 2.28187 bohr, and molecule B with a non-equilibrium bond length ranging from 2-3.3 bohr. For the calculation of these terms we have used our static multipole moments and polarizabilities obtained with the CASPT2[77,78] method, using the doubly augmented correlation consistent polarized valence quadruple zeta (d-aug-cc-pVQZ) basis set of Dunning[76].

Table 41. Direct multipolar induction, back-induction, and dispersion terms in the collision-induced dipole coefficients $D_{\lambda_A\lambda_B\lambda L}$ for r_B=2 bohr, at the CASPT2 level, with the d-aug-cc-pVQZ basis set

	$D^{i}_{\lambda_A\lambda_B\lambda L}$	$D^{b}_{\lambda_A\lambda_B\lambda L}R^7$	$D^{d}_{\lambda_A\lambda_B\lambda L}R^7$
D_{0001}	0	-22.9	217
D_{2021}	0	-74.2	237
D_{2023}	$4.010R^{-4}$	31.1	195
D_{4043}	0	-11.4	-101
D_{2201}	0	-0.801	0.273
D_{2211}	0	-1.30	-0.683
D_{2221}	0	-6.33	0.167
D_{2223}	$0.5065R^{-4}$	3.24	-0.021
D_{2233}	$-2.261R^{-4}$	20.9	-1.50
D_{2243}	$2.632R^{-4}$	10.0	-1.07
D_{2245}	$-51.27R^{-6}$	-36.1	1.83
D_{4221}	0	-0.236	-0.0805
D_{4223}	0	-0.032	-0.0110
D_{4233}	0	0.150	0.0512
D_{4243}	0	-0.326	-0.111
D_{4245}	$4.126R^{-6}$	-0.265	-0.0904
D_{4255}	$16.27R^{-6}$	1.34	0.458
D_{4265}	$1.572R^{-6}$	-4.61	-1.57
D_{2421}	0	0.642	0.110
D_{2423}	0	0.087	0.0150
D_{2433}	0	0.408	0.0702
D_{2443}	0	0.887	0.153
D_{2445}	$-6.853R^{-6}$	0.721	0.124
D_{2455}	$19.02R^{-6}$	3.65	0.628
D_{2465}	$-17.76R^{-6}$	12.6	2.16
D_{0221}	0	197	-459
D_{0223}	$-12.35R^{-4}$	-94.1	-93.0
D_{0443}	0	24.5	137
D_{0445}	$100.9R^{-6}$	0	0
D_{4045}	$-88.66R^{-6}$	0	0

Table 42. Direct multipolar induction, back-induction, and dispersion terms in the collision-induced dipole coefficients $D_{\lambda_A\lambda_B\lambda L}$ for r_B=2.1, at the CASPT2 level, with the d-aug-cc-pVQZ basis set

	$D^{i}_{\lambda_A\lambda_B\lambda L}$	$D^{b}_{\lambda_A\lambda_B\lambda L}R^7$	$D^{d}_{\lambda_A\lambda_B\lambda L}R^7$
D_{0001}	0	-17.0	85.4
D_{2021}	0	-77.3	243
D_{2023}	$4.168R^{-4}$	33.0	173
D_{4043}	0	-11.9	-101
D_{2201}	0	-0.587	0.133
D_{2211}	0	-1.23	-0.614
D_{2221}	0	-4.24	0.0779
D_{2223}	$0.3305\ R^{-4}$	2.16	-0.00808
D_{2233}	$-1.920R^{-4}$	18.4	-1.23
D_{2243}	$1.717R^{-4}$	6.87	-0.517
D_{2245}	$-33.50R^{-6}$	-24.4	0.876
D_{4221}	0	-0.268	-0.0805
D_{4223}	0	-0.0364	-0.0110
D_{4233}	0	0.170	0.0512
D_{4243}	0	-0.370	-0.111
D_{4245}	$5.049R^{-6}$	-0.301	-0.0904
D_{4255}	$16.64R^{-6}$	1.52	0.458
D_{4265}	$8.113R^{-6}$	-5.24	-1.57
D_{2421}	0	0.565	0.0950
D_{2423}	0	0.077	0.0129
D_{2433}	0	0.360	0.0605
D_{2443}	0	0.781	0.131
D_{2445}	$-6.616R^{-6}$	0.635	0.107
D_{2455}	$17.84R^{-6}$	3.22	0.541
D_{2465}	$-18.11R^{-6}$	11.1	1.86
D_{0221}	0	161	-350
D_{0223}	$-9.584R^{-4}$	-75.7	-128
D_{0443}	0	21.6	118
D_{0445}	$96.48R^{-6}$	0	0
D_{4045}	$-92.16R^{-6}$	0	0

Table 43. Direct multipolar induction, back-induction, and dispersion terms in the collision-induced dipole coefficients $D_{\lambda_A\lambda_B\lambda L}$ for r_B=2.2, at the CASPT2 level, with the d-aug-cc-pVQZ basis set

	$D^{i}_{\lambda_A\lambda_B\lambda L}$	$D^{b}_{\lambda_A\lambda_B\lambda L}R^7$	$D^{d}_{\lambda_A\lambda_B\lambda L}R^7$
D_{0001}	0	-8.86	19.1
D_{2021}	0	-81.2	247
D_{2023}	$4.359R^{-4}$	35.5	162
D_{4043}	0	-12.4	-101
D_{2201}	0	-0.301	0.0472
D_{2211}	0	-1.13	-0.570
D_{2221}	0	-1.99	0.0291
D_{2223}	$0.1498R^{-4}$	1.00	-0.00370
D_{2233}	$-1.588R^{-4}$	15.7	-1.07
D_{2243}	$0.7784R^{-4}$	3.30	-0.185
D_{2245}	$-15.24R^{-6}$	-11.5	0.318
D_{4221}	0	-0.304	-0.0805
D_{4223}	0	-0.0415	-0.0110
D_{4233}	0	0.194	0.0512
D_{4243}	0	-0.421	-0.111
D_{4245}	$6.090R^{-6}$	-0.343	-0.0904
D_{4255}	$17.25R^{-6}$	1.74	0.458
D_{4265}	$15.11R^{-6}$	-5.97	-1.57
D_{2421}	0	0.457	0.0850
D_{2423}	0	0.0623	0.0116
D_{2433}	0	0.291	0.0541
D_{2443}	0	0.632	0.117
D_{2445}	$-6.7105R^{-6}$	0.514	0.0955
D_{2455}	$17.57R^{-6}$	2.60	0.484
D_{2465}	$-19.38R^{-6}$	8.95	1.66
D_{0221}	0	122	-284
D_{0223}	$-6.805R^{-4}$	-55.7	-148
D_{0443}	0	17.5	106
D_{0445}	$96.86R^{-6}$	0	0
D_{4045}	$-96.39R^{-6}$	0	0

Table 44. Direct multipolar induction, back-induction, and dispersion terms in the collision-induced dipole coefficients $D_{\lambda_A\lambda_B\lambda L}$ for r_B=2.28187, at the CASPT2 level, with the d-aug-cc-pVQZ basis set

	$D^{i}_{\lambda_A\lambda_B\lambda L}$	$D^{b}_{\lambda_A\lambda_B\lambda L}R^7$	$D^{d}_{\lambda_A\lambda_B\lambda L}R^7$
D_{0001}	0	0	0
D_{2021}	0	-84.7	248
D_{2023}	$4.534R^{-4}$	37.9	159
D_{4043}	0	-12.9	-101
D_{2201}	0	0	0
D_{2211}	0	-1.00	-0.547
D_{2221}	0	0	0
D_{2223}	0	0	0
D_{2233}	$-1.322R^{-4}$	13.4	-0.981
D_{2243}	0	0	0
D_{2245}	0	0	0
D_{4221}	0	-0.338	-0.0805
D_{4223}	0	-0.0460	-0.0110
D_{4233}	0	0.215	0.0512
D_{4243}	0	-0.467	-0.111
D_{4245}	$7.003R^{-6}$	-0.380	-0.0904
D_{4255}	$17.89R^{-6}$	1.93	0.458
D_{4265}	$21.06R^{-6}$	-6.62	-1.57
D_{2421}	0	0.338	0.0805
D_{2423}	0	0.0460	0.0110
D_{2433}	0	0.215	0.0512
D_{2443}	0	0.467	0.111
D_{2445}	$-7.003R^{-6}$	0.380	0.0904
D_{2455}	$17.89R^{-6}$	1.93	0.458
D_{2465}	$-21.06R^{-6}$	6.62	1.57
D_{0221}	0	84.7	-248
D_{0223}	$-4.534R^{-4}$	-37.9	-159
D_{0443}	0	12.9	101
D_{0445}	$100.3R^{-6}$	0	0
D_{4045}	$-100.3R^{-6}$	0	0

Table 45. Direct multipolar induction, back-induction, and dispersion terms in the collision-induced dipole coefficients $D_{\lambda_A\lambda_B\lambda L}$ for r_B=2.296, at the CASPT2 level, with the d-aug-cc-pVQZ basis set

	$D^{i}_{\lambda_A\lambda_B\lambda L}$	$D^{b}_{\lambda_A\lambda_B\lambda L}R^7$	$D^{d}_{\lambda_A\lambda_B\lambda L}R^7$
D_{0001}	0	1.74	-1.66
D_{2021}	0	-85.4	248
D_{2023}	$4.565R^{-4}$	38.3	159
D_{4043}	0	-13.0	-101
D_{2201}	0	0.0584	-0.00610
D_{2211}	0	-0.974	-0.544
D_{2221}	0	0.357	-0.00245
D_{2223}	$-0.0259R^{-4}$	-0.179	-0.000240
D_{2233}	$-1.277R^{-4}$	13.0	-0.972
D_{2243}	$-0.1348R^{-4}$	-0.606	0.0223
D_{2245}	$2.648R^{-6}$	2.08	-0.0342
D_{4221}	0	-0.344	-0.0805
D_{4223}	0	-0.0468	-0.0110
D_{4233}	0	0.219	0.0512
D_{4243}	0	-0.476	-0.111
D_{4245}	$7.166R^{-6}$	-0.387	-0.0904
D_{4255}	$18.01R^{-6}$	1.96	0.458
D_{4265}	$22.10R^{-6}$	-6.74	-1.57
D_{2421}	0	0.315	0.0804
D_{2423}	0	0.0428	0.0109
D_{2433}	0	0.200	0.0511
D_{2443}	0	0.435	0.111
D_{2445}	$-7.072R^{-6}$	0.353	0.0903
D_{2455}	$17.99R^{-6}$	1.79	0.457
D_{2465}	$-21.41R^{-6}$	6.16	1.57
D_{0221}	0	78.0	-243
D_{0223}	$-4.144R^{-4}$	-34.6	-160
D_{0443}	0	12.0	101
D_{0445}	$101.1R^{-6}$	0	-1.66
D_{4045}	$-100.9R^{-6}$	0	248

Table 46. Direct multipolar induction, back-induction, and dispersion terms in the collision-induced dipole coefficients $D_{\lambda_A\lambda_B\lambda L}$ for r_B=2.36, at the CASPT2 level, with the d-aug-cc-pVQZ basis set

	$D^{i}_{\lambda_A\lambda_B\lambda L}$	$D^{b}_{\lambda_A\lambda_B\lambda L}R^7$	$D^{d}_{\lambda_A\lambda_B\lambda L}R^7$
D_{0001}	0	10.4	-5.81
D_{2021}	0	-88.4	248
D_{2023}	$4.710R^{-4}$	40.5	158
D_{4043}	0	-13.4	-101
D_{2201}	0	0.348	-0.0196
D_{2211}	0	-0.840	-0.537
D_{2221}	0	2.02	-0.0283
D_{2223}	$-0.1434R^{-4}$	-1.01	0.0104
D_{2233}	$-1.075R^{-4}$	11.0	-0.915
D_{2243}	$-0.7449R^{-4}$	-3.49	0.0959
D_{2245}	$14.70R^{-6}$	11.9	-0.218
D_{4221}	0	-0.372	-0.0805
D_{4223}	0	-0.0506	-0.0110
D_{4233}	0	0.237	0.0512
D_{4243}	0	-0.514	-0.111
D_{4245}	$7.916R^{-6}$	-0.418	-0.0904
D_{4255}=	$18.60R^{-6}$	2.12	0.458
D_{4265}	$26.87R^{-6}$	-7.28	-1.57
D_{2421}	0	0.196	0.0783
D_{2423}	0	0.0266	0.0107
D_{2433}	0	0.125	0.0498
D_{2443}	0	0.270	0.108
D_{2445}	$-7.445R^{-6}$	0.220	0.0880
D_{2455}	$18.61R^{-6}$	1.11	0.446
D_{2465}	$-23.17R^{-6}$	3.83	1.53
D_{0221}	0	46.4	-227
D_{0223}	$-2.385R^{-4}$	-19.4	-167
D_{0443}	0	7.49	98.6
D_{0445}	$105.8R^{-6}$	0	0
D_{4045}	$-104.1R^{-6}$	0	0

Table 47. Direct multipolar induction, back-induction, and dispersion terms in the collision-induced dipole coefficients $D_{\lambda_A\lambda_B\lambda L}$ for r_B=2.457, at the CASPT2 level, with the d-aug-cc-pVQZ basis set

	$D^{i}_{\lambda_A\lambda_B\lambda L}$	$D^{b}_{\lambda_A\lambda_B\lambda L}R^7$	$D^{d}_{\lambda_A\lambda_B\lambda L}R^7$
D_{0001}	0	26.1	13.3
D_{2021}	0	-93.1	247
D_{2023}	$4.936R^{-4}$	44.0	161
D_{4043}	0	-14.1	-101
D_{2201}	0	0.863	-0.0719
D_{2211}	0	-0.583	-0.511
D_{2221}	0	4.68	-0.0281
D_{2223}	$-0.3203R^{-4}$	-2.32	-0.00318
D_{2233}	$-0.7790R^{-4}$	7.87	-0.874
D_{2243}	$-1.664R^{-4}$	-8.26	0.262
D_{2245}	$32.96R^{-6}$	27.7	-0.399
D_{4221}	0	-0.416	-0.0805
D_{4223}	0	-0.0566	-0.0110
D_{4233}	0	0.265	0.0512
D_{4243}	0	-0.575	-0.111
D_{4245}	$9.091R^{-6}$	-0.467	-0.0904
D_{4255}	$19.60R^{-6}$	2.37	0.458
D_{4265}	$34.19R^{-6}$	-8.14	-1.57
D_{2421}	0	-0.0216	0.0791
D_{2423}	0	-0.00293	0.0108
D_{2433}	0	-0.0137	0.0504
D_{2443}		-0.0298	0.109
D_{2445}	$-8.195R^{-6}$	-0.0242	0.0889
D_{2455}	$19.96R^{-6}$	-0.123	0.450
D_{2465}	$-26.48R^{-6}$	-0.422	1.55
D_{0221}	0	-5.84	-197
D_{0223}	$0.2349R^{-4}$	5.26	-174
D_{0443}	0	-0.824	100
D_{0445}	$115.5R^{-6}$	0	0
D_{4045}	$-109.1R^{-6}$	0	0

Table 48. Direct multipolar induction, back-induction, and dispersion terms in the collision-induced dipole coefficients $D_{\lambda_A\lambda_B\lambda L}$ for r_B=2.646, at the CASPT2 level, with the d-aug-cc-pVQZ basis set

	$D^{i}_{\lambda_A\lambda_B\lambda L}$	$D^{b}_{\lambda_A\lambda_B\lambda L}R^7$	$D^{d}_{\lambda_A\lambda_B\lambda L}R^7$
D_{0001}	0	64.8	57.3
D_{2021}	0	-103	245
D_{2023}	$5.377R^{-4}$	51.8	169
D_{4043}	0	-15.3	-101
D_{2201}	0	2.11	-0.0959
D_{2211}	0	0.0901	-0.499
D_{2221}	0	10.2	-0.0377
D_{2223}	$-0.6535R^{-4}$	-5.01	-0.00414
D_{2233}	$-0.2474R^{-4}$	1.18	-0.838
D_{2243}	$-3.395R^{-4}$	-18.8	0.350
D_{2245}	$68.08R^{-6}$	61.2	-0.533
D_{4221}	0	-0.506	-0.0805
D_{4223}	0	-0.0688	-0.0110
D_{4233}	0	0.322	0.0512
D_{4243}	0	-0.699	-0.111
D_{4245}	$11.44R^{-6}$	-0.568	-0.0904
D_{4255}	$21.83R^{-6}$	2.88	0.458
D_{4265}	$48.38R^{-6}$	-9.89	-1.57
D_{2421}	0	-0.566	0.0886
D_{2423}	0	-0.077	0.0121
D_{2433}	0	-0.361	0.0564
D_{2443}	0	-0.783	0.122
D_{2445}	$-10.22R^{-6}$	-0.636	0.0996
D_{2455}	$23.92R^{-6}$	-3.22	0.504
D_{2465}	$-34.85R^{-6}$	-11.1	1.73
D_{0221}	0	-120	-180
D_{0223}	$5.081R^{-4}$	58.0	-178
D_{0443}	0	-21.7	113
D_{0445}	$142.2R^{-6}$	0	0
D_{4045}	$-118.9R^{-6}$	0	0

Table 49. Direct multipolar induction, back-induction, and dispersion terms in the collision-induced dipole coefficients $D_{\lambda_A\lambda_B\lambda L}$ for r_B=2.929, at the CASPT2 level, with the d-aug-cc-pVQZ basis set

	$D^{i}_{\lambda_A\lambda_B\lambda L}$	$D^{b}_{\lambda_A\lambda_B\lambda L}R^7$	$D^{d}_{\lambda_A\lambda_B\lambda L}R^7$
D_{0001}	0	134	124
D_{2021}	0	-116	241
D_{2023}	$5.959R^{-4}$	64.0	180
D_{4043}	0	-17.0	-101
D_{2201}	0	4.29	-0.103
D_{2211}	0	1.38	-0.495
D_{2221}	0	18.4	-0.0631
D_{2223}	$-1.083R^{-4}$	-8.90	0.00775
D_{2233}	$0.4367R^{-4}$	-9.46	-0.787
D_{2243}	$-5.629R^{-4}$	-35.3	0.403
D_{2245}	$117.5R^{-6}$	112	-0.693
D_{4221}	0	-0.621	-0.0805
D_{4223}	0	-0.0846	-0.0110
D_{4233}	0	0.396	0.0512
D_{4243}	0	-0.859	-0.111
D_{4245}	$14.48R^{-6}$	-0.698	-0.0904
D_{4255}	$24.73R^{-6}$	3.54	0.458
D_{4265}	$66.72R^{-6}$	-12.2	-1.57
D_{2421}	0	-1.55	0.129
D_{2423}	0	-0.211	0.0176
D_{2433}	0	-0.988	0.0822
D_{2443}	0	-2.15	0.179
D_{2445}	$-14.40R^{-6}$	-1.74	0.145
D_{2455}	$32.29R^{-6}$	-8.84	0.736
D_{2465}	$-51.81R^{-6}$	-30.4	2.53
D_{0221}	0	-303	-167
D_{0223}	$11.33R^{-4}$	134	-184
D_{0443}	0	-59.4	168
D_{0445}	$197.7R^{-6}$	0	0
D_{4045}	$-131.8R^{-6}$	0	0

Table 50. Direct multipolar induction, back-induction, and dispersion terms in the collision-induced dipole coefficients $D_{\lambda_A\lambda_B\lambda L}$ for r_B=3.123, at the CASPT2 level, with the d-aug-cc-pVQZ basis set

	$D^{i}_{\lambda_A\lambda_B\lambda L}$	$D^{b}_{\lambda_A\lambda_B\lambda L}R^7$	$D^{d}_{\lambda_A\lambda_B\lambda L}R^7$
D_{0001}	0	188	168
D_{2021}	0	-123	239
D_{2023}	$6.249R^{-4}$	72.2	187
D_{4043}	0	-17.8	-101
D_{2201}	0	5.92	-0.114
D_{2211}	0	2.48	-0.490
D_{2221}	0	24.4	-0.0925
D_{2223}	$-1.370R^{-4}$	-11.8	0.0210
D_{2233}	$1.028R^{-4}$	-19.0	-0.725
D_{2243}	$-7.120R^{-4}$	-47.6	0.473
D_{2245}	$161.6R^{-6}$	149	-0.886
D_{4221}	0	-0.665	-0.0805
D_{4223}	0	-0.0904	-0.0110
D_{4233}	0	0.423	0.0512
D_{4243}	0	-0.918	-0.111
D_{4245}	$15.80R^{-6}$	-0.747	-0.0904
D_{4255}	$24.85R^{-6}$	3.78	0.458
D_{4265}	$76.82R^{-6}$	-13.0	-1.57
D_{2421}	0	-2.34	0.203
D_{2423}	0	-0.318	0.0276
D_{2433}	0	-1.49	0.129
D_{2443}	0	-3.23	0.280
D_{2445}	$-19.72R^{-6}$	-2.62	0.228
D_{2455}	$42.61R^{-6}$	-13.3	1.15
D_{2465}	$-74.00R^{-6}$	-45.8	3.97
D_{0221}	0	-449	-151
D_{0223}	$15.96R^{-4}$	205	-191
D_{0443}	0	-89.5	275
D_{0445}	$267.7R^{-6}$	0	0
D_{4045}	$-138.2R^{-6}$	0	0

Table 51. Direct multipolar induction, back-induction, and dispersion terms in the collision-induced dipole coefficients $D_{\lambda_A\lambda_B\lambda L}$ for r_B=3.3, at the CASPT2 level, with the d-aug-cc-pVQZ basis set

	$D^{i}_{\lambda_A\lambda_B\lambda L}$	$D^{b}_{\lambda_A\lambda_B\lambda L}R^7$	$D^{d}_{\lambda_A\lambda_B\lambda L}R^7$
D_{0001}	0	196	172
D_{2021}	0	-123	239
D_{2023}	$6.258R^{-4}$	73.1	188
D_{4043}	0	-17.9	-101
D_{2201}	0	6.14	-0.124
D_{2211}	0	2.67	-0.485
D_{2221}	0	25.5	-0.104
D_{2223}	$-1.422R^{-4}$	-12.3	0.0246
D_{2233}	$1.196R^{-4}$	-21.3	-0.697
D_{2243}	$-7.387R^{-4}$	-49.6	0.518
D_{2245}	$173.7R^{-6}$	156	-0.980
D_{4221}	0	-0.656	-0.0805
D_{4223}	0	-0.089	-0.0110
D_{4233}	0	0.418	0.0512
D_{4243}	0	-0.907	-0.111
D_{4245}	$15.70R^{-6}$	-0.737	-0.0904
D_{4255}	$24.02R^{-6}$	3.74	0.458
D_{4265}	$77.62R^{-6}$	-12.8	-1.57
D_{2421}	0	-2.46	0.239
D_{2423}	0	-0.335	0.0325
D_{2433}	0	-1.57	0.152
D_{2443}	0	-3.40	0.330
D_{2445}	$-21.54R^{-6}$	-2.76	0.268
D_{2455}	$46.05R^{-6}$	-14.0	1.36
D_{2465}	$-81.73R^{-6}$	-48.1	4.68
D_{0221}	0	-477	-141
D_{0223}	$17.00R^{-4}$	218	-195
D_{0443}	0	-94.1	332
D_{0445}	$291.5R^{-6}$	0	0
D_{4045}	$-138.4R^{-6}$	0	0

Bohr and Hunt[69] have derived the following expression for the collision-induced dipole for two linear, centrosymmetric molecules in a T-shape configuration with $\hat{R} \parallel \hat{z}$, $\hat{r}_A \parallel \hat{z}$, $\hat{r}_B \parallel \hat{x}$, in terms of the $D_{\lambda_A \lambda_B \lambda L}$ coefficients

$$\mu_z = D_{0001} - \sqrt{2}D_{2021} + \frac{\sqrt{2}}{2}D_{0221} + \sqrt{3}D_{2023} - \frac{\sqrt{3}}{2}D_{0223} - 2D_{4043} - \frac{3}{4}D_{0443} + \sqrt{5}D_{4045} + \frac{3\sqrt{5}}{8}D_{0445} - \frac{5}{2}\sqrt{\frac{2}{7}}D_{2245} + \sqrt{\frac{10}{7}}D_{2243} + \frac{1}{2}\sqrt{\frac{30}{7}}D_{2223} - \sqrt{\frac{5}{7}}D_{2221} - \frac{\sqrt{5}}{2}D_{2201} + \frac{15}{2}\sqrt{\frac{6}{143}}D_{4265} - \frac{45}{8}\sqrt{\frac{6}{143}}D_{2465} + 5\sqrt{\frac{5}{77}}D_{4245} - \frac{15}{4}\sqrt{\frac{5}{77}}D_{2245} - 10\sqrt{\frac{1}{77}}D_{4243} + \frac{15}{2}\sqrt{\frac{1}{77}}D_{2443} - \frac{3}{2}\sqrt{\frac{6}{7}}D_{4223} + \frac{9}{8}\sqrt{\frac{6}{7}}D_{2423} + 3\sqrt{\frac{1}{7}}D_{4221} - \frac{9}{4}\sqrt{\frac{1}{7}}D_{2421} \quad (4.21)$$

We have derived corresponding expressions for two linear, centrosymmetric molecules for the X-shape, linear, and H-shape configurations as well, given by equations (4.22), (4.23), and (4.24), respectively:

$$\mu_z = D_{0001} + \frac{\sqrt{2}}{2}D_{2021} + \frac{\sqrt{2}}{2}D_{0221} - \frac{3}{4}D_{4043} - \frac{3}{4}D_{0443} + \frac{\sqrt{15}}{4}D_{2023} + \frac{\sqrt{15}}{4}D_{0223} + \frac{5}{8}\sqrt{\frac{2}{7}}D_{2245} + \frac{3\sqrt{5}}{8}D_{4045} + \frac{3\sqrt{5}}{8}D_{0445} - \frac{5}{2}\sqrt{\frac{1}{70}}D_{2243} - 5\sqrt{\frac{6}{35}}D_{2223} + \frac{10}{\sqrt{35}}D_{2221} - \frac{\sqrt{5}}{2}D_{2201} + \frac{15}{16}\sqrt{\frac{6}{143}}D_{4265} + \frac{15}{16}\sqrt{\frac{6}{143}}D_{2465} + \frac{15}{2}\sqrt{\frac{5}{77}}D_{4245} + \frac{15}{2}\sqrt{\frac{5}{77}}D_{2445} - \frac{15}{\sqrt{77}}D_{4243} - \frac{15}{\sqrt{77}}D_{2443} + \frac{3}{8}\sqrt{\frac{6}{7}}D_{4223} + \frac{3}{8}\sqrt{\frac{6}{7}}D_{2423} - \frac{3}{4\sqrt{7}}D_{4221} - \frac{3}{4\sqrt{7}}D_{2421} \quad (4.22)$$

$$\mu_z = D_{0001} - \sqrt{2}D_{2021} - \sqrt{2}D_{0221} - 2D_{4043} - 2D_{0443} + \sqrt{3}D_{2023} + \sqrt{3}D_{0223} + 5\sqrt{\frac{2}{7}}D_{2245} + \sqrt{5}D_{4045} + \sqrt{5}D_{0445} - 2\sqrt{\frac{10}{7}}D_{2243} - \sqrt{\frac{30}{7}}D_{2223} + 2\sqrt{\frac{5}{7}}D_{2221} + \sqrt{5}D_{2201} - \frac{15}{11}\sqrt{\frac{42}{13}}D_{4265} - \frac{15}{11}\sqrt{\frac{42}{13}}D_{2465} - \frac{10\sqrt{5}}{11}D_{4245} - \frac{10\sqrt{5}}{11}D_{2445} + \frac{20}{\sqrt{77}}D_{4243} + \frac{20}{\sqrt{77}}D_{2443} + 3\sqrt{\frac{6}{7}}D_{4223} + 3\sqrt{\frac{6}{7}}D_{2423} - \frac{6}{\sqrt{7}}D_{4221} - \frac{6}{\sqrt{7}}D_{2421} \quad (4.23)$$

$$\mu_z = D_{0001} + \frac{\sqrt{2}}{2}D_{2021} + \frac{\sqrt{2}}{2}D_{0221} - \frac{3}{4}D_{4043} - \frac{3}{4}D_{0443} + \frac{\sqrt{15}}{4}D_{2023} + \frac{\sqrt{15}}{4}D_{0223} - \frac{5}{16}\sqrt{\frac{1}{3}}D_{2245} + \frac{3\sqrt{5}}{8}D_{4045} + \frac{3\sqrt{5}}{8}D_{0445} - \frac{15}{2\sqrt{70}}D_{2243} + \frac{5}{2}\sqrt{\frac{6}{35}}D_{2223} - \frac{25}{2\sqrt{35}}D_{2221} + \frac{35}{4\sqrt{5}}D_{2201} + \frac{75}{16}\sqrt{\frac{6}{143}}D_{4265} + \frac{75}{16}\sqrt{\frac{6}{143}}D_{2465} - \frac{15}{4}\sqrt{\frac{5}{77}}D_{4245} - \frac{15}{4}\sqrt{\frac{5}{77}}D_{2445} + \frac{15}{4\sqrt{77}}D_{4243} + \frac{15}{4\sqrt{77}}D_{2443} - \frac{9}{\sqrt{42}}D_{4223} - \frac{9}{\sqrt{42}}D_{2423} + \frac{3}{\sqrt{7}}D_{4221} + \frac{3}{\sqrt{7}}D_{2421} \quad (4.24)$$

Using these equations for the different geometries, we can calculate the contributions to the dipole due to quadrupolar induction, hexadecapolar induction, induction via the E-tensor mechanism, back-induction, and dispersion. For example, from equation (4.22), the quadrupolar induction contribution to the dipole moment through order R^{-4} for O_2-O_2 in the X-shape geometry depends on the coefficients D_{2023} and D_{0223} and is given by the following:

$$\mu_z(quadrupolar\ induction) = \frac{\sqrt{15}}{4}D^i_{2023} + \frac{\sqrt{15}}{4}D^i_{0223} \quad (4.25)$$

The hexadecapolar induction contribution for the same geometry is calculated the following way:

$$\mu_z(hexadecapolar\ induction) = \frac{3\sqrt{5}}{8}D^i_{4045} + \frac{3\sqrt{5}}{8}D^i_{0445} + \frac{15}{16}\sqrt{\frac{6}{143}}D_{4265} + \frac{15}{16}\sqrt{\frac{6}{143}}D_{2465} + \frac{15}{2}\sqrt{\frac{5}{77}}D_{4245} + \frac{15}{2}\sqrt{\frac{5}{77}}D_{2445} \quad (4.26)$$

In this equation, D_{4245} is given by:

$$D_{4245} = \frac{2}{3}\sqrt{\frac{7}{55}}(\alpha^B_{||} - \alpha^B_{-|-})\Phi^{\mathrm{A}} \quad (4.27)$$

where $\alpha^B_{||}$ and $\alpha^B_{-|-}$ are the parallel and perpendicular components of the polarizability for molecule B (O_2 with non-equilibrium bond distance) and Φ^{A} is the hexadecapolar moment for molecule A (O_2 with equilibrium bond distance), and D_{4265} is given by:

$$D_{4265} = \sqrt{\frac{26}{33}}(\alpha^B_{||} - \alpha^B_{-|-})\Phi^{\mathrm{A}} \quad (4.28)$$

To find the induction contribution to the dipole moment from the E-tensor mechanism for O_2-O_2 in the X-shape geometry, equation (22) is used to find:

$$\mu_z(E-tensor\ induction) = \frac{15}{2}\sqrt{\frac{5}{77}}D^E_{4245} + \frac{15}{2}\sqrt{\frac{5}{77}}D^E_{2445} + \frac{15}{16}\sqrt{\frac{6}{143}}D^E_{4265} + \frac{15}{16}\sqrt{\frac{6}{143}}D^E_{2465} + \frac{5}{8}\sqrt{\frac{2}{7}}D^E_{2245} \quad (4.29)$$

where D^E_{4245} is given by

$$D^E_{4245} = -2\sqrt{\frac{1}{385}}(E^A_{Z,ZZZ} + 2E^A_{X,XXX})\Theta^{\mathrm{B}} \quad (4.30)$$

and $E^A_{Z,ZZZ}$ and $E^A_{X,XXX}$ are dipole-octupole polarizabilities for molecule A (O_2 with an equilibrium bond distance), and Θ^{B} is the quadrupole moment for molecule B (O_2 with an equilibrium or non- equilibrium bond distance).

The coefficient $D^E_{4265}$is given by the following:

$$D^E_{4265} = -2\sqrt{\frac{26}{33}}(E^A_{Z,ZZZ} + 2E^A_{X,XXX})\Theta^{\mathrm{B}} \quad (4.31)$$

and the coefficient D^E_{2245} is found using:

$$D^E_{2245} = \sqrt{\frac{2}{7}}\left(3E^A_{Z,ZZZ} - 8E^A_{X,XXX}\right)\Theta^{\mathrm{B}} - \sqrt{\frac{2}{7}}(3E^B_{Z,ZZZ} - 8E^B_{X,XXX})\Theta^{\mathrm{A}} \quad (4.32)$$

The back-induction contribution to the dipole moment using equation (22) for O_2-O_2 in the X-shape geometry is found by:

$$\mu_z = D^b_{0001} + \frac{\sqrt{2}}{2}D^b_{2021} + \frac{\sqrt{2}}{2}D^b_{0221} + \frac{\sqrt{15}}{4}D^b_{2023} + \frac{\sqrt{15}}{4}D^b_{0223} - \frac{3}{4}D^b_{4043} - \frac{3}{4}D^b_{0443} + \frac{5}{8}\sqrt{\frac{2}{7}}D^b_{2245} - \frac{5}{2}\sqrt{\frac{1}{70}}D^b_{2243} - 5\sqrt{\frac{6}{35}}D^b_{2223} + \frac{10}{\sqrt{35}}D^b_{2221} - \frac{\sqrt{5}}{2}D^b_{2201} + \frac{15}{16}\sqrt{\frac{6}{143}}D^b_{4265} + \frac{15}{16}\sqrt{\frac{6}{143}}D^b_{2465} + \frac{15}{2}\sqrt{\frac{5}{77}}D^b_{4245} + \frac{15}{2}\sqrt{\frac{5}{77}}D^b_{2445} - \frac{15}{\sqrt{77}}D^b_{4243} - \frac{15}{\sqrt{77}}D^b_{2443} + \frac{3}{8}\sqrt{\frac{6}{7}}D^b_{4223} + \frac{3}{8}\sqrt{\frac{6}{7}}D^b_{2423} - \frac{3}{4\sqrt{7}}D^b_{4221} - \frac{3}{4\sqrt{7}}D^b_{2421} \quad (4.33)$$

The dispersion contribution is calculated using the above equation and replacing the back-induction coefficients by dispersion coefficients.

From equation (4.23), the quadrupolar induction contribution through order R^{-4} to the dipole moment for O_2-O_2 in the linear geometry is given by:

$$\mu_z(quadrupolar\ induction) = \sqrt{3}D^i_{2023} + \sqrt{3}D^i_{0223} \tag{4.34}$$

and the hexadecapolar induction contribution is calculated using:

$$\mu_z(hexadecapolar\ induction) = \sqrt{5}D^i_{4045} + \sqrt{5}D^i_{0445} - \frac{15}{11}\sqrt{\frac{42}{13}}D^h_{4265} - \frac{15}{11}\sqrt{\frac{42}{13}}D^h_{2465} - \frac{10\sqrt{5}}{11}D^h_{4245} - \frac{10\sqrt{5}}{11}D^h_{2445} \tag{4.35}$$

Induction via the E-tensor is calculated using:

$$\mu_z(E - tensor\ Induction) = 5\sqrt{\frac{2}{7}}D_{2245} - \frac{15}{11}\sqrt{\frac{42}{13}}D^E_{4265} - \frac{15}{11}\sqrt{\frac{42}{13}}D^E_{2465} - 10\sqrt{\frac{5}{11}}D^E_{4245} - 10\sqrt{\frac{5}{11}}D^E_{2445} \tag{4.36}$$

Also from equation (4.23), the back-induction contribution to the dipole moment for the linear geometry is:

$$\mu_z(back - induction) = D^b_{0001} - \sqrt{2}D^b_{2021} - \sqrt{2}D^b_{0221} + \sqrt{3}D^b_{2023} + \sqrt{3}D^b_{0223} - 2D^b_{4043} - 2D^b_{0443} + 5\sqrt{\frac{2}{7}}D^b_{2245} - 2\sqrt{\frac{10}{7}}D^b_{2243} - \sqrt{\frac{30}{7}}D^b_{2223} + 2\sqrt{\frac{5}{7}}D^b_{2221} + \sqrt{5}D^b_{2201} - \frac{15}{11}\sqrt{\frac{42}{13}}D^b_{4265} - \frac{15}{11}\sqrt{\frac{42}{13}}D^b_{2465} - 10\frac{\sqrt{5}}{11}D^b_{4245} - 10\frac{\sqrt{5}}{11}D^b_{2445} + \frac{20}{\sqrt{77}}D^b_{4243} + \frac{20}{\sqrt{77}}D^b_{2443} + 3\sqrt{\frac{6}{7}}D^b_{4223} + 3\sqrt{\frac{6}{7}}D^b_{2423} - \frac{6}{\sqrt{7}}D^b_{4221} - \frac{6}{\sqrt{7}}D^b_{2421} \tag{4.37}$$

Again, the dispersion contribution for the linear geometry is found by using equation (4.23) and substituting the dispersion coefficients for the back-induction coefficients.

From equation (4.24), the quadrupolar induction contribution through order R^{-4} to the dipole moment for O_2-O_2 in the H-shape geometry is

$$\mu_z(quadrupolar\ induction) = \frac{\sqrt{15}}{4} D^i_{2023} + \frac{\sqrt{15}}{4} D^i_{0223} \quad (4.38)$$

and the hexadecapolar induction contribution is given by

$$\mu_z(hexadecapolar\ induction) = \frac{3\sqrt{5}}{8} D^i_{4045} + \frac{3\sqrt{5}}{8} D^i_{0445} + \frac{75}{16}\sqrt{\frac{6}{143}} D^h_{4265} + \frac{75}{16}\sqrt{\frac{6}{143}} D^h_{2465} - \frac{15}{4}\sqrt{\frac{5}{77}} D^h_{4245} - \frac{15}{4}\sqrt{\frac{5}{77}} D^h_{2445} \quad (4.39)$$

The contribution to the dipole from induction via the E-tensor for O_2-O_2 in the H-shape geometry can be obtained using:

$$\mu_z(E - tensor\ Induction) = -\frac{15}{6}\sqrt{\frac{1}{3}} D^E_{2245} + \frac{75}{16}\sqrt{\frac{6}{143}} D^E_{4265} + \frac{75}{16}\sqrt{\frac{6}{143}} D^E_{2465} - \frac{15}{4}\sqrt{\frac{5}{77}} D^E_{4245} - \frac{15}{4}\sqrt{\frac{5}{77}} D^E_{2445} \quad (4.40)$$

From equation (4.21), the quadrupolar induction contribution through order R^{-4} to the dipole moment for O_2-O_2 in the T-shape geometry is

$$\mu_z(quadrupolar\ induction) = \sqrt{3} D^i_{2023} - \frac{\sqrt{3}}{2} D^i_{0223} \quad (4.41)$$

The hexadecapolar induction contribution can be found using:

$$\mu_z(hexadecapolar\ induction) = \sqrt{5} D^i_{4045} + \frac{3\sqrt{5}}{8} D^i_{0445} + \frac{15}{2}\sqrt{\frac{6}{143}} D^h_{4265} - \frac{45}{8}\sqrt{\frac{6}{143}} D^h_{2465} + 5\sqrt{\frac{5}{77}} D^h_{4245} - \frac{15}{4}\sqrt{\frac{5}{77}} D^h_{2445} \quad (4.42)$$

The contribution to the dipole moment via E-tensor induction for O_2-O_2 in the T-shape geometry is given by:

$$\mu_z(E - tensor\ induction) = -\frac{5}{2}\sqrt{\frac{2}{7}} D^E_{2245} + \frac{15}{2}\sqrt{\frac{6}{143}} D^E_{4265} - \frac{45}{8}\sqrt{\frac{6}{143}} D^E_{2465} + 5\sqrt{\frac{5}{77}} D^E_{4245} - \frac{15}{4}\sqrt{\frac{5}{77}} D^E_{4245} \quad (4.43)$$

Using equation (4.21), the back-induction contribution to the dipole moment for O_2-O_2 in the T-shape geometry is found using:

$$\mu_z = D^b_{0001} - \sqrt{2}D^b_{2021} + \frac{\sqrt{2}}{2}D^b_{0221} + \sqrt{3}D^b_{2023} - \frac{\sqrt{3}}{2}D^b_{0223} - 2D^b_{4043} - \frac{3}{4}D^b_{0443} - \frac{5}{2}\sqrt{\frac{2}{77}}D^b_{2245} + \sqrt{\frac{10}{7}}D^b_{2243} + \frac{1}{2}\sqrt{\frac{30}{7}}D^b_{2223} - \sqrt{\frac{5}{7}}D^b_{2221} - \frac{\sqrt{5}}{2}D^b_{2201} + \frac{15}{2}\sqrt{\frac{6}{143}}D^b_{4265} - \frac{45}{8}\sqrt{\frac{6}{143}}D^b_{2465} + 5\sqrt{\frac{5}{77}}D^b_{4245} - \frac{15}{4}\sqrt{\frac{5}{77}}D^b_{2445} - 10\sqrt{\frac{1}{77}}D^b_{4243} + \frac{15}{2}\sqrt{\frac{1}{77}}D^b_{2443} - \frac{3}{2}\sqrt{\frac{6}{7}}D^b_{4223} + \frac{9}{8}\sqrt{\frac{6}{7}}D^b_{2423} + 3\sqrt{\frac{1}{7}}D^b_{4221} - \frac{9}{4}\sqrt{\frac{1}{7}}D^b_{2421} \quad (4.44)$$

Again, we can find the dispersion contribution to the dipole moment by replacing the back-induction coefficients in (4.44) by dispersion coefficients.

4.2 Contributions to the Collision-Induced Dipole Moment from Hexadecapolar Induction, Quadrupolar Induction, E-tensor Induction, Back Induction and Dispersion for Four Main Geometries

The direct quadrupolar induction through order R^{-4}, direct hexadecapolar induction, E-tensor induction, back-induction and dispersion terms calculated using the above formulas are given in Tables (52)-(63). The terms have been calculated for oxygen molecule A at the equilibrium bond distance, interacting with a second oxygen molecule B with a bond distance between 2-3.3 bohr.

Table 52. Contributions to the long-range dipole moment, for four main O_2-O_2 orientations, with $r_A=r_{eq}$ and r_B =2 bohr

r_B =2 CASPT2	Quadrupolar induction	Hexadecapolar induction	E-tensor induction	Back induction	Dispersion
X-shape	-8.075 R^{-4}	4.283 R^{-6}	-19.436 R^{-6}	-37.066 R^{-7}	132.116 R^{-7}
Linear	-14.446 R^{-4}	53.037 R^{-6}	-117.393 R^{-6}	-491.793 R^{-7}	644.298 R^{-7}
H-shape	-8.075 R^{-4}	4.283 R^{-6}	67.081 R^{-6}	12.104 R^{-7}	132.958 R^{-7}
T-shape	17.641 R^{-4}	-50.600 R^{-6}	28.175 R^{-6}	373.737 R^{-7}	65.686 R^{-7}

From Table (52), we see that the quadrupolar induction contributes a negative term to the dipole moment for all O_2-O_2 configurations except T-shape when oxygen A is at an equilibrium bond length, and oxygen B has a bond distance of 2 bohr (shorter than equilibrium). The T-shaped configuration quadrupolar induction term is largest in magnitude, followed by the linear quadrupolar induction term, and the X-shape and H-shape terms are identical. The hexadecapolar induction term is positive for all orientations except the T-shape. The linear orientation hexadecapolar induction term is largest in magnitude, followed by the T-shape orientation term, and as with the quadrupolar induction, the hexadecapolar induction is the same for the X-shape and H-shape, and is an order of magnitude smaller than the T-shape and linear terms.

The next term in Table (52) comes from the E-tensor induction. This term is negative for the X-shape and linear orientations, and positive for the H-shape and T-shape orientations. The term for the linear orientation is largest in magnitude, followed by the H-shape term, then the T-shape term, and the X-shape orientation term is the smallest term from induction via the E-tensor.

Also from Table (52), we see that the dipole for the X-shape and linear orientations contains a negative contribution from back-induction as well, and the term is positive for the H-shape and T-shape orientations. The linear orientation receives the largest contribution from back-induction, and the T-shape contribution is the second largest, and is of the same magnitude if not sign. The H-shape and X-shape terms are an order of magnitude smaller.

The last contribution in Table (52) arises from dispersion. This term is positive for all four orientations, and by far largest for the linear orientation. The X-shape and T-shape terms are less than 1% different, but not identical. The smallest contribution from dispersion occurs for the T-

shape orientation, and this term is an order of magnitude smaller than that for the linear orientation.

Table 53. Contributions to the long-range dipole moment, for four main O_2-O_2 orientations, with $r_A=r_{eq}$ and r_B =2.1 bohr

r_B =2.1 CASPT2	Quadrupolar induction	Hexadecapolar induction	E-tensor Induction	Back Induction	Dispersion
X-shape	-5.244 R^{-4}	0.301 R^{-6}	-12.786 R^{-6}	-26.632 R^{-7}	42.035 R^{-7}
Linear	-9.380 R^{-4}	23.777 R^{-6}	-75.953 R^{-6}	-338.136 R^{-7}	284.389 R^{-7}
H-shape	-5.244 R^{-4}	0.301 R^{-6}	43.564 R^{-6}	6.448 R^{-7}	42.475 R^{-7}
T-shape	15.519 R^{-4}	-59.357 R^{-6}	12.680 R^{-6}	338.679 R^{-7}	11.526 R^{-7}

Table (53) shows the five long-range contributions to the collision-induced dipole moment, for an O_2-O_2 supermolecular complex with oxygen molecule A at an equilibrium bond distance, and oxygen molecule B at a bond distance of 2.1 bohr. The terms possess the same signs as discussed for the terms in Table (52). The trends for the quadrupolar induction remain the same amongst the four orientations, but have all reduced slightly in magnitude. The hexadecapolar term is now largest in magnitude for the T-shape orientation, as the term for that orientation has grown in magnitude, while the term for the linear orientation has decreased in magnitude significantly.

The trends seen in Table (52) for the E-tensor contribution continue here. For the back-induction contribute however, the value of the contribution to the dipole in the linear and T-shape orientations are nearly identical, although opposite in sign. The contribution to the dipole via back-induction for the X-shape orientation is an order of magnitude smaller than for the linear and T-shape orientations, and the contribution to the dipole for the H-shape orientation is the smallest, being an order of magnitude smaller than the X-shape orientations term. Finally, the dispersion term is still the largest for the linear orientation.

Table 54. Contributions to the long-range dipole moment, for four main O_2-O_2 orientations, with $r_A=r_{eq}$ and r_B =2.2 bohr

r_B =2.2 CASPT2	Quadrupolar induction	Hexadecapolar induction	E-tensor induction	Back induction	Dispersion
X-shape	-2.36802 R^{-4}	-0.86383 R^{-6}	-5.84119 R^{-6}	-13.3986 R^{-7}	2.94658 R^{-7}
Linear	-4.23605 R^{-4}	6.388039 R^{-6}	-34.3306 R^{-6}	-162.975 R^{-7}	88.58555 R^{-7}
H-shape	-2.36802 R^{-4}	-0.86383 R^{-6}	19.73887 R^{-6}	2.158335 R^{-7}	3.080553 R^{-7}
T-shape	13.44424 R^{-4}	-63.4552 R^{-6}	-3.94721 R^{-6}	304.2219 R^{-7}	-4.24005 R^{-7}

Table (54) shows the contributions to the dipole for the four main O_2-O_2 configurations studied when oxygen A is at an equilibrium bond length, and oxygen B has a bond distance of 2.2 bohr. The sign and relative contributions for the quadrupolar induction remain the same as in Tables (52) and (53). However, at this distance, the hexadecapolar contributions to the collision-induced dipole for the X-shape and H-shape have become negative. The hexadecapolar contribution is still largest for the T-shape orientation.

For oxygen molecule B at 2.2 bohr, the induction via the E-tensor now contributes a negative term for the T-shape orientation. The linear orientation still possesses the largest term for E-tensor induction. At this point, the term for back induction possessed by the T-shape orientation has overcome that of the linear orientation, but dispersion still contributes the most to the linear orientation out of the four orientations.

Table 55. Contributions to the long-range dipole moment, for four main O_2-O_2 orientations, with $r_A=r_{eq}$ and r_B =r_{eq}

r_B =2.28187 CASPT2	Quadrupolar induction	Hexadecapolar induction	E-tensor induction	Back induction	Dispersion
X-shape	0	0	0	0	0
Linear	0	0	0	0	0
H-shape	0	0	0	0	0
T-shape	11.781 R^{-4}	-63.771 R^{-6}	-18.199 R^{-6}	275.929 R^{-7}	10.433 R^{-7}

Table (55) is a good check for the accuracy of our dipole equations; all terms for the contribution to the dipole for the X-shape, linear, and H-shape orientations are zero. This is because these three orientations are centrosymmetric, and thus have no dipole moment when both oxygen molecules are at equilibrium. Only the T-shape orientation contains non-zero contributions. Note that the dispersion term for the T-shape orientation has switched signs here, becoming positive.

Table 56. Contributions to the long-range dipole moment, for four main O_2-O_2 orientations, with $r_A=r_{eq}$ and r_B =2.296 bohr

r_B =2.296 CASPT2	Quadrupolar induction	Hexadecapolar induction	E-tensor induction	Back induction	Dispersion
X-shape	0.4078 R^{-4}	0.316389 R^{-6}	1.017649 R^{-6}	2.56186 R^{-7}	0.018696 R^{-7}
Linear	0.729495 R^{-4}	-0.40313 R^{-6}	5.944907 R^{-6}	30.01532 R^{-7}	-10.4399 R^{-7}
H-shape	0.4078 R^{-4}	0.316389 R^{-6}	-3.42286 R^{-6}	-0.2384 R^{-7}	-0.00116 R^{-7}
T-shape	11.49593 R^{-4}	-63.5292 R^{-6}	-20.7022 R^{-6}	271.0092 R^{-7}	12.42856 R^{-7}

Table (56) contains the terms for contributions to the dipole when oxygen B has a bond distance of 2.296 bohr, slightly longer than equilibrium. All contributions from the quadrupolar induction are now positive. The T-shape orientation continues to possess the largest quadrupolar induction term.

Concerning the hexadecapolar induction, the term for the linear orientation has now for the first time become negative, while the term for the H-shape and X-shape orientations have reverted back to positive values. The T-shape orientation continues to possess the largest contribution from hexadecapolar induction of the four geometries.

The terms arising via the E-tensor mechanism have switched sign for the X-shape and Linear orientations. These terms are now positive. The E-tensor contribution term for the H-shape orientation has switched sign as well, now becoming negative. The E-tensor contribution is now largest for the T-shape orientation, as the linear orientation term has decreased in magnitude.

The terms for the back induction have switched sign as well; the terms are now positive for the X-shape and linear orientations, and negative for the H-shape orientation. The T-shape contribution from back-induction remains positive and is still the largest of the four.

Concerning the dispersion contribution when oxygen molecule B is at 2.296 bohr, the contribution to the linear orientation has now become negative, as has the H-shape term. The T-shape term has now become larger in magnitude than the linear term.

Table 57. Contributions to the long-range dipole moment, for four main O_2-O_2 orientations, with $r_A=r_{eq}$ and r_B =2.36 bohr

r_B =2.36 CASPT2	Quadrupolar induction	Hexadecapolar induction	E-tensor Induction	Back Induction	Dispersion
X-shape	2.25119 R^{-4}	2.247441 R^{-6}	5.655948 R^{-6}	15.10757 R^{-7}	2.263756 R^{-7}
Linear	4.027051 R^{-4}	0.018957 R^{-6}	32.92205 R^{-6}	172.979 R^{-7}	-47.2249 R^{-7}
H-shape	2.25119 R^{-4}	2.247441 R^{-6}	-18.9711 R^{-6}	-0.78169 R^{-7}	2.324716 R^{-7}
T-shape	10.22455 R^{-4}	-61.6178 R^{-6}	-32.1975 R^{-6}	248.9452 R^{-7}	26.43155 R^{-7}

Table (57) shows the contributions to the dipole for the four main O_2-O_2 orientations when oxygen molecule B has a bond distance of 2.36 bohr. The signs and trends for the quadrupolar induction are the same as for the data in Table (56). For the hexadecapolar induction, the term for the contribution to the linear orientation dipole has reverted to a positive value, having been negative only when oxygen molecule B had a bond length of 2.296 bohr. It will remain positive for the over the range of the rest of the bond lengths considered. The hexadecapolar contribution to the T-shape orientation remains larger than the contribution for the other three orientations.

The largest contribution to the dipole via the E-tensor is now the term for the linear orientation, although it is only about 2% larger in magnitude than the T-shape term (but opposite in sign).

The signs and trends for the back-induction term in Table (56) remain the same as in Table (55), with the largest term contributing to the T-shape orientation. The largest term from dispersion now contributes to the linear orientation, over-taking the T-shape orientation term. The dispersion contribution term for the H-shape orientation has once again become positive, and will remain so for the rest of the bond distances for oxygen molecule B examined.

Table 58. Contributions to the long-range dipole moment, for four main O_2-O_2 orientations, with $r_A=r_{eq}$ and r_B =2.457 bohr

r_B =2.457 CASPT2	Quadrupolar induction	Hexadecapolar induction	E-tensor induction	Back induction	Dispersion
X-shape	5.007147 R^{-4}	6.83522 R^{-6}	12.6871 R^{-6}	37.05524 R^{-7}	36.92338 R^{-7}
Linear	8.957057 R^{-4}	7.740126 R^{-6}	73.80978 R^{-6}	410.9558 R^{-7}	-78.1674 R^{-7}
H-shape	5.007147 R^{-4}	6.83522 R^{-6}	-42.5375 R^{-6}	0.108028 R^{-7}	36.68581 R^{-7}
T-shape	8.346778 R^{-4}	-55.7851 R^{-6}	-49.8056 R^{-6}	215.3483 R^{-7}	78.0336 R^{-7}

In Table (58), we can see that the quadrupolar induction term is close in value for the linear and T-shape orientations, with oxygen molecule B at a bond distance of r=2.457 bohr. However, the T-shape term is still about 7% larger.

The largest hexadecapolar induction contribution is still the term for the T-shape orientation. The linear E-tensor contribution term has now over-taken that of the T-shape orientation in magnitude.

Concerning the back-induction contribution, the H-shape term has now once again become positive, and will remain so for all longer bond distances of oxygen molecule B considered. As with the E-tensor induction contribution, the linear back-induction contribution has now becoming larger for the linear orientation than for the T-shape orientation. As for the dispersion contribution, the largest term still contributes to the linear orientation, though it is only slightly larger in magnitude than the T-shape term.

Table 59. Contributions to the long-range dipole moment, for four main O_2-O_2 orientations, with $r_A=r_{eq}$ and r_B =2.646

r_B =2.646 CASPT2	Quadrupolar induction	Hexadecapolar induction	E-tensor induction	Back induction	Dispersion
X-shape	10.1259 R^{-4}	20.99384 R^{-6}	26.18792 R^{-6}	89.09999 R^{-7}	83.80728 R^{-7}
Linear	18.11376 R^{-4}	45.67368 R^{-6}	152.6361 R^{-6}	937.2741 R^{-7}	-77.8011 R^{-7}
H-shape	10.1259 R^{-4}	20.99384 R^{-6}	-87.9285 R^{-6}	8.003046 R^{-7}	83.65027 R^{-7}
T-shape	4.913846 R^{-4}	-34.9795 R^{-6}	-84.3609 R^{-6}	150.6621 R^{-7}	144.1964 R^{-7}

In Table (59), the bond distance for oxygen molecule B has been lengthened to 2.646 bohr. The largest quadrupolar induction term still contributes to the linear orientation dipole. In addition, the largest term for the hexadecapolar induction now contributes to the linear orientation dipole as well, replacing the T-shape orientation contribution.

The largest contribution via E-tensor induction continues to be for the linear orientation. As far as back-induction is concerned, the largest term by far is that for the linear orientation, which has more than doubled in going from r_B=2.457 bohr to r_B=2.646 bohr. The largest dispersion term now contributes to the T-shape orientation.

Table 60. Contributions to the long-range dipole moment, for four main O_2-O_2 orientations, with $r_A=r_{eq}$ and r_B =2.929

r_B =2.929 CASPT2	Quadrupolar induction	Hexadecapolar induction	E-tensor induction	Back induction	Dispersion
X-shape	16.73762 R^{-4}	52.68705 R^{-6}	44.88263 R^{-6}	177.969 R^{-7}	121.1966 R^{-7}
Linear	29.94117 R^{-4}	158.5104 R^{-6}	266.4013 R^{-6}	1780.611 R^{-7}	-128.085 R^{-7}
H-shape	16.73762 R^{-4}	52.68705 R^{-6}	-152.828 R^{-6}	30.88505 R^{-7}	121.833 R^{-7}
T-shape	0.511506 R^{-4}	15.69696 R^{-6}	-134.069 R^{-6}	61.11158 R^{-7}	207.0611 R^{-7}

The trends in Table (59) continue for the quadrupolar induction terms in Table (60), now for an oxygen molecule B bond distance of 2.929 bohr. The largest hexadecapolar induction term, E-

tensor induction term, and back-induction term all contribute to the linear orientation. The largest contribution from dispersion now contributes to the T-shape orientation dipole.

Table 61. Contributions to the long-range dipole moment, for four main O_2-O_2 orientations, with $r_A=r_{eq}$ and r_B =3.213

r_B =3.213 CASPT2	Quadrupolar induction	Hexadecapolar induction	E-tensor induction	Back induction	Dispersion
X-shape	21.50182 R^{-4}	94.97172 R^{-6}	60.68108 R^{-6}	245.7033 R^{-7}	95.71674 R^{-7}
Linear	38.46362 R^{-4}	347.8871 R^{-6}	374.6841 R^{-6}	2430.554 R^{-7}	-321.211 R^{-7}
H-shape	21.50182 R^{-4}	94.97172 R^{-6}	-213.057 R^{-6}	49.93977 R^{-7}	97.68184 R^{-7}
T-shape	-2.9961 R^{-4}	87.92899 R^{-6}	-178.679 R^{-6}	-16.1983 R^{-7}	203.2541 R^{-7}

The trends for the quadrupolar induction have continued in Table (61), with the largest term belonging to the linear orientation. The only difference is that the T-shape term is now negative and will be negative for the last bond distance next considered as well. The largest terms for the hexadecapolar, E-tensor, and back induction continue to be for the linear orientation. The largest dispersion contribution now belongs to the linear orientation as well. These trends continue in Table (62), when the bond distance for oxygen molecule B is extended to the longest bond distance considered, 3.3 bohr.

Table 62. Contributions to the long-range dipole moment, for four main O_2-O_2 orientations, with $r_A=r_{eq}$ and r_B =3.3

r_B =3.3 CASPT2	Quadrupolar induction	Hexadecapolar induction	E-tensor induction	Back induction	Dispersion
X-shape	22.51966 R^{-4}	109.6372 R^{-6}	64.81026 R^{-6}	255.7391 R^{-7}	60.74578 R^{-7}
Linear	40.2844 R^{-4}	422.0736 R^{-6}	406.3436 R^{-6}	2543.824 R^{-7}	-451.641 R^{-7}
H-shape	22.51966 R^{-4}	109.6372 R^{-6}	-230.288 R^{-6}	51.38599 R^{-7}	63.31649 R^{-7}
T-shape	-3.88434 R^{-4}	113.7906 R^{-6}	-191.011 R^{-6}	-37.0266 R^{-7}	174.7359 R^{-7}

The above information is summarized in Table (63).

Table 63. Orientations with largest contribution from quadrupolar induction, hexadecapolar induction, E-tensor induction, back-induction and dispersion for r_B=2-3.3 bohr

Oxygen molecule B bond distance (r_B)	Quadrupolar induction	Hexadecapolar induction	E-tensor induction	Back induction	Dispersion
2 bohr	T-shape	Linear	Linear	Linear	Linear
2.1 bohr	T-shape	T-shape	Linear	T-shape	Linear
2.2 bohr	T-shape	T-shape	Linear	T-shape	Linear
2.28187 bohr (eq)	T-shape	T-shape	T-shape	T-shape	T-shape
2.296 bohr	T-shape	T-shape	T-shape	T-shape	T-shape
2.36 bohr	T-shape	T-shape	Linear	T-shape	Linear
2.457 bohr	Linear	T-shape	Linear	Linear	Linear
2.646 bohr	Linear	Linear	Linear	Linear	T-shape
2.929 bohr	Linear	Linear	Linear	Linear	T-shape
3.213 bohr	Linear	Linear	Linear	Linear	Linear
3.3 bohr	Linear	Linear	Linear	Linear	Linear

4.3 Contributions to the Dipole Moment at an Intermolecular Distance of 10 bohr

The intermolecular distance of R=10 bohr has been substituted into the terms in tables (51)-(61) to illustrate the relative magnitudes of the direct quadrupolar induction, direct hexadecapolar induction, E-tensor induction, back-induction, and dispersion contributions to the collision-induced dipole moment. This corresponds to a distance that is about 4 bohr outside of the H-shape and X-shape potential energy minimum, about 3 bohr outside the potential energy minimum for the T-shape orientation, and about 2 bohr outside of the potential energy minimum for the linear orientation of the O_2-O_2 supermolecule. Figure (55) shows the direct quadrupolar induction contribution for the four main geometries (T-shaped, Linear, H-shaped and X-shaped), versus the O_2 bond length for the non-equilibrium oxygen molecule in the O_2-O_2 supermolecule. This contribution is by far the largest to the collision-induced dipole moment, accounting for ~80% or more of the total dipole for all geometries and all at bond distances considered.

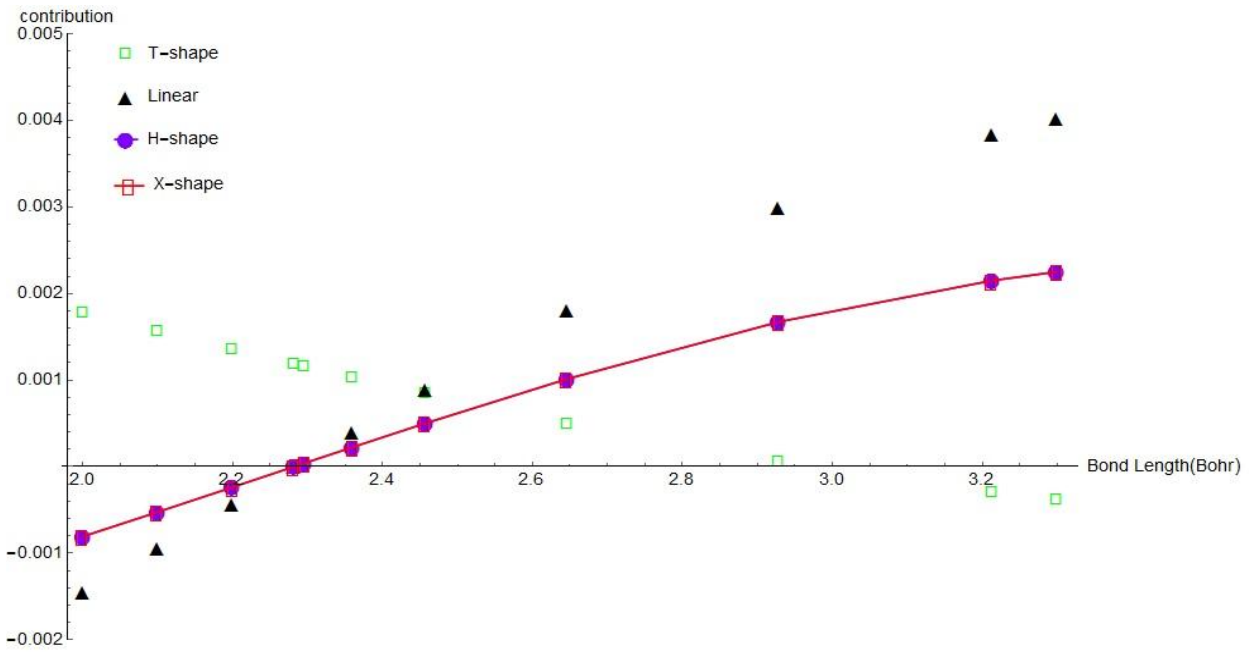

Figure 55. The direct quadrupolar induction contribution to the dipole for the four main geometries, at an intermolecular distance of R=10 bohr.

From the figure, we can see that at distances less than equilibrium, the contribution to the dipole moment for O_2-O_2 in the T-shape is positive in value, with a negative slope, while the opposite is true for the other three geometries. The contribution to the dipole becomes zero at equilibrium for the X-shape, H-shape, and linear geometries, due to the fact that these arrangements are centrosymmetric. After this point the contribution becomes positive for these three geometries. The contribution for the T-shaped geometry is also still positive at this point, and does not become negative until we reach the two longest distances we considered. It is clear from the figure that the magnitude of this component is generally largest for the linear geometry. Also note that that quadrupolar induction contribution to the collision-induced dipole has the same value for the X-shape and the H-shape geometries.

The second largest contribution to the collision-induced dipole moment for the X-shaped orientation is the E-tensor induction, at ~2-3% of the dipole, except for at the three longest bond distances of oxygen B considered, in which the hexadecapolar induction becomes larger. For the

H-shaped orientation of the two oxygen molecules, the E-tensor is the second largest contribution for all bond distances, contributing 9-11% to the collision-induced dipole. For the linear orientation, the E-tensor induction is the second largest contribution for all but the longest bond length of 3.3 bohr, where hexadecapolar induction contributes slightly more. The contribution to the dipole from E-tensor induction in this case is 7-8%. For the T-shaped geometry, E-tensor induction is the second largest contribution as well, contributing ~3-7% to the dipole, until the non-equilibrium oxygen molecule in the collision pair becomes stretched past 2.5 bohr, at which point the hexadecapolar induction becomes larger. The E-tensor induction contribution to the dipole at an intermolecular distance of 10 bohr is shown in Figure (56). From the figure, we can see that the linear geometry displays the largest magnitude of this component, as was seen for quadrupolar induction.

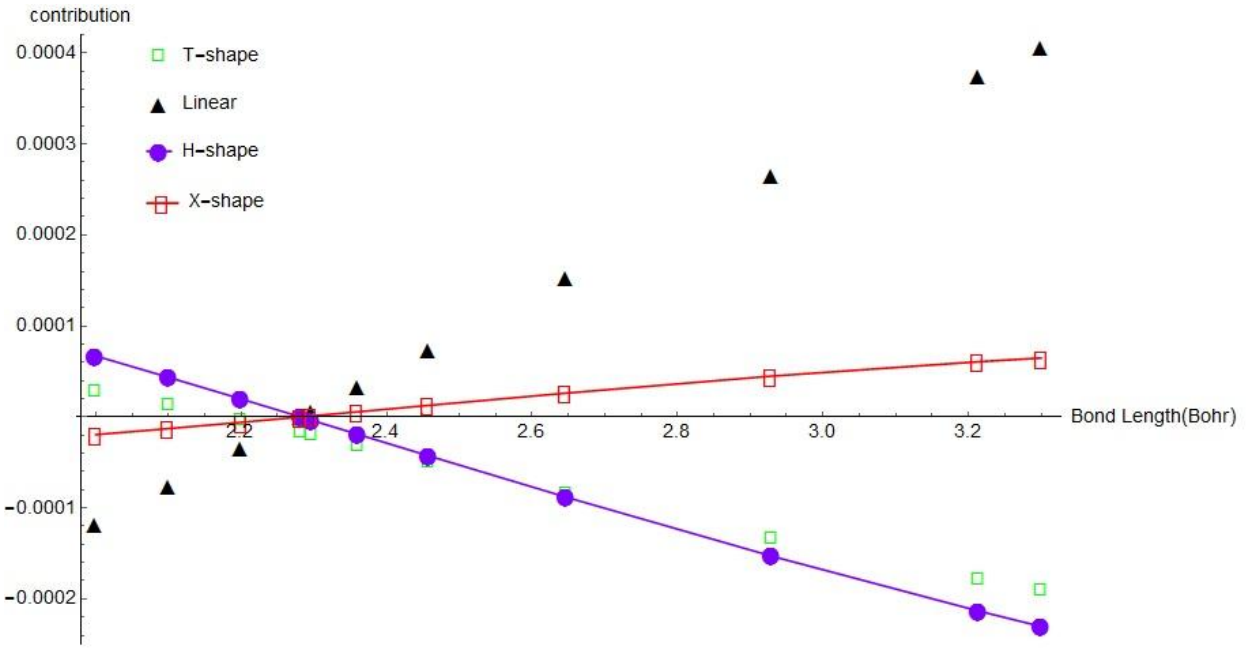

Figure 56. E-tensor induction contribution to the collision-induced dipole moment for the four main geometries studied, at an intermolecular distance of 10 bohr.

Figure (57) shows the direct hexadecapolar contribution to the collision-induced dipole moment. For the linear orientation, hexadecapolar induction contributes between 0.004-4.4% to the dipole moment when the bond distance of oxygen molecule B is between 2 and 2.929 bohr. This makes it the fourth and fifth largest out of the five contributions to the dipole for the linear orientation. We can see clearly in the figure that as the bond is stretched to the longest two distances, the hexadecapolar contribution increases significantly. At these distances, the hexadecapolar induction contributes 7-8% to the dipole moment, making it the third largest contribution to the dipole at a bond length of 3.213 bohr, and the second largest contribution at the bond length of 3.3 bohr.

In regards to the T-shaped geometry, the hexadecapolar induction is second only to the quadrupolar induction contribution for bond distances of r_B=2-2.5 bohr. At longer distances, it decreases to become the third largest contribution.

For the H-shape orientation, hexadecapolar induction is the third largest contribution to the dipole, after quadrupolar induction and E-tensor induction, being 4-48% that of the E-tensor contribution in the range from 2.2-3.3 bohr. At distances shorter than 2.2 bohr, the hexadecapolar term is smaller, as seen in Figure (57), and the dispersion replaces hexadecapolar induction as the third largest contribution.

Note that as was seen with quadrupolar induction, the hexadecapolar contribution to the dipole for the X-shape and H-shape geometries has the same value. Therefore the hexadecapolar induction is overcome by dispersion at shorter distances for this orientation as well. As was also seen for the H-shape orientation, it is the third largest contribution for r_B>2.2 bohr. However, at bond distances>2.646 bohr, the hexadecapolar induction becomes the second largest contribution

to the dipole for the X-shape orientation; this is because the E-tensor induction term does not become as large in magnitude at long distances as was seen for the H-shape (See Figure 56).

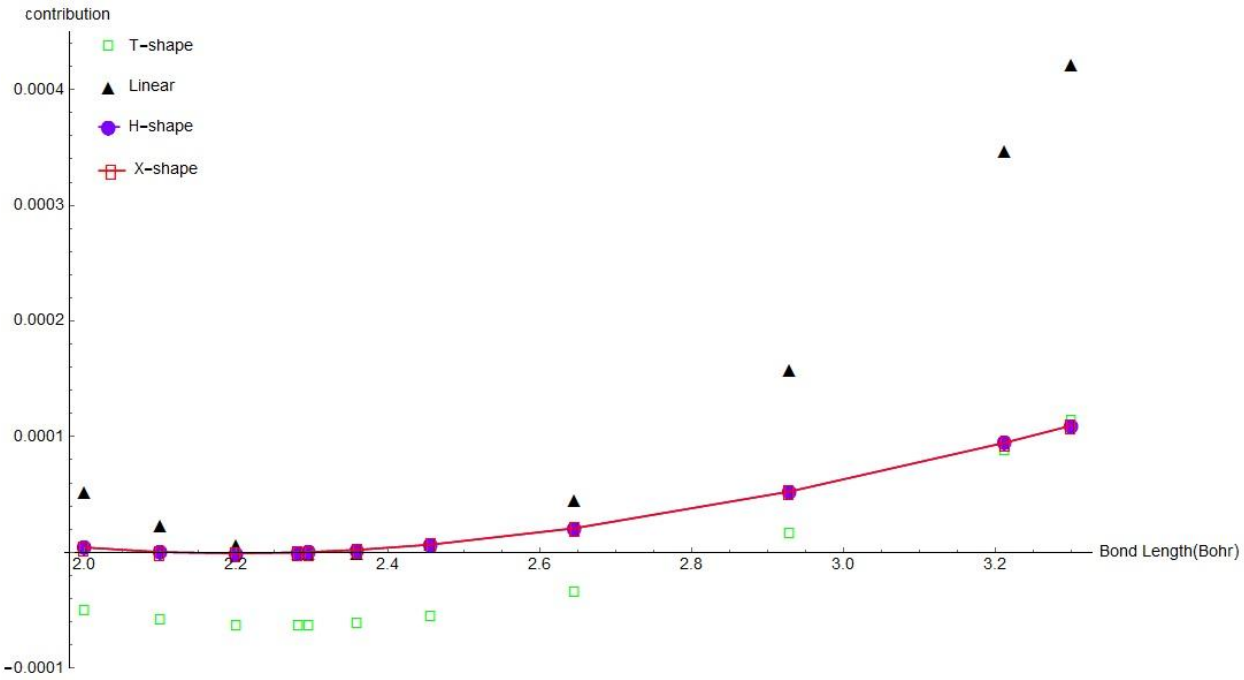

Figure 57. Direct hexadecapolar induction contribution to the collision-induced dipole moment, for the four main geometries studied, at an intermolecular distance of R=10 bohr.

Figure (58) shows the back-induction contribution to the dipole moment. It is apparent that again the magnitude of this contribution to the dipole moment is much larger for the linear geometry than for the other three geometries. For the T-shaped geometry, this contribution accounts for ~0.5-4% of the collision-induced dipole. For the linear, H-shaped, and X-shaped geometries, back-induction contributes ~3-5%, less than 1%, and ~0.5-1% to the dipole, respectively.

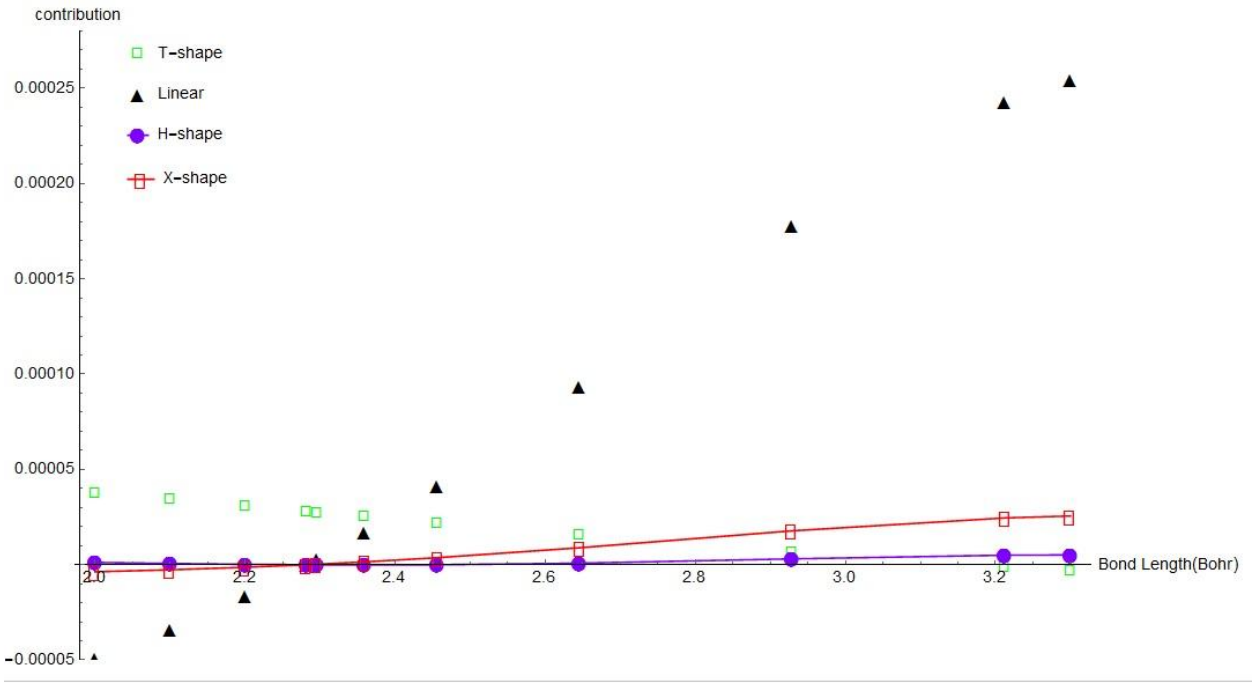

Figure 58. The back-induction contribution to the collision-induced dipole for the four main geometries studied, at an intermolecular distance of R=10 bohr.

The fifth and final contribution to the collision-induced dipole moment in the long-range approximation comes from the dispersion, Figure (59). It is interesting to note that although almost all of the terms in the collision-induced dipole equations for the H-shaped and X-shaped geometries have different coefficients, this contribution ends up being so similar in value for the two geometries. As with the previous four contributions, we also note that the magnitude of this contribution is largest for the linear geometry. For the T-shaped geometry, dispersion accounts for up to ~5% of the collision-induced dipole, but for most bond distances it contributes far less than 1%. For the linear geometry, dispersion only accounts for ~0.4-3% for all bond distances studied, while for the H-shaped geometry, dispersion accounts for only 2% or less of the total dipole. The situation is very similar for the X-shaped geometry, with dispersion only accounting for at most ~2% of the dipole, though for most distances the contribution is under 1%.

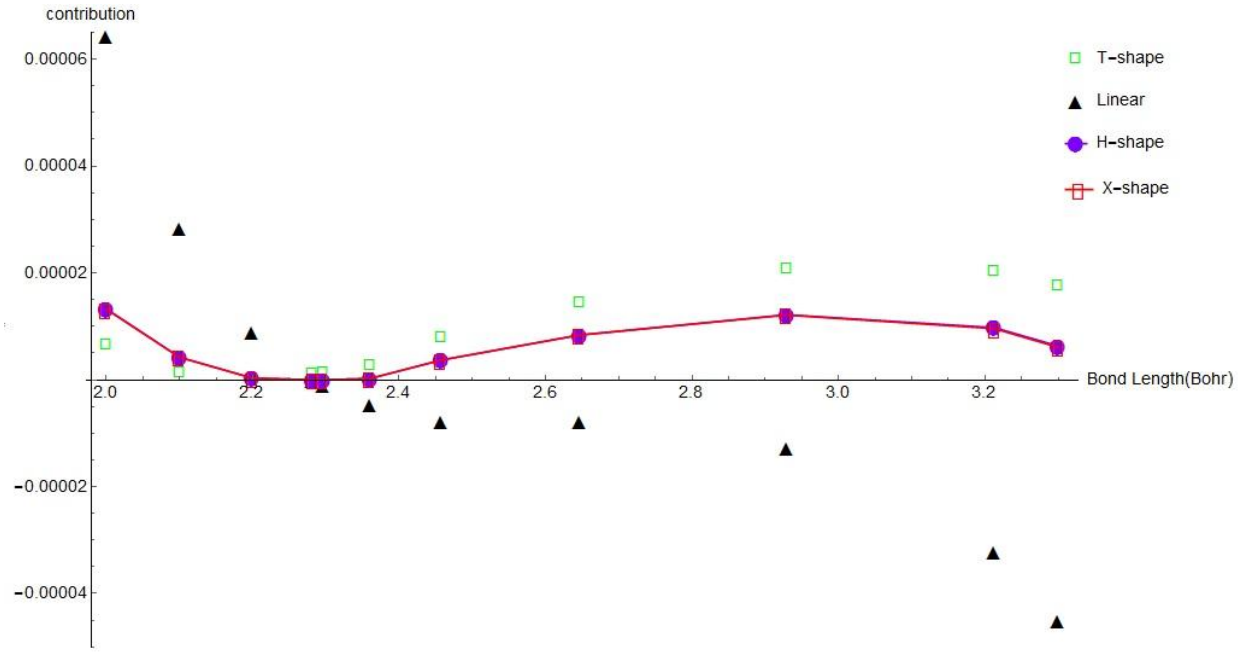

Figure 59. The dispersion contribution to the collision-induced dipole moment, for the four main geometries considered, at an intermolecular distance of 10 bohr.

4.4 Discussion and Summary

We have calculated the long-range z-component of the collision-induced dipole moments, using a previously derived equation for the T-shape orientation of two linear, centrosymmetric molecules[8]. In addition, we have now derived equations for the collision-induced dipole moment for two linear molecules in an H-shape, X-shape, and linear orientation. Using our static multipole moments and (hyper)polarizabilities that were obtained with the CASPT2 method and d-aug-cc-pVQZ basis set, we have calculated the necessary coefficients $D_{\lambda_A\lambda_B\lambda L}$ for use in the dipole expressions. We have thus calculated the z-component of the collision-induced dipole moment, for comparison with our *ab initio* values of the dipole moment in the next chapter.

We have separated the dipole moment equations into contributions from direct quadrupolar induction through order R^{-4} in the intermolecular separation R, contributions from direct

hexadecapolar induction and induction via non-uniformities of the local field acting on each molecule (via the E-tensor mechanism) through order R^{-6}, and contributions from back-induction and dispersion through order R^{-7}. Table (72) shows that the largest terms from all five contributions to the collision-induced dipole occur for the linear and T-shaped orientations.

We have also evaluated these contributions to the collision-induced dipole numerically, for an intermolecular distance of 10 bohr. From this analysis, we can see that the direct quadrupolar induction contributes the most to the collision-induced dipole moment, accounting for 80% or more of the total dipole for all four orientations studied. The second largest contribution to the dipole moment comes from the E-tensor induction for all orientations except the T-shape, contributing about 2-11% of the dipole over the range of non-equilibrium bond distances for oxygen molecule B. Some exceptions occur as the bond of oxygen molecule B is stretched to the longest distances considered, where hexadecapolar induction becomes slightly larger than the E-tensor induction contribution.

For the H-shape and X-shape orientations, the hexadecapolar induction term is the third largest for most bond distances, except for at the same longer bond lengths mentioned above, where it becomes the second largest contribution, and at some distances shorter than equilibrium, where it is overcome by the dispersion terms.

For the linear orientation, the third largest contribution to the dipole at most bond lengths is the back-induction term, with 3-5% of the total dipole. Depending on the bond distance of oxygen molecule B, the smallest contributions come from the hexadecapolar induction and dispersion contribution.

For the T-shape orientation, hexadecapolar induction makes the second largest contribution, at ~2-7% of the total dipole, except for the longest three bond distances, at which the E-tensor term takes over, at 21-42% of the total collision-induced dipole. The fourth largest contribution comes from back-induction for r_B=2-2.646 bohr, with the dispersion contributing the least in this region, at less than 1% of the total dipole in most cases. The situation is reversed for the bond distances in the region from 2.929-3.3 bohr, with back induction contributing the least there.

CHAPTER 5: *Ab Initio* Versus Long-Range Approximation from the Dipole Moments

5.1 Introduction: Methodology Used in Obtaining *Ab Initio* Dipole Moments

The long-range approximation discussed in the last chapter has one large advantage. That is, the moments and polarizabilities required are found for the O_2 monomer, and therefore complex and costly supermolecular calculations are avoided. However, the long-range method only takes into account the long-range effects acting on the molecule(s), as its name suggests. These include electrostatic, induction, and dispersion effects, which all vary with the intermolecular distance as R^{-n}. Short-range effects, which vary with the intermolecular distance as $e^{-\alpha R}$, are neglected. These effects include resonance interactions, exchange-repulsion effects, charge transfer effects, and penetration and damping effects[82]. Therefore, it would be helpful to know at what intermolecular distances the long-range method is valid, and at what intermolecular distances it begins to fail due to the neglect of the short-range effects. In this section, we will compare the z-components of the dipole moment calculated using *ab initio* methods, and those found using the long-range method.

As noted in the beginning of the last chapter, electric multiple moments can be calculated by using the appropriate derivative of the energy E as follows:

$$\mathrm{E} = \mathrm{E}_0 - \mu\mathrm{F}_\alpha - \frac{1}{3}\Theta_{\alpha\beta}\mathrm{F}_{\alpha\beta} - \frac{1}{15}\Omega_{\alpha\beta\gamma}\mathrm{F}_{\alpha\beta\gamma} - \frac{1}{105}\Phi_{\alpha\beta\gamma\delta}\mathrm{F}_{\alpha\beta\gamma\delta} - \frac{1}{2}\alpha_{\alpha\beta}\mathrm{F}_\alpha\mathrm{F}_\beta \tag{5.1}$$

As was done in chapter 3, the finite field approach can be used to find the dipole moment, using the following derivative[113]:

$$\mu_\alpha = -\frac{\partial E}{\partial F_\alpha^0} \tag{5.2}$$

We will use a simple two-point model, which has an associated error of $-(F_\alpha^0)^2$, as follows:

$$\mu_\alpha = -\frac{E(F_\alpha^0)-E(-F_\alpha^0)}{2F_\alpha^0} \tag{5.3}$$

5.2 Comparison of Ab Initio and Long-Range Dipole Moments

Over 4,380 points have been obtained *ab initio*, using the CASPT2 method and aug-cc-pVQZ basis set. Table (64) shows the geometries and symmetry point groups used to obtain this data.

Table 64. Geometries Used in the Calculation of *Ab Initio* Dipole Moments

Θ-φ-Θ-φ	Symmetry Point Group
0-0-0-0	D_{2h}
90-0-0-0	C_{2v}
90-0-90-0	D_{2h}
90-0-90-90	C_{2v}
30-0-0-0	C_s
60-0-0-0	C_s
105-0-60-60	C_1
40-0-115-45	C_1
20-0-115-45	C_1
15-0-75-30	C_1
15-0-95-10	C_1
10-0-160-15	C_1
20-0-145-25	C_1
30-0-130-35	C_1
30-0-60-0	C_s
30-0-90-0	C_s
35-0-65-80	C_1
45-0-30-0	C_s
45-0-60-0	C_s
45-0-90-0	C_s
50-0-95-55	C_1
60-0-80-65	C_1
70-0-65-75	C_1

We will now compare the dipole moments from the long-range and *ab initio* methods, beginning with the linear (0-0-0-0) geometry and proceeding through the above geometries, ending with the

70-0-65-75 conformation. In the interest of brevity, we will compare the dipole moments with monomer A having a bond distance fixed at equilibrium (2.28187 bohr), and monomer B having a bond distance of 2 bohr (the shortest bond length considered), 2.28187 bohr (equilibrium bond distance), and 3.3 bohr (the longest bond distance considered).

Figure (60) details the long-range and CASPT2 dipole moments for the linear geometry, with monomer B fixed at a bond distance of 2 bohr.

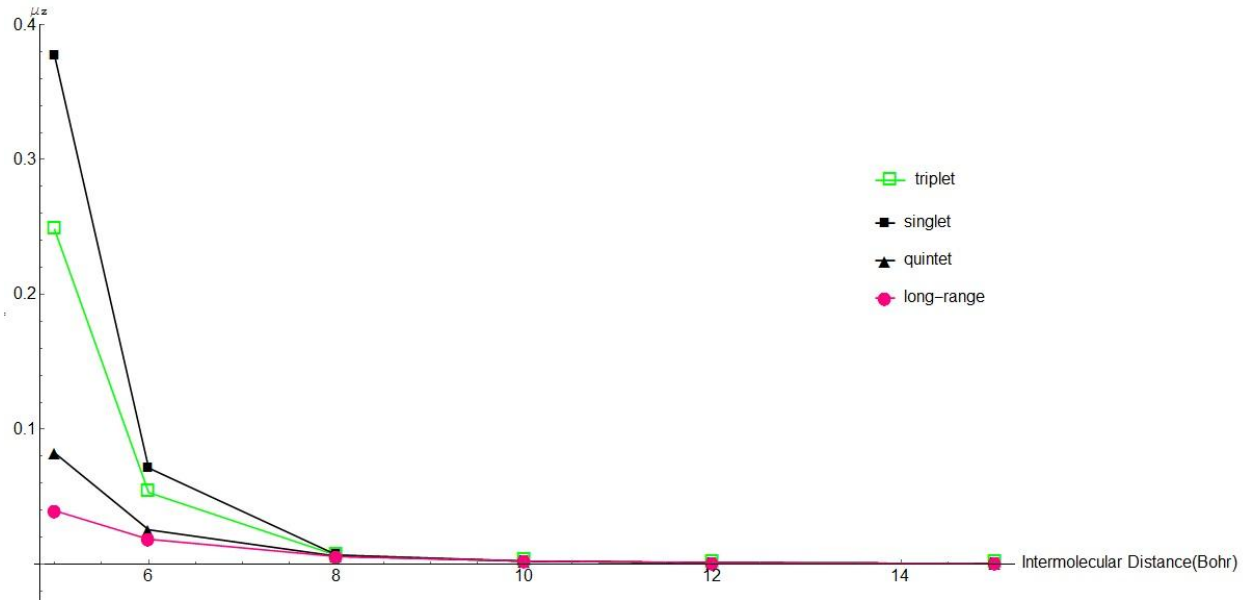

Figure 60. Comparison of dipole moments as a function of intermolecular distance (R) for the linear geometry, with r=2 bohr for O_2^B. The dipole moment has atomic units, ea_0.

From Figure (60), we see that the dipole moments for the *ab initio* triplet, singlet, and quintet spin states, as well as the dipole calculated using the long-range method, are in good agreement for the four longest intermolecular distances (8,10,12, and 15 bohr). At an intermolecular distance of of 6 bohr, the four values begin to separate, with the ground spin state (the singlet) having the largest magnitude. The difference is even more pronounced as the molecules draw nearer to each other, at R=5 bohr. Neglect of the short range effects in the long-range dipole

gives this dipole the smallest magnitude at this distance. We also note that the long-range dipole most closely replicates the *ab initio* quintet spin state.

Figure (61) makes the same comparison for the linear geometry's dipole moments, but with monomer B fixed at a bond distance of 3.3 bohr.

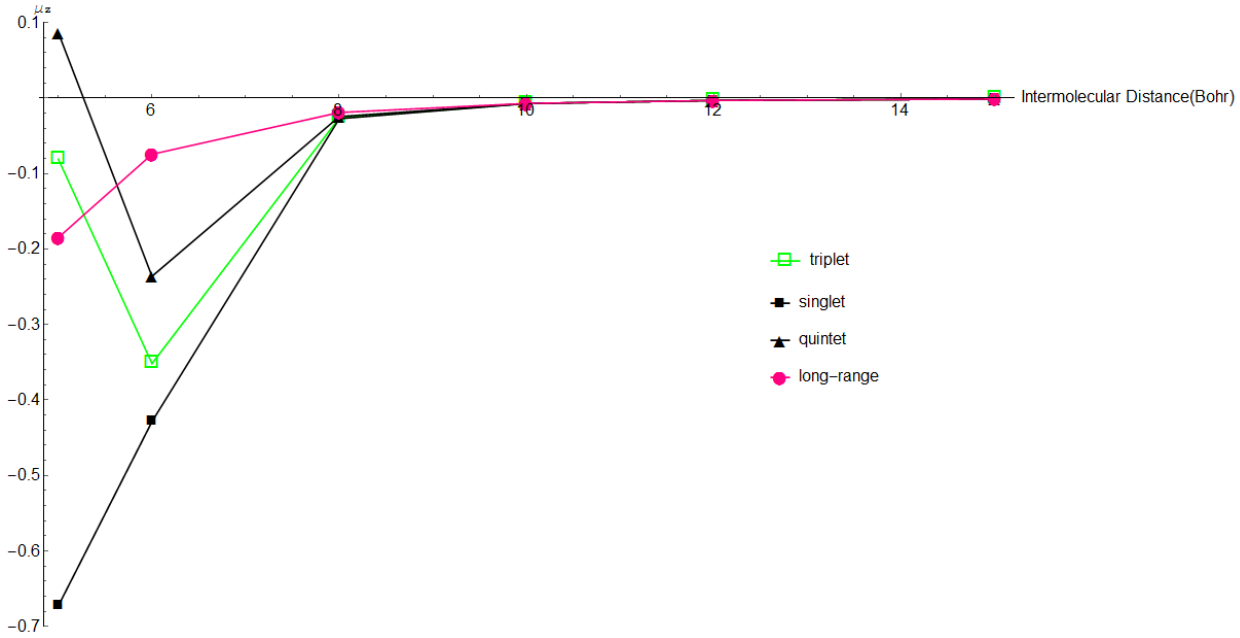

Figure 61. Comparison of dipole moments as a function of intermolecular distance (R) for the linear geometry, with r=3.3 bohr for O_2^B . The dipole moment has atomic units, ea_0.

We note immediately that the z-component of the dipole moment has switched direction, becoming negative for all points save the quintet spin state dipole at R=5 bohr. As in Figure (60), the four values we compare are in good agreement until the molecules are at R=6 bohr, at which point we clearly see separation amongst them of a large magnitude, with differences of over 100%. With monomer B at this longest bond distance, the separation is more pronounced than for the case of monomer B at the shortest bond distance (Figure (60)). Again, the singlet state *ab initio* value is largest in magnitude, and the long-range method value is the smallest. The long-

range values most closely replicate the quintet spin state values, until a distance of R=5 bohr, where the triplet state is closer to the long-range value. We do not discuss values of the dipole moment for both monomers fixed at equilibrium, as in the linear geometry, the supermolecular complex is centrosymmetric, and therefore gives a dipole moment of zero.

Figure (62a) depicts the dipole moment as a function of intermolecular distance for the T-shaped (90-0-0-0) geometry.

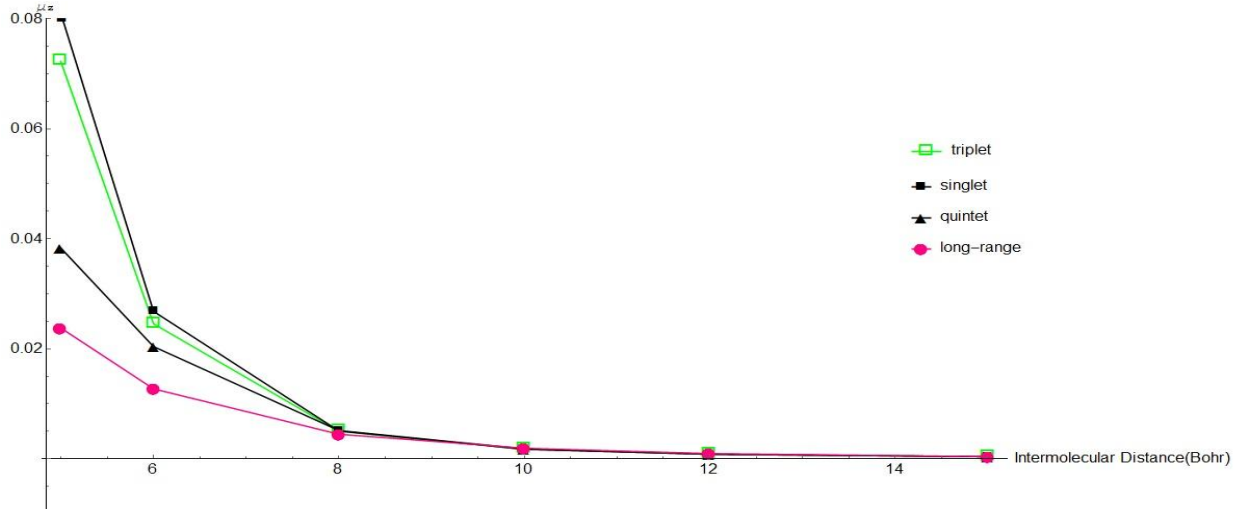

Figure 62a. Comparison of dipole moments as a function of intermolecular distance (R) for the T-shaped geometry, with r=2 bohr for O_2^B. The dipole moment has atomic units, ea_0.

As for the linear geometry, Figure (62a) shows that there is good agreement between the four values until R=6 bohr. The singlet state again has the largest magnitude dipole moment, and the long-range values are closest to those of the quintet state. In Figure (62b), we see a close up of the dipole moment values from 8-15 bohr, where the long-range method can be seen to be valid.

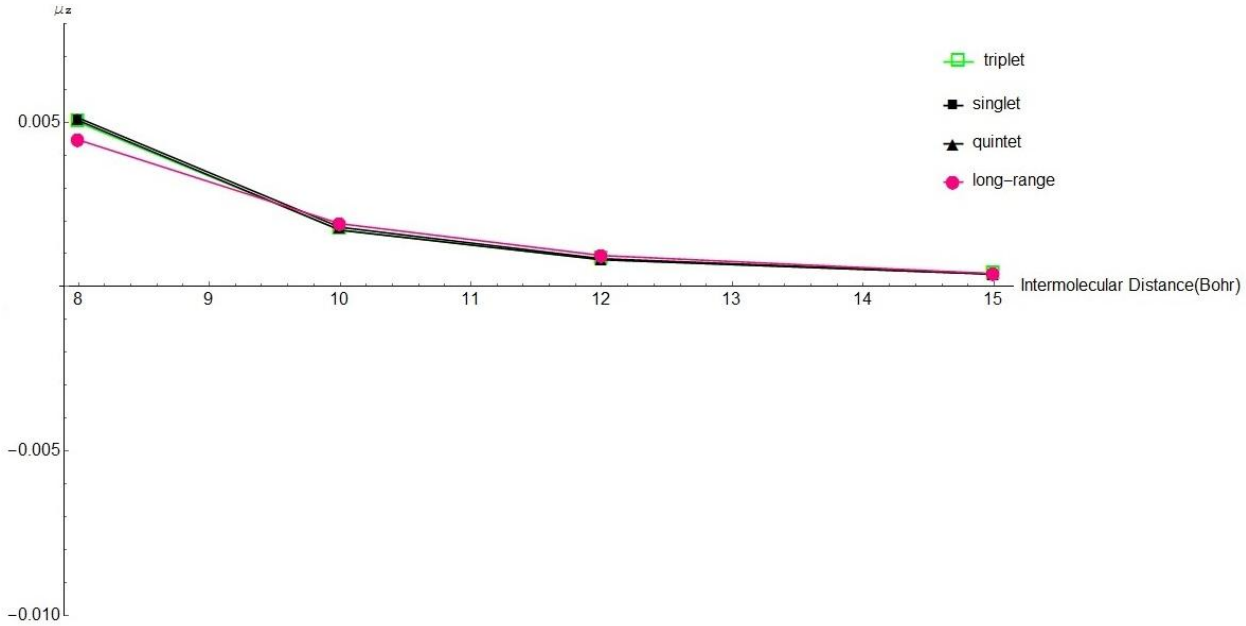

Figure 62b. Close-up view of dipole moments as a function of intermolecular distance (R) for the T-shaped geometry, with r=2 bohr for O_2^B. The dipole moment has atomic units, ea_0.

Figure (63) shows the dipole moments obtained with both monomers fixed at equilibrium.

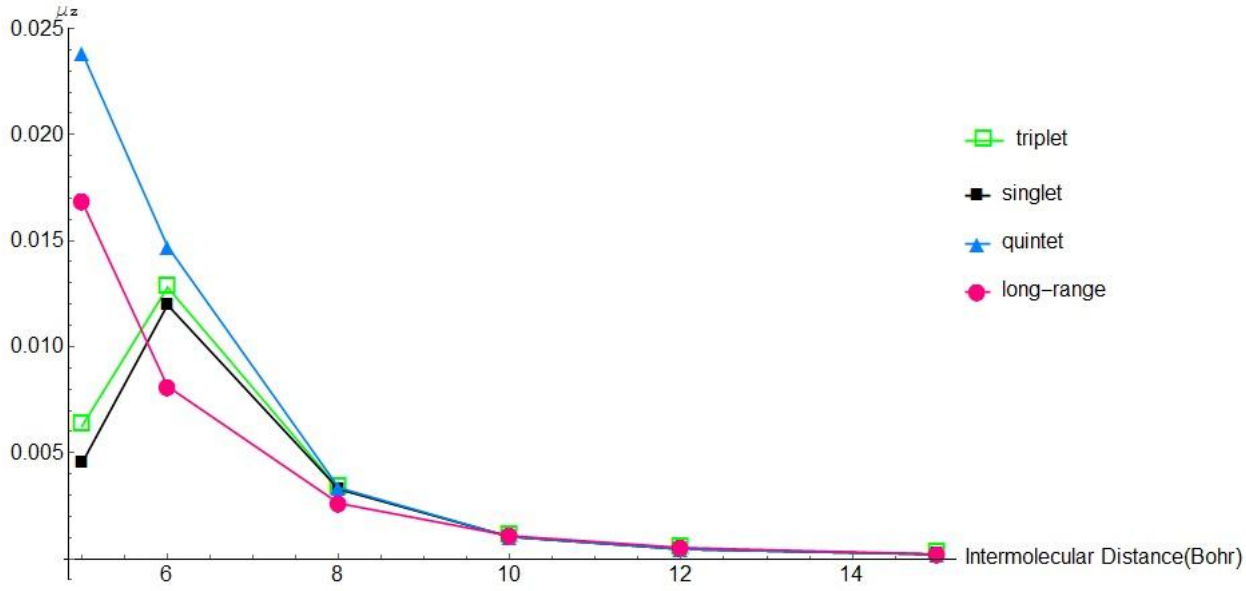

Figure 63. Comparison of dipole moments as a function of intermolecular distance (R) for the T-shaped geometry, with r=r_{eq} for O_2^B . The dipole moment has atomic units, ea_0.

We note that when both molecules are at the equilibrium bond distance,. the quintet state dipole moments are now largest in magnitude, and the long-range values again are closest to those of the quintet spin state dipole moments.

In Figure (64), we see the dipole moments for monomer B fixed at 3.3 bohr for the T-shaped geometry.

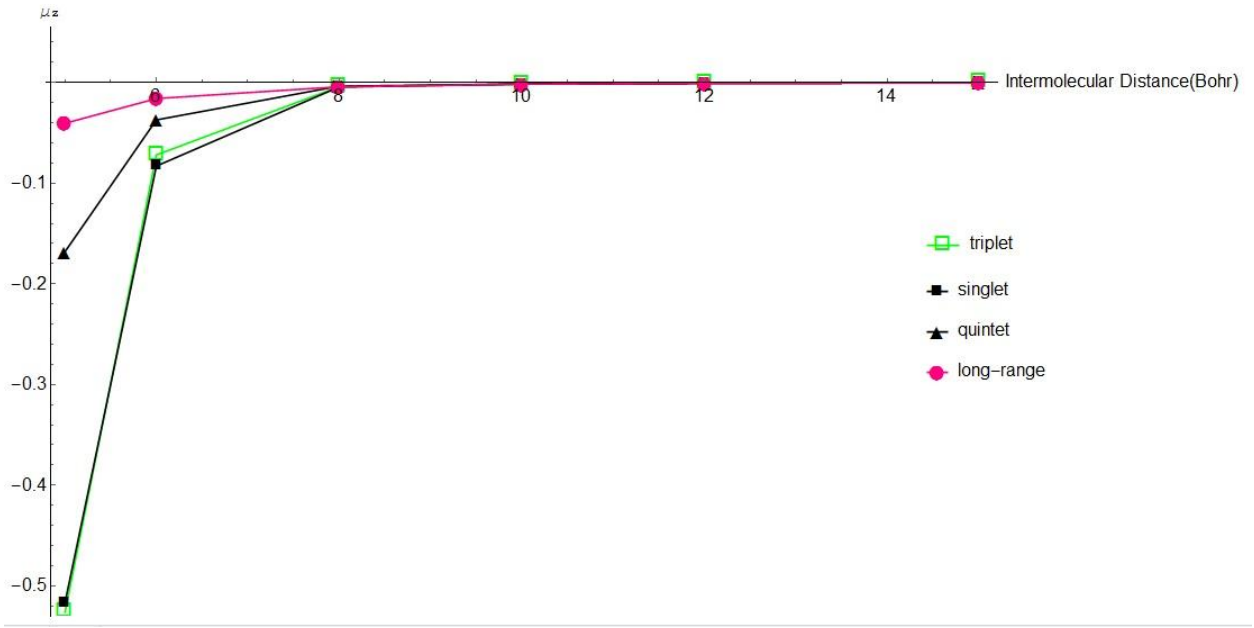

Figure 64. Comparison of dipole moments as a function of intermolecular distance (R) for the T-shaped geometry, with r=3.3 bohr for O_2^B. The dipole moment has atomic units, ea_0.

In Figure (64), the values of the dipole moment have again become mostly negative, as was the case for monomer B fixed at the shortest distance (r=2 bohr). The singlet state dipole moment is the largest in magnitude, and the long-range values are again closest to that of the quintet spin state values.

The next geometry considered is the H-shape geometry, with angles 90-0-90-0, and D_{2h} point group symmetry. Figure (65a) shows the z-component of the dipole moment for this geometry when monomer B has its bond length constricted to a length of r=2 bohr. Here, the z-component for the *ab initio* singlet spin state is the largest in magnitude. The long-range dipole is much closer in magnitude to the triplet and quintet dpiole, which are nearly identical.

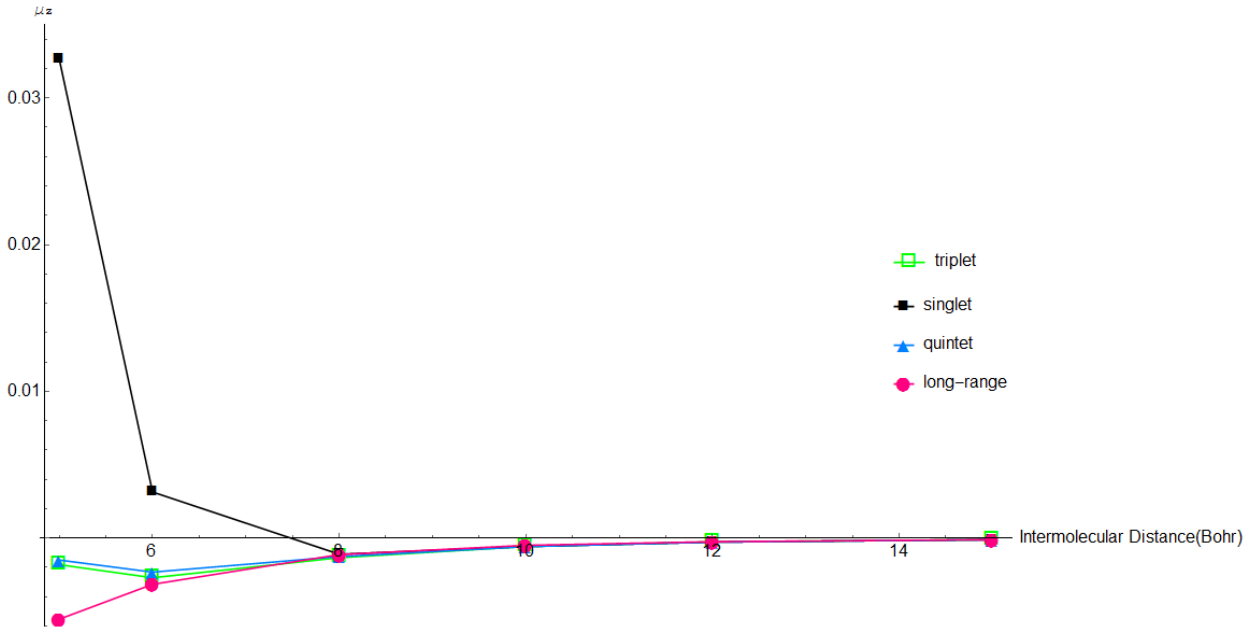

Figure 65a. Comparison of dipole moments as a function of intermolecular distance (R) for the H-shaped geometry, with r=2 bohr for O_2^B. The dipole moment has atomic units, ea_0.

Figure (65b) shows a zoomed in view of the dipole moments in Figure (65a), from 8-15 bohr, where the long-range method is valid.

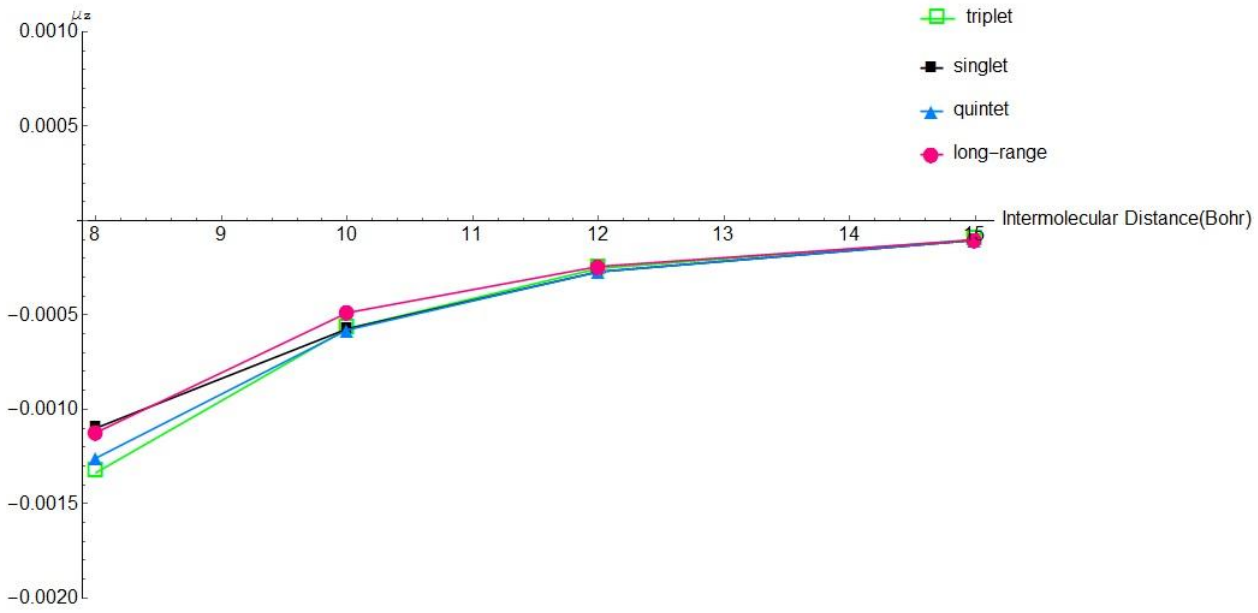

Figure 65b. Close-up view of dipole moments as a function of intermolecular distance (R) for the T-shaped geometry, with r=2 bohr for O_2^B. The dipole moment has atomic units, ea_0.

Figure (66) shows the z-component of the dipole moment for the H-shape geometry, with monomer B having a bond distance of r=3.3 bohr.

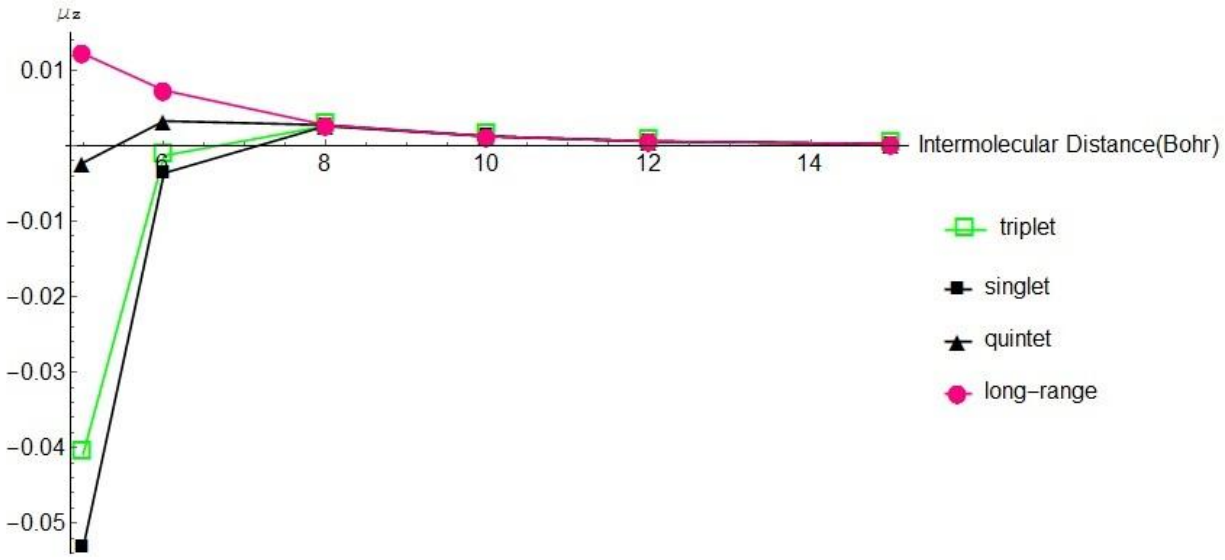

Figure 66. Comparison of dipole moments as a function of intermolecular distance (R) for the H-shaped geometry, with r=3.3 bohr for O_2^B. The dipole moment has atomic units, ea_0.

The values are in good agreement until an intermolecular distance of R=6 bohr. The singlet spin state again has the largest magnitude, and the long-range values are closest to the quintet spin state *ab initio* values.

Figure (67) compares the z-component of the dipole moments for the X-shape geometry, with the bond distance of monomer B fixed at 2 bohr.

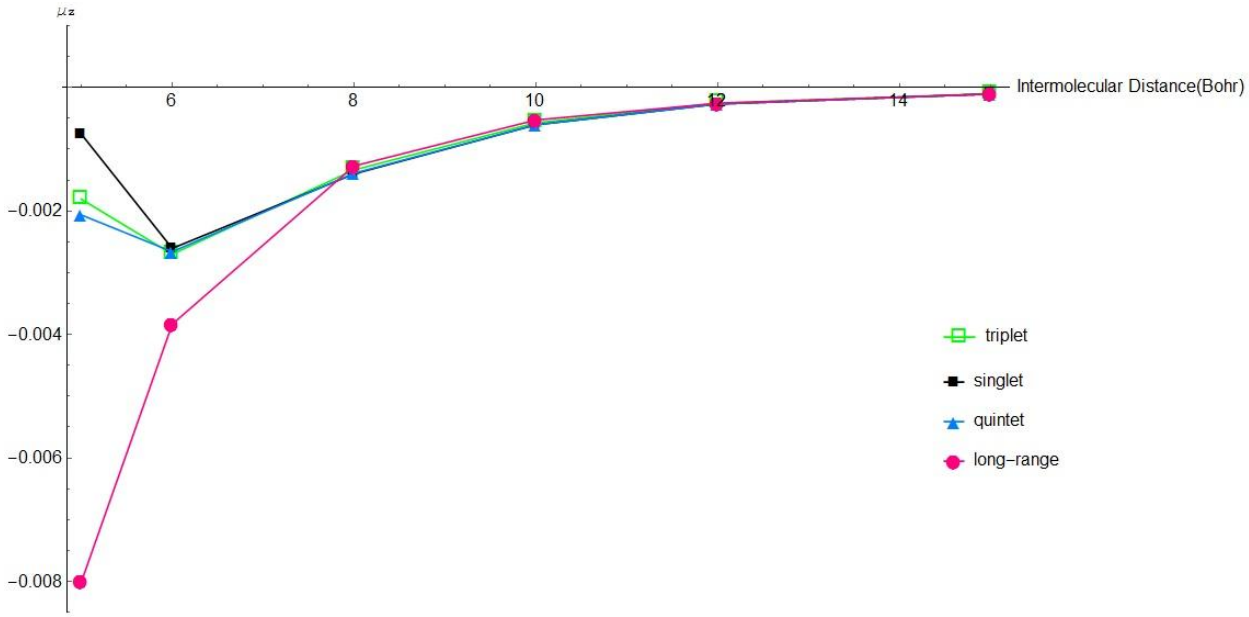

Figure 67 . Comparison of dipole moments as a function of intermolecular distance (R) for the X-shaped geometry, with r=2 bohr for O_2^B. The dipole moment has atomic units, ea_0.

This geometry is different from the last three that we considered in that the largest magnitude dipole moment is the long-range value (apparent at 6 bohr and 5 bohr). However, the long-range values again most closely replicate the quintet spin state values, and the values are in good agreement until R=6 bohr.

In Figure (68), we compare values for the same geometry but at a monomer B bond distance of 3.3 bohr. As in Figure (67), the long-range dipole has the largest magnitude, and is somewhat closer to the quintet spin state values than the other two multiplet states; however, the difference between the three *ab initio* spin state values is much less than the difference between the *ab initio* and long-range values.

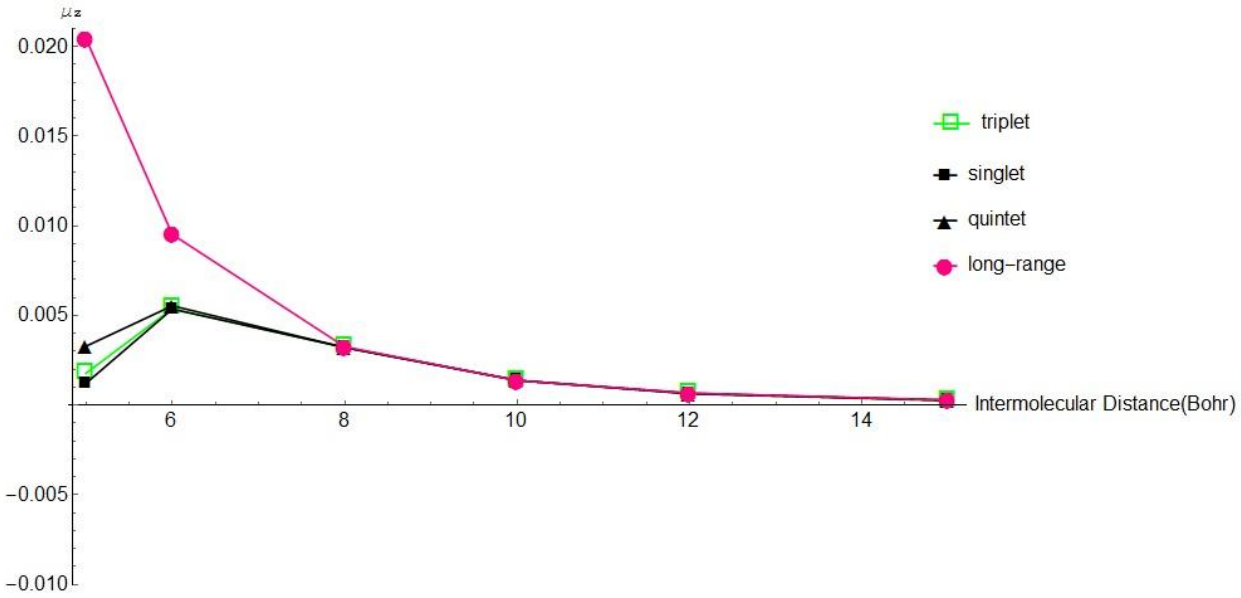

Figure 68. Comparison of dipole moments as a function of intermolecular distance (R) for the X-shaped geometry, with r=3.3 bohr for O_2^B. The dipole moment has atomic units, ea_0.

The next geometry we will consider is that with angles 30-0-0-0. This is a similar orientation to the T-shape, but because of the reduction of the first angle to 30 degrees, the only symmetry plane it contains is the reflection plane. In Figure (69), we compare the dipole moments with monomer B at the shortest bond distance, r=2.1 bohr.

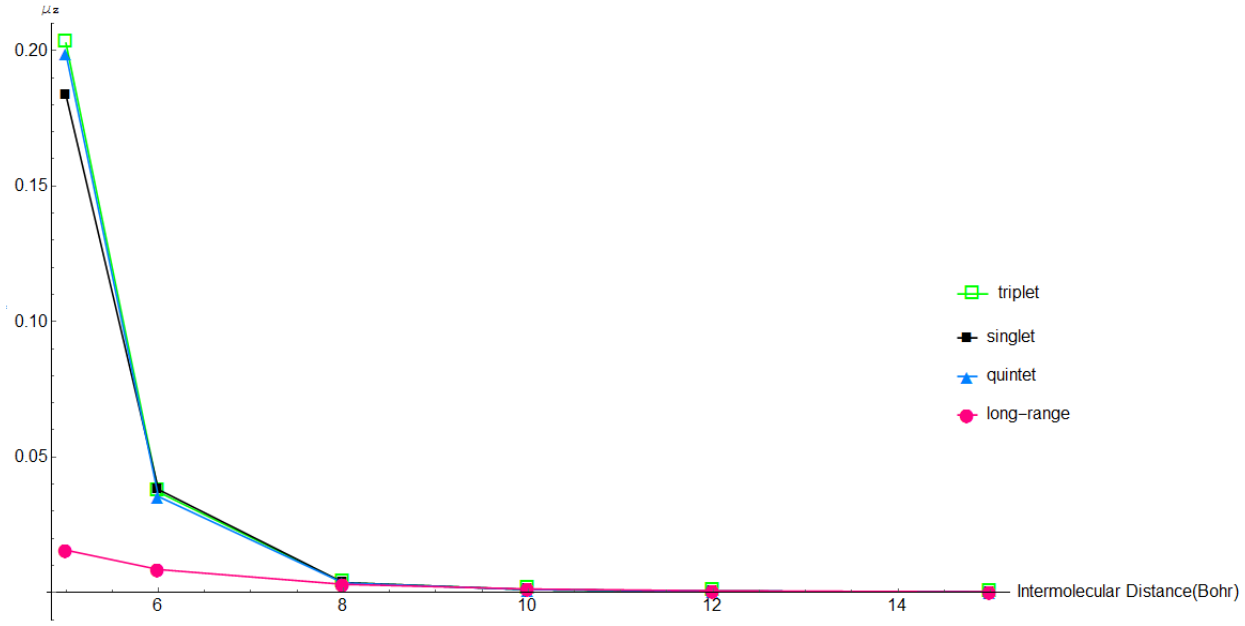

Figure 69. Comparison of dipole moments as a function of intermolecular distance (R) for the 30-0-0-0 geometry, with r=2.1 bohr for O_2^B. The dipole moment has atomic units, ea_0.

The *ab initio* dipole moment calculated for the triplet spin state is the largest in magnitude at the intermolecular distance of nearest approach of the two monomers studied in this work (R=5 bohr).

Figure (70) shows the dipole moments for this geometry when monomer A is at the equilibrium bond length (r=2.28187 bohr), and the bond length of monomer B is very near this, at r=2.296 bohr. We see that at this geometry and with the monomers at/near equilibrium, the dipole of the quintet state is the largest in magnitude. The singlet state has the smallest dipoles of the three spin states, and thus the long-range dipole moments most closely model the singlet state data.

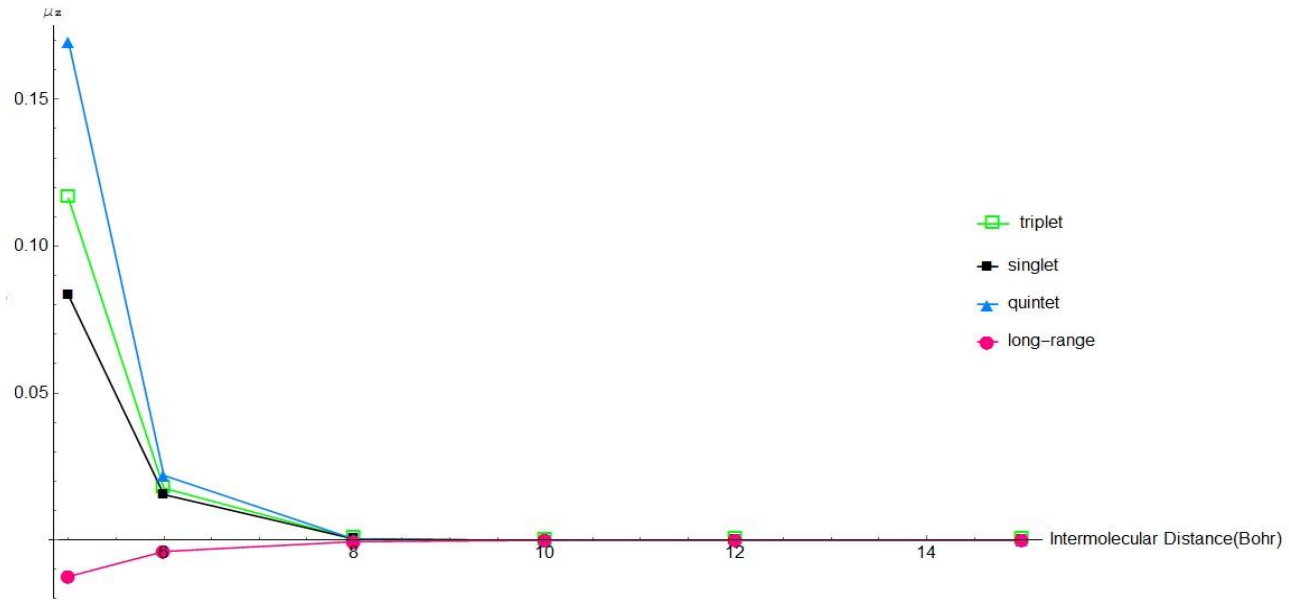

Figure 70. Comparison of dipole moments as a function of intermolecular distance (R) for the 30-0-0-0 geometry, with r=2.296 bohr for O_2^B. The dipole moment has atomic units, $ea_{0.}$

Finally, Figure (71) compares the dipole moments with monomer B at the longest bond length considered.

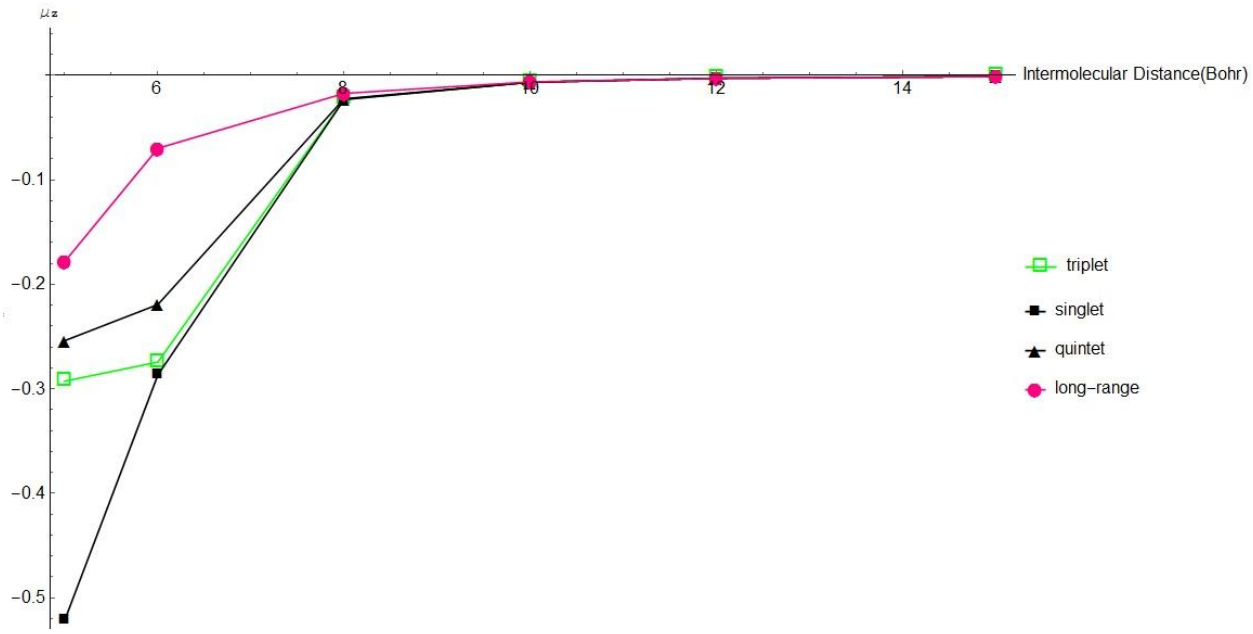

Figure 71. Comparison of dipole moments as a function of intermolecular distance (R) for the 30-0-0-0 geometry, with r=3.3 bohr for O_2^B. The dipole moment has atomic units, $ea_{0.}$

The dipoles are in good agreement until the distance of R=6 bohr. All other previous trends hold here, with the long-range dipoles closest to those of the quintet spin state *ab initio* values, and the singlet state *ab initio* dipoles largest in magnitude.

In Figure (72), we compare the dipole moments for the geometry with angles 60-0-0-0 ("halfway" between the T-shaped and 30-0-0-0 geometries), at the shortest monomer B bond distance.

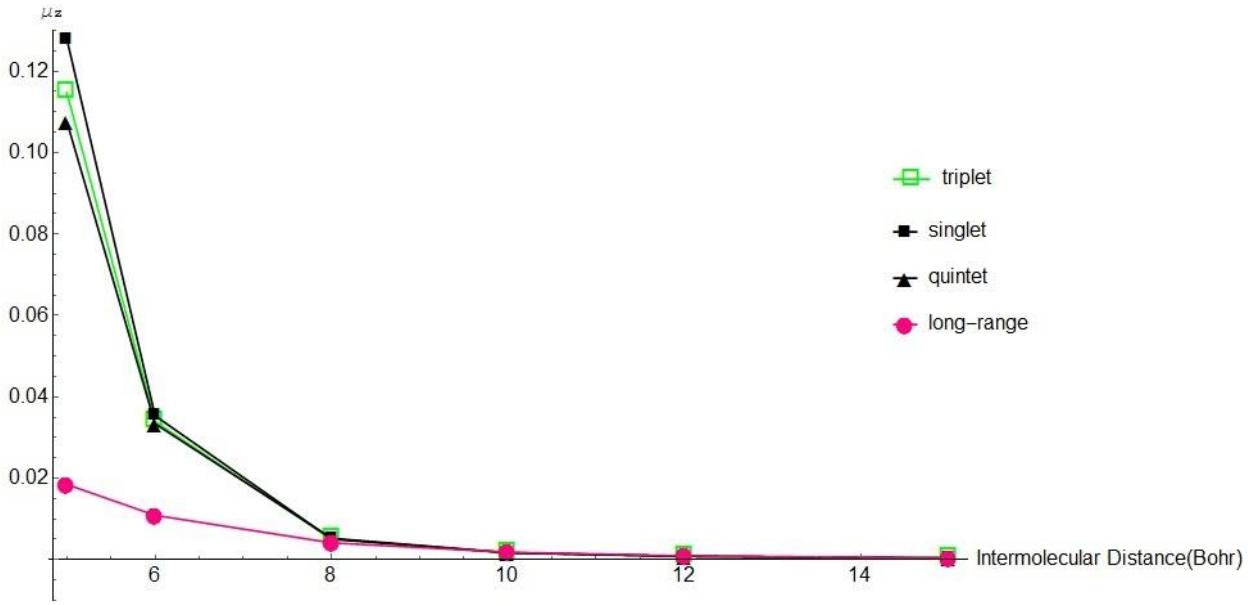

Figure 72. Comparison of dipole moments as a function of intermolecular distance (R) for the 60-0-0-0 geometry, with r=2 bohr for O_2^B. The dipole moment has atomic units, ea_0.

The previous trends in the data hold here again. We note that at this geometry, the dipoles have the same overall trends as those for the T-shape geometry, but at least for the *ab initio* values, are almost twice as large as the T-shape values.

In Figure (73), the z-component of the dipole moment versus the intermolecular distance is given for the 60-0-0-0 geometry with monomer A at the O_2 equilibrium bond length (r=2.28187 bohr), and monomer B very near equilibrium, at r=2.296 bohr.

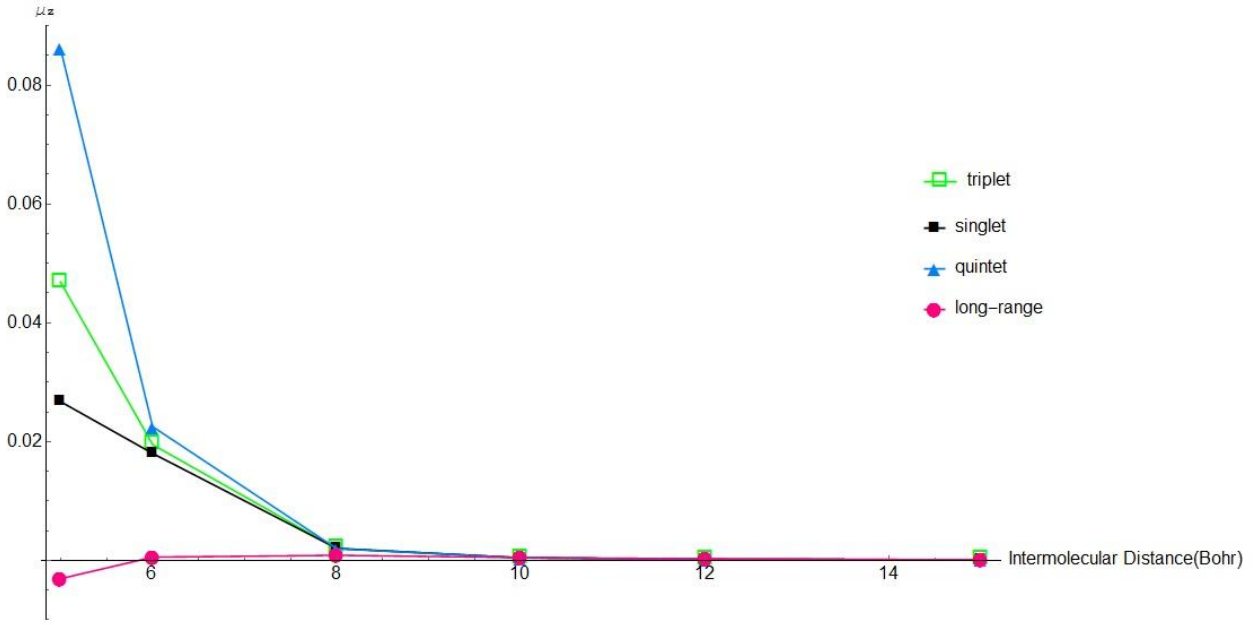

Figure 73. Comparison of dipole moments as a function of intermolecular distance (R) for the 60-0-0-0 geometry, with r=2.296 bohr for O_2^B. The dipole moment has atomic units, ea_0.

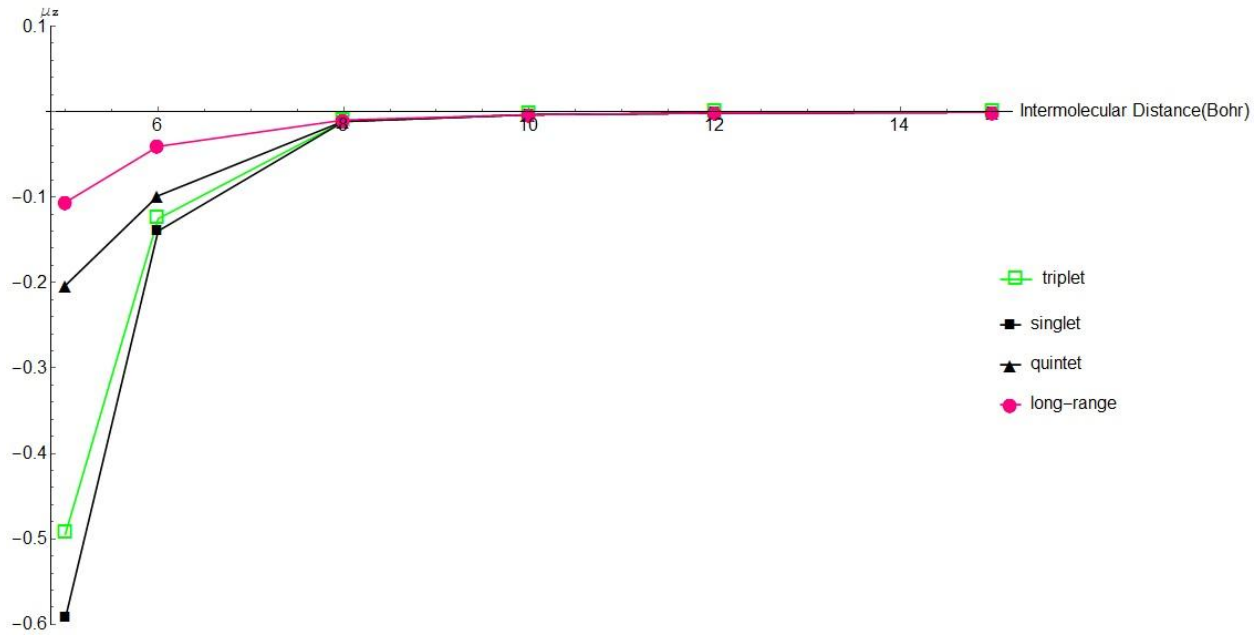

Figure 74. Comparison of dipole moments as a function of intermolecular distance (R) for the 60-0-0-0 geometry, with r=3.3 bohr for O_2^B. The dipole moment has atomic units, ea_0.

Figure (74) shows the dipole moments for the 60-0-0-0 conformation but with monomer B at the longest bond distance considered, 3.3 bohr. The dipoles are about five times larger than they were when monomer B was constricted below the equilibrium bond length at r=2 bohr.

We now turn to our first geometry that was obtained *ab initio* with a C_1 symmetry point group (the point group containing only the identity element, *E*). The angles for this geometry are 105-0-60-60 and no higher symmetry can be imposed. Figure (75) shows the dipole moments obtained for this geometry with the bond distance of monomer B constricted to r=2 bohr.

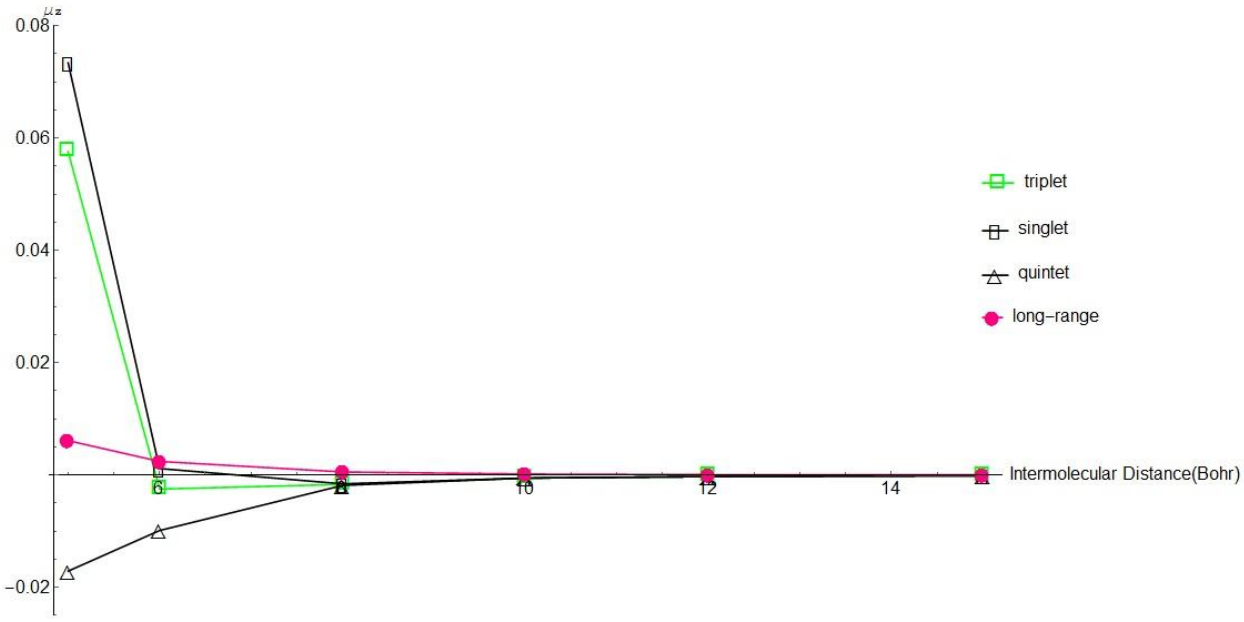

Figure 75. Comparison of dipole moments as a function of intermolecular distance (R) for the 105-0-60-60 geometry, with r=2 bohr for O_2^B. The dipole moment has atomic units, ea_0.

For this geometry and bond distance, the previously observed trends hold, except the long-range value at R=6 bohr is closer to the value for the singlet and triplet states than the value for the

quintet state. The separation in values starts at R=8 bohr here, with more separation at 6 bohr and then the largest differences at the shortest distance (R=5), compared with all previous data.

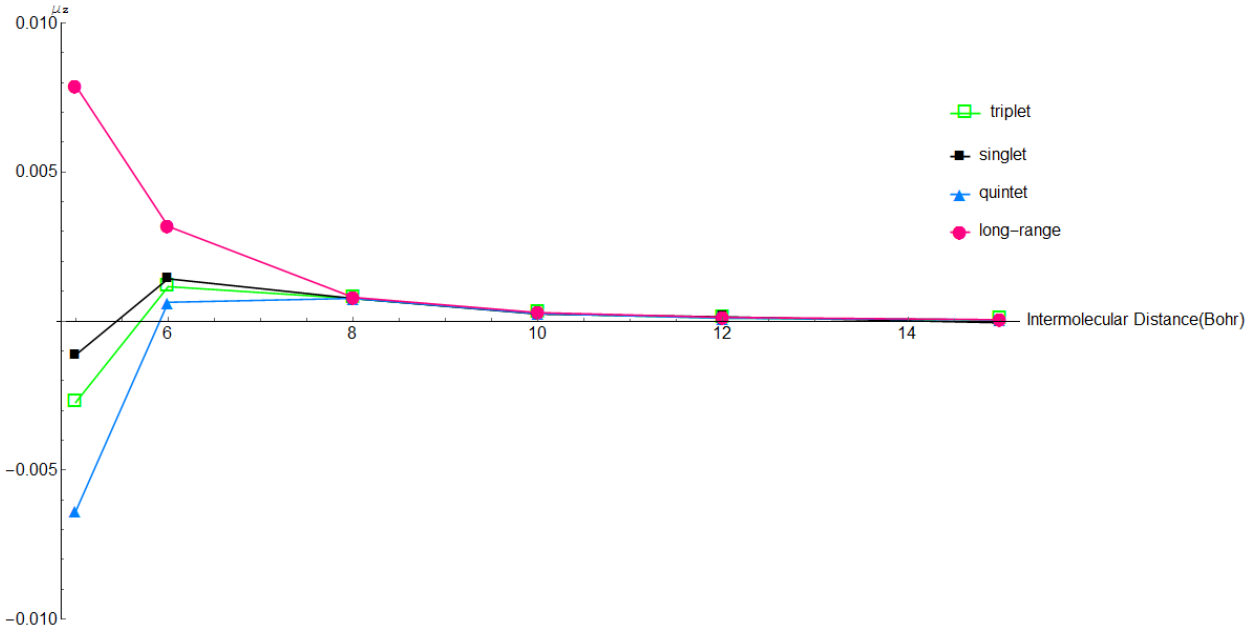

Figure 76. Comparison of dipole moments as a function of intermolecular distance (R) for the 105-0-60-60 geometry, with r=r_{eq} for O_2^B. The dipole moment has atomic units, ea_0.

Figure (76) shows the dipole moments obtained for the geometry with angles 105-0-60-60 when both monomers are at the equilibrium bond length of r=2.28187 bohr. Here, the long-range dipole is actually larger in magnitude than the *ab initio* dipoles at near range. Out of the three dipoles calculated *ab initio* at R=5 bohr, the quintet state dipole is largest in magnitude.

In Figure (77), we compare the z-components of the dipole moment for the 105-0-60-60 geometry, but with monomer B at r=3.3 bohr. For this distance, the values at R=8 bohr are in better agreement than they were with monomer B constricted to r=2 bohr, and there is not much

separation until R=6 bohr. One difference from previous trends here is that the *ab initio* values are closer to that of the triplet state values than to the quintet state values, and this is most clearly seen at R=5 bohr.

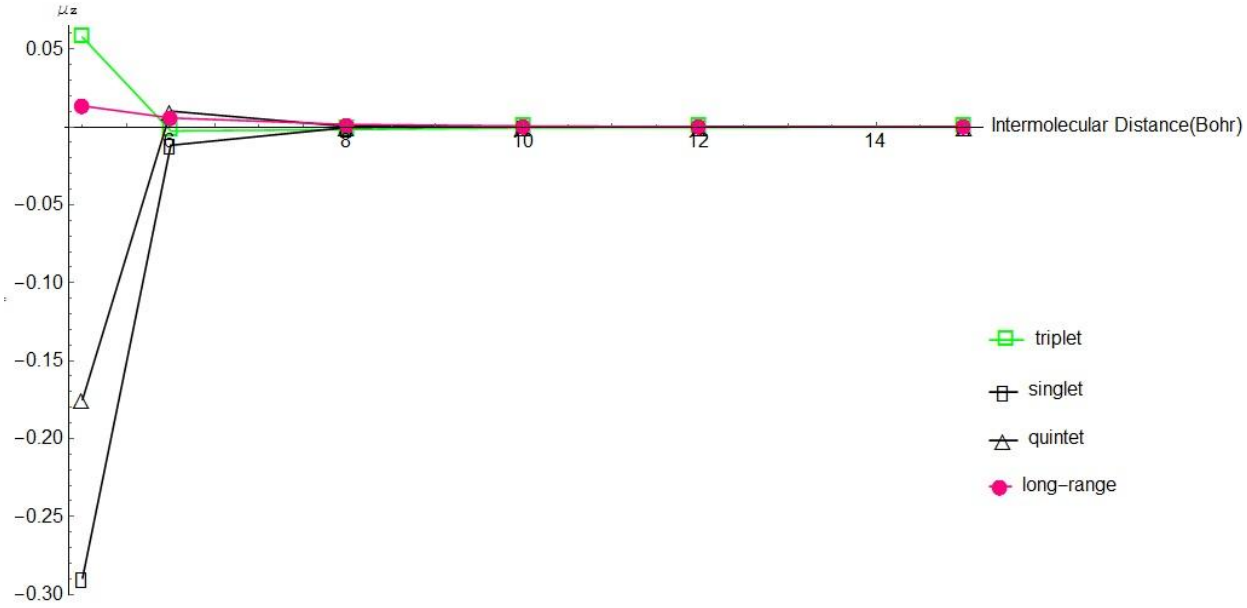

Figure 77. Comparison of dipole moments as a function of intermolecular distance (R) for the 105-0-60-60 geometry, with r=3.3 bohr for O_2^B. The dipole moment has atomic units, ea_0.

The next geometry we examine is that with angles 40-0-115-45. This again is a C_1 point group symmetry arrangement. Figure (78) shows the dipoles at this geometry with monomer B at the most constricted bond length.

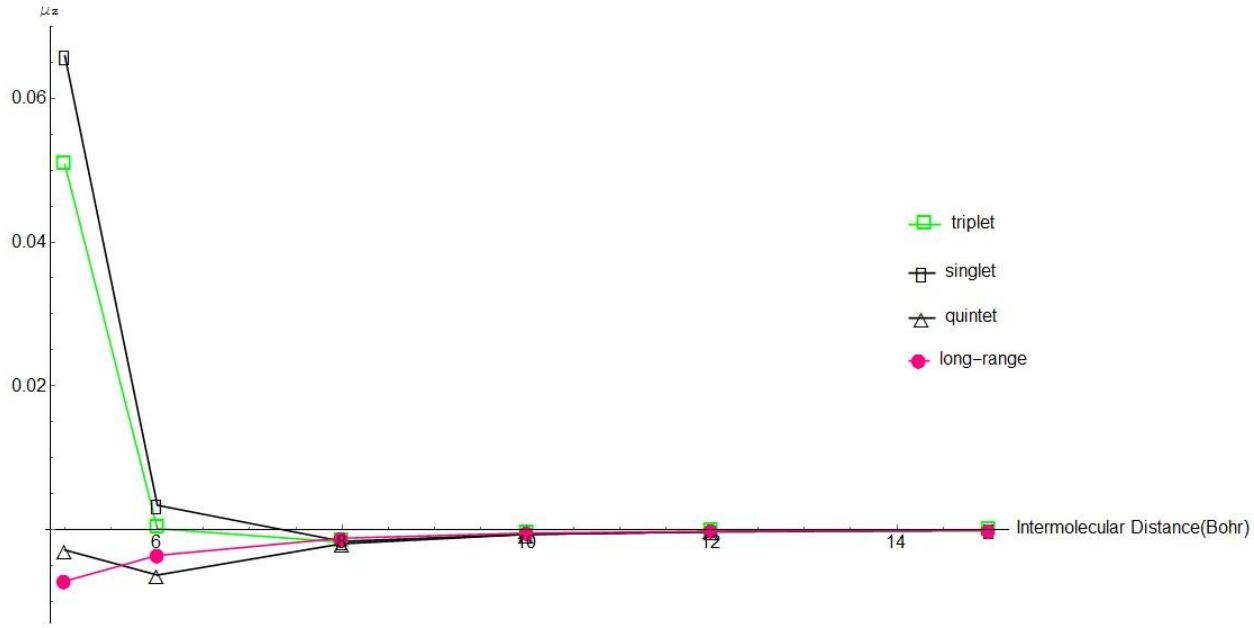

Figure 78 . Comparison of dipole moments as a function of intermolecular distance (R) for the 40-0-115-45 geometry, with r=2 bohr for O_2^B. The dipole moment has atomic units, ea_0.

In Figure (78), we see that all previous observed trends are seen here again.

Figure (79) shows the data for this geometry with both monomers at equilibrium. In this case, all three *ab initio* values are in good agreement for the entire curve, and the *ab initio* as well as long-range values show the same trends, curving downward (becoming more negative) the shorter R becomes, though the long-range values become less negative than the *ab initio* values. This is presumably due to the neglect of short range effects in the interaction.

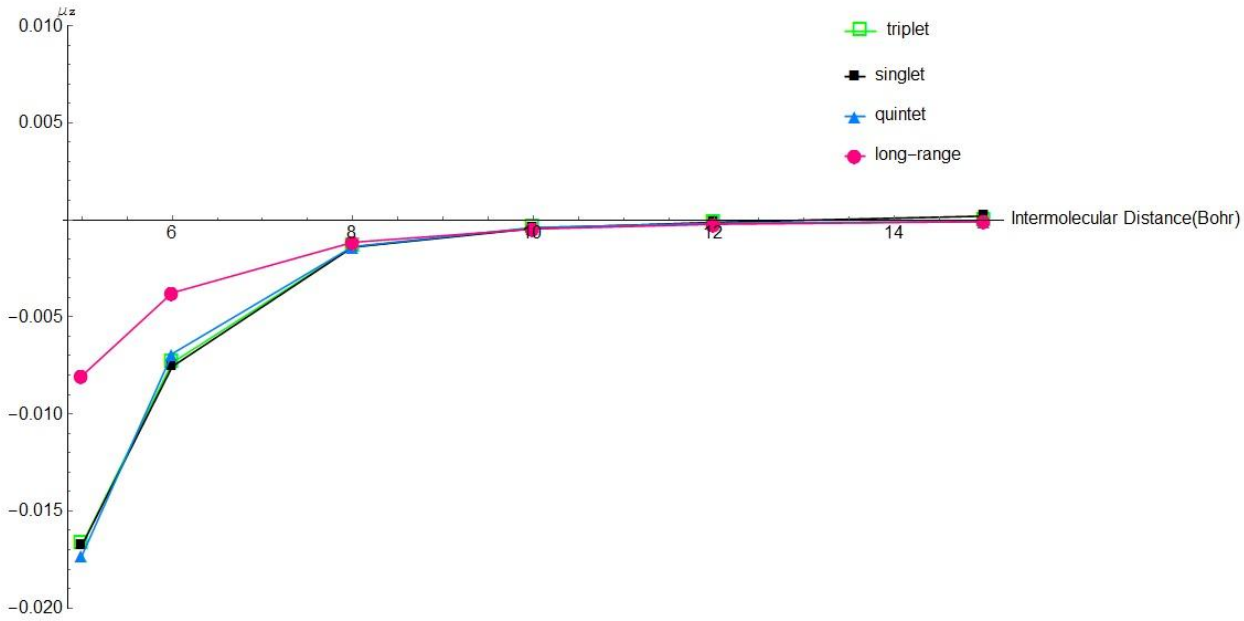

Figure 79. Comparison of dipole moments as a function of intermolecular distance (R) for the 40-0-115-45 geometry, with r=r_{eq} for O_2^B. The dipole moment has atomic units, ea_0.

Figure (80) shows the values for the dipoles at this geometry when the bond distance for monomer B is longest. Previous trends are seen here again, and there is no strange behavior at R=15 bohr as there was for the data with the constricted monomer B bond distance.

Figure 80. Comparison of dipole moments as a function of intermolecular distance (R) for the 40-0-115-45 geometry, with r=3.3 bohr for O_2^B. The dipole moment has atomic units, ea_0.

The next geometry we compare values for has angles 20-0-115-45, similar to our last geometry.

Figure (81) shows the dipoles obtained when monomer B is constricted to r=2 bohr.

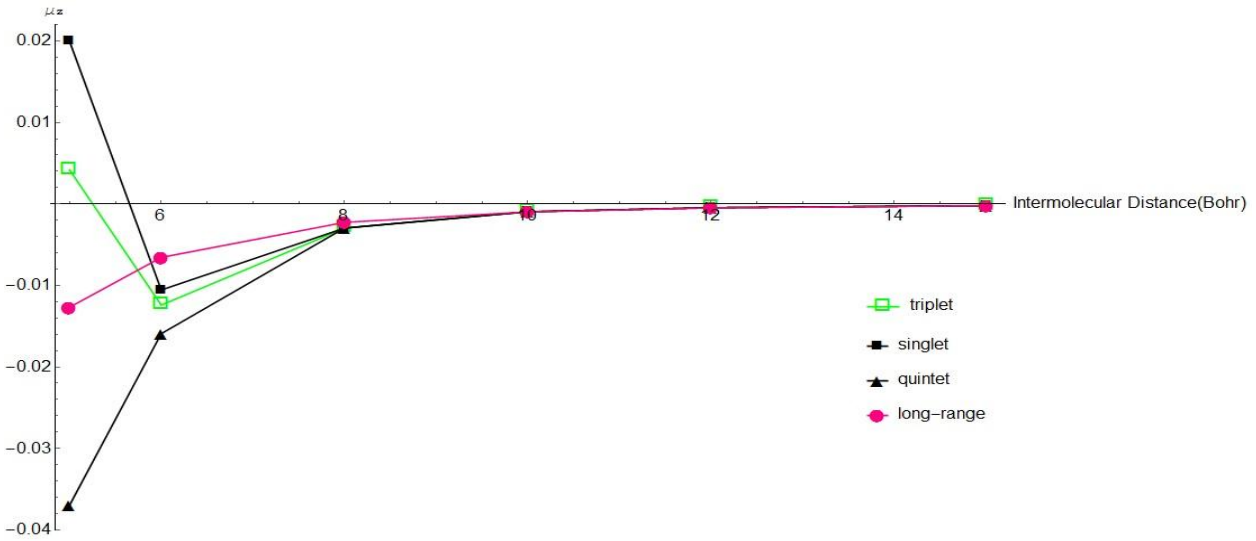

Figure 81. Comparison of dipole moments as a function of intermolecular distance (R) for the 20-0-115-45 geometry, with r=2 bohr for O_2^B. The dipole moment has atomic units, ea_0.

For this geometry and these bond distances, the quintet state is largest in magnitude, and is about twice as large as the value for the dipole for the singlet state at R=5 bohr. The long-range dipole component is actually closer to that of the singlet and triplet state at intermolecular distances of 5 and 6 bohr, respectively.

The data for the dipole moment for this geometry with both monomers at their equilibrium bond lengths is seen in Figure (82).

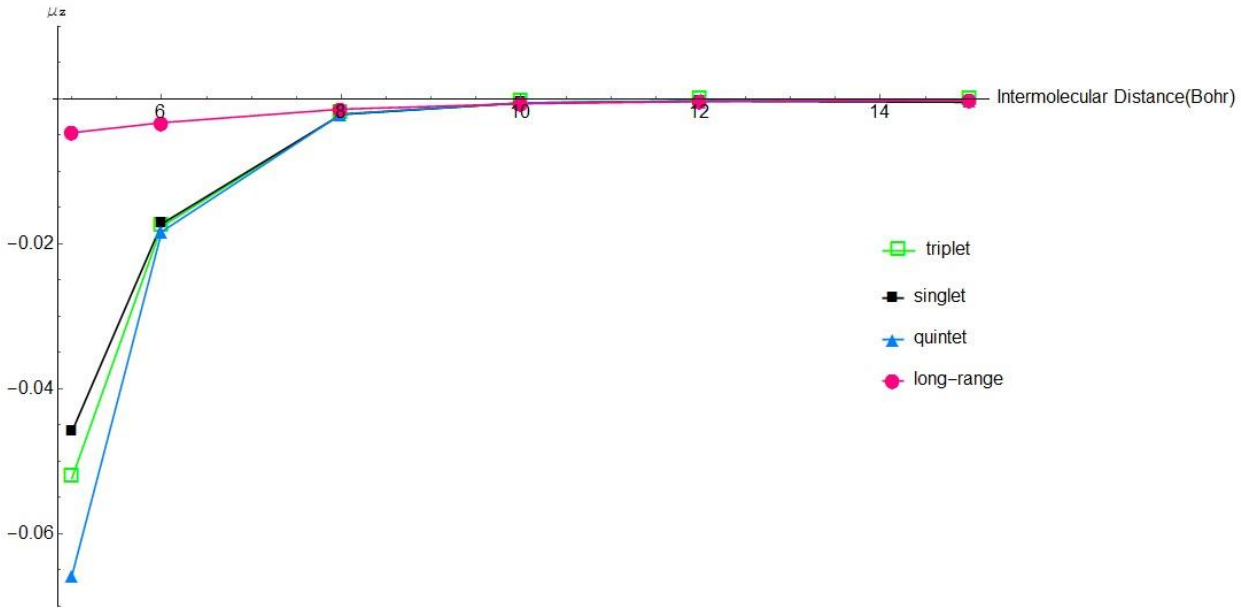

Figure 82 . Comparison of dipole moments as a function of intermolecular distance (R) for the 20-0-115-45 geometry, with r=r_{eq} for O_2^B. The dipole moment has atomic units, ea_0.

Here there is very little difference between the three *ab initio* values until an intermolecular distance of R=5 bohr. As seen for most of the previous data, the *ab initio* and long-range data are in good agreement for intermolecular distances of R=8,10,12, and 15 bohr.

The last figure for this geometry, with monomer B at the longest bond distance, is Figure (83).

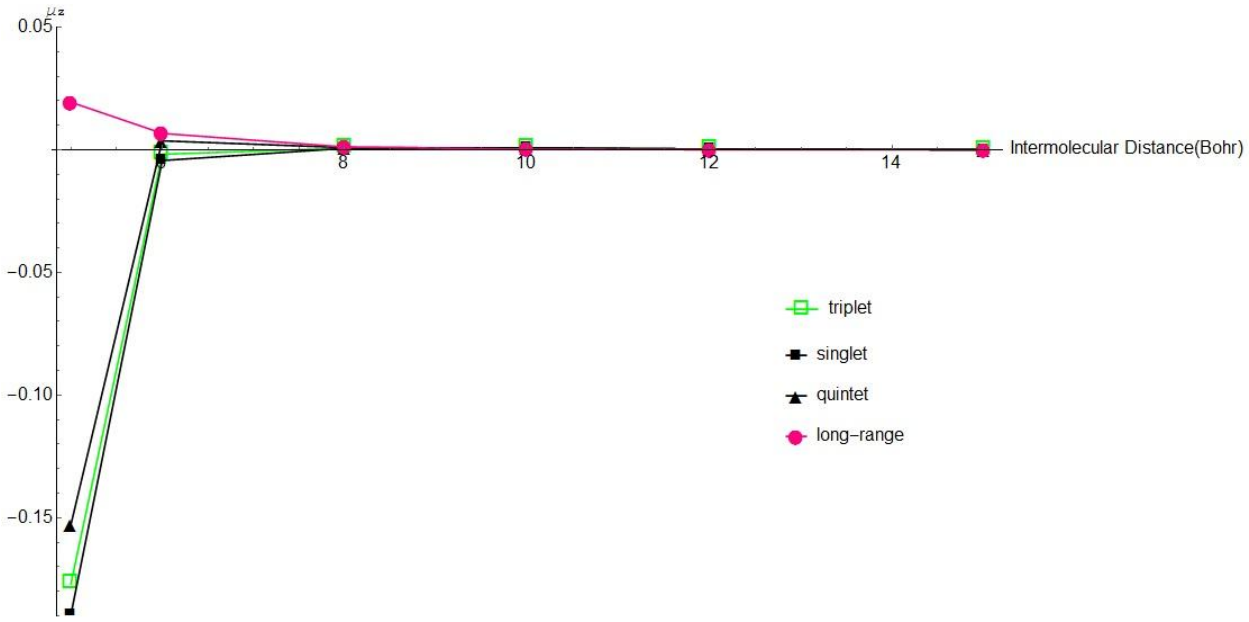

Figure 83 . Comparison of dipole moments as a function of intermolecular distance (R) for the 20-0-115-45 geometry, with r=3.3 bohr for O_2^B. The dipole moment has atomic units, ea_0.

It can be seen from this figure that the *ab initio* values become steeply negative when the molecules are five bohr apart, while the long-range value changes very little.

The next geometry discussed is again of C_1 symmetry, with angles 15-0-75-30. Figure (84) shows the dipole moments when monomer B is most constricted.

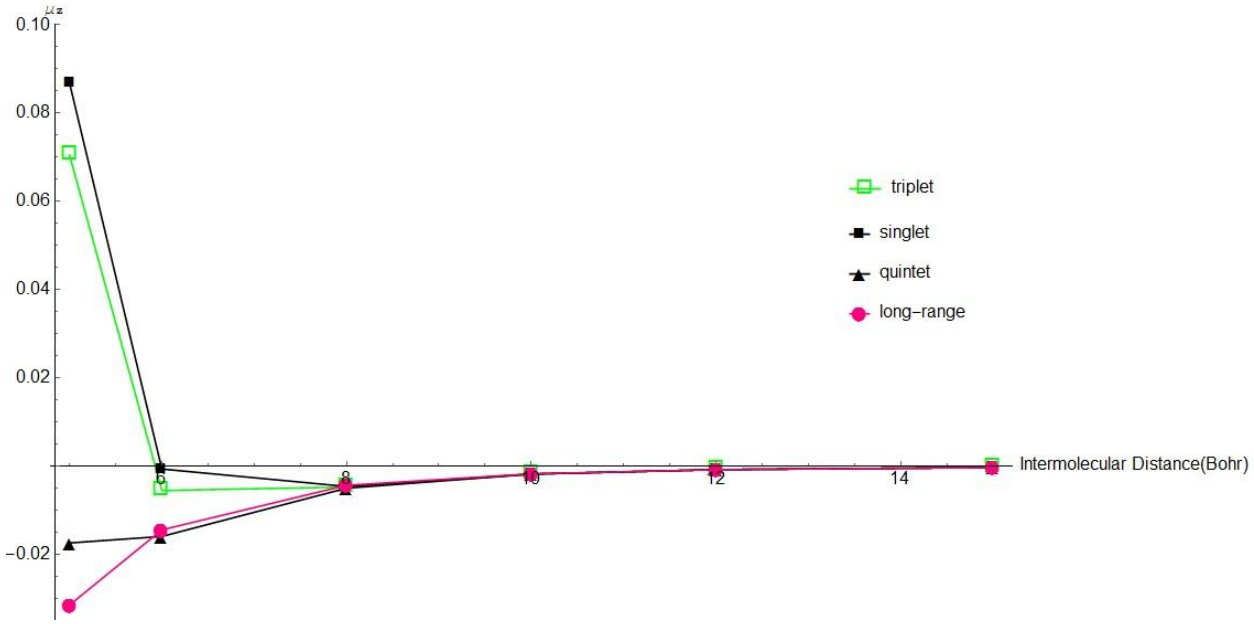

Figure 84. Comparison of dipole moments as a function of intermolecular distance (R) for the 15-0-75-30 geometry, with r=2 bohr for O_2^B. The dipole moment has atomic units, ea_0.

These data show no marked deviation from the overwhelming trends, with the singlet spin state having the largest dipole moment.

In Figure (85), we view the dipole moments for this geometry with both monomers at equilibrium. Again, there is no deviation from previous trends.

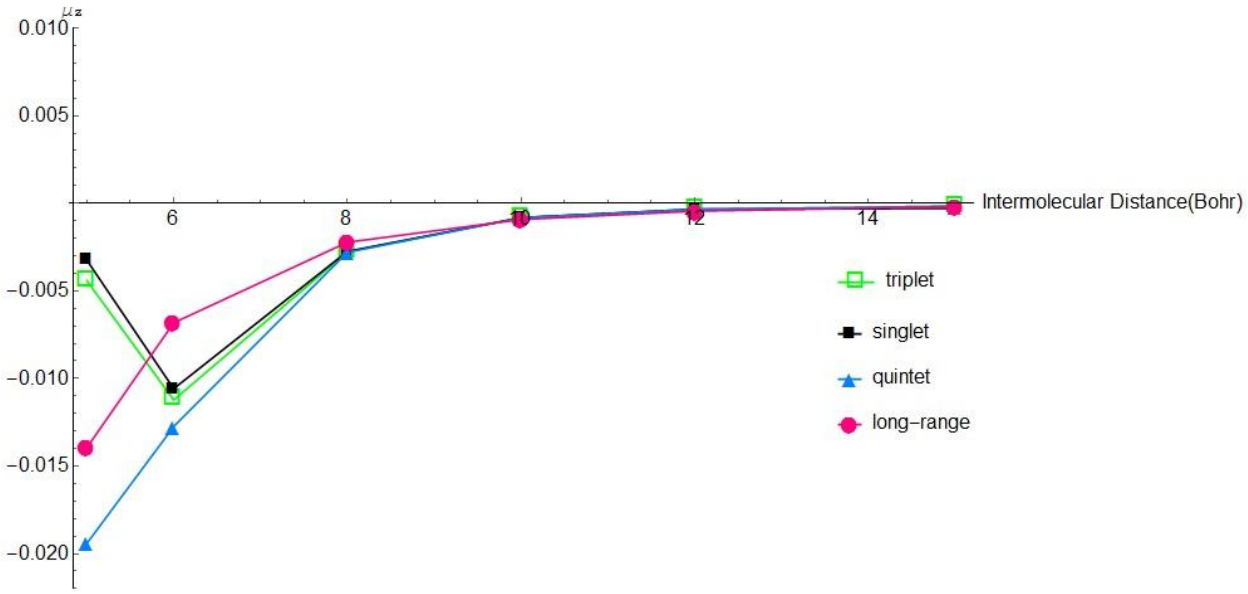

Figure 85. Comparison of dipole moments as a function of intermolecular distance (R) for the 15-0-75-30 geometry, with r=r_{eq} for O_2^B. The dipole moment has atomic units, ea_0.

Finally, we discuss the data for this geometry with monomer B at r=3.3 bohr in Figure (86).

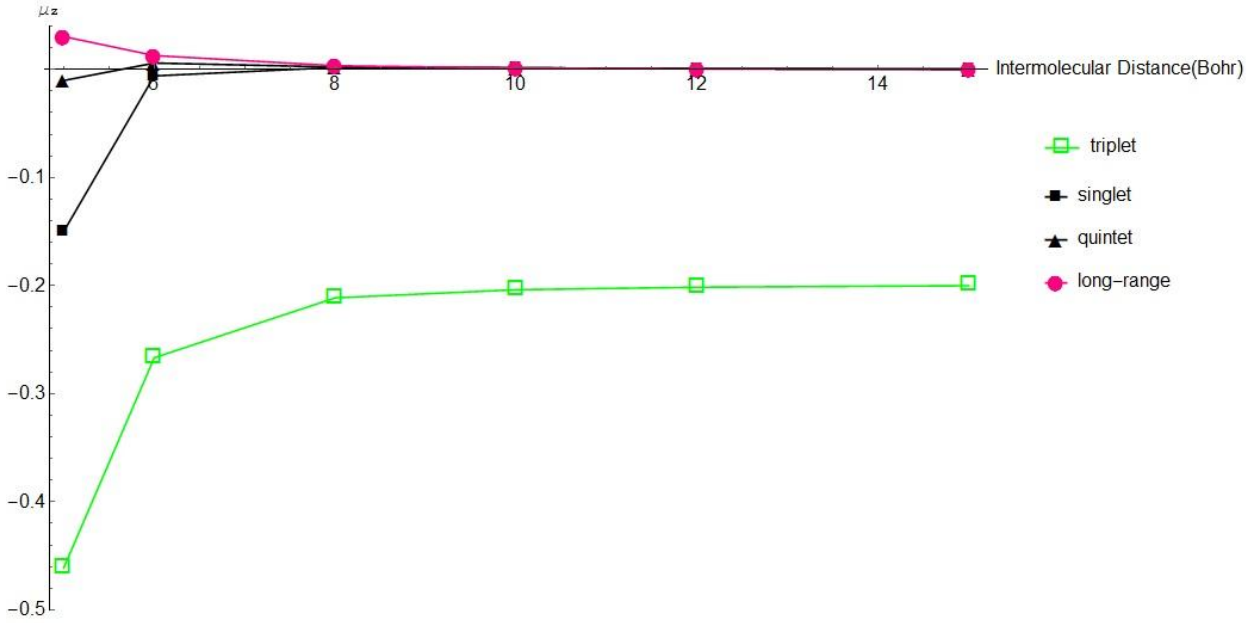

Figure 86. Comparison of dipole moments as a function of intermolecular distance (R) for the 15-0-75-30 geometry, with r=3.3 bohr for O_2^B. The dipole moment has atomic units, ea_0.

Here, there is a significant difference from past behavior seen for this geometry or any others. The *ab initio* triplet state data, though displaying the same overall behavior as the data for the other two spin states, is significantly separated from the other *ab initio* data and the long-range dipole, and is additionally largest in magnitude.

The next geometry keeps monomer A at the same angles (θ=15°, φ=0°), but changes the orientation of monomer B, for an overall geometry with angles 15-0-95-10. The data for monomer B at the most constricted bond length are shown in Figure (87).

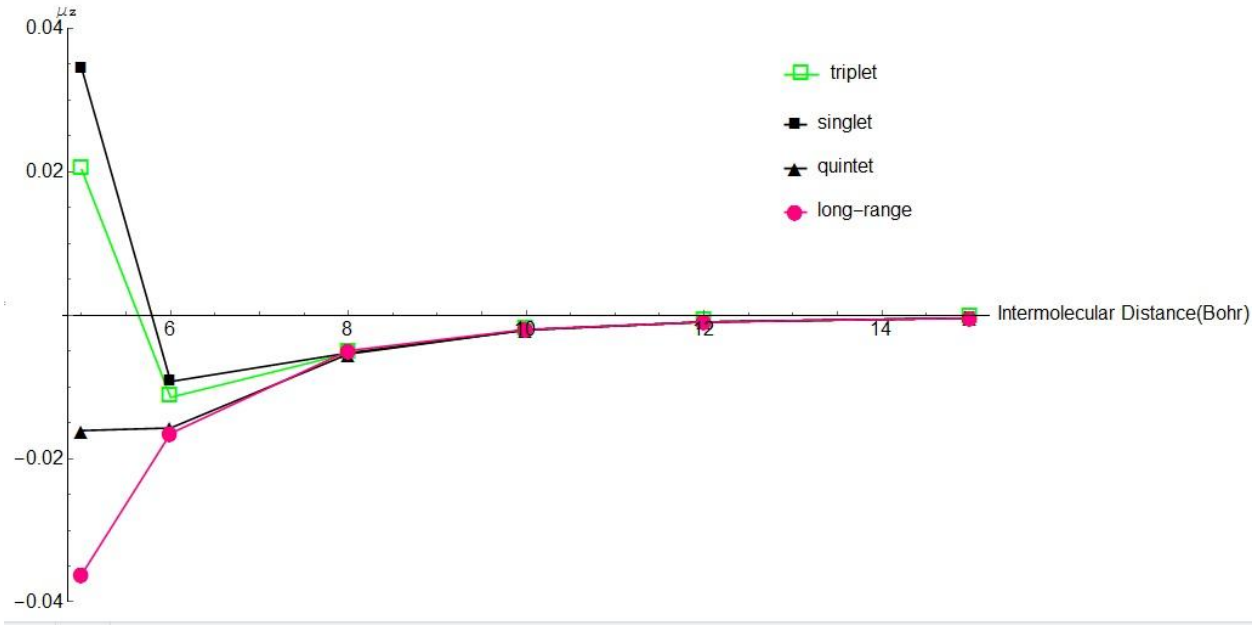

Figure 87. Comparison of dipole moments as a function of intermolecular distance (R) for the 15-0-95-10 geometry, with r=2 bohr for O_2^B. The dipole moment has atomic units, ea_0.

This figure shows very little difference from previously observed trends.

Figure (88) shows the z-component of the dipole moment for this geometry when both monomers are at equilibrium.

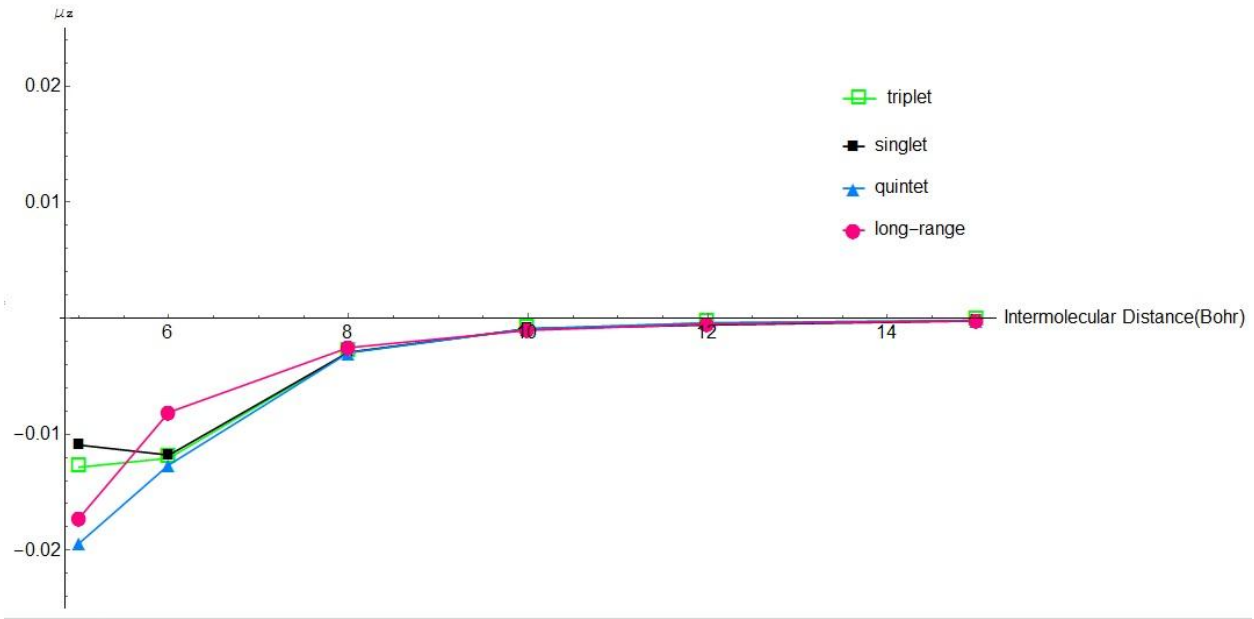

Figure 88. Comparison of dipole moments as a function of intermolecular distance (R) for the 15-0-95-10 geometry, with r=r_{eq} for O_2^B. The dipole moment has atomic units, ea_0.

This figure shows that the long-range dipole is closer to the singlet and triplet state dipoles at R=6 bohr than to the quintet state dipole. When the molecules become closer at R=5 bohr, the long-range dipole reverts to the commonly observed behavior of most closely replicating the quintet state dipole moment.

In Figure (89), we observe the dipole moment when monomer B is at r=3.3 bohr. These data show the same trends as seen previously for other geometries.

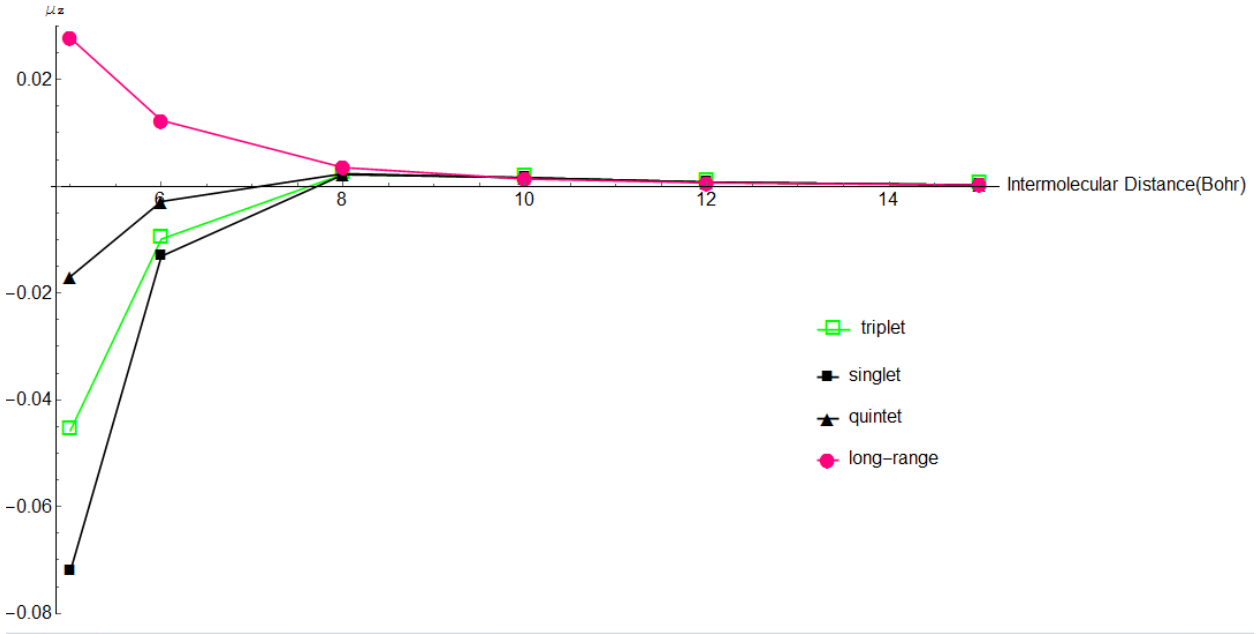

Figure 89. Comparison of dipole moments as a function of intermolecular distance (R) for the 15-0-95-10 geometry, with r=3.3 bohr for O_2^B. The dipole moment has atomic units, ea_0.

The next geometry we discuss is another C_1 symmetry point group conformation, with angles 10-0-160-15. Figure (90) shows the z-components of the dipole moment for this geometry, with monomer B constricted shorter than equilibrium to r=2 bohr.

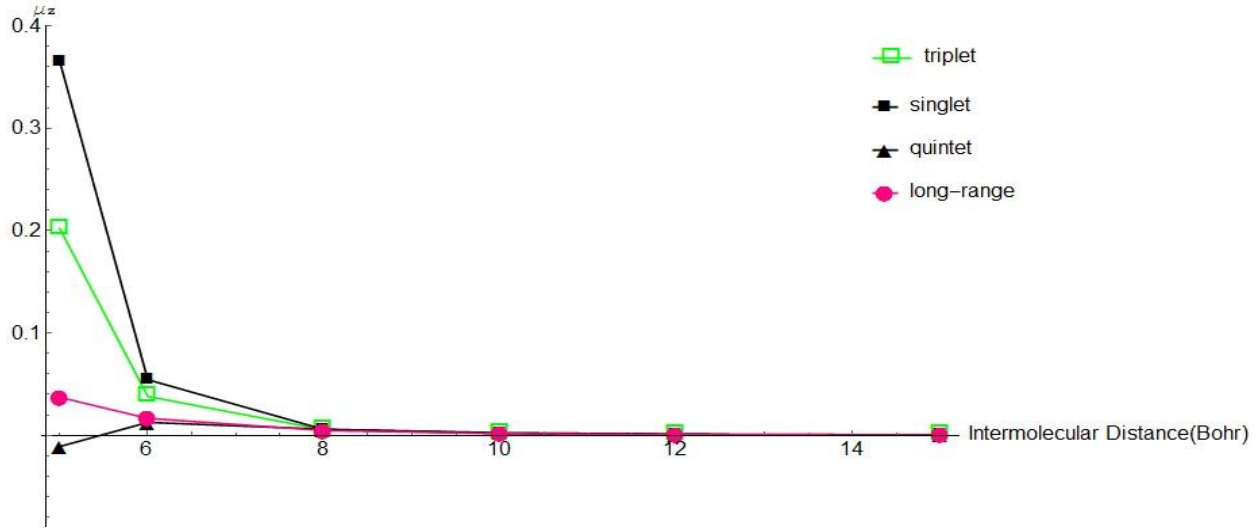

Figure (90). Comparison of dipole moments as a function of intermolecular distance (R) for the 10-0-160-15 geometry, with r=2 bohr for O_2^B. The dipole moment has atomic units, ea_0.

This geometry possesses dipole moments that are larger than those for the last few geometries discussed.

Figure (91) shows the dipoles for the same geometry but with both monomers at their equilibrium bond distances.

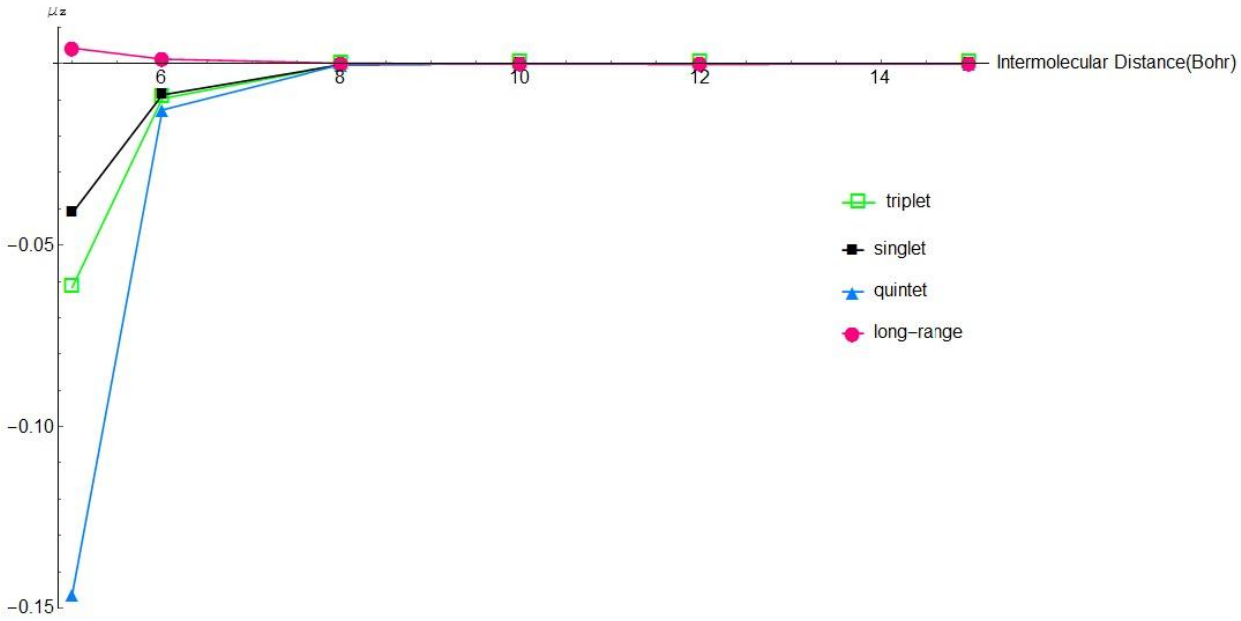

Figure (91). Comparison of dipole moments as a function of intermolecular distance (R) for the 10-0-160-15 geometry, with r=r_{eq} for O_2^B. The dipole moment has atomic units, ea_0.

Unlike most of the previous cases we have examined, for this geometry the quintet spin state possesses the largest magnitude of the z-component of the dipole moment.

In Figure (92), we examine the z-component of the dipole moment for the geometry with angles 10-0-160-15, with the bond distance of monomer B at r=3.3 bohr.

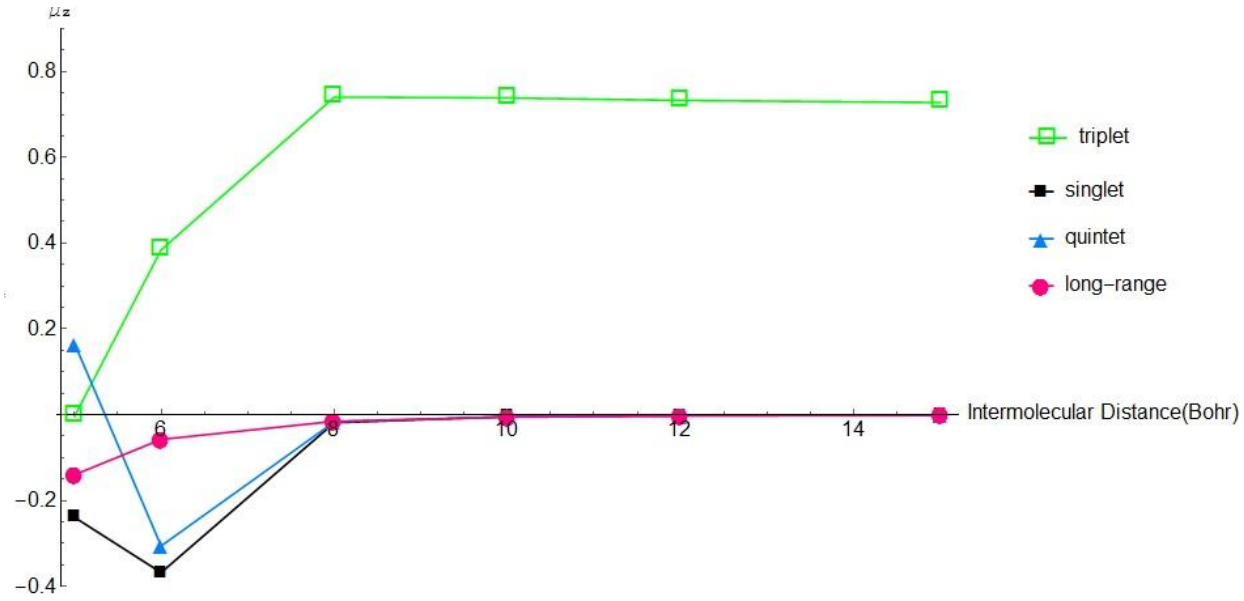

Figure 92. Comparison of dipole moments as a function of intermolecular distance (R) for the 10-0-160-15 geometry, with r=3.3 bohr for O_2^B. The dipole moment has atomic units, ea_0.

As with Figure (86), which displays the dipole moment for a geometry with angles 15-0-75-30, and for monomer B at the bond distance of r=3.3 bohr, the triplet spin state dipole moment is well separated from the singlet and quintet spin state *ab initio* dipoles, as well as from the long-range dipole.

Figure (93) shows the z-component of the dipole moment for the geometry given by the angles 20-0-145-25, with monomer B's bond length at r=2 bohr.

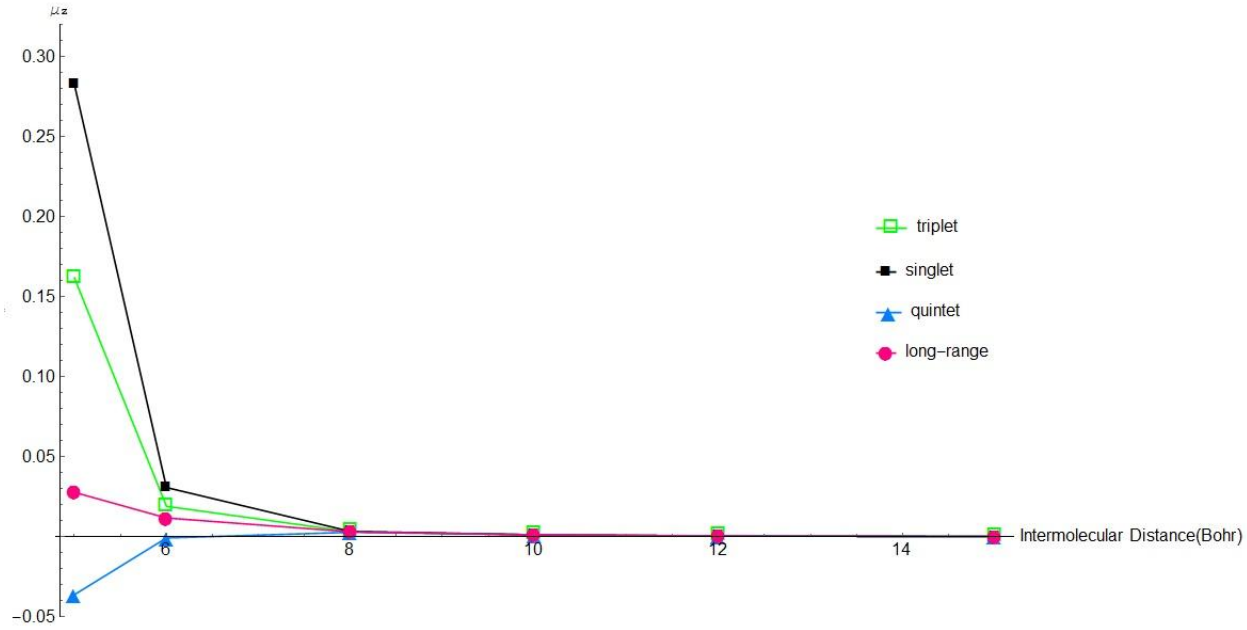

Figure 93. Comparison of dipole moments as a function of intermolecular distance (R) for the 20-0-145-25 geometry, with r=2 bohr for O_2^B. The dipole moment has atomic units, ea_0.

Previous trends are observed here, with the singlet state having the largest magnitude of dipole moment, and the long-range data most closely resembling the quintet state *ab initio* dipole.

Figure (94) shows the same data but for both O_2 molecules at the equilibrium bond distance of 2.28187 bohr. In this figure, we see that the *ab initio* quintet spin state dipole moment is now largest in magnitude. In addition, the long-range dipole moment most closely resembles the singlet state, both in magnitude and behavior.

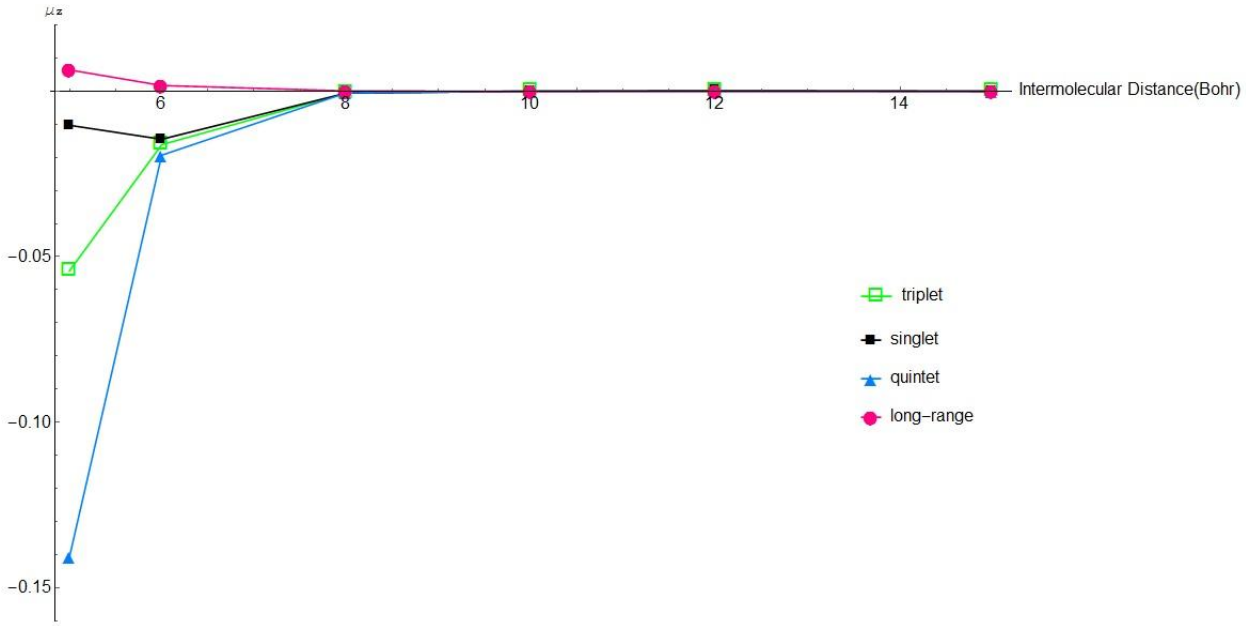

Figure 94. Comparison of dipole moments as a function of intermolecular distance (R) for the 20-0-145-25 geometry, with r=r_{eq} for O_2^B. The dipole moment has atomic units, ea_0.

The dipole moments for this geometry and the situation in which monomer A is at its equilibrium bond distance and monomer B is at a bond distance of 3.3 bohr are shown in Figure (95). As the two molecules approach, the difference between the *ab initio* and long-range data becomes more stark than in some previous geometries, with differences of over 100% between the dipole moments obtained from the two methods at an intermolecular distance of R=6 bohr.

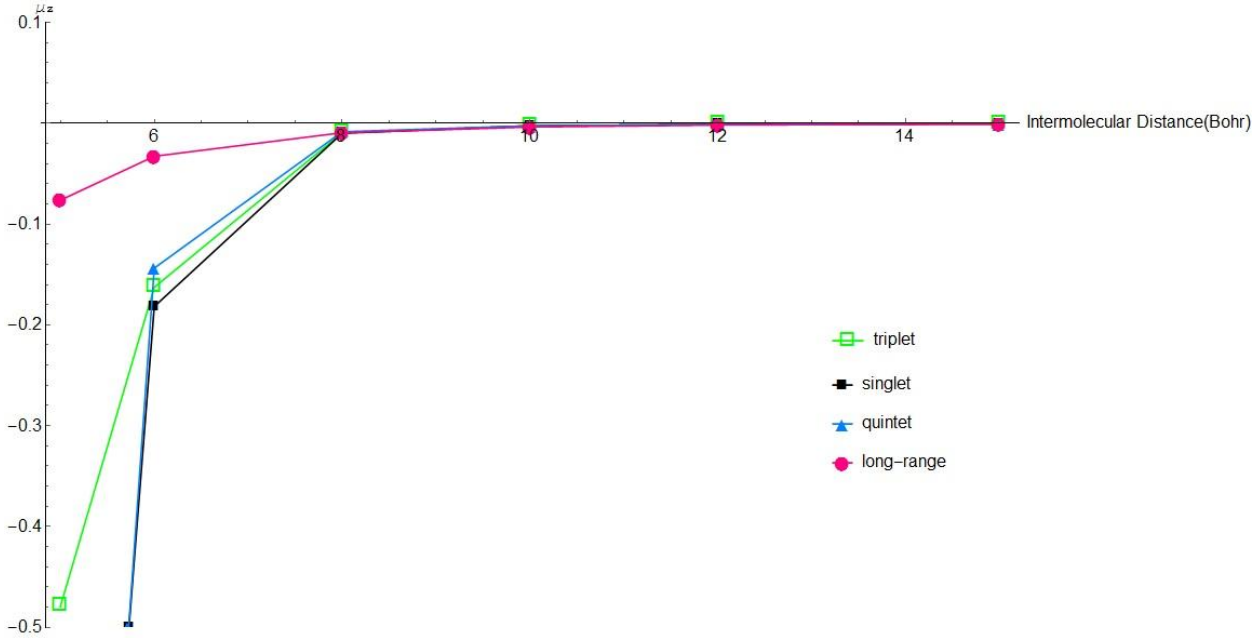

Figure 95. Comparison of dipole moments as a function of intermolecular distance (R) for the 20-0-145-25 geometry, with r=3.3 bohr for O_2^B. The dipole moment has atomic units, ea_0.

Figure (96) shows the dipole moments calculated for the geometry with angles 30-0-130-35. Monomer B has been fixed at the constricted bond distance of 2 bohr. The *ab initio* dipoles calculated for the singlet spin state are largest in magnitude for this geometry and these bond lengths. As with most previous cases, the long-range approximation is valid up to an intermolecular separation of 8 bohr.

The next figure shows the z-component of the dipole moment for the same geometry, but with both monomers at the equilibrium bond distance, r=2.28187 bohr. When both monomers are at equilibrium, the *ab initio* dipole moment calculated for the quintet state is largest in magnitude.

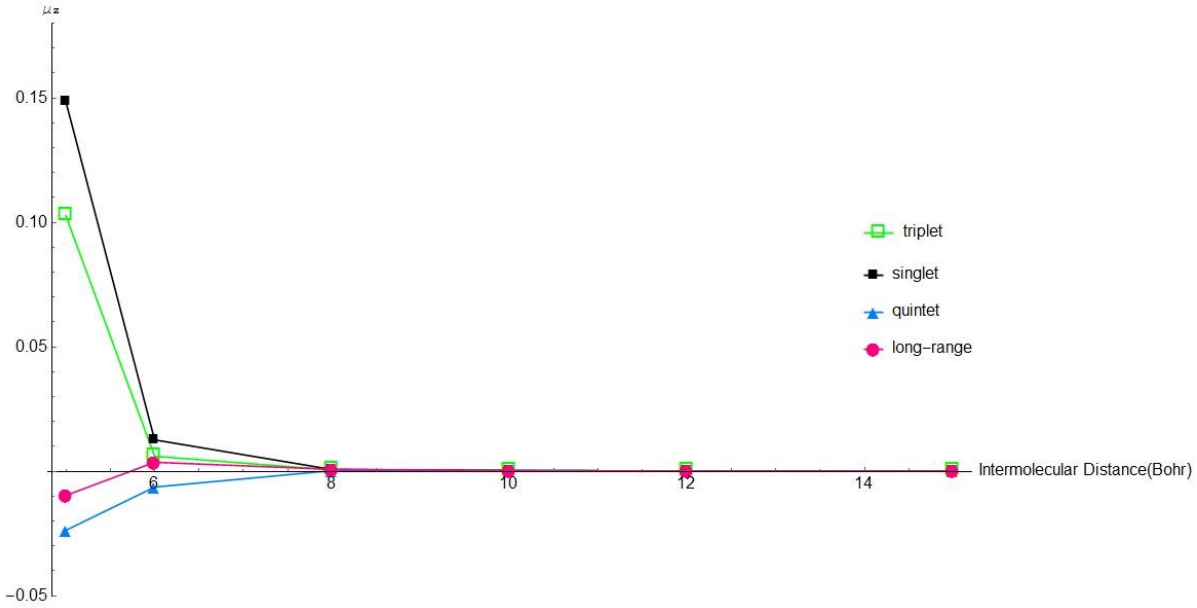

Figure 96. Comparison of dipole moments as a function of intermolecular distance (R) for the 30-0-135-35 geometry, with r=2 bohr for O_2^B. The dipole moment has atomic units, ea_0.

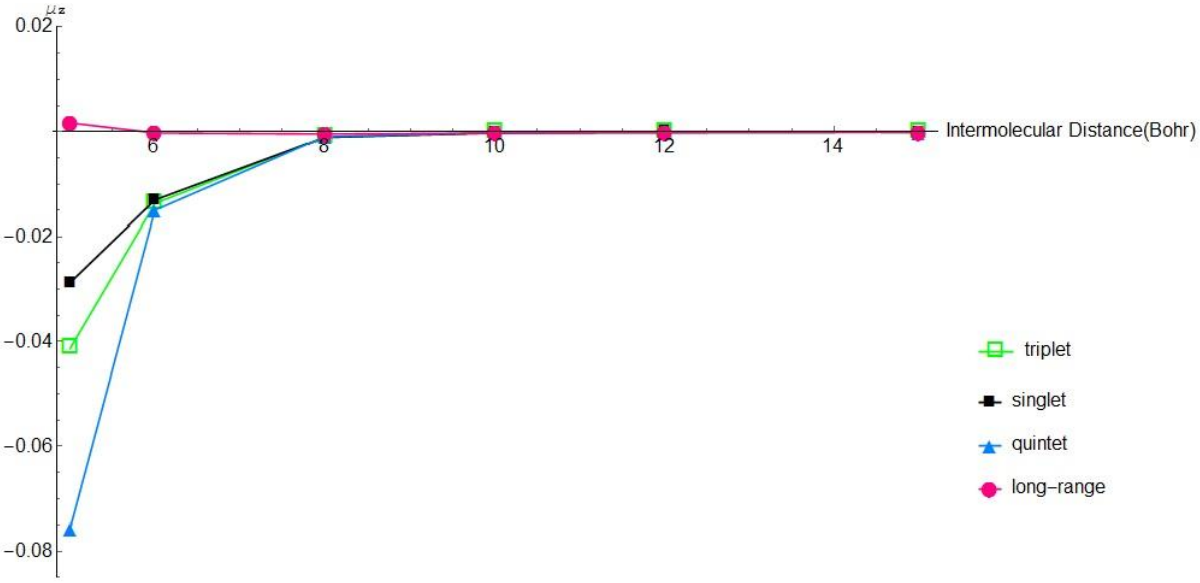

Figure 97. Comparison of dipole moments as a function of intermolecular distance (R) for the 30-0-135-35 geometry, with r=r_{eq} for O_2^B. The dipole moment has atomic units, ea_0.

Figure (98) shows the dipole moments for this geometry when monomer B has been stretched past equilibrium to the bond length of 3.3 bohr. The dipole moment calculated for the quintet spin state is slightly larger in magnitude than the magnitude of the dipole for the singlet and triplet states, though all three *ab initio* values are close in magnitude for this geometry and set of bond lengths.

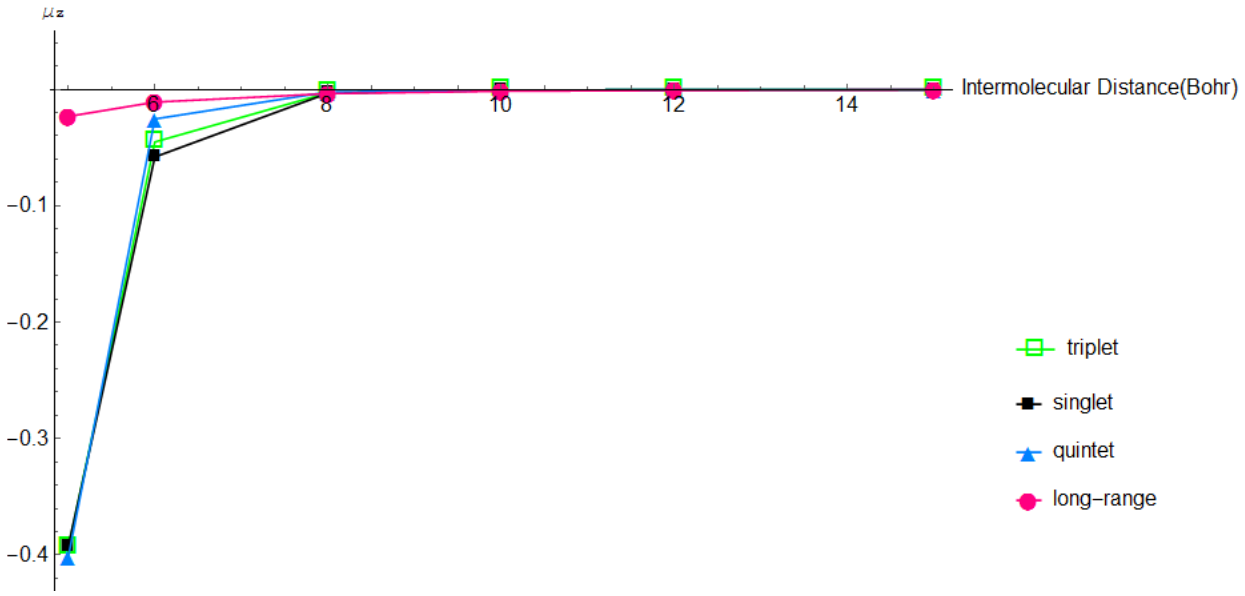

Figure 98. Comparison of dipole moments as a function of intermolecular distance (R) for the 30-0-135-35 geometry, with r=3.3 bohr for O_2^B. The dipole moment has atomic units, ea_0.

We know turn to a geometry that contains one symmetry plane (the reflection plane) and thus has C_s point group symmetry. Figure (99) shows the z-components of the dipoles calculated for this geometry, which has angles of 30-0-60-0. In Figure (99), monomer B is constricted to 2 bohr. Previous trends are observed, with the *ab initio* dipoles calculated for the singlet spin state largest in magnitude.

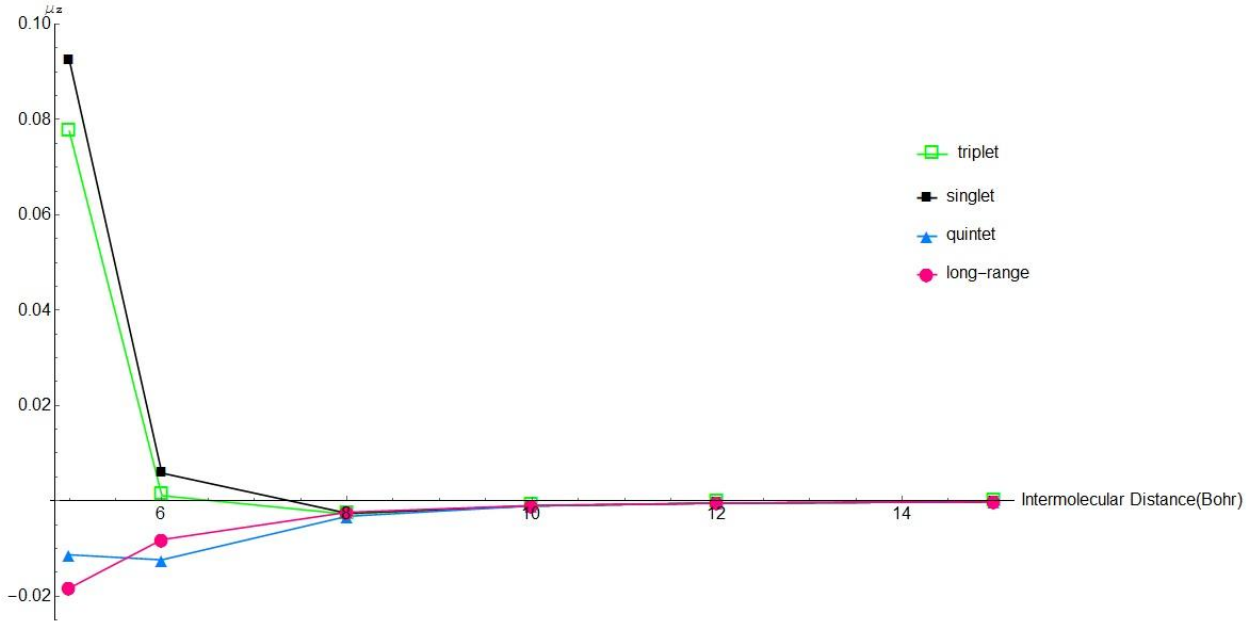

Figure 99. Comparison of dipole moments as a function of intermolecular distance (R) for the 30-0-60-0 geometry, with r=2 bohr for O_2^B. The dipole moment has atomic units, ea_0.

Figure (100) shows the z-component of the dipole moment for the same geometry, but with both monomers at their equilibrium bond distances.

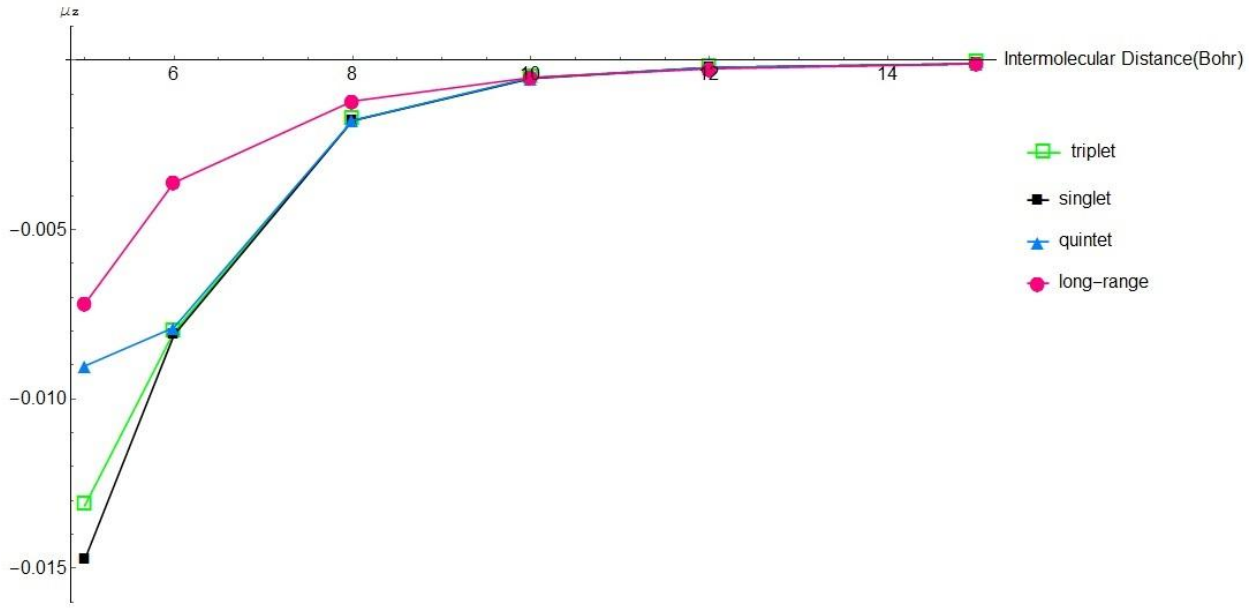

Figure 100. Comparison of dipole moments as a function of intermolecular distance (R) for the 30-0-60-0 geometry, with r=2.296 bohr for O_2^B. The dipole moment has atomic units, ea_0.

In Figure (101), we examine the dipole moments for the geometry with angles 30-0-60-0, and for monomer B at the bond distance of 3.3 bohr. Previous trends are shown here as well, with the singlet state dipole largest in magnitude. However, the *ab initio* dipole moment for the triplet sin state is nearly as large as the singlet state dipole.

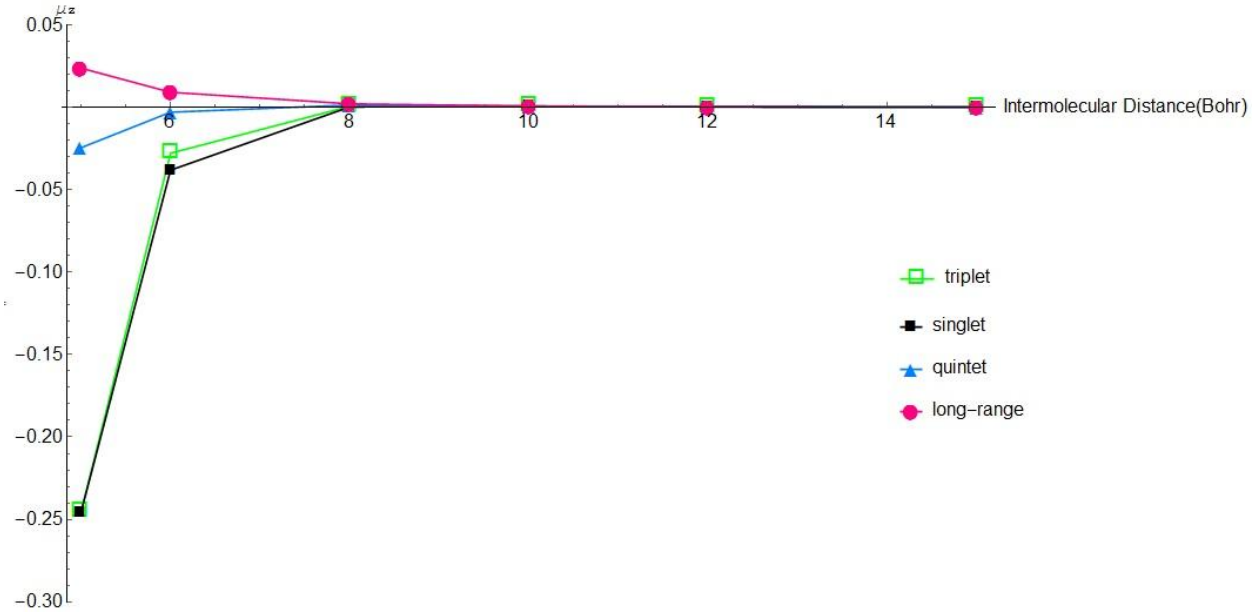

Figure 101. Comparison of dipole moments as a function of intermolecular distance (R) for the 30-0-60-0 geometry, with r=3.3 bohr for O_2^B. The dipole moment has atomic units, ea_0.

The next geometry examined is similar to that we just considered, and has the same point group symmetry. The angles of this geometry are 30-0-90-0. Figure (102) shows the z-component of the dipole moment for this geometry, with the bond distance of monomer B contracted to r=2 bohr. The dipole moments here are quite a bit smaller (about 80%) than the dipole moments for the last geometry.

Figure (103) shows the z-component of the dipole moment for this geometry when each monomer is fixed at its equilibrium bond distance.

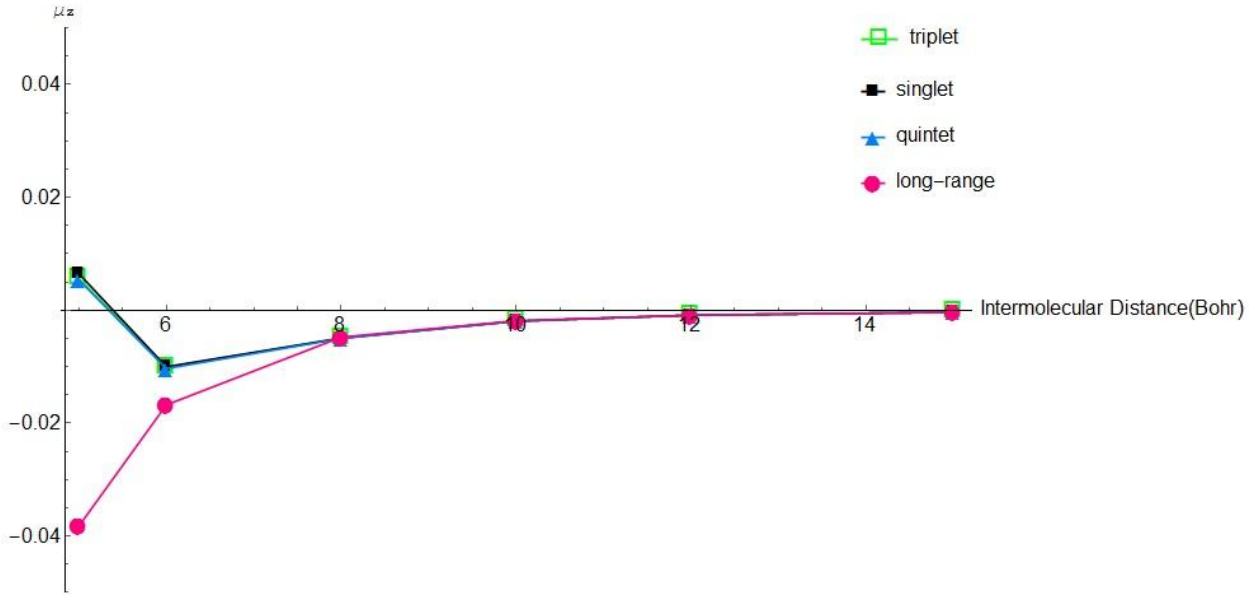

Figure 102. Comparison of dipole moments as a function of intermolecular distance (R) for the 30-0-90-0 geometry, with r=2 bohr for O_2^B. The dipole moment has atomic units, ea_0.

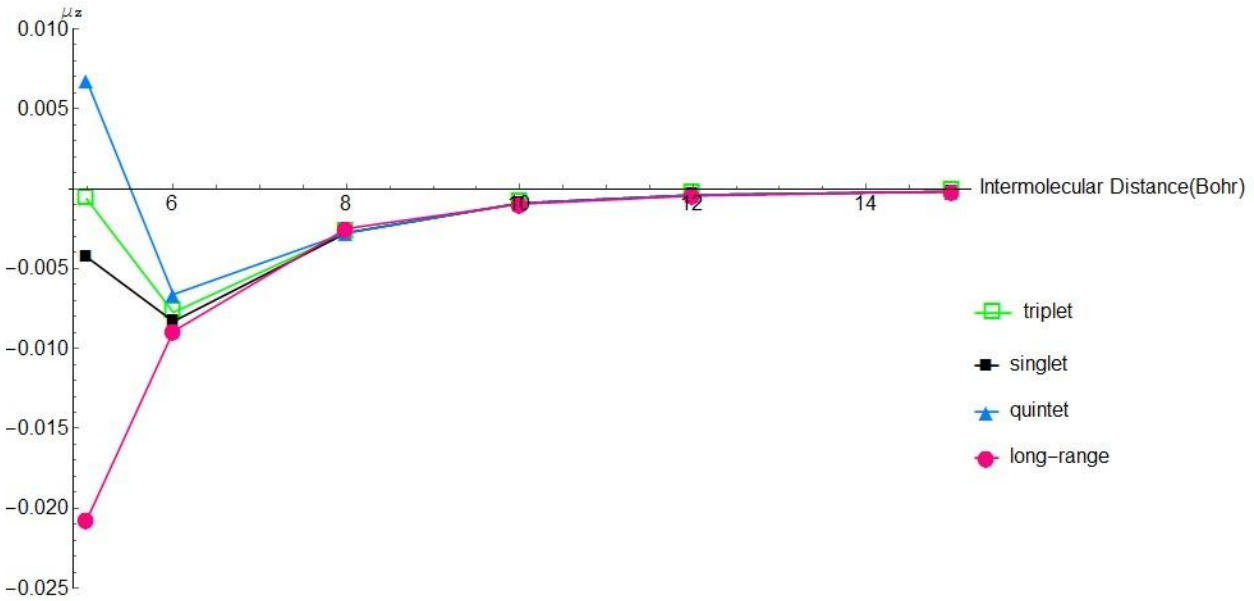

Figure 103. Comparison of dipole moments as a function of intermolecular distance (R) for the 30-0-90-0 geometry, with r=r_{eq} for O_2^B. The dipole moment has atomic units, ea_0.

The final figure for this geometry is Figure (104), where we see the z-component of the dipole moments when monomer B is stretched past equilibrium to r=3.3 bohr. The dipole component here displays the same type of behavior as for the last geometry in Figure (101), but again the magnitude of this component is an order of magnitude smaller, due to monomer B being at a right angle to the intermolecular axis.

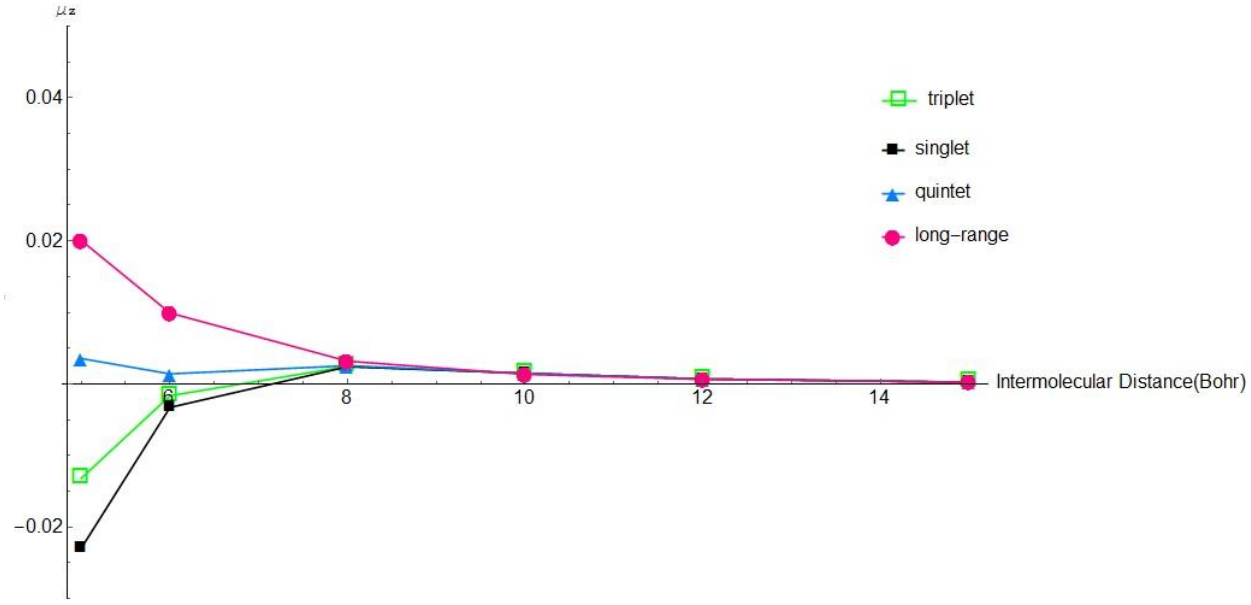

Figure 104. Comparison of dipole moments as a function of intermolecular distance (R) for the 30-0-90-0 geometry, with r=3.3 bohr for O_2^B. The dipole moment has atomic units, ea_0.

Our next geometry belongs to the C_1 symmetry point group, containing only the identity element *E*. In Figure (105), the z-component of the dipole moment is displayed for this geometry, with monomer B fixed at a bond distance of r=2 bohr. This geometry displays the same trends we have observed previously, with the dipole component for the *ab initio* singlet state the largest in magnitude.

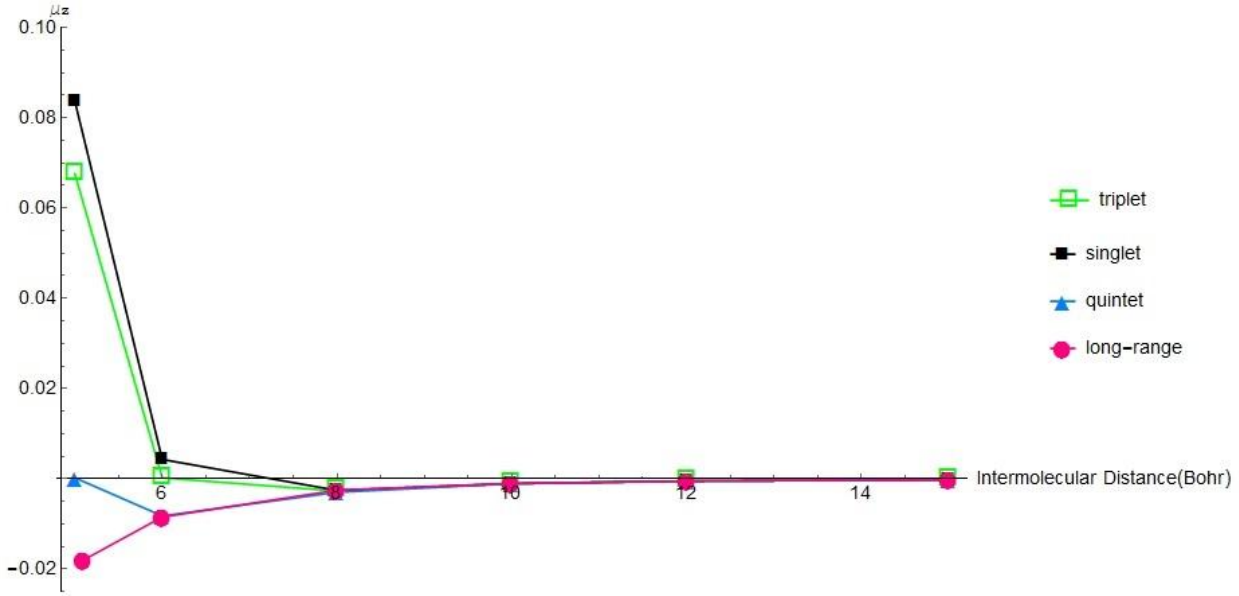

Figure 105. Comparison of dipole moments as a function of intermolecular distance (R) for the 35-0-65-80 geometry, with r=2 bohr for O_2^B. The dipole moment has atomic units, ea_0.

Figure (106) now examines this component of the dipole at this geometry with both monomers at equilibrium. The *ab initio* dipole is largest in magnitude for the quintet state.

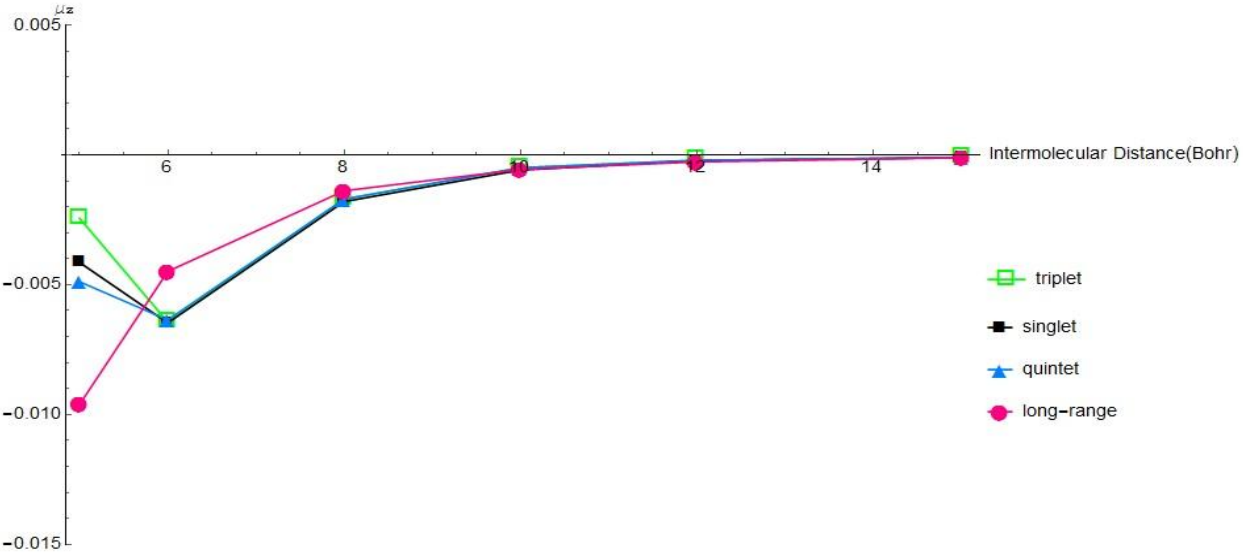

Figure 106. Comparison of dipole moments as a function of intermolecular distance (R) for the 35-0-65-80 geometry, with r=r_{eq} for O_2^B. The dipole moment has atomic units, ea_0.

Figure (107) displays the z-components of the dipole for this geometry, with the bond length of monomer B now stretched past equilibrium to 3.3 bohr.

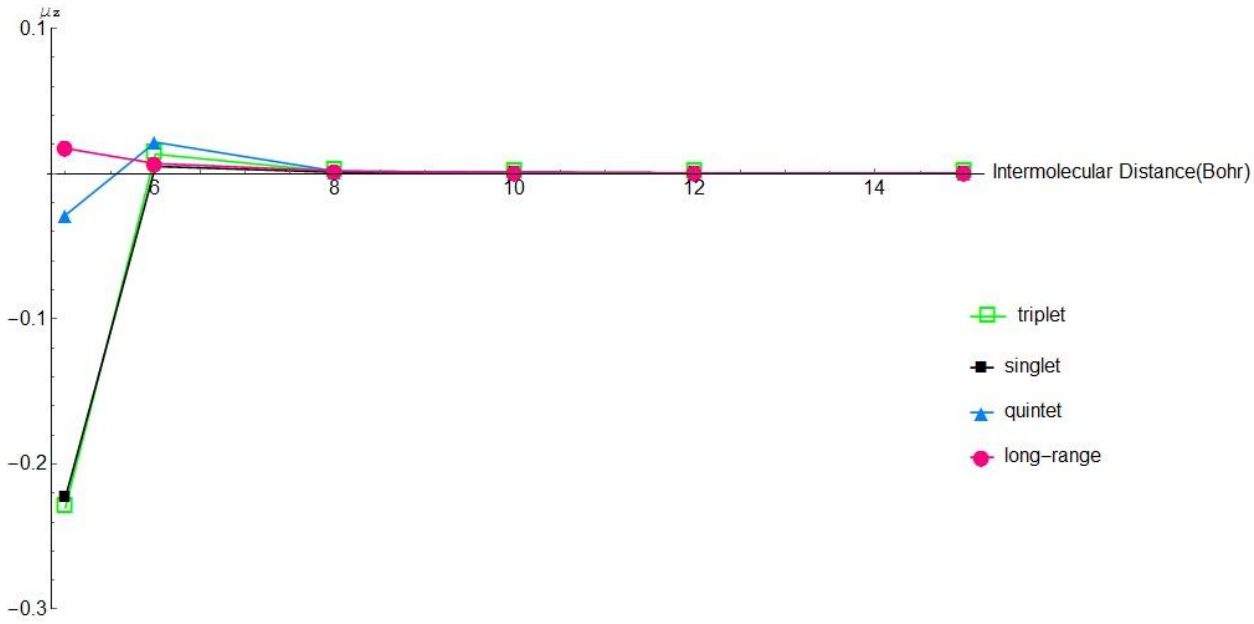

Figure 107. Comparison of dipole moments as a function of intermolecular distance (R) for the 35-0-65-80 geometry, with r=3.3 bohr for O_2^B. The dipole moment has atomic units, ea_0.

The z-component of the dipole moment has now become about an order of magnitude larger than it was when both monomers were at equilibrium bond lengths.

The next three geometries we will consider are all of C_s symmetry, containing only the identity element *E* and one reflection plane. Figure (108) shows the z-components of the dipole for a geometry with angles 45-0-30-0, and with monomer B at the shortest contracted bond distance considered.

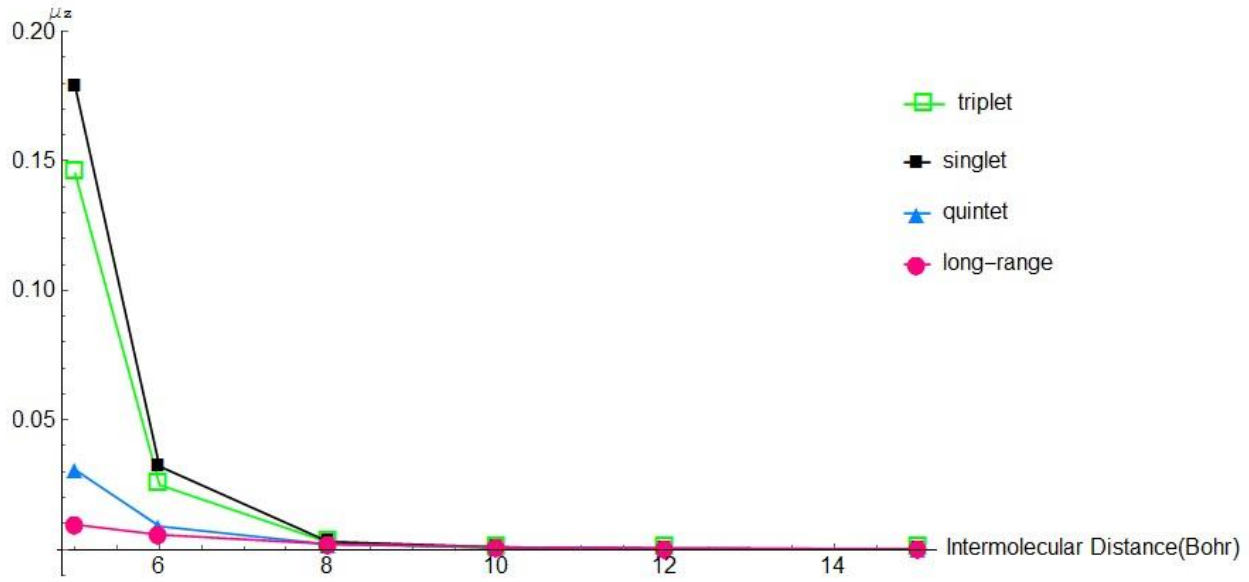

Figure 108. Comparison of dipole moments as a function of intermolecular distance (R) for the 45-0-30-0 geometry, with r=2 bohr for O_2^B. The dipole moment has atomic units, ea_0.

Previous trends are displayed in this figure. We also note that the long-range method underestimates the magnitude of the dipole moment at the smallest intermolecular distance of R=5 bohr by about a factor of four.

The z-component for this geometry when both monomers are fixed at the equilibrium bond lengths is shown in Figure (109). Here, the *ab initio* data predicts that the dipole is largest in magnitude for the quintet spin state. The long-range dipole is almost always smallest in magnitude, and therefore it is closer to the *ab initio* singlet state dipole here. Again, the long-range dipole is about one fourth the value of the largest *ab initio* dipole here.

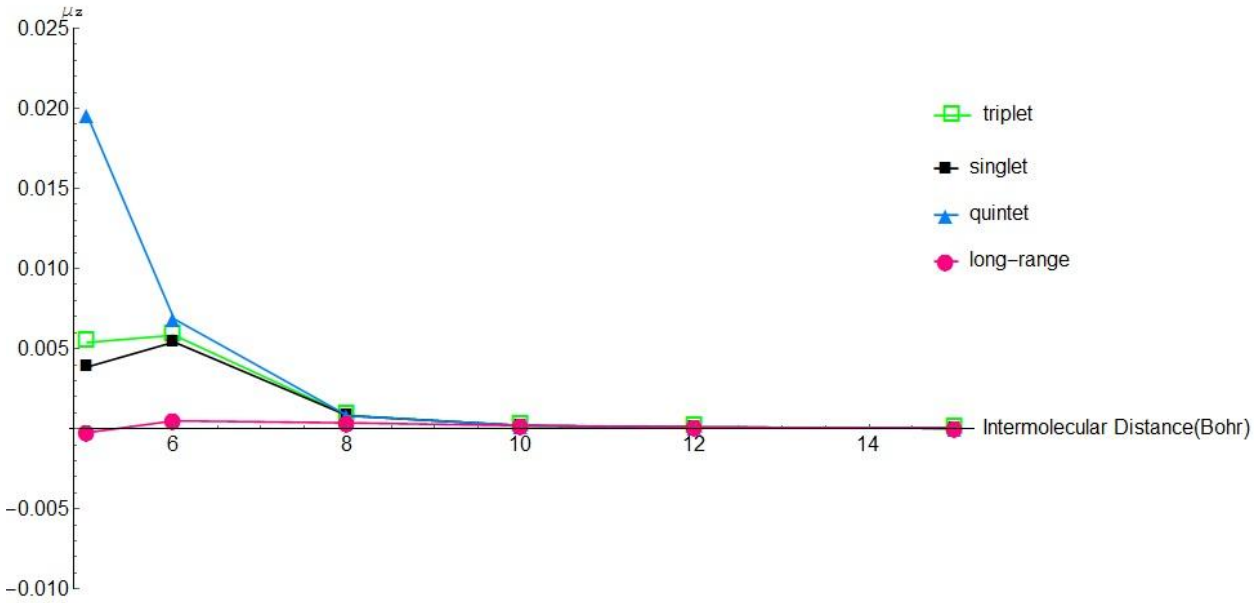

Figure 109. Comparison of dipole moments as a function of intermolecular distance (R) for the 45-0-30-0 geometry, with r=r_{eq} for O_2^B. The dipole moment has atomic units, ea_0.

Finally, Figure (110) shows the z-component of the dipole when monomer B is stretched to a bond distance of r=3.3 bohr. Previous trends are observed for this set of dipoles, and their magnitude is about twice of those in the last two figures, for monomer B contracted or at equilibrium.

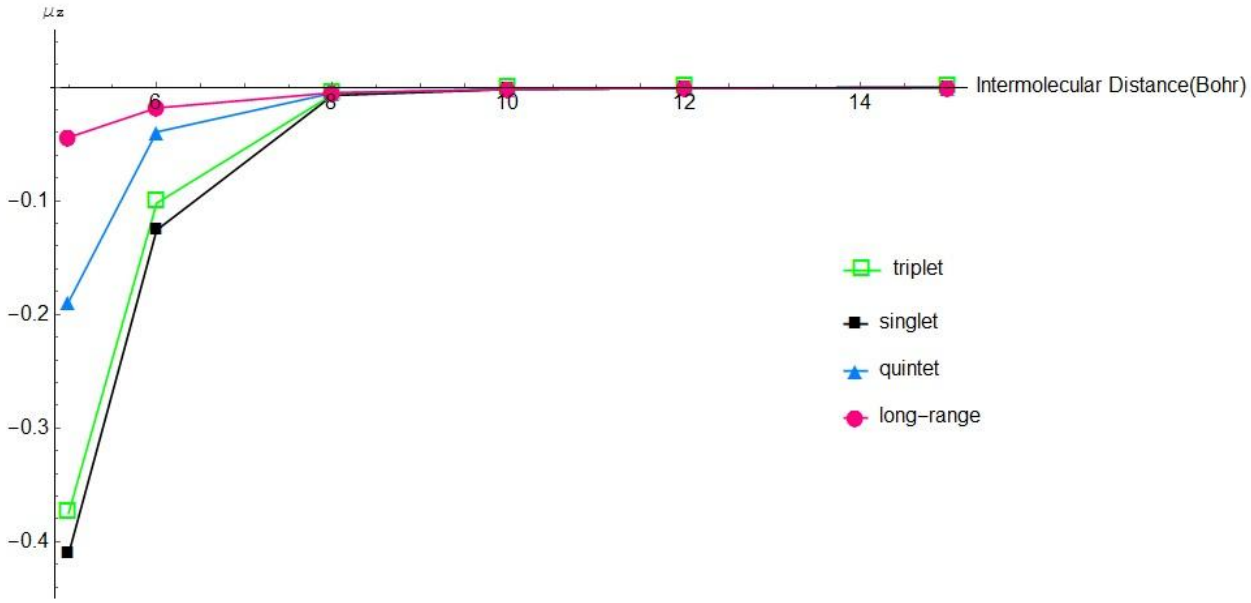

Figure 110. Comparison of dipole moments as a function of intermolecular distance (R) for the 45-0-30-0 geometry, with r=3.3 bohr for O_2^B. The dipole moment has atomic units, ea_0.

Figure (111) displays the behavior of the z-component of the dipole moment when the angle of the second monomer, with respect to the intermolecular axis, has been increased by 30 degrees, resulting in a geometry with angles 45-0-60-0. The data in the figure is for this geometry when monomer B is contracted to r=2 bohr.

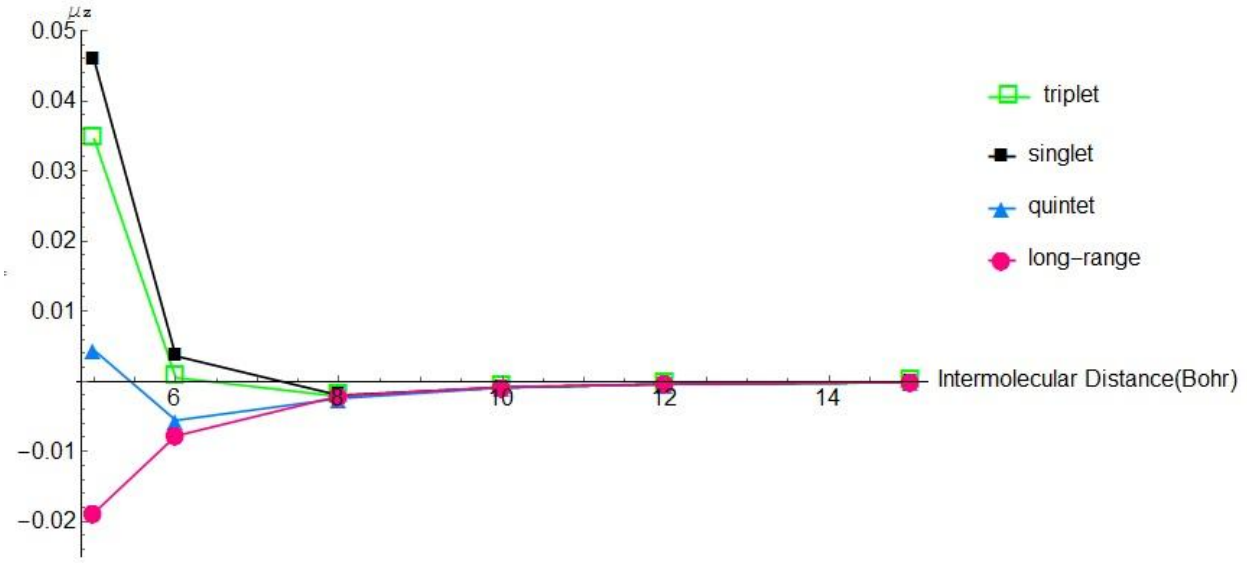

Figure 111. Comparison of dipole moments as a function of intermolecular distance (R) for the 45-0-60-0 geometry, with r=2 bohr for O_2^B. The dipole moment has atomic units, ea_0.

From Figure (111), we see that increasing the angle theta of the second monomer has caused the z-component of the dipole moment to decrease by about a factor of four.

Figure (112) shows the dipole moments for this geometry when both monomers are at their equilibrium bond lengths.

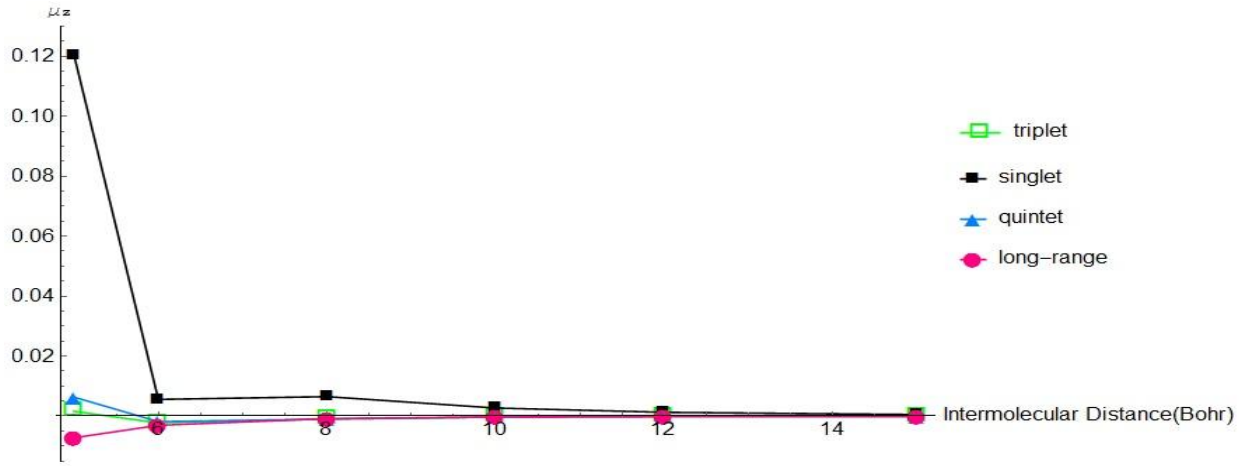

Figure 112. Comparison of dipole moments as a function of intermolecular distance (R) for the 45-0-60-0 geometry, with r=r_{eq} for O_2^B. The dipole moment has atomic units, ea_0.

When both monomers are at equilibrium, the z-component of the dipole moment for the quintet and triplet spin state have become smaller, while the z-component of the dipole moment for the singlet state has more than doubled in size when the distance between the monomers is R=5 bohr. Additionally, the singlet dipole is inconsistent with the data for the long-range dipole at an intermolecular separation of 12 bohr here.

In Figure (113), the z-component of the dipole for this geometry and with monomer B with a bond length of r=3.3 bohr is examined. Again, the singlet spin state dipole is the largest, but the triplet dipole has also increased by an order of magnitude and is nearly as large as the singlet dipole.

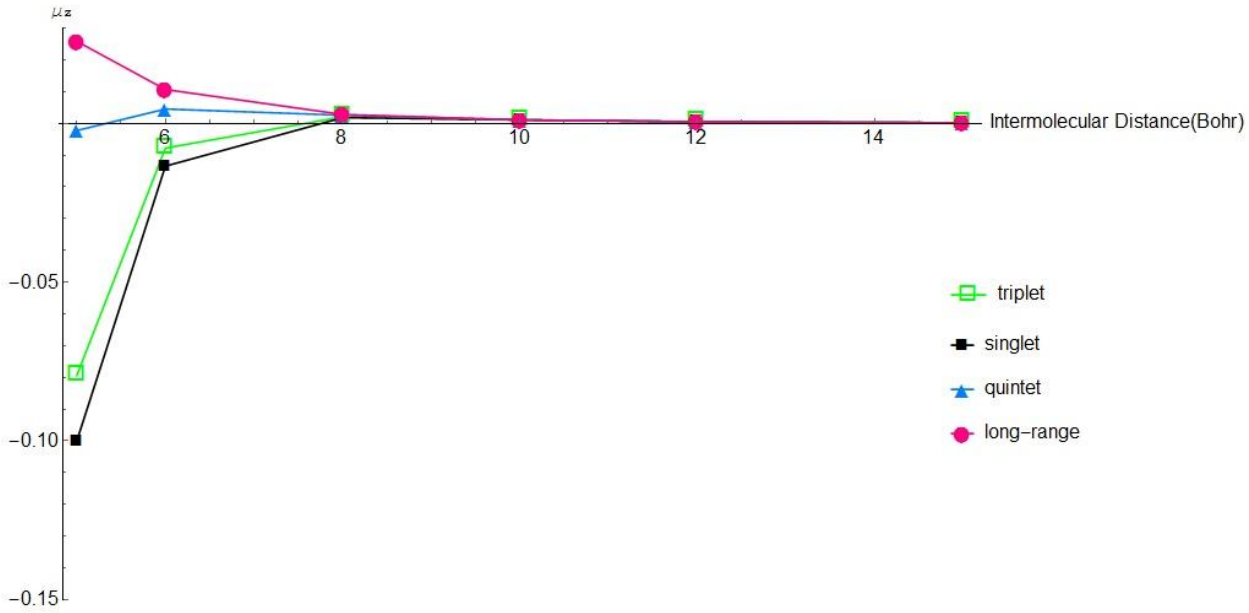

Figure 113. Comparison of dipole moments as a function of intermolecular distance (R) for the 45-0-60-0 geometry, with r=3.3 bohr for O_2^B. The dipole moment has atomic units, ea_0.

In constructing the next geometry, the angle of the second monomer with respect to the intermolecular axis has again been increased by 30 degrees, so that the angles for this geometry are 45-0-90-0 (the second monomer is now at a right angle with respect to the intermolecular axis). Figure (114) shows the z-component of the dipole moment when monomer B is contracted to its shortest distance for this geometry.

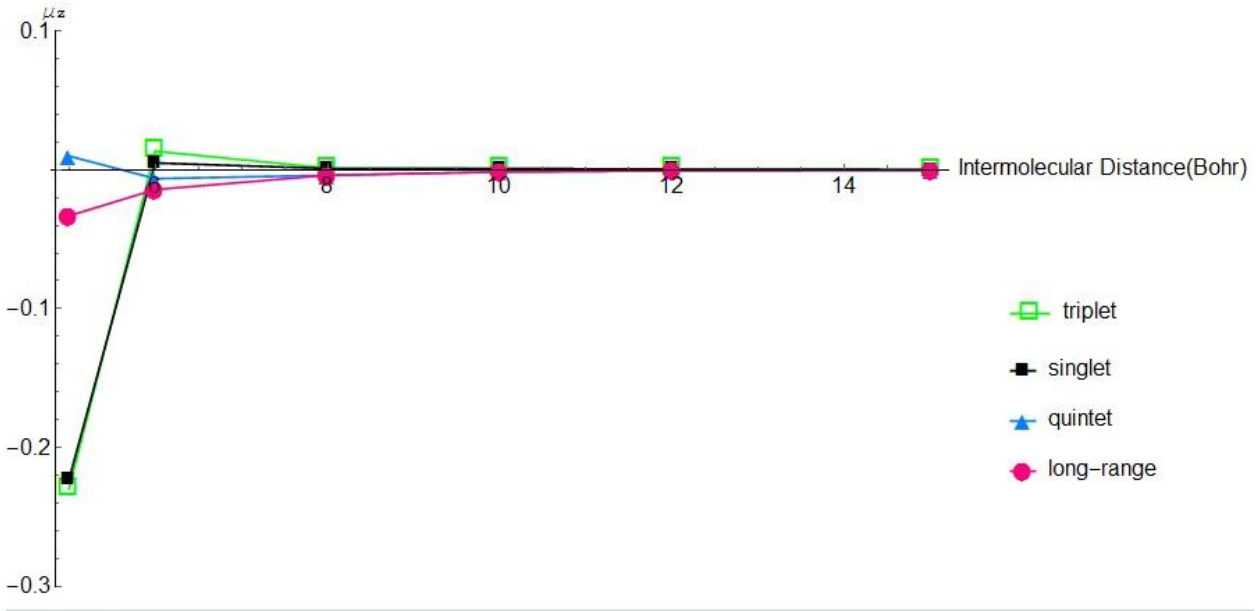

Figure 114. Comparison of dipole moments as a function of intermolecular distance (R) for the 45-0-90-0 geometry, with r=2 bohr for O_2^B. The dipole moment has atomic units, ea_0.

When the dipoles are at their largest in Figure (116), they are about 4 times as large as the dipoles were with a geometry of 45-0-60-0, when monomer B was at this contracted bond distance.

Figure (115) shows the z-components of the dipole for this geometry when the bond distance of both monomers is at equilibrium. It is unusual, when compared to previous geometries, that the long-range z-component of the dipole is actually the largest here in magnitude. That is followed by the quintet and triplet dipoles, with the singlet dipole the smallest in magnitude.

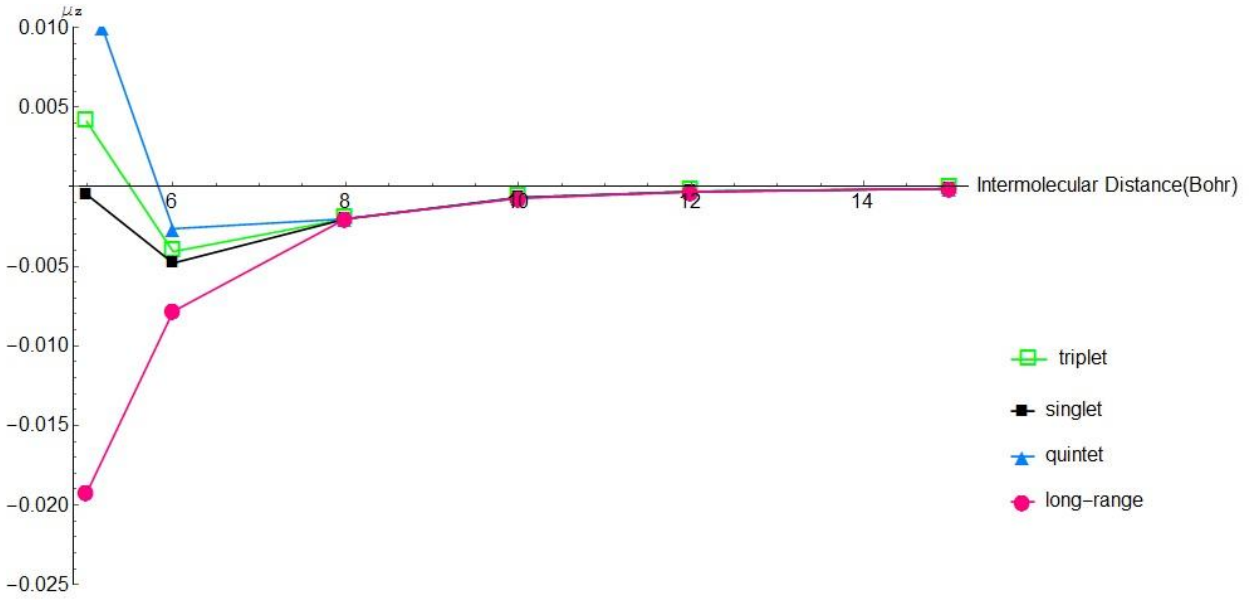

Figure 115. Comparison of dipole moments as a function of intermolecular distance (R) for the 45-0-90-0 geometry, with r=r_{eq} for O_2^B. The dipole moment has atomic units, ea_0.

Finally, the z-component of the dipole moment is shown in Figure (116) for this geometry when the bond of monomer B is stretched to r=3.3 bohr.

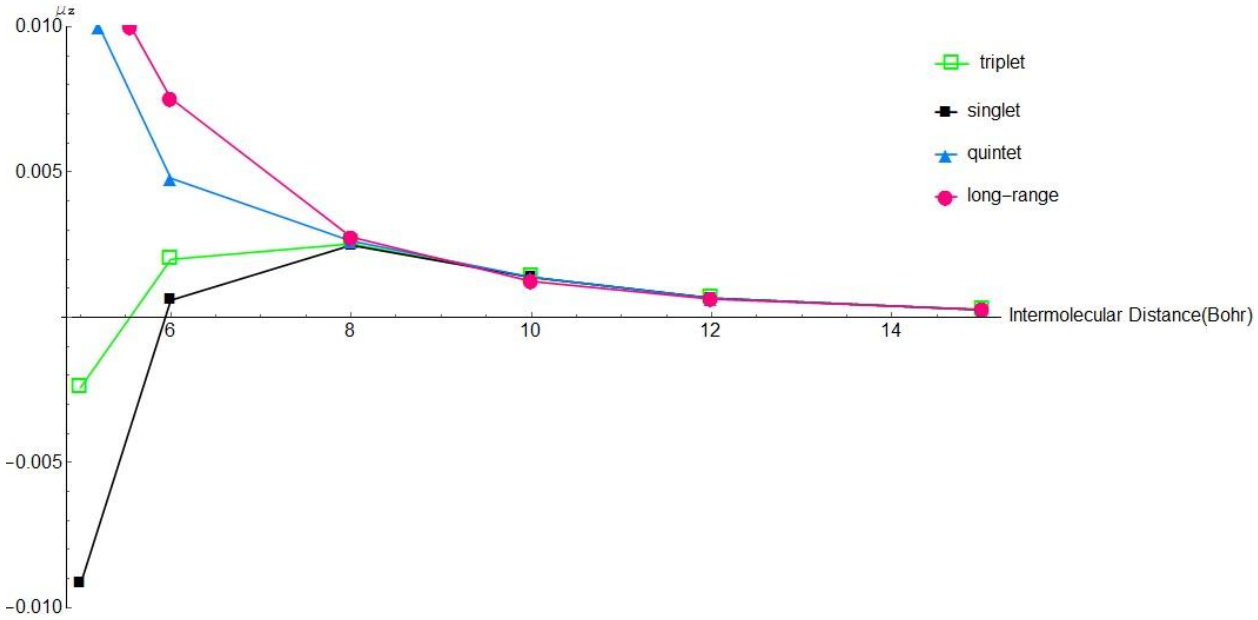

Figure 116. Comparison of dipole moments as a function of intermolecular distance (R) for the 45-0-90-0 geometry, with r=3.3 bohr for O_2^B. The dipole moment has atomic units, ea_0.

In Figure (116), the dipole calculated with the long-range method and the *ab initio* dipole for the singlet spin state are roughly equal in magnitude, but opposite in sign.

The next geometry for which we compare the *ab initio* and long-range dipoles is the geometry with angles 50-0-95-55 (of the C_1 symmetry point group). Figure (117) shows the z-component of the dipole when monomer B is contracted to r=2 bohr.

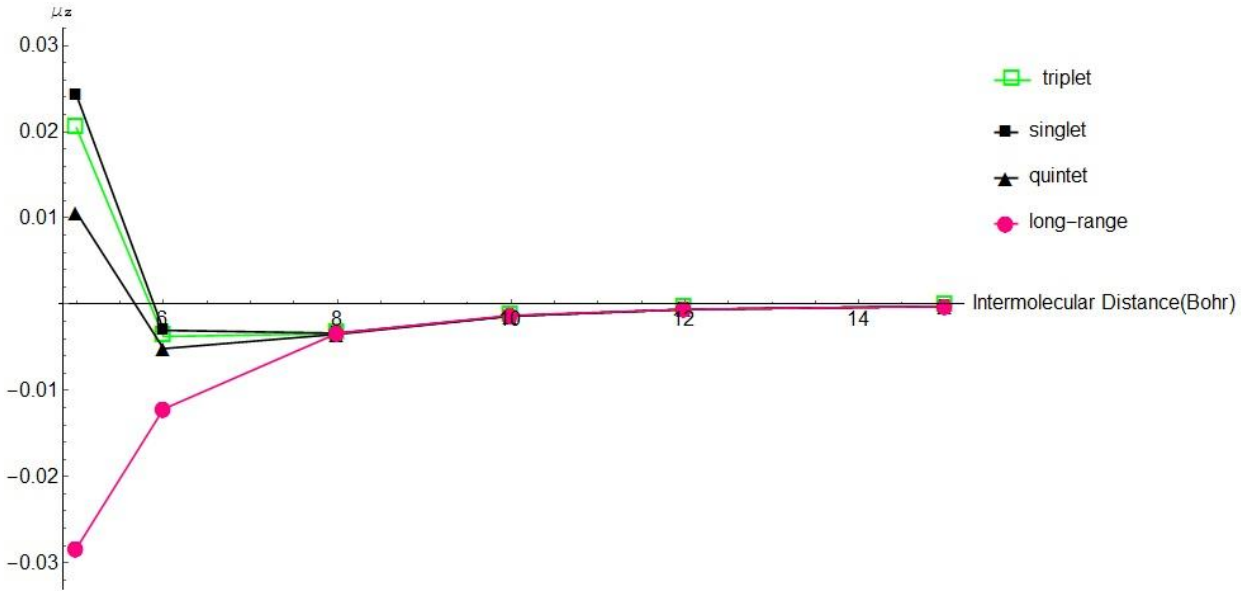

Figure 117. Comparison of dipole moments as a function of intermolecular distance (R) for the 50-0-95-55 geometry, with r=2 bohr for O_2^B. The dipole moment has atomic units, ea_0.

Here again, the long-range dipole is actually the largest in magnitude, then followed by the singlet *ab initio* dipole, which is opposite in sign.

Figure (118) shows the z-components of the dipole when both monomers are at equilibrium bond distances for this geometry.

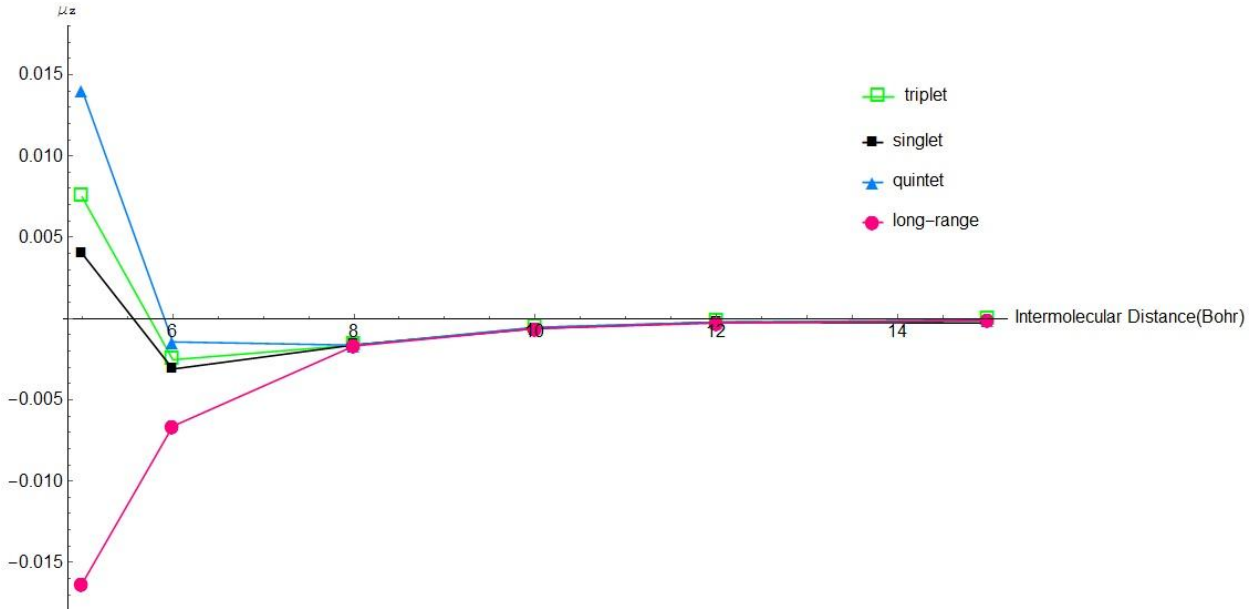

Figure 118. Comparison of dipole moments as a function of intermolecular distance (R) for the 50-0-95-55 geometry, with r=r_{eq} bohr for O_2^B. The dipole moment has atomic units, ea_0.

The long-range dipole is still the largest in magnitude in Figure (120), followed by the quintet, triplet, and then singlet dipoles (the quintet and singlet dipoles have now reversed order here).

In Figure (119), the corresponding dipoles for monomer B stretched to r=3.3 bohr are shown. When monomer B is stretched to this distance, the quintet state displays the largest z-component dipole.

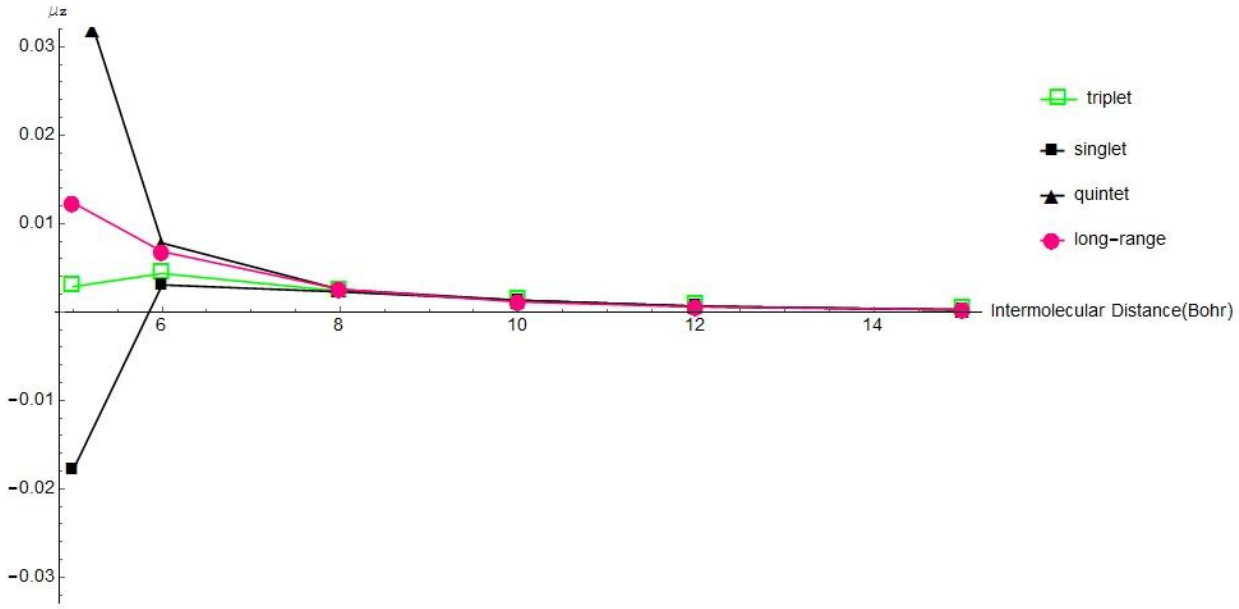

Figure 119. Comparison of dipole moments as a function of intermolecular distance (R) for the 50-0-95-55 geometry, with r=3.3 bohr for O_2^B. The dipole moment has atomic units, ea_0.

The next to last geometry for which dipoles have been obtained is again a geometry belonging to the C_1 symmetry point group, with angles 60-0-80-65. Figure (120) shows this data for this geometry when the bond length of monomer B is fixed at r=2 bohr. The long-range dipole moment is the largest in magnitude for this geometry.

Figure (121) shows the corresponding dipoles for this geometry when the bond length of monomer B is at equilibrium.

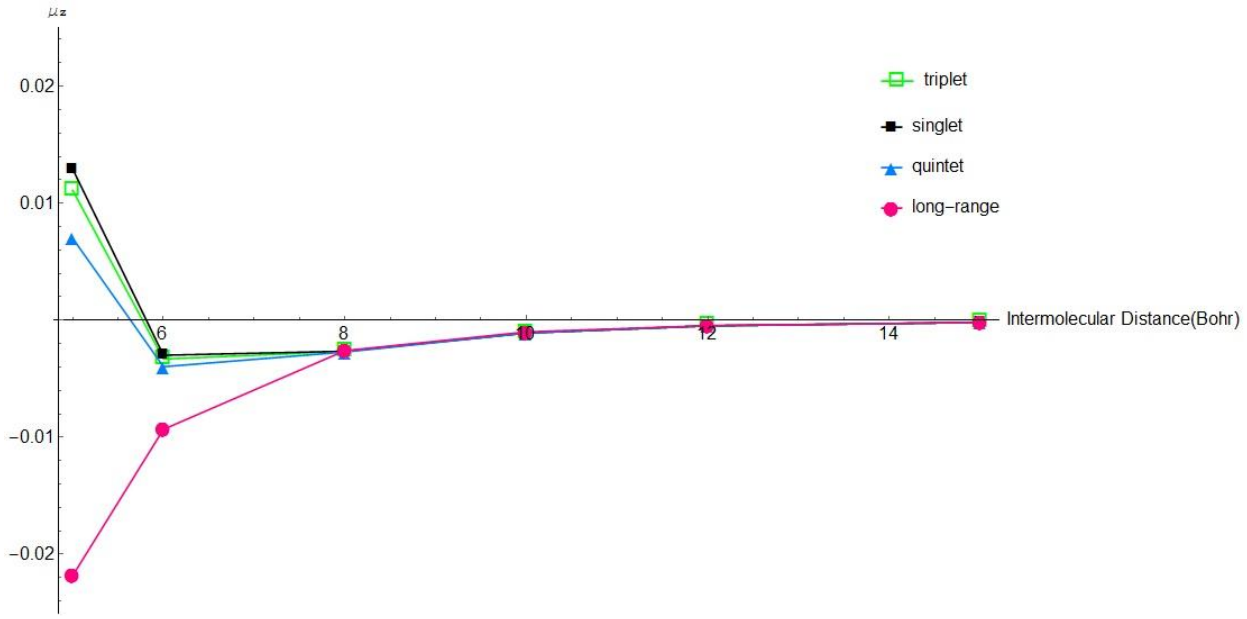

Figure 120. Comparison of dipole moments as a function of intermolecular distance (R) for the 60-0-80-65 geometry, with r=2 bohr for O_2^B. The dipole moment has atomic units, ea_0.

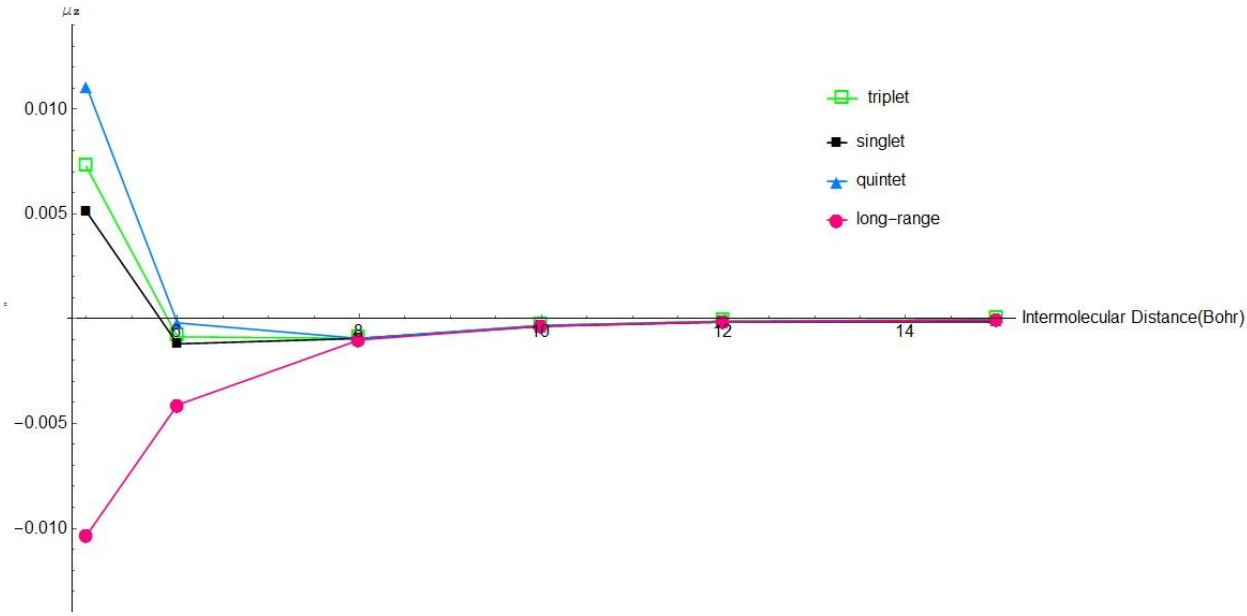

Figure 121. Comparison of dipole moments as a function of intermolecular distance (R) for the 60-0-80-65 geometry, with r=r_{eq} for O_2^B. The dipole moment has atomic units, ea_0.

As for the last geometry considered (Figure (118)), the singlet state dipole and quintet state dipole have reversed in their orders of magnitude, so that now the quintet state dipole is the largest, when both monomers are at equilibrium.

Figure (122) displays the behavior of the z-component of the dipole moment for the 60-0-80-65 geometry when the bond length of monomer B is r=3.3 bohr. The long-range dipole is the largest in magnitude, followed by the *ab initio* quintet, triplet and singlet dipole.

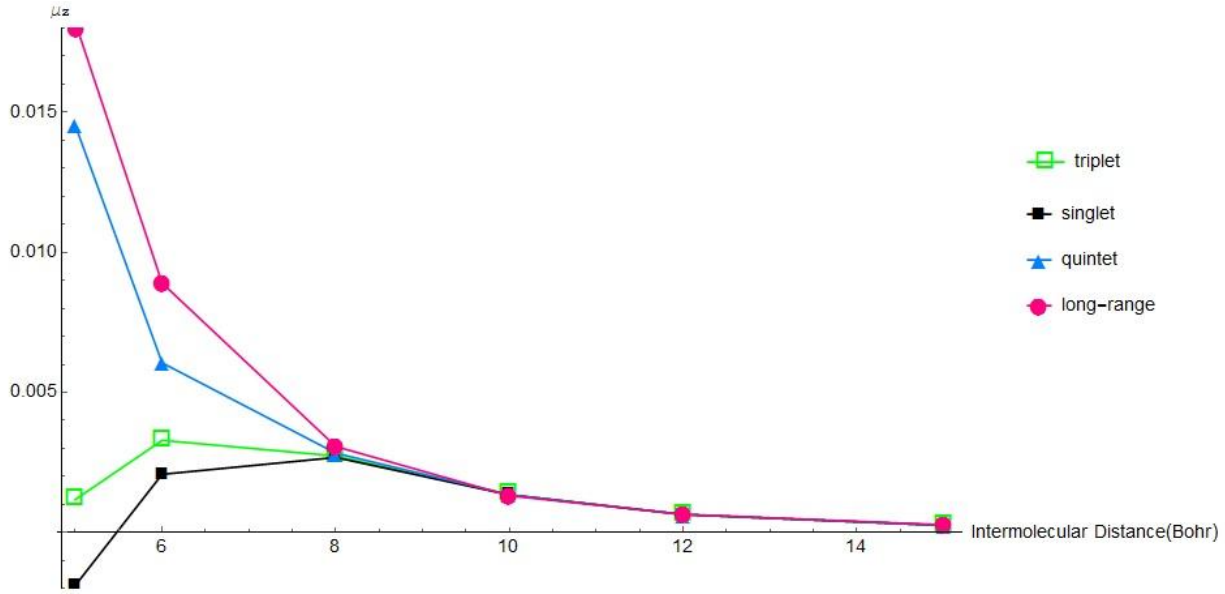

Figure 122. Comparison of dipole moments as a function of intermolecular distance (R) for the 60-0-80-65 geometry, with r=3.3 bohr for O_2^B. The dipole moment has atomic units, ea_0.

Finally, the last geometry for which dipole moments have been calculated for is that with angles 70-0-65-75. Figure (123) shows the z-component for the dipoles for this geometry when the bond distance of monomer B is at r=2 bohr.

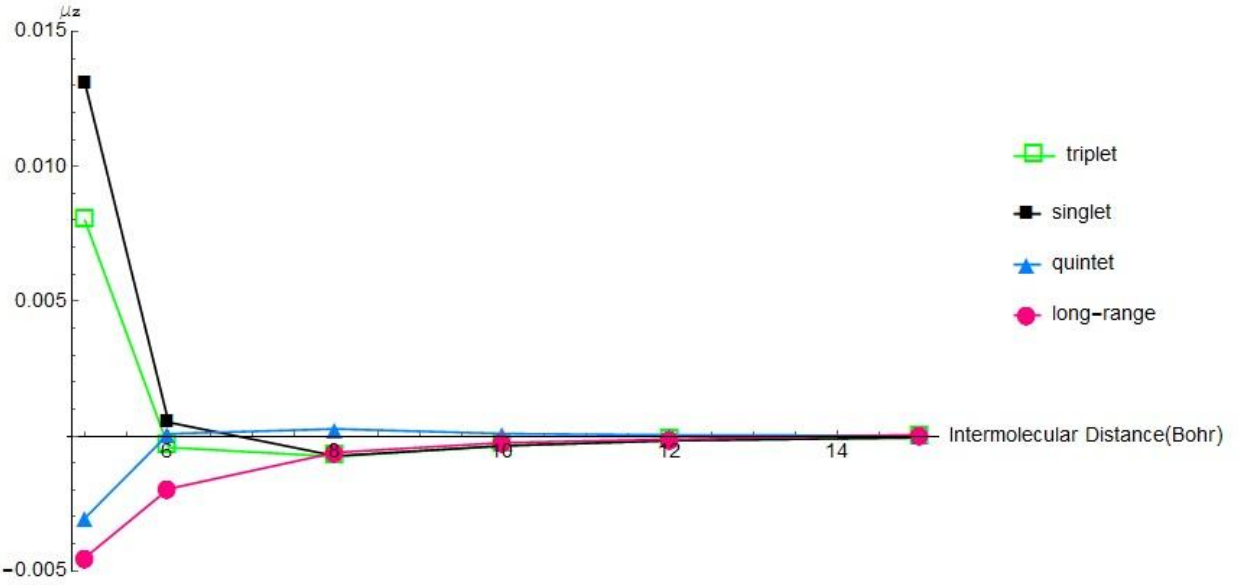

Figure 123. Comparison of dipole moments as a function of intermolecular distance (R) for the 70-0-65-75 geometry, with r=2 bohr for O_2^B. The dipole moment has atomic units, ea_0.

This figure follows the overriding previous trends, with the singlet state dipole the largest in magnitude.

In Figure (124), the z-component of the dipole moment for this geometry, with both monomers at their equilibrium bond length, is shown. The triplet spin state z-component shows some strange behavior, deviating away from the other two *ab initio* values as the molecules approach each other. At the shortest intermolecular distance of 5 bohr, the triplet state dipole becomes large and positive, and is the largest in magnitude of the four dipoles.

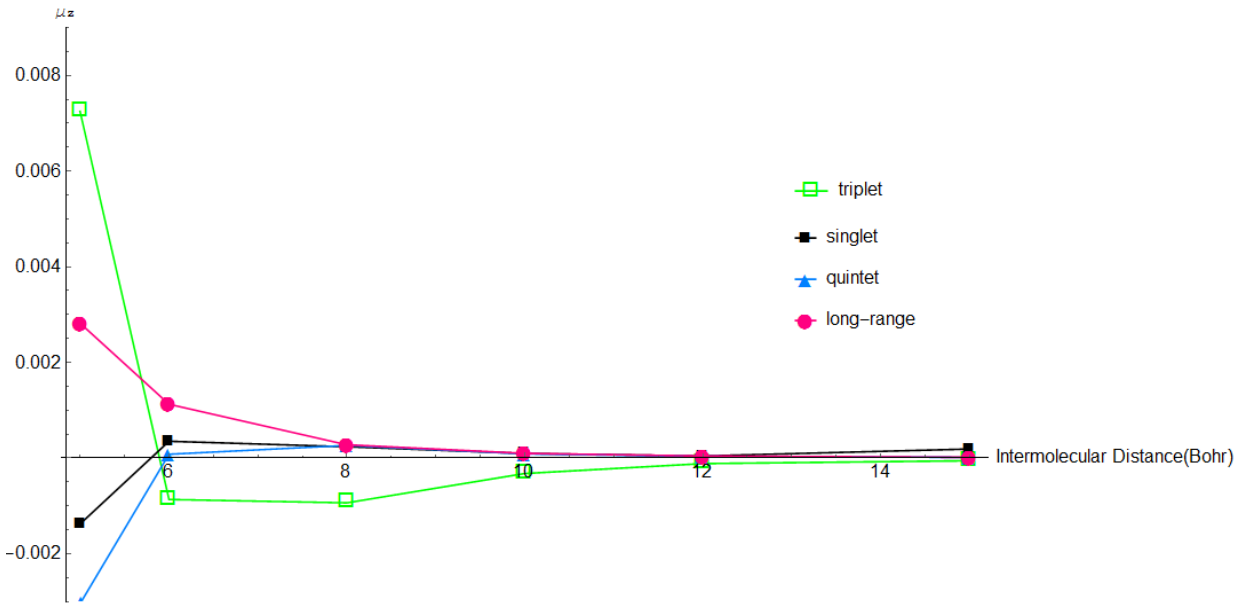

Figure 124. Comparison of dipole moments as a function of intermolecular distance (R) for the 70-0-65-75 geometry, with r=r_{eq} for O_2^B. The dipole moment has atomic units, ea_0.

Figure (125) is the last for this chapter. In it, we see the dipoles for the 70-0-65-75 geometry, with the bond distance of monomer B stretched to r=3.3 bohr. In this figure, the long-range dipole is the largest in magnitude, shown clearly at the intermolecular distance of R=5 bohr.

The figures analyzed in this section are only a small portion of the dipole moment data acquired. The z-components of the dipole moment calculated using *ab initio* energy calculations for the singlet, triplet, and quintet spin states are tabulated in the appendix, in Tables (65)-(312).

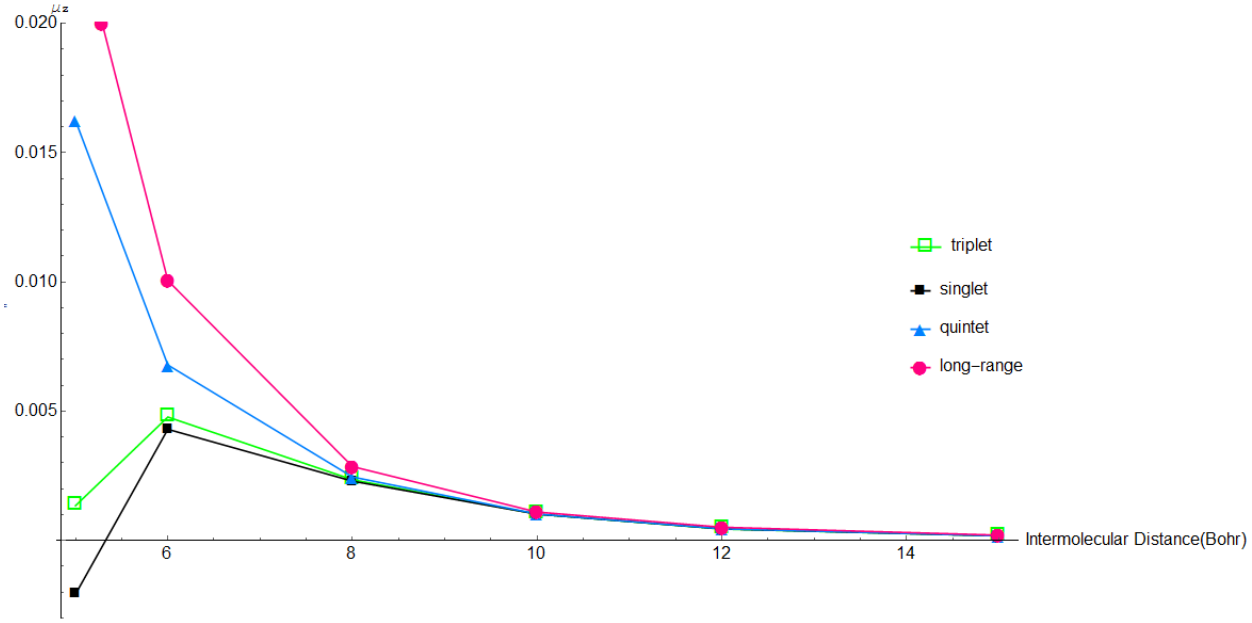

Figure 125. Comparison of dipole moments as a function of intermolecular distance (R) for the 70-0-65-75 geometry, with r=3.3 bohr for O_2^B. The dipole moment has atomic units, ea_0.

5.3 Conclusions and Future Directions

We have obtained the z-component of the collision-induced dipole moment for 23 angular geometries for the O_2-O_2 system, for use in modeling spectroscopic line profiles. Over 4,000 energies were calculated for this purpose, while applying a perturbative field with a strength of 0.001 a.u.

The geometries that result in the largest magnitude (0.1-1.0 ea_0, or 0.25-2.5 Debye) of dipole moment include the linear, T-shaped, 30-0-0-0, 60-0-0-0, and 10-0-160-15 geometries. In all of these cases, at least one of the monomers in the O_2-O_2 system is approaching the second monomer in a linear, or near linear, head-on orientation. This results in the largest distortion of the electronic charge around the oxygen atoms. For the same reason, for all geometries, the distortion and thus resulting dipole moment is larger when monomer B is at a non-equilibrium bond length, whether contracted shorter or stretched longer than the equilibrium bond length. In

most cases, the singlet spin state, which is the ground state of the three asymptotic spin states for the O_2-O_2 system, displays the largest magnitude of the dipole moment.

We have compared the *ab initio* dipole moments to the same component that was calculated using multipole moments and polarizabilities for the monomers, and making use of the long-range approximation. In general, the long-range expansion is a good approximation for intermolecular distances of 8 bohr or larger.

The *ab initio* calculations of the dipole moment require a large amount of CPU time and are costly to perform. For this reason, we have only obtained the z-component of the dipole moment. If the x and y components of the dipole are calculated *ab initio*, the total dipole moment can be obtained, and then the expansion coefficients in equation (1.19) can be calculated and compared directly to those that were obtained using the long-range approximation. This is a next step in future directions of this project.

APPENDIX

APPENDIX

All dipole moments in the appendix are in atomic units (ea_0).

Table 65. The z-component of the collision-induced dipole moment at an internuclear distance of 2 bohr for geometry 0-0-0-0 (linear)

Intermolecular Distance (bohr)	μ_z (singlet)	μ_z (triplet)	μ_z (quintet)
5	0.377021	0.248095	0.082433
6	0.071249	0.053053	0.02546
8	0.006778	0.006448	0.005829
10	0.00217	0.002172	0.002148
12	0.001022	0.001023	0.001022
15	0.000431	0.000431	0.000431
20	0.000137	0.000137	0.000137

Table 66. The z-component of the collision-induced dipole moment at an internuclear distance of 2.1 bohr for geometry 0-0-0-0 (linear)

Intermolecular Distance (bohr)	μ_z (singlet)	μ_z (triplet)	μ_z (quintet)
5	0.239599	0.163078	0.062996
6	0.045774	0.034755	0.018044
8	0.004439	0.004265	0.003902
10	0.001434	0.001433	0.001422
12	0.000686	0.000676	0.000673
15	0.000281	0.000282	0.000281
20	8.91E-05	8.91E-05	8.91E-05

Table 67. The z-component of the collision-induced dipole moment at an internuclear distance of 2.2 bohr for geometry 0-0-0-0 (linear)

Intermolecular Distance (bohr)	μ_z (singlet)	μ_z (triplet)	μ_z (quintet)
5	0.107269	0.075721	0.033086
6	0.020979	0.016145	0.008867
8	0.002035	0.001979	0.001813
10	0.000676	0.070126	0.000653
12	0.000306	0.000307	0.000307
15	0.000128	0.000128	0.000128
20	4.03E-05	4.03E-05	4.03E-05

Table 68. The z-component of the collision-induced dipole moment at an internuclear distance of 2.296 bohr for geometry 0-0-0-0 (linear)

Intermolecular Distance (bohr)	μ_z (singlet)	μ_z (triplet)	μ_z (quintet)
5	-0.01845	-0.01349	-0.00651
6	-0.00373	-0.0029	-0.00165
8	-0.00036	-0.00038	-0.00032
10	-0.00011	-0.00012	-0.00011
12	-5.2E-05	-5.4E-05	-5.3E-05
15	-2.2E-05	-2.2E-05	-2.2E-05
20	-7E-06	-7E-06	-7E-06

Table 69. The z-component of the collision-induced dipole moment at an internuclear distance of 2.36 bohr for geometry 0-0-0-0 (linear)

Intermolecular Distance (bohr)	μ_z (singlet)	μ_z (triplet)	μ_z (quintet)
5	-0.10158	-0.07606	-0.02247
6	-0.02118	-0.01652	-0.01728
8	-0.00198	-0.00193	-0.00973
10	-0.00064	-0.10682	-0.00774
12	-0.0003	-0.0003	-0.00714
15	-0.00012	-0.00012	-0.00682
20	-3.9E-05	-3.9E-05	-0.00666

Table 70. The z-component of the collision-induced dipole moment at an internuclear distance of 2.457 bohr for geometry 0-0-0-0 (linear)

Intermolecular Distance (bohr)	μ_z (singlet)	μ_z (triplet)	μ_z (quintet)
5	-0.22472	-0.17359	-0.09542
6	-0.04962	-0.03886	-0.02325
8	-0.00454	-0.00439	-0.00412
10	-0.00144	-0.00143	-0.00143
12	-0.00067	-0.00066	-0.00067
15	-0.00027	-0.00027	-0.00027
20	-8.6E-05	-8.6E-05	-8.6E-05

Table 71. The z-component of the collision-induced dipole moment at an internuclear distance of 2.646 bohr for geometry 0-0-0-0 (linear)

Intermolecular Distance (bohr)	μ_z (singlet)	μ_z (triplet)	μ_z (quintet)
5	-0.44061	-0.35034	-0.2037
6	-0.11541	-0.08914	-0.05523
8	-0.01855	-0.00939	-0.00879
10	-0.01216	-0.00298	-0.00297
12	-0.0106	-0.00137	-0.00137
15	-0.00979	-0.00056	-0.00056
20	-0.00939	-0.00017	-0.00017

Table 72. The z-component of the collision-induced dipole moment at an internuclear distance of 2.929 bohr for geometry 0-0-0-0 (linear)

Intermolecular Distance (bohr)	μ_z (singlet)	μ_z (triplet)	μ_z (quintet)
5	-0.65431	-0.53422	-0.13891
6	-0.23243	-0.30686	-0.11817
8	-0.01752	-0.02427	-0.01589
10	-0.00512	-0.00686	-0.00509
12	-0.00231	-0.00303	-0.00231
15	-0.00096	-0.00128	-0.00093
20	-0.00029	-0.00037	-0.00029

Table 73. The z-component of the collision-induced dipole moment at an internuclear distance of 3.213 bohr for geometry 0-0-0-0 (linear)

Intermolecular Distance (bohr)	μ_z (singlet)	μ_z (triplet)	μ_z (quintet)
5	-0.6678	-0.4887	0.091813
6	-0.37965	-0.16174	-0.20466
8	-0.02514	-0.00543	-0.02266
10	-0.00687	0.005506	-0.00683
12	-0.00305	0.00806	-0.00304
15	-0.00122	0.009313	-0.00122
20	-0.00038	0.009879	-0.00038

Table 74. The z-component of the collision-induced dipole moment at an internuclear distance of 3.3 bohr for geometry 0-0-0-0 (linear)

Intermolecular Distance (bohr)	μ_z (singlet)	μ_z (triplet)	μ_z (quintet)
5	-0.67239	-0.08092	0.086246
6	-0.42854	-0.35174	-0.23611
8	-0.02735	-0.02629	-0.0246
10	-0.0073	-0.00728	-0.00726
12	-0.00322	-0.00321	-0.00322
15	-0.0013	-0.00124	-0.00128
20	-0.0004	-0.0004	-0.0004

Table 75. The z-component of the collision-induced dipole moment at an internuclear distance of 2 bohr for geometry 90-0-0-0 (T-shaped)

Intermolecular Distance (bohr)	μ_z (singlet)	μ_z (triplet)	μ_z (quintet)
5	0.080953	0.072238	0.038309
6	0.026797	0.024538	0.020391
8	0.005055	0.004996	0.005134
10	0.001717	0.001723	0.001806
12	0.000816	0.00082	0.00085
15	0.000377	0.000377	0.000386
20	0.000124	0.000124	0.000128

Table 76. The z-component of the collision-induced dipole moment at an internuclear distance of 2.1 bohr for geometry 90-0-0-0 (T-shaped)

Intermolecular Distance (bohr)	μ_z (singlet)	μ_z (triplet)	μ_z (quintet)
5	0.051272	0.047376	0.034422
6	0.021035	0.020084	0.018246
8	0.004287	0.004263	0.004213
10	0.001435	0.001432	0.001431
12	0.000674	0.000675	0.000674
15	0.000311	0.00031	0.00031
20	0.000102	0.000102	0.000102

Table 77. The z-component of the collision-induced dipole moment at an internuclear distance of 2.2 bohr for geometry 90-0-0-0 (T-shaped)

Intermolecular Distance (bohr)	μ_z (singlet)	μ_z (triplet)	μ_z (quintet)
5	0.028411	0.027541	0.029298
6	0.01656	0.016551	0.016027
8	0.003884	0.003886	0.003506
10	0.001269	0.001273	0.001134
12	0.000573	0.000576	0.000524
15	0.00026	0.000261	0.000243
20	8.71E-05	8.7E-05	8.04E-05

Table 78. The z-component of the collision-induced dipole moment at an internuclear distance of 2.296 bohr for geometry 90-0-0-0 (T-shaped)

Intermolecular Distance (bohr)	μ_z (singlet)	μ_z (triplet)	μ_z (quintet)
5	0.00023	0.002376	0.022787
6	0.011155	0.012126	0.014366
8	0.003176	0.003206	0.003256
10	0.000996	0.000997	0.000999
12	0.000436	0.000438	0.000436
15	0.000198	0.000202	0.0002
20	6.77E-05	6.77E-05	6.77E-05

Table 79. The z-component of the collision-induced dipole moment at an internuclear distance of 2.36 bohr for geometry 90-0-0-0 (T-shaped)

Intermolecular Distance (bohr)	μ_z (singlet)	μ_z (triplet)	μ_z (quintet)
5	-0.01988	-0.01605	0.019561
6	0.007349	0.008959	0.013032
8	0.002698	0.002738	0.002607
10	0.000815	0.000822	0.000692
12	0.000344	0.000344	0.000282
15	0.00016	0.00016	0.000135
20	5.5E-05	5.5E-05	4.69E-05

Table 80. The z-component of the collision-induced dipole moment at an internuclear distance of 2.457 bohr for geometry 90-0-0-0 (T-shaped)

Intermolecular Distance (bohr)	μ_z (singlet)	μ_z (triplet)	μ_z (quintet)
5	-0.05309	-0.04727	0.007684
6	0.001156	0.003714	0.009556
8	0.001963	0.002027	0.002152
10	0.000537	0.000543	0.000545
12	0.000211	0.000209	0.000209
15	0.000102	0.000102	0.000102
20	3.62E-05	3.62E-05	3.62E-05

Table 81. The z-component of the collision-induced dipole moment at an internuclear distance of 2.646 bohr for geometry 90-0-0-0 (T-shaped)

Intermolecular Distance (bohr)	μ_z (singlet)	μ_z (triplet)	μ_z (quintet)
5	-0.12932	-0.12225	-0.01669
6	-0.01272	-0.00804	0.002473
8	0.000522	0.000629	0.000837
10	1.78E-05	2.74E-05	3.18E-05
12	-4.5E-05	-4.5E-05	-4.5E-05
15	-6.9E-06	-6.9E-06	-6.9E-06
20	1.79E-06	1.75E-06	1.81E-06

Table 82. The z-component of the collision-induced dipole moment at an internuclear distance of 2.929 bohr for geometry 90-0-0-0 (T-shaped)

Intermolecular Distance (bohr)	μ_z (singlet)	μ_z (triplet)	μ_z (quintet)
5	-0.27528	-0.27403	-0.06827
6	-0.0388	-0.03078	-0.01136
8	-0.00161	-0.00145	-0.00111
10	-0.00067	-0.00067	-0.00066
12	-0.00038	-0.00038	-0.00038
15	-0.00015	-0.00015	-0.00015
20	-4.3E-05	-4.3E-05	-4.3E-05

Table 83. The z-component of the collision-induced dipole moment at an internuclear distance of 3.213 bohr for geometry 90-0-0-0 (T-shaped)

Intermolecular Distance (bohr)	μ_z (singlet)	μ_z (triplet)	μ_z (quintet)
5	-0.45121	-0.45764	-0.14135
6	-0.07186	-0.06104	-0.03015
8	-0.00376	-0.00351	-0.00301
10	-0.00127	-0.00128	-0.00126
12	-0.00066	-0.00066	-0.00066
15	-0.00026	-0.00031	-0.00026
20	-7.8E-05	-7.8E-05	-7.8E-05

Table 84. The z-component of the collision-induced dipole moment at an internuclear distance of 3.3 bohr for geometry 90-0-0-0 (T-shaped)

Intermolecular Distance (bohr)	μ_z (singlet)	μ_z (triplet)	μ_z (quintet)
5	-0.51662	-0.52613	-0.16807
6	-0.08294	-0.07188	-0.03709
8	-0.00439	-0.00411	-0.00357
10	-0.00145	-0.00149	-0.00141
12	-0.00074	-0.00074	-0.00074
15	-0.00029	-0.00029	-0.00029
20	-8.7E-05	-8.7E-05	-8.7E-05

Table 85. The z-component of the collision-induced dipole moment at an internuclear distance of 2 bohr for geometry 90-0-90-0 (H-shaped)

Intermolecular Distance (bohr)	μ_z (singlet)	μ_z (triplet)	μ_z (quintet)
5	0.032664174	-0.001807933	-0.001492126
6	0.003142046	-0.002699614	-0.002317612
8	-0.001098531	-0.001334431	-0.001257441
10	-0.000572854	-0.000571589	-0.000579044
12	-0.000270651	-0.000252792	-0.000270573
15	-0.000103089	-9.932E-05	-0.000103051
20	-3.28355E-05	-3.16545E-05	-3.283E-05

Table 86. The z-component of the collision-induced dipole moment at an internuclear distance of 2.1 bohr for geometry 90-0-90-0 (H-shaped)

Intermolecular Distance (bohr)	μ_z (singlet)	μ_z (triplet)	μ_z (quintet)
5	0.018571174	0.013151735	-0.000555847
6	0.001625818	0.000618447	-0.001352498
8	-0.000714349	-0.000742677	-0.000794234
10	-0.000358792	-0.000364055	-0.000365078
12	-0.000171416	-0.000170589	-0.000170799
15	-6.6299E-05	-6.6257E-05	-6.628E-05
20	-2.12235E-05	-2.1222E-05	-2.1221E-05

Table 87. The z-component of the collision-induced dipole moment at an internuclear distance of 2.2 bohr for geometry 90-0-90-0 (H-shaped)

Intermolecular Distance (bohr)	μ_z (singlet)	μ_z (triplet)	μ_z (quintet)
5	0.007604828	0.005418126	-0.000112935
6	0.000617271	0.000219947	-0.000557593
8	-0.000322302	-0.000330525	-0.000350138
10	-0.000159499	-0.000156803	-0.00016064
12	-7.62935E-05	-7.44485E-05	-7.52515E-05
15	-2.9693E-05	-2.9787E-05	-2.9669E-05
20	-9.56149E-06	-9.57502E-06	-9.54702E-06

Table 88. The z-component of the collision-induced dipole moment at an internuclear distance of 2.296 bohr for geometry 90-0-90-0 (H-shaped)

Intermolecular Distance (bohr)	μ_z (singlet)	μ_z (triplet)	μ_z (quintet)
5	-0.001223966	-0.000877103	1.41802E-06
6	-9.3438E-05	-3.2527E-05	8.93875E-05
8	4.3606E-05	5.2751E-05	5.91645E-05
10	2.615E-05	2.75745E-05	2.7101E-05
12	-8.504E-06	1.2762E-05	1.2713E-05
15	5.10451E-06	5.03351E-06	5.07998E-06
20	1.63902E-06	1.6355E-06	1.6415E-06

Table 89. The z-component of the collision-induced dipole moment at an internuclear distance of 2.36 bohr for geometry 90-0-90-0 (H-shaped)

Intermolecular Distance (bohr)	μ_z (singlet)	μ_z (triplet)	μ_z (quintet)
5	-0.006509539	-0.00468223	-3.58225E-05
6	-0.000483635	-0.000162563	0.000465138
8	0.000300857	0.000307024	0.000321828
10	0.000146554	0.000146137	0.000147383
12	6.8986E-05	6.92375E-05	6.9215E-05
15	2.78425E-05	2.78505E-05	2.78855E-05
20	9.02651E-06	9.03151E-06	9.02651E-06

Table 90. The z-component of the collision-induced dipole moment at an internuclear distance of 2.457 bohr for geometry 90-0-90-0 (H-shaped)

Intermolecular Distance (bohr)	μ_z (singlet)	μ_z (triplet)	μ_z (quintet)
5	-0.013873828	-0.010036202	-0.00021081
6	-0.000997227	-0.000328662	0.000980201
8	0.000658445	0.000674754	0.000702408
10	0.000320664	0.0003207	0.000321407
12	0.000149483	0.000151378	0.000151181
15	6.1616E-05	6.16005E-05	6.1604E-05
20	1.99725E-05	1.9969E-05	1.99705E-05

Table 91. The z-component of the collision-induced dipole moment at an internuclear distance of 2.646 bohr for geometry 90-0-90-0 (H-shaped)

Intermolecular Distance (bohr)	μ_z (singlet)	μ_z (triplet)	μ_z (quintet)
5	-0.026612266	-0.019446753	-0.000760019
6	-0.001853874	-0.000619212	0.001794119
8	0.001293608	0.001320693	0.001372668
10	0.000625663	0.000626417	0.000627532
12	0.000296343	0.000296496	0.000296457
15	0.00012324	0.00012322	0.000123233
20	4.0204E-05	4.01945E-05	4.01965E-05

Table 92. The z-component of the collision-induced dipole moment at an internuclear distance of 2.929 bohr for geometry 90-0-90-0 (H-shaped)

Intermolecular Distance (bohr)	μ_z (singlet)	μ_z (triplet)	μ_z (quintet)
5	-0.042138557	-0.03124864	-0.001614153
6	-0.002910275	-0.001022437	0.002654339
8	0.002052387	0.002089907	0.002163685
10	0.000990094	0.000990965	0.000991066
12	0.000473282	0.00047049	0.000471987
15	0.000201017	0.000196354	0.000200756
20	6.62395E-05	6.57925E-05	6.5907E-05

Table 93. The z-component of the collision-induced dipole moment at an internuclear distance of 3.213 bohr for geometry 90-0-90-0 (H-shaped)

Intermolecular Distance (bohr)	μ_z (singlet)	μ_z (triplet)	μ_z (quintet)
5	-0.051844839	-0.039338699	-0.002131642
6	-0.003545545	-0.001271731	0.003200946
8	0.002540543	0.002584656	0.002678435
10	0.001229398	0.00124104	0.001234128
12	0.000592768	0.000601174	0.000593133
15	0.000255038	0.000267267	0.000256205
20	8.47495E-05	8.40285E-05	8.47255E-05

Table 94. The z-component of the collision-induced dipole moment at an internuclear distance of 3.3 bohr for geometry 90-0-90-0 (H-shaped)

Intermolecular Distance (bohr)	μ_z (singlet)	μ_z (triplet)	μ_z (quintet)
5	-0.053182254	-0.040804785	-0.002213646
6	-0.00359987	-0.001287265	0.003309089
8	0.002634653	0.002658444	0.002778047
10	0.001280079	0.001281476	0.001283648
12	0.00061584	0.00058639	0.000618762
15	0.000267023	0.000268167	0.000268026
20	8.8727E-05	8.8729E-05	8.8685E-05

Table 95. The z-component of the collision-induced dipole moment at an internuclear distance of 2 bohr for geometry 90-0-90-90 (X-shaped)

Intermolecular Distance (bohr)	μ_z (singlet)	μ_z (triplet)	μ_z (quintet)
5	-0.0007545	-0.00180793	-0.00206339
6	-0.0026053	-0.00269961	-0.00265887
8	-0.001399	-0.00133443	-0.00138858
10	-0.0006038	-0.00057159	-0.00060324
12	-0.0002676	-0.00025279	-0.00026763
15	-0.000105	-9.932E-05	-0.00010507
20	-3.344E-05	-3.1654E-05	-3.3443E-05

Table 96. The z-component of the collision-induced dipole moment at an internuclear distance of 2.1 bohr for geometry 90-0-90-90 (X-shaped)

Intermolecular Distance (bohr)	μ_z (singlet)	μ_z (triplet)	μ_z (quintet)
5	-0.00042	-0.00067559	-0.00116044
6	-0.00162	-0.00162971	-0.00164827
8	-0.00089	-0.00089175	-0.0008848
10	-0.00038	-0.00038309	-0.00038339
12	-0.00017	-0.00016838	-0.00017076
15	-6.8E-05	-6.7356E-05	-6.7766E-05
20	-2.2E-05	-3.2982E-05	-2.162E-05

Table 97. The z-component of the collision-induced dipole moment at an internuclear distance of 2.2 bohr for geometry 90-0-90-90 (X-shaped)

Intermolecular Distance (bohr)	μ_z (singlet)	μ_z (triplet)	μ_z (quintet)
5	-0.00016	-0.00026874	-0.0004672
6	-0.0007	-0.00070769	-0.00071758
8	-0.00039	-0.00039727	-0.00039266
10	-0.00017	-0.00017303	-0.00016967
12	-7.1E-05	-7.5556E-05	-7.5801E-05
15	-3E-05	-3.0227E-05	-3.0393E-05
20	-9.7E-06	-9.7595E-06	-9.7315E-06

Table 98. The z-component of the collision-induced dipole moment at an internuclear distance of 2.296 bohr for geometry 90-0-90-90 (X-shaped)

Intermolecular Distance (bohr)	μ_z (singlet)	μ_z (triplet)	μ_z (quintet)
5	2.5382E-05	4.11145E-05	7.40345E-05
6	0.00011535	0.000119454	0.000123286
8	6.6981E-05	6.68835E-05	6.6877E-05
10	2.9545E-05	5.8636E-05	2.8712E-05
12	1.4514E-05	1.3342E-05	1.28525E-05
15	5.533E-06	7.37748E-06	5.20399E-06
20	1.675E-06	1.68748E-06	1.67E-06

Table 99. The z-component of the collision-induced dipole moment at an internuclear distance of 2.36 bohr for geometry 90-0-90-90 (X-shaped)

Intermolecular Distance (bohr)	μ_z (singlet)	μ_z (triplet)	μ_z (quintet)
5	0.000131	0.000219081	-0.00069105
6	0.000633	0.000637981	0.000530715
8	0.000366	0.000349621	0.000486198
10	0.000153	0.000149927	0.000220337
12	7.17E-05	6.9705E-05	9.8668E-05
15	2.88E-05	2.59445E-05	3.94215E-05
20	9.2E-06	9.20201E-06	1.26465E-05

Table 100. The z-component of the collision-induced dipole moment at an internuclear distance of 2.457 bohr for geometry 90-0-90-90 (X-shaped)

Intermolecular Distance (bohr)	μ_z (singlet)	μ_z (triplet)	μ_z (quintet)
5	0.00027	0.001352359	0.001883054
6	0.001369	0.001476301	0.001519432
8	0.000801	0.000680756	0.000677524
10	0.000342	0.000280084	0.000279552
12	0.000154	0.000128763	0.000126312
15	6.32E-05	5.30885E-05	5.29005E-05
20	2.04E-05	1.703E-05	1.70115E-05

Table 101. The z-component of the collision-induced dipole moment at an internuclear distance of 2.646 bohr for geometry 90-0-90-90 (X-shaped)

Intermolecular Distance (bohr)	μ_z (singlet)	μ_z (triplet)	μ_z (quintet)
5	0.000512	0.000882771	0.001575633
6	0.002646	0.002667611	0.002708654
8	0.001572	0.001569746	0.001564577
10	0.000671	0.000670603	0.000670138
12	0.000303	0.000303638	0.000303081
15	0.000127	0.000127965	0.000126856
20	4.1E-05	4.0997E-05	4.09955E-05

Table 102. The z-component of the collision-induced dipole moment at an internuclear distance of 2.929 bohr for geometry 90-0-90-90 (X-shaped)

Intermolecular Distance (bohr)	μ_z (singlet)	μ_z (triplet)	μ_z (quintet)
5	0.000891	0.001412741	0.002542371
6	0.004133	0.004196042	0.004275948
8	0.002498	0.002497056	0.002485307
10	0.001064	0.00106795	0.001062597
12	0.000483	0.000485822	0.000484465
15	0.000207	0.000208773	0.000207034
20	6.73E-05	6.7289E-05	6.72385E-05

Table 103. The z-component of the collision-induced dipole moment at an internuclear distance of 3.213 bohr for geometry 90-0-90-90 (X-shaped)

Intermolecular Distance (bohr)	μ_z (singlet)	μ_z (triplet)	μ_z (quintet)
5	0.001181	0.001755721	0.00320051
6	0.00516	0.005211106	0.005333383
8	0.003102	0.003109162	0.003094536
10	0.001325	0.001333343	0.001327877
12	0.000609	0.000638792	0.000611505
15	0.000264	0.000254868	0.000264949
20	8.65E-05	0.000132413	8.6535E-05

Table 104. The z-component of the collision-induced dipole moment at an internuclear distance of 3.3 bohr for geometry 90-0-90-90 (X-shaped)

Intermolecular Distance (bohr)	μ_z (singlet)	μ_z (triplet)	μ_z (quintet)
5	0.001223	0.001781882	0.003291267
6	0.00536	0.005386253	0.005546102
8	0.003223	0.003215423	0.003217491
10	0.001383	0.0013798	0.001383636
12	0.000667	0.000641964	0.000639178
15	0.000276	0.000237446	0.000277544
20	9.07E-05	9.06905E-05	9.07895E-05

Table 105. The z-component of the collision-induced dipole moment at an internuclear distance of 2 bohr for geometry 30-0-0-0

Intermolecular Distance (bohr)	μ_z (singlet)	μ_z (triplet)	μ_z (quintet)
5	0.24899	-	0.210709
6	0.053624	-	0.043862
8	0.006148	-	0.005758
10	0.001881	-	0.001862
12	0.000927	-	0.000927
15	0.000411	-	0.000411
20	0.000132	-	0.000132

Table 106. The z-component of the collision-induced dipole moment at an internuclear distance of 2.1 bohr for geometry 30-0-0-0

Intermolecular Distance (bohr)	μ_z (singlet)	μ_z (triplet)	μ_z (quintet)
5	0.183603	0.202742	0.198831
6	0.038029	0.003678	0.035441
8	0.003696	0.037085	0.003538
10	0.001095	0.001089	0.001081
12	0.000557	0.000528	0.000556
15	0.000257	0.000256	0.000256
20	8.38E-05	8.3E-05	8.37E-05

Table 107. The z-component of the collision-induced dipole moment at an internuclear distance of 2.2 bohr for geometry 30-0-0-0

Intermolecular Distance (bohr)	μ_z (singlet)	μ_z (triplet)	μ_z (quintet)
5	0.143861	0.155759	0.190949
6	0.028882	0.001642	0.030602
8	0.002327	0.026233	0.002179
10	0.000546	0.000483	0.000532
12	0.0003	0.000214	0.000299
15	0.000147	0.000113	0.000147
20	4.81E-05	3.93E-05	4.81E-05

Table 108. The z-component of the collision-induced dipole moment at an internuclear distance of 2.28187 bohr for geometry 30-0-0-0

Intermolecular Distance (bohr)	μ_z (singlet)	μ_z (triplet)	μ_z (quintet)
5	0.09276	-	0.173306
6	0.017546	-	0.023367
8	0.000642	-	0.000567
10	-3.1E-05	-	-3.1E-05
12	4.13E-05	-	4.96E-05
15	-1.5E-05	-	4.15E-05
20	1.88E-05	-	2.79E-05

Table 109. The z-component of the collision-induced dipole moment at an internuclear distance of 2.296 bohr for geometry 30-0-0-0

Intermolecular Distance (bohr)	μ_z (singlet)	μ_z (triplet)	μ_z (quintet)
5	0.083189	0.116187	0.169583
6	0.015481	0.000319	0.022003
8	0.000347	0.017648	0.00028
10	-0.00014	-0.00014	-0.00015
12	-1.7E-05	-1.8E-05	-1.8E-05
15	1.67E-05	1.69E-05	1.67E-05
20	7.35E-06	7.35E-06	7.34E-06

Table 110. The z-component of the collision-induced dipole moment at an internuclear distance of 2.36 bohr for geometry 30-0-0-0

Intermolecular Distance (bohr)	μ_z (singlet)	μ_z (triplet)	μ_z (quintet)
5	0.036699	0.072648	0.150166
6	0.005628	-0.00103	0.015348
8	-0.00102	0.008839	-0.00103
10	-0.0006	-0.0006	-0.00061
12	-0.00023	-0.00023	-0.00023
15	-7E-05	-7E-05	-7E-05
20	-2E-05	-2E-05	-2E-05

Table 111. The z-component of the collision-induced dipole moment at an internuclear distance of 2.457 bohr for geometry 30-0-0-0

Intermolecular Distance (bohr)	μ_z (singlet)	μ_z (triplet)	μ_z (quintet)
5	-0.04409	-0.00398	0.11258
6	-0.01101	-0.00315	0.003708
8	-0.00317	-0.00617	-0.00312
10	-0.00131	-0.00131	-0.00132
12	-0.00056	-0.00056	-0.00056
15	-0.0002	-0.0002	-0.0002
20	-6.1E-05	-6.1E-05	-6.1E-05

Table 112. The z-component of the collision-induced dipole moment at an internuclear distance of 2.646 bohr for geometry 30-0-0-0

Intermolecular Distance (bohr)	μ_z (singlet)	μ_z (triplet)	μ_z (quintet)
5	-0.21342	-0.17384	0.019225
6	-0.05054	-0.00747	-0.02507
8	-0.00753	-0.04235	-0.00735
10	-0.00269	-0.00269	-0.0027
12	-0.00117	-0.00117	-0.00117
15	-0.00045	-0.00045	-0.00045
20	-0.00014	-0.00014	-0.00014

Table 113. The z-component of the collision-induced dipole moment at an internuclear distance of 2.929 bohr for geometry 30-0-0-0

Intermolecular Distance (bohr)	μ_z (singlet)	μ_z (triplet)	μ_z (quintet)
5	-0.87639	-0.34226	-0.08526
6	-0.13188	-0.01417	-0.08735
8	-0.01435	-0.11878	-0.0139
10	-0.00459	-0.00459	-0.0046
12	-0.002	-0.002	-0.002
15	-0.00077	-0.00077	-0.00077
20	-0.00024	-0.00024	-0.00024

Table 114. The z-component of the collision-induced dipole moment at an internuclear distance of 3.213 bohr for geometry 30-0-0-0

Intermolecular Distance (bohr)	μ_z (singlet)	μ_z (triplet)	μ_z (quintet)
5	-0.65283	-0.32931	-0.22403
6	-0.24602	-0.02098	-0.18259
8	-0.02113	-0.23348	-0.0204
10	-0.00616	-0.00616	-0.00617
12	-0.00265	-0.00258	-0.00265
15	-0.00102	-0.00102	-0.00102
20	-0.00031	-0.00031	-0.00031

Table 115. The z-component of the collision-induced dipole moment at an internuclear distance of 3.3 bohr for geometry 30-0-0-0

Intermolecular Distance (bohr)	μ_z (singlet)	μ_z (triplet)	μ_z (quintet)
5	-0.5214	-0.29269	-0.25393
6	-0.28675	-0.02288	-0.21935
8	-0.02317	-0.27451	-0.02236
10	-0.00656	-0.00658	-0.00654
12	-0.0028	-0.0028	-0.0028
15	-0.00108	-0.00108	-0.00107
20	-0.00033	-0.00033	-0.00033

Table 116. The z-component of the collision-induced dipole moment at an internuclear distance of 2 bohr for geometry 60-0-0-0

Intermolecular Distance (bohr)	μ_z (singlet)	μ_z (triplet)	μ_z (quintet)
5	0.12791	0.114761	0.107634
6	0.035354	0.033962	0.033405
8	0.005064	0.005008	0.00524
10	0.001679	0.00163	0.001718
12	0.00084	0.000798	0.000838
15	0.000373	0.000373	0.000388
20	0.000123	0.000123	0.000127

Table 117. The z-component of the collision-induced dipole moment at an internuclear distance of 2.1 bohr for geometry 60-0-0-0

Intermolecular Distance (bohr)	μ_z (singlet)	μ_z (triplet)	μ_z (quintet)
5	0.094175	0.093327	0.101247
6	0.029115	0.028873	0.028918
8	0.003883	0.003868	0.003799
10	0.001208	0.001189	0.00119
12	0.000587	0.000588	0.000588
15	0.000282	0.000281	0.000281
20	9.38E-05	9.3E-05	9.37E-05

Table 118. The z-component of the collision-induced dipole moment at an internuclear distance of 2.2 bohr for geometry 60-0-0-0

Intermolecular Distance (bohr)	μ_z (singlet)	μ_z (triplet)	μ_z (quintet)
5	0.05693	0.068898	0.09651
6	0.022512	0.023316	0.026832
8	0.002652	0.002642	0.003107
10	0.00074	0.00072	0.000876
12	0.000367	0.000365	0.000429
15	0.000188	0.000185	0.000212
20	6.42E-05	6.42E-05	7.16E-05

Table 119. The z-component of the collision-induced dipole moment at an internuclear distance of 2.28187 bohr for geometry 60-0-0-0

Intermolecular Distance (bohr)	μ_z (singlet)	μ_z (triplet)	μ_z (quintet)
5	0.033086	-	0.087902
6	0.019092	-	0.023209
8	0.002212	-	0.002151
10	0.000525	-	0.000527
12	0.00026	-	0.00025
15	0.000133	-	0.000139
20	4.86E-05	-	4.89E-05

Table 120. The z-component of the collision-induced dipole moment at an internuclear distance of 2.296 bohr for geometry 60-0-0-0

Intermolecular Distance (bohr)	μ_z (singlet)	μ_z (triplet)	μ_z (quintet)
5	0.026741	0.046878	0.086138
6	0.018029	0.019501	0.022525
8	0.002038	0.002013	0.001985
10	0.000461	0.000453	0.000448
12	0.000218	0.000224	0.000224
15	0.000127	0.000127	0.000127
20	4.48E-05	4.48E-05	4.48E-05

Table 121. The z-component of the collision-induced dipole moment at an internuclear distance of 2.36 bohr for geometry 60-0-0-0

Intermolecular Distance (bohr)	μ_z (singlet)	μ_z (triplet)	μ_z (quintet)
5	0.015424	0.024383	0.07702
6	0.015901	0.015061	0.019189
8	0.001369	0.001209	0.001207
10	0.000127	0.000155	0.000157
12	6.7E-05	8.75E-05	8.69E-05
15	6.07E-05	7.04E-05	7.04E-05
20	2.36E-05	2.71E-05	2.71E-05

Table 122. The z-component of the collision-induced dipole moment at an internuclear distance of 2.457 bohr for geometry 60-0-0-0

Intermolecular Distance (bohr)	μ_z (singlet)	μ_z (triplet)	μ_z (quintet)
5	-0.05879	-0.01653	0.073222
6	0.004348	0.007477	0.016077
8	-1.1E-05	-1.2E-05	1.85E-05
10	-0.00028	-0.00028	-0.00034
12	-0.00012	-0.00012	-0.00015
15	-1.5E-05	-1.5E-05	-2.8E-05
20	5.97E-07	-5.8E-06	-4.1E-06

Table 123. The z-component of the collision-induced dipole moment at an internuclear distance of 2.646 bohr for geometry 60-0-0-0

Intermolecular Distance (bohr)	μ_z (singlet)	μ_z (triplet)	μ_z (quintet)
5	-0.22757	-0.12521	0.009187
6	-0.01904	-0.01078	-0.00104
8	-0.00342	-0.00254	-0.00246
10	-0.0014	-0.00112	-0.00113
12	-0.00063	-0.00051	-0.00051
15	-0.00022	-0.00017	-0.00017
20	-6.3E-05	-4.8E-05	-4.8E-05

Table 124. The z-component of the collision-induced dipole moment at an internuclear distance of 2.929 bohr for geometry 60-0-0-0

Intermolecular Distance (bohr)	μ_z (singlet)	μ_z (triplet)	μ_z (quintet)
5	-0.43584	-0.33796	-0.10787
6	-0.05852	-0.04887	-0.03202
8	-0.00643	-0.00635	-0.00623
10	-0.00229	-0.00229	-0.0023
12	-0.00103	-0.00105	-0.00104
15	-0.00038	-0.00038	-0.00038
20	-0.00011	-0.00011	-0.00011

Table 125. The z-component of the collision-induced dipole moment at an internuclear distance of 3.213 bohr for geometry 60-0-0-0

Intermolecular Distance (bohr)	μ_z (singlet)	μ_z (triplet)	μ_z (quintet)
5	-0.59612	-0.52856	-0.20986
6	-0.11801	-0.10408	-0.07951
8	-0.01034	-0.01021	-0.01
10	-0.00326	-0.00327	-0.00327
12	-0.00146	-0.00146	-0.00146
15	-0.00054	-0.00054	-0.00054
20	-0.00016	-0.00016	-0.00016

Table 126. The z-component of the collision-induced dipole moment at an internuclear distance of 3.3 bohr for geometry 60-0-0-0

Intermolecular Distance (bohr)	μ_z (singlet)	μ_z (triplet)	μ_z (quintet)
5	-0.59257	-0.49433	-0.20332
6	-0.13962	-0.12521	-0.09841
8	-0.01152	-0.01137	-0.01113
10	-0.00352	-0.00352	-0.00349
12	-0.00156	-0.00156	-0.00155
15	-0.00058	-0.00058	-0.00058
20	-0.00017	-0.00017	-0.00017

Table 127. The z-component of the collision-induced dipole moment at an internuclear distance of 2 bohr for geometry 105-0-60-60

Intermolecular Distance (bohr)	μ_z (singlet)	μ_z (triplet)	μ_z (quintet)
5	0.073382	0.057572	-0.0171
6	0.001165	-0.00248	-0.00986
8	-0.00156	-0.00166	-0.00184
10	-0.00053	-0.00053	-0.00054
12	-0.00026	-0.00026	-0.00026
15	-0.00012	-0.00012	-0.00012
20	-3.5E-05	-3.8E-05	-3.5E-05

Table 128. The z-component of the collision-induced dipole moment at an internuclear distance of 2.1 bohr for geometry 105-0-60-60

Intermolecular Distance (bohr)	μ_z (singlet)	μ_z (triplet)	μ_z (quintet)
5	0.035371	0.02461	-0.02489
6	-0.00356	-0.00578	-0.01027
8	-0.00153	-0.00157	-0.00166
10	-0.00047	-0.00047	-0.00047
12	-0.00022	-0.00022	-0.00022
15	0.067422	0.068422	0.068338
20	-3.4E-05	-3.4E-05	-3.4E-05

Table 129. The z-component of the collision-induced dipole moment at an internuclear distance of 2.2 bohr for geometry 105-0-60-60

Intermolecular Distance (bohr)	μ_z (singlet)	μ_z (triplet)	μ_z (quintet)
5	0.00025	-0.00623	-0.03477
6	-0.00833	-0.0093	-0.01141
8	-0.00155	-0.00155	-0.00156
10	-0.00042	-0.00043	-0.00042
12	-0.0002	-0.0002	-0.0002
15	0.116822	0.117736	0.117665
20	-3.3E-05	-3.3E-05	-3.3E-05

Table 130. The z-component of the collision-induced dipole moment at an internuclear distance of 2.28187 bohr for geometry 105-0-60-60

Intermolecular Distance (bohr)	μ_z (singlet)	μ_z (triplet)	μ_z (quintet)
5	-0.001132967	-0.002726543	-0.006380962
6	0.001419402	0.001157685	0.000632795
8	0.000761469	0.00075914	0.000761863
10	0.000237468	0.000251805	0.000250892
12	0.000143739	0.000102293	0.000100046
15	-5.455E-05	3.9957E-05	4.45315E-05
20	1.14425E-05	1.1644E-05	1.379E-05

Table 131. The z-component of the collision-induced dipole moment at an internuclear distance of 2.296 bohr for geometry 105-0-60-60

Intermolecular Distance (bohr)	μ_z (singlet)	μ_z (triplet)	μ_z (quintet)
5	-0.03191	-0.03494	-0.04531
6	-0.01275	-0.01282	-0.01292
8	-0.0016	-0.00156	-0.00152
10	-0.00044	-0.00039	-0.00038
12	-0.00015	-0.00017	-0.00017
15	-9.5E-05	-9.5E-05	-9.5E-05
20	-3.2E-05	-3.2E-05	-3.2E-05

Table 132. The z-component of the collision-induced dipole moment at an internuclear distance of 2.36 bohr for geometry 105-0-60-60

Intermolecular Distance (bohr)	μ_z (singlet)	μ_z (triplet)	μ_z (quintet)
5	-0.05232	-0.05337	-0.05224
6	-0.01567	-0.01513	-0.01399
8	-0.0016	-0.00157	-0.0015
10	-0.00036	-0.00036	-0.00035
12	-0.00016	-0.00016	-0.00016
15	-9.1E-05	-9.2E-05	-9.1E-05
20	-3.1E-05	-3.1E-05	-3.1E-05

Table 133. The z-component of the collision-induced dipole moment at an internuclear distance of 2.457 bohr for geometry 105-0-60-60

Intermolecular Distance (bohr)	μ_z (singlet)	μ_z (triplet)	μ_z (quintet)
5	-0.08038	-0.07898	-0.06135
6	-0.01982	-0.0184	-0.01546
8	-0.00164	-0.00158	-0.00145
10	-0.00033	-0.00031	-0.00031
12	-0.00014	-0.00013	-0.00014
15	-8.5E-05	-8.6E-05	-8.5E-05
20	-3E-05	-3E-05	-3E-05

Table 134. The z-component of the collision-induced dipole moment at an internuclear distance of 2.646 bohr for geometry 105-0-60-60

Intermolecular Distance (bohr)	μ_z (singlet)	μ_z (triplet)	μ_z (quintet)
5	-0.11795	-0.1132	-0.06928
6	-0.02597	-0.02306	-0.017
8	-0.00161	-0.0015	-0.00128
10	-0.0002	-0.0002	-0.00019
12	-8.6E-05	-8.3E-05	-8.5E-05
15	-6.8E-05	-6.9E-05	-6.8E-05
20	-2.5E-05	-2.4E-05	-2.5E-05

Table 135. The z-component of the collision-induced dipole moment at an internuclear distance of 2.929 bohr for geometry 105-0-60-60

Intermolecular Distance (bohr)	μ_z (singlet)	μ_z (triplet)	μ_z (quintet)
5	-0.16734	-0.15969	-0.07316
6	-0.02852	-0.02436	-0.01477
8	-0.00131	-0.00114	-0.00079
10	2.87E-05	3.91E-05	4.64E-05
12	1.76E-05	1.83E-05	1.83E-05
15	-3.1E-05	-3.1E-05	-3.1E-05
20	-1.3E-05	-1.3E-05	-1.3E-05

Table 136. The z-component of the collision-induced dipole moment at an internuclear distance of 3.213 bohr for geometry 105-0-60-60

Intermolecular Distance (bohr)	μ_z (singlet)	μ_z (triplet)	μ_z (quintet)
5	-0.2682	-0.27247	-0.15093
6	-0.01299	-0.00832	0.0025
8	-0.00077	-0.00061	-0.00012
10	0.000259	0.000261	0.000284
12	0.000118	0.000118	0.000119
15	3.83E-06	3.81E-06	4E-06
20	-3.3E-06	-3.3E-06	-3.2E-06

Table 137. The z-component of the collision-induced dipole moment at an internuclear distance of 3.3 bohr for geometry 105-0-60-60

Intermolecular Distance (bohr)	μ_z (singlet)	μ_z (triplet)	μ_z (quintet)
5	-0.28948	0.057572	-0.17492
6	-0.01172	-0.00248	0.010214
8	-0.00031	-0.00166	0.000345
10	0.000337	-0.00053	0.000364
12	0.000149	-0.00026	0.00015
15	1.38E-05	-0.00012	1.42E-05
20	-6.3E-07	-3.8E-05	-5E-07

Table 138. The z-component of the collision-induced dipole moment at an internuclear distance of 2 bohr for geometry 40-0-115-45

Intermolecular Distance (bohr)	μ_z (singlet)	μ_z (triplet)	μ_z (quintet)
5	0.065926	0.050802	-0.00286
6	0.003377	0.000121	-0.00634
8	-0.00165	-0.00176	-0.00198
10	-0.00066	-0.00067	-0.00067
12	-0.00031	-0.00031	-0.00031
15	0.038356	0.0394	0.039311
20	-3.9E-05	-3.9E-05	-3.9E-05

Table 139. The z-component of the collision-induced dipole moment at an internuclear distance of 2.1 bohr for geometry 40-0-115-45

Intermolecular Distance (bohr)	μ_z (singlet)	μ_z (triplet)	μ_z (quintet)
5	0.03431	0.025402	-0.00673
6	-0.00065	-0.00246	-0.00607
8	-0.00155	-0.0016	-0.00171
10	-0.00057	-0.00056	-0.00057
12	-0.00026	-0.00026	-0.00026
15	0.067413	0.068411	0.068327
20	-3.5E-05	-3.5E-05	-3.5E-05

Table 140. The z-component of the collision-induced dipole moment at an internuclear distance of 2.2 bohr for geometry 40-0-115-45

Intermolecular Distance (bohr)	μ_z (singlet)	μ_z (triplet)	μ_z (quintet)
5	0.005545	0.001866	-0.01217
6	-0.00449	-0.00514	-0.00638
8	-0.00145	-0.00148	-0.00151
10	-0.00047	-0.00047	-0.00047
12	-0.00021	-0.00021	-0.00021
15	0.116811	0.117725	0.117654
20	-3.1E-05	-3.1E-05	-3.1E-05

Table 141. The z-component of the collision-induced dipole moment at an internuclear distance of 2.28187 bohr for geometry 40-0-115-45

Intermolecular Distance (bohr)	μ_z (singlet)	μ_z (triplet)	μ_z (quintet)
5	-0.01677	-0.01672899	-0.0173
6	-0.00756	-0.00736159	-0.0069
8	-0.0014	-0.00139343	-0.00138
10	-0.00044	-0.00039839	-0.0004
12	-0.00013	-0.00017371	-0.00017
15	0.000193	-8.6111E-05	-8.6E-05
20	-2.8E-05	-2.7504E-05	-2.8E-05

Table 142. The z-component of the collision-induced dipole moment at an internuclear distance of 2.296 bohr for geometry 40-0-115-45

Intermolecular Distance (bohr)	μ_z (singlet)	μ_z (triplet)	μ_z (quintet)
5	-0.02051	-0.01987	-0.01821
6	-0.00808	-0.00774	-0.007
8	-0.0014	-0.00138	-0.00135
10	-0.00039	-0.00038	-0.00039
12	-0.00016	-0.00016	-0.00017
15	-8.4E-05	-8.4E-05	-8.4E-05
20	-2.7E-05	-2.7E-05	-2.7E-05

Table 143. The z-component of the collision-induced dipole moment at an internuclear distance of 2.36 bohr for geometry 40-0-115-45

Intermolecular Distance (bohr)	μ_z (singlet)	μ_z (triplet)	μ_z (quintet)
5	-0.03692	-0.03376	-0.02223
6	-0.01039	-0.00943	-0.00748
8	-0.00131	-0.00131	-0.00125
10	-0.00033	-0.00033	-0.00033
12	-0.00014	-0.00014	-0.00014
15	-7.5E-05	-7.5E-05	-7.5E-05
20	-2.4E-05	-2.4E-05	-2.4E-05

Table 144. The z-component of the collision-induced dipole moment at an internuclear distance of 2.457 bohr for geometry 40-0-115-45

Intermolecular Distance (bohr)	μ_z (singlet)	μ_z (triplet)	μ_z (quintet)
5	-0.05954	-0.05315	-0.02753
6	-0.01371	-0.0118	-0.00811
8	-0.00128	-0.00122	-0.0011
10	-0.00027	-0.00025	-0.00025
12	-0.0001	-9.7E-05	-0.0001
15	-6.1E-05	-6.1E-05	-6.1E-05
20	-2E-05	-2E-05	-2E-05

Table 145. The z-component of the collision-induced dipole moment at an internuclear distance of 2.646 bohr for geometry 40-0-115-45

Intermolecular Distance (bohr)	μ_z (singlet)	μ_z (triplet)	μ_z (quintet)
5	-0.09051	-0.01992	-0.03169
6	-0.01836	-0.00378	-0.0085
8	-0.0011	-0.00024	-0.00074
10	-7.2E-05	-1.7E-05	-6.2E-05
12	-1.8E-05	-3.2E-06	-1.7E-05
15	-3E-05	-7.9E-06	-3E-05
20	-1E-05	-2.6E-06	-1E-05

Table 146. The z-component of the collision-induced dipole moment at an internuclear distance of 2.929 bohr for geometry 40-0-115-45

Intermolecular Distance (bohr)	μ_z (singlet)	μ_z (triplet)	μ_z (quintet)
5	-0.12162	-0.10790316	-0.02241
6	-0.02035	-0.01593643	-0.00633
8	-0.0006	-0.00043337	-8.6E-05
10	0.000215	0.000173164	0.000231
12	0.000114	0.00011396	0.000114
15	1.95E-05	1.9518E-05	1.94E-05
20	5.26E-06	5.32802E-06	5.28E-06

Table 147. The z-component of the collision-induced dipole moment at an internuclear distance of 3.213 bohr for geometry 40-0-115-45

Intermolecular Distance (bohr)	μ_z (singlet)	μ_z (triplet)	μ_z (quintet)
5	-0.22056	-0.2266882	-0.07412
6	-0.00565	-0.00089932	0.007251
8	-3.4E-05	0.00018111	0.00061
10	0.000463	0.000467813	0.000486
12	0.000225	0.000225785	0.000226
15	6.02E-05	6.02215E-05	6.04E-05
20	1.78E-05	1.78185E-05	1.79E-05

Table 148. The z-component of the collision-induced dipole moment at an internuclear distance of 3.3 bohr for geometry 40-0-115-45

Intermolecular Distance (bohr)	μ_z (singlet)	μ_z (triplet)	μ_z (quintet)
5	-0.24612	-0.25325903	-0.10001
6	0.002133	0.009164444	0.01855
8	0.000353	0.000567235	0.000983
10	0.000538	0.000545603	0.000563
12	0.000256	0.000256543	0.000257
15	7.03E-05	7.13705E-05	7.1E-05
20	2.1E-05	2.0973E-05	2.11E-05

Table 149. The z-component of the collision-induced dipole moment at an internuclear distance of 2 bohr for geometry 20-0-115-45

Intermolecular Distance (bohr)	μ_z (singlet)	μ_z (triplet)	μ_z (quintet)
5	0.019952	0.004181	-0.03697
6	-0.01055	-0.01241	-0.01592
8	-0.00297	-0.00298	-0.00295
10	-0.00096	-0.00096	-0.00095
12	-0.00046	-0.00046	-0.00046
15	-0.00021	-0.0002	-0.00021
20	-6.3E-05	-6.2E-05	-6.3E-05

Table 150. The z-component of the collision-induced dipole moment at an internuclear distance of 2.1 bohr for geometry 20-0-115-45

Intermolecular Distance (bohr)	μ_z (singlet)	μ_z (triplet)	μ_z (quintet)
5	-0.00503	-0.01676	-0.04593
6	-0.01274	-0.01397	-0.01626
8	-0.00261	-0.00261	-0.00258
10	-0.00078	-0.00079	-0.00079
12	-0.00038	-0.00038	-0.00038
15	0.067363	-0.00018	0.06828
20	-5.6E-05	-5.6E-05	-5.6E-05

Table 151. The z-component of the collision-induced dipole moment at an internuclear distance of 2.2 bohr for geometry 20-0-115-45

Intermolecular Distance (bohr)	μ_z (singlet)	μ_z (triplet)	μ_z (quintet)
5	-0.02817	-0.03662	-0.05655
6	-0.01514	-0.01586	-0.01723
8	-0.00233	-0.00232	-0.00227
10	-0.00065	-0.00065	-0.00064
12	-0.0003	-0.0003	-0.0003
15	0.116778	0.117691	0.117621
20	-5E-05	-5E-05	-5E-05

Table 152. The z-component of the collision-induced dipole moment at an internuclear distance of 2.28187 bohr for geometry 20-0-115-45

Intermolecular Distance (bohr)	μ_z (singlet)	μ_z (triplet)	μ_z (quintet)
5	-0.04591	-0.05232	-0.06581
6	-0.01722	-0.0176	-0.0183
8	-0.00212	-0.00211	-0.00206
10	-0.00054	-0.00053	-0.00053
12	-0.00028	-0.00024	-0.00025
15	-0.00044	-0.00013	-0.00013
20	-4.6E-05	-4.5E-05	-4.5E-05

Table 153. The z-component of the collision-induced dipole moment at an internuclear distance of 2.296 bohr for geometry 20-0-115-45

Intermolecular Distance (bohr)	μ_z (singlet)	μ_z (triplet)	μ_z (quintet)
5	-0.04888	-0.06646	-0.0674
6	-0.01756	-0.01924	-0.01849
8	-0.00209	-0.00193	-0.00203
10	-0.00055	-0.00042	-0.00051
12	-0.00025	-0.0002	-0.00024
15	-0.00013	-0.00011	-0.00013
20	-4.4E-05	-4E-05	-4.4E-05

Table 154. The z-component of the collision-induced dipole moment at an internuclear distance of 2.36 bohr for geometry 20-0-115-45

Intermolecular Distance (bohr)	μ_z (singlet)	μ_z (triplet)	μ_z (quintet)
5	-0.06186	-0.06646	-0.07434
6	-0.01909	-0.01924	-0.01938
8	-0.00196	-0.00193	-0.00187
10	-0.00042	-0.00042	-0.00042
12	-0.0002	-0.0002	-0.0002
15	-0.00011	-0.00011	-0.00011
20	-4E-05	-4E-05	-4E-05

Table 155. The z-component of the collision-induced dipole moment at an internuclear distance of 2.457 bohr for geometry 20-0-115-45

Intermolecular Distance (bohr)	μ_z (singlet)	μ_z (triplet)	μ_z (quintet)
5	-0.07941	-0.08191	-0.08318
6	-0.02134	-0.02107	-0.02057
8	-0.00173	-0.00168	-0.00164
10	-0.00028	-0.00029	-0.00029
12	-0.00014	-0.00014	-0.00014
15	-9.3E-05	-9.3E-05	-9.3E-05
20	-3.3E-05	-3.3E-05	-3.3E-05

Table 156. The z-component of the collision-induced dipole moment at an internuclear distance of 2.646 bohr for geometry 20-0-115-45

Intermolecular Distance (bohr)	μ_z (singlet)	μ_z (triplet)	μ_z (quintet)
5	-0.10192	-0.10135	-0.09023
6	-0.02419	-0.02331	-0.02162
8	-0.00128	-0.00123	-0.00115
10	-2.4E-05	-2.2E-05	-1.8E-05
12	-1.3E-05	-1.8E-05	-1.3E-05
15	-4.9E-05	-4.9E-05	-4.9E-05
20	-2E-05	-2E-05	-2E-05

Table 157. The z-component of the collision-induced dipole moment at an internuclear distance of 2.929 bohr for geometry 20-0-115-45

Intermolecular Distance (bohr)	μ_z (singlet)	μ_z (triplet)	μ_z (quintet)
5	-0.111	-0.11094	-0.09181
6	-0.02441	-0.02267	-0.01904
8	-0.00053	-0.00047	-0.00035
10	0.000371	0.000373	0.000378
12	0.000166	0.000183	0.000166
15	1.75E-05	1.74E-05	1.74E-05
20	1.42E-06	1.43E-06	1.42E-06

Table 158. The z-component of the collision-induced dipole moment at an internuclear distance of 3.213 bohr for geometry 20-0-115-45

Intermolecular Distance (bohr)	μ_z (singlet)	μ_z (triplet)	μ_z (quintet)
5	-0.16961	-0.15148	-0.13925
6	-0.01227	-0.00982	-0.00368
8	0.000219	0.000311	0.000495
10	0.000701	0.000705	0.000711
12	0.000312	0.00033	0.000313
15	7.19E-05	7.22E-05	7.2E-05
20	1.8E-05	1.8E-05	1.82E-05

Table 159. The z-component of the collision-induced dipole moment at an internuclear distance of 3.3 bohr for geometry 20-0-115-45

Intermolecular Distance (bohr)	μ_z (singlet)	μ_z (triplet)	μ_z (quintet)
5	-0.18937	-0.17686	-0.15273
6	-0.00435	-0.0018	0.003677
8	0.000615	0.000718	0.000944
10	0.000798	0.000778	0.00081
12	0.000353	0.000354	0.000354
15	8.62E-05	8.44E-05	8.65E-05
20	2.23E-05	2.23E-05	2.24E-05

Table 160. The z-component of the collision-induced dipole moment at an internuclear distance of 2 bohr for geometry 15-0-75-30

Intermolecular Distance (bohr)	μ_z (singlet)	μ_z (triplet)	μ_z (quintet)
5	0.086681	0.070393	-0.01745
6	-0.0007	-0.00557	-0.01598
8	-0.00465	-0.00478	-0.00505
10	-0.00184	-0.00185	-0.00185
12	-0.00084	-0.00084	-0.00084
15	-0.00035	-0.00035	-0.00035
20	-0.00011	-0.00011	-0.00011

Table 161. The z-component of the collision-induced dipole moment at an internuclear distance of 2.1 bohr for geometry 15-0-75-30

Intermolecular Distance (bohr)	μ_z (singlet)	μ_z (triplet)	μ_z (quintet)
5	0.048914	0.038865	-0.01755
6	-0.00502	-0.00803	-0.01453
8	-0.00398	-0.00405	-0.0042
10	-0.00147	-0.00147	-0.00148
12	-0.00066	-0.00066	-0.00066
15	-0.00028	-0.00028	-0.00028
20	-9.2E-05	-9.2E-05	-9.2E-05

Table 162. The z-component of the collision-induced dipole moment at an internuclear distance of 2.2 bohr for geometry 15-0-75-30

Intermolecular Distance (bohr)	μ_z (singlet)	μ_z (triplet)	μ_z (quintet)
5	0.018333	0.01355	-0.01843
6	-0.00832	-0.00992	-0.01346
8	-0.00329	-0.00334	-0.00342
10	-0.00114	-0.00111	-0.00112
12	-0.00049	-0.00049	-0.00049
15	-0.00022	-0.00022	-0.00022
20	-7.3E-05	-7.3E-05	-7.3E-05

Table 163. The z-component of the collision-induced dipole moment at an internuclear distance of 2.28187 bohr for geometry 15-0-75-30

Intermolecular Distance (bohr)	μ_z (singlet)	μ_z (triplet)	μ_z (quintet)
5	-0.00325	-0.00442	-0.01941
6	-0.01059	-0.01123	-0.01275
8	-0.00275	-0.00277	-0.0028
10	-0.00082	-0.00083	-0.00083
12	-0.00034	-0.00036	-0.00035
15	-0.00029	-0.00017	-0.00017
20	-5.8E-05	-5.8E-05	-5.8E-05

Table 164. The z-component of the collision-induced dipole moment at an internuclear distance of 2.296 bohr for geometry 15-0-75-30

Intermolecular Distance (bohr)	μ_z (singlet)	μ_z (triplet)	μ_z (quintet)
5	-0.00679	-0.00733	-0.01959
6	-0.01095	-0.01144	-0.01263
8	-0.00262	-0.00268	-0.0027
10	-0.00079	-0.00078	-0.00078
12	-0.00034	-0.00032	-0.00033
15	0.031621	0.032044	0.031999
20	-5.5E-05	-5.5E-05	-5.5E-05

Table 165. The z-component of the collision-induced dipole moment at an internuclear distance of 2.36 bohr for geometry 15-0-75-30

Intermolecular Distance (bohr)	μ_z (singlet)	μ_z (triplet)	μ_z (quintet)
5	-0.02191	-0.01993	-0.02032
6	-0.01247	-0.01231	-0.01212
8	-0.00228	-0.00225	-0.00224
10	-0.00057	-0.00055	-0.00056
12	-0.00023	-0.00023	-0.00023
15	-0.00012	-0.00012	-0.00012
20	-4.3E-05	-4.3E-05	-4.3E-05

Table 166. The z-component of the collision-induced dipole moment at an internuclear distance of 2.457 bohr for geometry 15-0-75-30

Intermolecular Distance (bohr)	μ_z (singlet)	μ_z (triplet)	μ_z (quintet)
5	-0.04252	-0.03722	-0.02108
6	-0.01449	-0.01343	-0.01136
8	-0.00165	-0.00165	-0.00157
10	-0.00027	-0.00025	-0.00025
12	-8E-05	-7.9E-05	-8.3E-05
15	-6.9E-05	-6.9E-05	-6.9E-05
20	-2.6E-05	-2.6E-05	-2.6E-05

Table 167. The z-component of the collision-induced dipole moment at an internuclear distance of 2.646 bohr for geometry 15-0-75-30

Intermolecular Distance (bohr)	μ_z (singlet)	μ_z (triplet)	μ_z (quintet)
5	-0.07394	-0.06404	-0.02037
6	-0.01746	-0.01489	-0.00968
8	-0.00058	-0.00051	-0.00039
10	0.000303	0.000303	0.000307
12	0.000176	0.000174	0.000176
15	2.85E-05	2.65E-05	2.8E-05
20	5.79E-06	5.8E-06	5.78E-06

Table 168. The z-component of the collision-induced dipole moment at an internuclear distance of 2.929 bohr for geometry 15-0-75-30

Intermolecular Distance (bohr)	μ_z (singlet)	μ_z (triplet)	μ_z (quintet)
5	-0.09259	-0.07977	-0.01033
6	-0.01944	-0.01529	-0.00664
8	0.000688	0.000805	0.001015
10	0.000953	0.000954	0.00096
12	0.000479	0.000475	0.000479
15	0.000142	0.000143	0.000143
20	4.38E-05	4.39E-05	4.38E-05

Table 169. The z-component of the collision-induced dipole moment at an internuclear distance of 3.213 bohr for geometry 15-0-75-30

Intermolecular Distance (bohr)	μ_z (singlet)	μ_z (triplet)	μ_z (quintet)
5	-0.52802	-0.12604	0.003248
6	-0.27869	-0.00923	-0.00024
8	-0.20843	0.00164	0.001981
10	-0.20093	0.001402	0.001392
12	-0.19875	0.000682	0.000682
15	-0.19739	0.000219	0.000222
20	-0.19652	7E-05	7E-05

Table 170. The z-component of the collision-induced dipole moment at an internuclear distance of 3.3 bohr for geometry 15-0-75-30

Intermolecular Distance (bohr)	μ_z (singlet)	μ_z (triplet)	μ_z (quintet)
5	-0.14985	-0.46116	-0.01022
6	-0.00598	-0.26671	0.00592
8	0.001817	-0.21133	0.00226
10	0.001479	-0.20381	0.001492
12	0.000729	-0.20149	0.000729
15	0.000241	-0.20009	0.00024
20	7.61E-05	-0.19923	7.61E-05

Table 171. The z-component of the collision-induced dipole moment at an internuclear distance of 2 bohr for geometry 15-0-95-10

Intermolecular Distance (bohr)	μ_z (singlet)	μ_z (triplet)	μ_z (quintet)
5	0.034444	0.020291	-0.01609
6	-0.00925	-0.01144	-0.01572
8	-0.00526	-0.00531	-0.0054
10	-0.00204	-0.00204	-0.00204
12	-0.00093	-0.00093	-0.00093
15	-0.00038	-0.00039	-0.00038
20	-0.00012	-0.00012	-0.00012

Table 172. The z-component of the collision-induced dipole moment at an internuclear distance of 2.1 bohr for geometry 15-0-95-10

Intermolecular Distance (bohr)	μ_z (singlet)	μ_z (triplet)	μ_z (quintet)
5	0.015009	0.006193	-0.0169
6	-0.0105	-0.01183	-0.01443
8	-0.00443	-0.00446	-0.0045
10	-0.00162	-0.00162	-0.00163
12	-0.00073	-0.00073	-0.00073
15	-0.00031	-0.00031	-0.00031
20	-0.0001	-0.0001	-0.0001

Table 173. The z-component of the collision-induced dipole moment at an internuclear distance of 2.2 bohr for geometry 15-0-95-10

Intermolecular Distance (bohr)	μ_z (singlet)	μ_z (triplet)	μ_z (quintet)
5	-0.00024	-0.00499	-0.01819
6	-0.01131	-0.01199	-0.01338
8	-0.0036	-0.00361	-0.00364
10	-0.00124	-0.00122	-0.00122
12	-0.00054	-0.00054	-0.00054
15	0.047317	-0.00024	-0.00024
20	-7.9E-05	-7.9E-05	-7.9E-05

Table 174. The z-component of the collision-induced dipole moment at an internuclear distance of 2.28187 bohr for geometry 15-0-95-10

Intermolecular Distance (bohr)	μ_z (singlet)	μ_z (triplet)	μ_z (quintet)
5	-0.01093	-0.01284	-0.0194
6	-0.01179	-0.01206	-0.01264
8	-0.00293	-0.00295	-0.00297
10	-0.0009	-0.00091	-0.00091
12	-0.00057	-0.00039	-0.0004
15	-0.00022	-0.00018	-0.00019
20	-6.3E-05	-6.2E-05	-6.2E-05

Table 175. The z-component of the collision-induced dipole moment at an internuclear distance of 2.296 bohr for geometry 15-0-95-10

Intermolecular Distance (bohr)	μ_z (singlet)	μ_z (triplet)	μ_z (quintet)
5	-0.01263	0.019361	-0.01962
6	-0.01199	-0.00637	-0.01252
8	-0.00283	-0.00238	-0.00285
10	-0.00082	-0.00063	-0.00085
12	-0.00037	-0.0003	-0.00037
15	-0.00018	-0.00015	-0.00018
20	-5.9E-05	-6.5E-05	-5.9E-05

Table 176. The z-component of the collision-induced dipole moment at an internuclear distance of 2.36 bohr for geometry 15-0-95-10

Intermolecular Distance (bohr)	μ_z (singlet)	μ_z (triplet)	μ_z (quintet)
5	-0.02005	-0.0196	-0.02058
6	-0.01217	-0.01209	-0.012
8	-0.00239	-0.00234	-0.00235
10	-0.00062	-0.00061	-0.00061
12	-0.00026	-0.00025	-0.00026
15	-0.00013	-0.00013	-0.00013
20	-4.6E-05	-4.6E-05	-4.6E-05

Table 177 The z-component of the collision-induced dipole moment at an internuclear distance of 2.457 bohr for geometry 15-0-95-10

Intermolecular Distance (bohr)	μ_z (singlet)	μ_z (triplet)	μ_z (quintet)
5	-0.03033	-0.02721	-0.00877
6	-0.01263	-0.01209	-0.0045
8	-0.00163	-0.00167	-0.00065
10	-0.00027	-0.00026	-0.00011
12	-9.4E-05	-9.3E-05	-3.8E-05
15	-7.3E-05	-7.3E-05	-2.9E-05
20	-2.7E-05	-2.7E-05	-1.1E-05

Table 178. The z-component of the collision-induced dipole moment at an internuclear distance of 2.646 bohr for geometry 15-0-95-10

Intermolecular Distance (bohr)	μ_z (singlet)	μ_z (triplet)	μ_z (quintet)
5	-0.04768	-0.03993	-0.02356
6	-0.01309	-0.012	-0.00993
8	-0.00037	-0.00035	-0.00032
10	0.000353	0.000353	0.000352
12	0.000193	0.000192	0.000193
15	3.49E-05	3.49E-05	3.48E-05
20	8.75E-06	8.78E-06	8.74E-06

Table 179. The z-component of the collision-induced dipole moment at an internuclear distance of 2.929 bohr for geometry 15-0-95-10

Intermolecular Distance (bohr)	μ_z (singlet)	μ_z (triplet)	μ_z (quintet)
5	-0.06708	-0.05342	-0.02161
6	-0.01363	-0.01175	-0.00811
8	0.001076	0.001112	0.001172
10	0.001068	0.001074	0.001069
12	0.000528	0.000528	0.000528
15	0.000163	0.000163	0.000163
20	5.16E-05	5.16E-05	5.16E-05

Table 180. The z-component of the collision-induced dipole moment at an internuclear distance of 3.213 bohr for geometry 15-0-95-10

Intermolecular Distance (bohr)	μ_z (singlet)	μ_z (triplet)	μ_z (quintet)
5	-0.07534	-0.05263	-0.01354
6	-0.01353	-0.01085	-0.0053
8	0.001996	0.002053	0.002147
10	0.001531	0.001534	0.001534
12	0.00075	0.00075	0.00075
15	0.00025	0.00025	0.000251
20	8.1E-05	8.1E-05	8.11E-05

Table 181. The z-component of the collision-induced dipole moment at an internuclear distance of 3.3 bohr for geometry 15-0-95-10

Intermolecular Distance (bohr)	μ_z (singlet)	μ_z (triplet)	μ_z (quintet)
5	-0.07207	-0.04574	-0.0169
6	-0.01309	-0.00986	-0.00282
8	0.002209	0.00227	0.00238
10	0.001635	0.001635	0.001639
12	0.0008	0.000801	0.000801
15	0.00027	0.00027	0.000271
20	8.79E-05	8.78E-05	8.79E-05

Table 182. The z-component of the collision-induced dipole moment at an internuclear distance of 2 bohr for geometry 10-0-160-15

Intermolecular Distance (bohr)	μ_z (singlet)	μ_z (triplet)	μ_z (quintet)
5	0.365406	0.202099	-0.010841206
6	0.054463	0.03809	0.012776947
8	0.00583	0.005567	0.006065028
10	0.002047	0.002045	0.002651276
12	0.000933	0.000934	0.00130332
15	0.000384	0.000385	0.000556095
20	0.000124	0.000124	0.000179697

Table 183. The z-component of the collision-induced dipole moment at an internuclear distance of 2.1 bohr for geometry 10-0-160-15

Intermolecular Distance (bohr)	μ_z (singlet)	μ_z (triplet)	μ_z (quintet)
5	0.231097	0.111604	-0.046575872
6	0.031765	0.021397	0.004850827
8	0.003772	0.003617	0.003348964
10	0.001366	0.001369	0.001367184
12	0.000617	0.000619	0.000617186
15	0.067721	0.068723	0.068637251
20	7.98E-05	7.97E-05	7.975E-05

Table 184. The z-component of the collision-induced dipole moment at an internuclear distance of 2.2 bohr for geometry 10-0-160-15

Intermolecular Distance (bohr)	μ_z (singlet)	μ_z (triplet)	μ_z (quintet)
5	0.102549	0.020091	-0.096361072
6	0.009832	0.004427	-0.004227737
8	0.001612	0.00154	0.001440999
10	0.000652	0.000647	0.00065081
12	0.000279	0.000279	0.000279186
15	0.11701	0.117924	0.117852914
20	3.39E-05	3.39E-05	3.39265E-05

Table 185. The z-component of the collision-induced dipole moment at an internuclear distance of 2.28187 bohr for geometry 10-0-160-15

Intermolecular Distance (bohr)	μ_z (singlet)	μ_z (triplet)	μ_z (quintet)
5	-0.04113	-0.06164	-0.146201016
6	-0.00856	-0.00957	-0.012720113
8	-0.00024	-0.00024	-0.000211757
10	5.25E-05	3.6E-05	4.7051E-05
12	-0.00016	-3.4E-06	-3.79148E-06
15	8.16E-05	-1.5E-05	-9.6405E-06
20	0.000162	-6.6E-06	-3.7785E-06

Table 186. The z-component of the collision-induced dipole moment at an internuclear distance of 2.296 bohr for geometry 10-0-160-15

Intermolecular Distance (bohr)	μ_z (singlet)	μ_z (triplet)	μ_z (quintet)
5	-0.01892	-0.06966	-0.155560463
6	-0.01175	-0.01255	-0.014269185
8	-0.00064	-0.00054	-0.000502449
10	-7.3E-05	-6.1E-05	-5.72165E-05
12	-5.9E-05	-5.3E-05	-5.3132E-05
15	-3.1E-05	-3.1E-05	-3.1221E-05
20	-1E-05	-1E-05	-1.0256E-05

Table 187. The z-component of the collision-induced dipole moment at an internuclear distance of 2.36 bohr for geometry 10-0-160-15

Intermolecular Distance (bohr)	μ_z (singlet)	μ_z (triplet)	μ_z (quintet)
5	-0.12903	-0.06966	-0.200464723
6	-0.0243	-0.01255	-0.021580441
8	-0.00194	-0.00054	-0.001819628
10	-0.00053	-6.1E-05	-0.000526257
12	-0.00027	-5.3E-05	-0.000272184
15	-0.00012	-3.1E-05	-0.000121481
20	-3.9E-05	-1E-05	-3.90655E-05

Table 188. The z-component of the collision-induced dipole moment at an internuclear distance of 2.457 bohr for geometry 10-0-160-15

Intermolecular Distance (bohr)	μ_z (singlet)	μ_z (triplet)	μ_z (quintet)
5	-0.21439	-0.21414	-0.276151875
6	-0.04974	-0.04287	-0.033622997
8	-0.00416	-0.00403	-0.003789075
10	-0.00125	-0.00122	-0.001208922
12	-0.00059	-0.00058	-0.000588761
15	-0.00025	-0.00025	-0.000251332
20	-8E-05	-8E-05	-8.0317E-05

Table 189. The z-component of the collision-induced dipole moment at an internuclear distance of 2.646 bohr for geometry 10-0-160-15

Intermolecular Distance (bohr)	μ_z (singlet)	μ_z (triplet)	μ_z (quintet)
5	-0.41577	-0.40002	-0.458151182
6	-0.09931	-0.08351	-0.062456951
8	-0.00804	-0.00779	-0.007312326
10	-0.00237	-0.00236	-0.002352078
12	-0.00111	-0.00111	-0.001111405
15	-0.00046	-0.00046	-0.000463808
20	-0.00015	-0.00015	-0.000147402

Table 190. The z-component of the collision-induced dipole moment at an internuclear distance of 2.929 bohr for geometry 10-0-160-15

Intermolecular Distance (bohr)	μ_z (singlet)	μ_z (triplet)	μ_z (quintet)
5	-0.00029	-0.50865	-0.54798761
6	2.15E-06	-0.16958	-0.132947468
8	-3.1E-08	-0.01253	-0.011730657
10	-9.9E-10	-0.00354	-0.00351567
12	5.12E-10	-0.00163	-0.001631469
15	2.98E-09	-0.00067	-0.000674148
20	-4.8E-10	-0.00021	-0.000212946

Table 191. The z-component of the collision-induced dipole moment at an internuclear distance of 3.213 bohr for geometry 10-0-160-15

Intermolecular Distance (bohr)	μ_z (singlet)	μ_z (triplet)	μ_z (quintet)
5	-0.18852	0.029837	-1.93008005
6	-0.32304	0.433593	-0.251160581
8	-0.0174	0.732041	-0.015631827
10	-0.00422	0.728828	-0.004185123
12	-0.00193	0.722891	-0.00192752
15	-0.0008	0.718157	-0.000797123
20	-0.00025	0.714536	-0.000251578

Table 192. The z-component of the collision-induced dipole moment at an internuclear distance of 3.3 bohr for geometry 10-0-160-15

Intermolecular Distance (bohr)	μ_z (singlet)	μ_z (triplet)	μ_z (quintet)
5	-0.23929	-0.00366	0.166188261
6	-0.36813	0.384309	-0.305979138
8	-0.01862	0.74055	-0.01665117
10	-0.00435	0.738684	-0.004312118
12	-0.00199	0.732818	-0.001984403
15	-0.00082	0.727945	-0.000821525
20	-0.00026	0.724468	-0.000259672

Table 193. The z-component of the collision-induced dipole moment at an internuclear distance of 2 bohr for geometry 20-0-145-25

Intermolecular Distance (bohr)	μ_z (singlet)	μ_z (triplet)	μ_z (quintet)
5	0.282384	0.161716	-0.03608645
6	0.030805	0.019108	-0.00068699
8	0.003417	0.003215	0.002849082
10	0.001327	0.001323	0.001320641
12	0.000571	0.000573	0.000573525
15	0.000222	0.000221	0.000222171
20	7.45E-05	7.45E-05	7.4466E-05

Table 194. The z-component of the collision-induced dipole moment at an internuclear distance of 2.1 bohr for geometry 20-0-145-25

Intermolecular Distance (bohr)	μ_z (singlet)	μ_z (triplet)	μ_z (quintet)
5	0.173167	0.084347	-0.06598896
6	0.014504	0.006983	-0.00594467
8	0.002079	0.001973	0.001787188
10	0.000893	0.00088	0.000881377
12	0.000373	0.000375	0.000373269
15	0.067628	0.068629	0.068543665
20	4.49E-05	4.48E-05	4.48475E-05

Table 195. The z-component of the collision-induced dipole moment at an internuclear distance of 2.2 bohr for geometry 20-0-145-25

Intermolecular Distance (bohr)	μ_z (singlet)	μ_z (triplet)	μ_z (quintet)
5	0.071043	0.008275	-0.10434333
6	-0.00139	-0.00553	-0.01281815
8	0.000399	0.000612	0.000564775
10	0.000406	0.000417	0.000409936
12	0.000154	0.000155	0.000155531
15	0.116954	0.117867	0.117796404
20	1.42E-05	1.42E-05	1.42375E-05

Table 196. The z-component of the collision-induced dipole moment at an internuclear distance of 2.28187 bohr for geometry 20-0-145-25

Intermolecular Distance (bohr)	μ_z (singlet)	μ_z (triplet)	μ_z (quintet)
5	-0.01031	-0.05433845	-0.14083996
6	-0.01453	-0.01617649	-0.01935133
8	-0.00057	-0.00055559	-0.00050836
10	-3.6E-05	9.23802E-06	1.3633E-05
12	0.000191	-3.3215E-05	-2.8163E-05
15	-4.4E-05	-2.7751E-05	-3.4404E-05
20	-8.8E-06	-7.4025E-06	-1.0908E-05

Table 197. The z-component of the collision-induced dipole moment at an internuclear distance of 2.296 bohr for geometry 20-0-145-25

Intermolecular Distance (bohr)	μ_z (singlet)	μ_z (triplet)	μ_z (quintet)
5	-0.02417	-0.06512	-0.14747054
6	-0.01688	-0.01805	-0.02054002
8	-0.00086	-0.00076	-0.00069694
10	-8.3E-05	-6.7E-05	-5.4927E-05
12	-5.5E-05	-5.6E-05	-6.0237E-05
15	-4.4E-05	-4.4E-05	-4.4146E-05
20	-1.5E-05	-1.5E-05	-1.522E-05

Table 198. The z-component of the collision-induced dipole moment at an internuclear distance of 2.36 bohr for geometry 20-0-145-25

Intermolecular Distance (bohr)	μ_z (singlet)	μ_z (triplet)	μ_z (quintet)
5	-0.08596	-0.11335	-0.17818552
6	-0.02715	-0.02659	-0.02607067
8	-0.00187	-0.00168	-0.00155102
10	-0.00036	-0.00037	-0.00036072
12	-0.00021	-0.0002	-0.00020226
15	-0.0001	-0.0001	-0.00010316
20	-3.4E-05	-3.4E-05	-3.4368E-05

Table 199. The z-component of the collision-induced dipole moment at an internuclear distance of 2.457 bohr for geometry 20-0-145-25

Intermolecular Distance (bohr)	μ_z (singlet)	μ_z (triplet)	μ_z (quintet)
5	-0.17446	-0.18221	-0.22516202
6	-0.04283	-0.03952	-0.03470479
8	-0.00316	-0.00304	-0.00280974
10	-0.00081	-0.00082	-0.00079983
12	-0.00041	-0.0004	-0.0004058
15	-0.00019	-0.00019	-0.00018701
20	-6.2E-05	-6.2E-05	-6.155E-05

Table 200. The z-component of the collision-induced dipole moment at an internuclear distance of 2.646 bohr for geometry 20-0-145-25

Intermolecular Distance (bohr)	μ_z (singlet)	μ_z (triplet)	μ_z (quintet)
5	-0.31147	-0.29181	-0.32161457
6	-0.07215	-0.06396	-0.05154333
8	-0.00553	-0.00533	-0.0049335
10	-0.00153	-0.00152	-0.00150479
12	-0.00073	-0.00073	-0.00073042
15	-0.00032	-0.00032	-0.00032083
20	-0.0001	-0.0001	-0.0001046

Table 201. The z-component of the collision-induced dipole moment at an internuclear distance of 2.929 bohr for geometry 20-0-145-25

Intermolecular Distance (bohr)	μ_z (singlet)	μ_z (triplet)	μ_z (quintet)
5	-0.49833	-0.50683	-0.53987267
6	-0.11257	-0.09905	-0.07718967
8	-0.00813	-0.00779	-0.00716317
10	-0.00217	-0.00216	-0.00214036
12	-0.00102	-0.00102	-0.00102155
15	-0.00044	-0.00044	-0.00044285
20	-0.00014	-0.00014	-0.000144

Table 202. The z-component of the collision-induced dipole moment at an internuclear distance of 3.213 bohr for geometry 20-0-145-25

Intermolecular Distance (bohr)	μ_z (singlet)	μ_z (triplet)	μ_z (quintet)
5	-0.44862	-0.45963	-1.49121727
6	-0.15138	-0.13409	-0.11373172
8	-0.00981	-0.00937	-0.00850087
10	-0.00246	-0.00245	-0.00241743
12	-0.00116	-0.00116	-0.00115631
15	-0.00051	-0.00051	-0.00050522
20	-0.00017	-0.00017	-0.0001655

Table 203. The z-component of the collision-induced dipole moment at an internuclear distance of 3.3 bohr for geometry 20-0-145-25

Intermolecular Distance (bohr)	μ_z (singlet)	μ_z (triplet)	μ_z (quintet)
5	-1.35945	-0.4794	-1.45079488
6	-0.1818	-0.16263	-0.14369502
8	-0.00989	-0.00941	-0.00844852
10	-0.00248	-0.00247	-0.00244262
12	-0.00118	-0.00117	-0.00117387
15	-0.00052	-0.00052	-0.00051588
20	-0.00017	-0.00017	-0.00016968

Table 204. The z-component of the collision-induced dipole moment at an internuclear distance of 2 bohr for geometry 30-0-130-35

Intermolecular Distance (bohr)	μ_z (singlet)	μ_z (triplet)	μ_z (quintet)
5	0.148445	0.102646	-0.023732643
6	0.012617	0.006031	-0.006345359
8	0.000708	0.00055	0.000263747
10	0.000314	0.000312	0.000306958
12	0.000113	0.00011	0.000110506
15	3.04E-05	3.53E-05	3.0443E-05
20	1.37E-05	1.38E-05	1.3729E-05

Table 205. The z-component of the collision-induced dipole moment at an internuclear distance of 2.1 bohr for geometry 30-0-130-35

Intermolecular Distance (bohr)	μ_z (singlet)	μ_z (triplet)	μ_z (quintet)
5	0.081429	0.049905	-0.038740809
6	0.003354	-0.00073	-0.008497206
8	0.000163	7.59E-05	-6.6192E-05
10	0.000143	0.000154	0.000152744
12	3.92E-05	5.03E-05	4.8316E-05
15	0.067512	0.068514	0.068428131
20	2.07E-06	2.03E-06	2.05949E-06

Table 206. The z-component of the collision-induced dipole moment at an internuclear distance of 2.2 bohr for geometry 30-0-130-35

Intermolecular Distance (bohr)	μ_z (singlet)	μ_z (triplet)	μ_z (quintet)
5	0.019752	-0.00055	-0.057892688
6	-0.00568	-0.00777	-0.011772396
8	-0.00042	-0.00048	-0.000510123
10	-2.5E-05	-3E-05	-2.073E-05
12	-2.7E-05	-2.7E-05	-2.67445E-05
15	0.116879	0.117792	0.117721846
20	-1E-05	-1E-05	-1.0132E-05

Table 207. The z-component of the collision-induced dipole moment at an internuclear distance of 2.28187 bohr for geometry 30-0-130-35

Intermolecular Distance (bohr)	μ_z (singlet)	μ_z (triplet)	μ_z (quintet)
5	-0.02876	-0.04139223	-0.075747379
6	-0.01307	-0.01373987	-0.015005416
8	-0.00106	-0.000967	-0.000920926
10	-0.00021	-0.00017078	-0.000168553
12	8.38E-05	-0.00010076	-9.2773E-05
15	-0.0001	-6.2303E-05	-6.10115E-05
20	-2E-05	-1.7043E-05	-2.01845E-05

Table 208. The z-component of the collision-induced dipole moment at an internuclear distance of 2.296 bohr for geometry 30-0-130-35

Intermolecular Distance (bohr)	μ_z (singlet)	μ_z (triplet)	μ_z (quintet)
5	-0.03693	-0.04837	-0.078938109
6	-0.01437	-0.01478	-0.01559169
8	-0.00102	-0.00104	-0.000993836
10	-0.00021	-0.0002	-0.000194149
12	-0.00012	-1E-04	-0.000104523
15	-6.5E-05	-6.5E-05	-6.45905E-05
20	-2.2E-05	-2.2E-05	-2.18875E-05

Table 209. The z-component of the collision-induced dipole moment at an internuclear distance of 2.36 bohr for geometry 30-0-130-35

Intermolecular Distance (bohr)	μ_z (singlet)	μ_z (triplet)	μ_z (quintet)
5	-0.03693	-0.0794	-0.093429824
6	-0.01437	-0.01945	-0.018291343
8	-0.00102	-0.00144	-0.001322688
10	-0.00021	-0.00031	-0.000307067
12	-0.00012	-0.00016	-0.000156059
15	-6.5E-05	-8.7E-05	-8.67525E-05
20	-2.2E-05	-2.9E-05	-2.94165E-05

Table 210. The z-component of the collision-induced dipole moment at an internuclear distance of 2.457 bohr for geometry 30-0-130-35

Intermolecular Distance (bohr)	μ_z (singlet)	μ_z (triplet)	μ_z (quintet)
5	-0.12266	-0.12266	-0.114095128
6	-0.02828	-0.02623	-0.022266435
8	-0.00204	-0.00198	-0.001792772
10	-0.00048	-0.00047	-0.000463352
12	-0.00023	-0.00022	-0.000228053
15	-0.00012	-0.00012	-0.000117711
20	-4E-05	-4E-05	-3.9793E-05

Table 211. The z-component of the collision-induced dipole moment at an internuclear distance of 2.646 bohr for geometry 30-0-130-35

Intermolecular Distance (bohr)	μ_z (singlet)	μ_z (triplet)	μ_z (quintet)
5	-0.18789	-0.1807	-0.143020098
6	-0.04164	-0.03713	-0.028342025
8	-0.00298	-0.00281	-0.002479804
10	-0.0007	-0.00069	-0.000679518
12	-0.00033	-0.00032	-0.000328992
15	-0.00016	-0.00016	-0.000161842
20	-5.5E-05	-5.4E-05	-5.45315E-05

Table 212. The z-component of the collision-induced dipole moment at an internuclear distance of 2.929 bohr for geometry 30-0-130-35

Intermolecular Distance (bohr)	μ_z (singlet)	μ_z (triplet)	μ_z (quintet)
5	-0.26254	-0.26849	-0.215726009
6	-0.05157	-0.04507	-0.030981135
8	-0.00365	-0.0034	-0.002891027
10	-0.00081	-0.0008	-0.000780367
12	-0.00038	-0.00038	-0.000380242
15	-0.00019	-0.00019	-0.000188196
20	-6.4E-05	-6.4E-05	-6.39085E-05

Table 213. The z-component of the collision-induced dipole moment at an internuclear distance of 3.213 bohr for geometry 30-0-130-35

Intermolecular Distance (bohr)	μ_z (singlet)	μ_z (triplet)	μ_z (quintet)
5	-0.36629	-0.37101	-0.361711346
6	-0.04616	-0.03717	-0.019628479
8	-0.00366	-0.00335	-0.002686595
10	-0.00076	-0.00075	-0.000722282
12	-0.00037	-0.00037	-0.000365951
15	-0.00019	-0.00019	-0.000190241
20	-6.7E-05	-6.7E-05	-6.6446E-05

Table 214. The z-component of the collision-induced dipole moment at an internuclear distance of 3.3 bohr for geometry 30-0-130-35

Intermolecular Distance (bohr)	μ_z (singlet)	μ_z (triplet)	μ_z (quintet)
5	-0.3923	-0.39421	-0.401692429
6	-0.05801	-0.04512	-0.025381138
8	-0.0032	-0.00286	-0.002215044
10	-0.00071	-0.0007	-0.000673055
12	-0.00035	-0.00035	-0.000351641
15	-0.00019	-0.00019	-0.000187686
20	-6.7E-05	-6.7E-05	-6.64425E-05

Table 215. The z-component of the collision-induced dipole moment at an internuclear distance of 2 bohr for geometry 30-0-60-0

Intermolecular Distance (bohr)	μ_z (singlet)	μ_z (triplet)	μ_z (quintet)
5	0.092503	0.077519	-0.01131
6	0.005819	0.001093	-0.01236
8	-0.00258	-0.00278	-0.00325
10	-0.00104	-0.00107	-0.00106
12	-0.00047	-0.00048	-0.00047
15	-0.00019	-0.00019	-0.00019
20	-5.9E-05	-6E-05	-5.7E-05

Table 216. The z-component of the collision-induced dipole moment at an internuclear distance of 2.1 bohr for geometry 30-0-60-0

Intermolecular Distance (bohr)	μ_z (singlet)	μ_z (triplet)	μ_z (quintet)
5	0.042792	0.032481	-0.01224
6	-0.00113	-0.00448	-0.0112
8	-0.00237	-0.00249	-0.00273
10	-0.00084	-0.00085	-0.00085
12	-0.00038	-0.00037	-0.00037
15	-0.00016	-0.00016	-0.00016
20	-4.8E-05	-4.9E-05	-4.8E-05

Table 217. The z-component of the collision-induced dipole moment at an internuclear distance of 2.2 bohr for geometry 30-0-60-0

Intermolecular Distance (bohr)	μ_z (singlet)	μ_z (triplet)	μ_z (quintet)
5	0.017292	0.013124	-0.00764
6	-0.00384	-0.00534	-0.00851
8	-0.00204	-0.00209	-0.00219
10	-0.00068	-0.00069	-0.00069
12	-0.00029	-0.00029	-0.00029
15	-0.00013	-0.00013	-0.00013
20	-4.2E-05	-4.2E-05	-4.2E-05

Table 218. The z-component of the collision-induced dipole moment at an internuclear distance of 2.28187 bohr for geometry 30-0-60-0

Intermolecular Distance (bohr)	μ_z (singlet)	μ_z (triplet)	μ_z (quintet)
5	-0.01016	-	-0.00879
6	-0.0075	-	-0.00796
8	-0.00182	-	-0.00183
10	-0.00054	-	-0.00056
12	-0.00022	-	-0.00023
15	-0.00012	-	-0.00011
20	-3.4E-05	-	-3.5E-05

Table 219. The z-component of the collision-induced dipole moment at an internuclear distance of 2.36 bohr for geometry 30-0-60-0

Intermolecular Distance (bohr)	μ_z (singlet)	μ_z (triplet)	μ_z (quintet)
5	-0.03508	-0.03015	-0.01025
6	-0.01082	-0.00975	-0.0076
8	-0.00162	-0.00158	-0.00152
10	-0.00041	-0.00041	-0.0004
12	-0.00015	-0.00016	-0.00016
15	-8.4E-05	-8.3E-05	-8.3E-05
20	-2.9E-05	-2.9E-05	-2.9E-05

Table 220.The z-component of the collision-induced dipole moment at an internuclear distance of 2.457 bohr for geometry 30-0-60-0

Intermolecular Distance (bohr)	μ_z (singlet)	μ_z (triplet)	μ_z (quintet)
5	-0.08142	-0.05568	-0.01247
6	-0.01768	-0.01235	-0.0073
8	-0.00142	-0.00129	-0.00114
10	-0.0002	-0.00024	-0.00024
12	-6.5E-05	-8.7E-05	-8.7E-05
15	-4.7E-05	-5.6E-05	-5.6E-05
20	-1.7E-05	-2E-05	-2E-05

Table 221. The z-component of the collision-induced dipole moment at an internuclear distance of 2.646 bohr for geometry 30-0-60-0

Intermolecular Distance (bohr)	μ_z (singlet)	μ_z (triplet)	μ_z (quintet)
5	-0.12097	-0.10569	-0.01769
6	-0.02236	-0.01742	-0.00701
8	-0.00093	-0.00077	-0.00047
10	4.91E-05	5.49E-05	6.36E-05
12	4.58E-05	4.59E-05	4.62E-05
15	-7.7E-06	-7.7E-06	-7.7E-06
20	-5.2E-06	-5.2E-06	-5.2E-06

Table 222. The z-component of the collision-induced dipole moment at an internuclear distance of 2.929 bohr for geometry 30-0-60-0

Intermolecular Distance (bohr)	μ_z (singlet)	μ_z (triplet)	μ_z (quintet)
5	-0.1939	-0.17598	-0.02555
6	-0.03261	-0.02443	-0.00657
8	-0.00039	-0.00013	0.000392
10	0.000425	0.000435	0.00045
12	0.000213	0.000197	0.000213
15	5.53E-05	5.75E-05	5.44E-05
20	1.46E-05	1.47E-05	1.47E-05

Table 223. The z-component of the collision-induced dipole moment at an internuclear distance of 3.213 bohr for geometry 30-0-60-0

Intermolecular Distance (bohr)	μ_z (singlet)	μ_z (triplet)	μ_z (quintet)
5	-0.23724	-0.23004	-0.02601
6	-0.03857	-0.02849	-0.00455
8	0.000127	0.000406	0.001128
10	0.000718	0.00073	0.000751
12	0.000339	0.00034	0.000341
15	0.000102	0.000103	0.000102
20	2.97E-05	3.01E-05	2.98E-05

Table 224. The z-component of the collision-induced dipole moment at an internuclear distance of 3.3 bohr for geometry 30-0-60-0

Intermolecular Distance (bohr)	μ_z (singlet)	μ_z (triplet)	μ_z (quintet)
5	-0.24585	-0.24547	-0.02452
6	-0.0381	-0.02783	-0.00294
8	0.000248	0.000656	0.001373
10	0.000791	0.000802	0.000825
12	0.000371	0.000373	0.000347
15	0.000113	0.000115	8.72E-05
20	3.33E-05	3.34E-05	2.32E-05

Table 225. The z-component of the collision-induced dipole moment at an internuclear distance of 2 bohr for geometry 30-0-90-0

Intermolecular Distance (bohr)	μ_z (singlet)	μ_z (triplet)	μ_z (quintet)
5	0.006464679	0.005642	0.005368
6	-0.010010896	-0.01015	-0.01034
8	-0.004928792	-0.00496	-0.005
10	-0.001931991	-0.00193	-0.00194
12	-0.000864529	-0.00086	-0.00086
15	-0.000345852	-0.00035	-0.00035
20	-0.000109145	-0.00011	-0.00011

Table 226. The z-component of the collision-induced dipole moment at an internuclear distance of 2.1 bohr for geometry 30-0-90-0

Intermolecular Distance (bohr)	μ_z (singlet)	μ_z (triplet)	μ_z (quintet)
5	0.001886712	0.002995	0.006008
6	-0.009435215	-0.00928	-0.00891
8	-0.004145383	-0.00416	-0.00418
10	-0.001556671	-0.00157	-0.00156
12	-0.000689202	-0.00069	-0.00069
15	-0.000282595	-0.00028	-0.00028
20	-8.9909E-05	-9E-05	-9E-05

Table 227. The z-component of the collision-induced dipole moment at an internuclear distance of 2.2 bohr for geometry 30-0-90-0

Intermolecular Distance (bohr)	μ_z (singlet)	μ_z (triplet)	μ_z (quintet)
5	-0.001750832	0.000858	0.008249
6	-0.008816007	-0.00842	-0.00681
8	-0.003371818	-0.00338	-0.00313
10	-0.001192453	-0.00119	-0.00111
12	-0.000520875	-0.00052	-0.00049
15	-0.000220798	-0.00022	-0.00021
20	-7.08165E-05	-7.1E-05	-6.6E-05

Table 228. The z-component of the collision-induced dipole moment at an internuclear distance of 2.28187 bohr for geometry 30-0-90-0

Intermolecular Distance (bohr)	μ_z (singlet)	μ_z (triplet)	μ_z (quintet)
5	-0.004273687	-0.00064	0.006752
6	-0.008305458	-0.00774	-0.00661
8	-0.002756501	-0.00276	-0.00276
10	-0.000903478	-0.0009	-0.00091
12	-0.000386785	-0.00039	-0.00039
15	-0.000172343	-0.00017	-0.00017
20	-5.525E-05	-5.5E-05	-5.5E-05

Table 229. The z-component of the collision-induced dipole moment at an internuclear distance of 2.296 bohr for geometry 30-0-90-0

Intermolecular Distance (bohr)	μ_z (singlet)	μ_z (triplet)	μ_z (quintet)
5	-0.003788305	-0.00088	0.006794
6	-0.007409649	-0.00763	-0.00645
8	-0.002301896	-0.00266	-0.00266
10	-0.000737951	-0.00086	-0.00086
12	-0.000319215	-0.00037	-0.00036
15	-0.000145981	-0.00016	-0.00016
20	-4.65545E-05	-5.3E-05	-5.3E-05

Table 230. The z-component of the collision-induced dipole moment at an internuclear distance of 2.36 bohr for geometry 30-0-90-0

Intermolecular Distance (bohr)	μ_z (singlet)	μ_z (triplet)	μ_z (quintet)
5	-0.006408292	0.006962	0.006794
6	-0.007818475	-0.00571	-0.00645
8	-0.002190451	-0.00218	-0.00266
10	-0.000643865	-0.00064	-0.00086
12	-0.000264425	-0.00026	-0.00036
15	-0.000125593	-0.00013	-0.00016
20	-4.0724E-05	-4.1E-05	-5.3E-05

Table 231. The z-component of the collision-induced dipole moment at an internuclear distance of 2.457 bohr for geometry 30-0-90-0

Intermolecular Distance (bohr)	μ_z (singlet)	μ_z (triplet)	μ_z (quintet)
5	-0.008752539	-0.00333	0.007154
6	-0.00721826	-0.00635	-0.00465
8	-0.001521297	-0.0015	-0.00149
10	-0.000324489	-0.00033	-0.00033
12	-0.000118953	-0.00012	-0.00012
15	-7.0579E-05	-7.1E-05	-7.1E-05
20	-2.2991E-05	-2.3E-05	-2.3E-05

Table 232. The z-component of the collision-induced dipole moment at an internuclear distance of 2.646 bohr for geometry 30-0-90-0

Intermolecular Distance (bohr)	μ_z (singlet)	μ_z (triplet)	μ_z (quintet)
5	-0.011382545	-0.00568	0.007265
6	-0.004835466	-0.00495	-0.00275
8	0.000331852	-0.00028	-0.00025
10	0.000456514	0.00024	0.000239
12	0.000218044	0.00014	0.00014
15	6.0548E-05	2.84E-05	2.84E-05
20	2.16635E-05	9.6E-06	9.6E-06

Table 233. The z-component of the collision-induced dipole moment at an internuclear distance of 2.929 bohr for geometry 30-0-90-0

Intermolecular Distance (bohr)	μ_z (singlet)	μ_z (triplet)	μ_z (quintet)
5	-0.017371782	-0.0088	0.00648
6	-0.004598694	-0.00317	-0.00042
8	0.001171391	0.001221	0.001283
10	0.000899784	0.00093	0.000929
12	0.000455144	0.00046	0.000454
15	0.000151605	0.00015	0.000152
20	5.1268E-05	5.13E-05	5.13E-05

Table 234. The z-component of the collision-induced dipole moment at an internuclear distance of 3.213 bohr for geometry 30-0-90-0

Intermolecular Distance (bohr)	μ_z (singlet)	μ_z (triplet)	μ_z (quintet)
5	-0.021616919	-0.01206	0.010649
6	-0.003566443	-0.00194	0.002831
8	0.002212485	0.002209	0.003268
10	0.001403526	0.001404	0.001722
12	0.000674036	0.000675	0.000781
15	0.000240207	0.000161	0.000288
20	8.17755E-05	8.21E-05	0.000102

Table 235. The z-component of the collision-induced dipole moment at an internuclear distance of 3. 3 bohr for geometry 30-0-90-0

Intermolecular Distance (bohr)	μ_z (singlet)	μ_z (triplet)	μ_z (quintet)
5	-0.022959014	-0.01318	0.00357
6	-0.003265422	-0.00163	0.001423
8	0.002428736	0.002475	0.002571
10	0.001503007	0.001504	0.001506
12	0.00072073	0.000722	0.000719
15	0.000259939	0.000261	0.000252
20	8.8543E-05	8.87E-05	8.52E-05

Table 236. The z-component of the collision-induced dipole moment at an internuclear distance of 2 bohr for geometry 45-0-30-0

Intermolecular Distance (bohr)	μ_z (singlet)	μ_z (triplet)	μ_z (quintet)
5	0.178755	0.145031778	0.030725
6	0.03208	0.024874276	0.008939
8	0.003008	0.002756865	0.001995
10	0.000889	0.000394083	0.000811
12	0.000393	6.2951E-05	0.000368
15	0.000182	0.000183022	0.000173
20	6.3E-05	3.99899E-06	6.12E-05

Table 237. The z-component of the collision-induced dipole moment at an internuclear distance of 2.1 bohr for geometry 45-0-30-0

Intermolecular Distance (bohr)	μ_z (singlet)	μ_z (triplet)	μ_z (quintet)
5	0.093682	0.077568598	0.025297
6	0.018528	0.014727622	0.007656
8	0.00187	0.001732602	0.001475
10	0.000588	0.000574586	0.000569
12	0.000259	0.000264504	0.000259
15	0.000124	0.000123255	0.000124
20	4.37E-05	4.2973E-05	4.36E-05

Table 238. The z-component of the collision-induced dipole moment at an internuclear distance of 2.2 bohr for geometry 45-0-30-0

Intermolecular Distance (bohr)	μ_z (singlet)	μ_z (triplet)	μ_z (quintet)
5	0.05363	0.046814083	0.026599
6	0.013182	0.011639747	0.008751
8	0.001477	0.001409576	0.001291
10	0.000408	0.000410402	0.000398
12	0.000176	0.000181145	0.00018
15	8.78E-05	8.76935E-05	8.79E-05
20	2.99E-05	2.9925E-05	2.99E-05

Table 239. The z-component of the collision-induced dipole moment at an internuclear distance of 2.28187 bohr for geometry 45-0-30-0

Intermolecular Distance (bohr)	μ_z (singlet)	μ_z (triplet)	μ_z (quintet)
5	0.00386	0.005388901	0.019562
6	0.005415	0.005846457	0.006859
8	0.000815	0.00083474	0.000807
10	0.000199	0.000204036	0.000206
12	0.000103	8.8184E-05	0.000108
15	2.7E-05	3.43535E-05	3.81E-05
20	2.62E-05	2.9053E-05	3.12E-05

Table 240. The z-component of the collision-induced dipole moment at an internuclear distance of 2.296 bohr for geometry 45-0-30-0

Intermolecular Distance (bohr)	μ_z (singlet)	μ_z (triplet)	μ_z (quintet)
5	-0.00481	-0.001978181	0.006205
6	0.004025	0.004807257	0.002568
8	0.000725	0.000705883	0.000209
10	0.000164	0.000159242	5.08E-05
12	7E-05	7.0032E-05	1.99E-05
15	4.13E-05	4.03675E-05	2.16E-05
20	1.41E-05	1.4084E-05	9.17E-06

Table 241. The z-component of the collision-induced dipole moment at an internuclear distance of 2.36 bohr for geometry 45-0-30-0

Intermolecular Distance (bohr)	μ_z (singlet)	μ_z (triplet)	μ_z (quintet)
5	-0.04449	-0.036251565	0.011286
6	-0.00234	-6.34905E-05	0.004646
8	0.00018	0.000229283	0.000322
10	1.84E-06	-1.53545E-05	1.26E-05
12	-9E-06	-5.41201E-06	-5.8E-06
15	8.51E-06	8.81099E-06	8.69E-06
20	3.63E-06	3.62201E-06	3.6E-06

Table 242. The z-component of the collision-induced dipole moment at an internuclear distance of 2.457 bohr for geometry 45-0-30-0

Intermolecular Distance (bohr)	μ_z (singlet)	μ_z (triplet)	μ_z (quintet)
5	-0.10597	-0.091053242	-0.0011
6	-0.01264	-0.008023429	0.001398
8	-0.00063	-0.000515618	-0.00031
10	-0.00025	-0.000248519	-0.00024
12	-0.00012	-0.00011788	-0.00012
15	-3.9E-05	-3.88225E-05	-3.9E-05
20	-1.2E-05	-1.19295E-05	-1.2E-05

Table 243. The z-component of the collision-induced dipole moment at an internuclear distance of 2.646 bohr for geometry 45-0-30-0

Intermolecular Distance (bohr)	μ_z (singlet)	μ_z (triplet)	μ_z (quintet)
5	-0.22711	-0.203606575	-0.01592
6	-0.03513	-0.025815259	-0.00159
8	-0.00224	-0.002007177	-0.00118
10	-0.00071	-0.000698241	-0.00066
12	-0.00033	-0.000332158	-0.00032
15	-0.00013	-0.000127566	-0.00013
20	-4.1E-05	-4.0581E-05	-4.1E-05

Table 244. The z-component of the collision-induced dipole moment at an internuclear distance of 2.929 bohr for geometry 45-0-30-0

Intermolecular Distance (bohr)	μ_z (singlet)	μ_z (triplet)	μ_z (quintet)
5	-0.37964	-0.314454281	-0.09206
6	-0.07482	-0.050449264	-0.02061
8	-0.00463	-0.003738215	-0.00338
10	-0.00131	-	-0.00127
12	-0.00063	-0.000613394	-0.00061
15	-0.00024	-0.00024299	-0.00024
20	-7.7E-05	-7.26905E-05	-7.7E-05

Table 245. The z-component of the collision-induced dipole moment at an internuclear distance of 3.213 bohr for geometry 45-0-30-0

Intermolecular Distance (bohr)	μ_z (singlet)	μ_z (triplet)	μ_z (quintet)
5	-0.42386	-0.387211069	-0.14453
6	-0.11589	-0.094386138	-0.03577
8	-0.0067	-0.006065344	-0.00486
10	-0.00175	-0.001781796	-0.0017
12	-0.00081	-0.000807321	-0.00081
15	-0.00033	-0.000326461	-0.00033
20	-0.0001	-0.000104431	-0.0001

Table 246. The z-component of the collision-induced dipole moment at an internuclear distance of 3.3 bohr for geometry 45-0-30-0

Intermolecular Distance (bohr)	μ_z (singlet)	μ_z (triplet)	μ_z (quintet)
5	-0.41054	-0.374806757	-0.1889
6	-0.12579	-0.102082999	-0.03943
8	-0.00726	-0.006526824	-0.00521
10	-0.00184	-0.001820741	-0.00174
12	-0.00085	-0.000849412	-0.00083
15	-0.00035	-0.000344841	-0.00032
20	-0.00011	-0.000110314	-0.00013

Table 247. The z-component of the collision-induced dipole moment at an internuclear distance of 2 bohr for geometry 45-0-60-0

Intermolecular Distance (bohr)	μ_z (singlet)	μ_z (triplet)	μ_z (quintet)
5	0.045842	0.03457	0.004436
6	0.003611	0.00052	-0.00556
8	-0.00199	-0.00215	-0.00244
10	-0.00087	-0.00087	-0.00089
12	-0.00039	-0.00039	-0.00039
15	-0.00015	-0.00016	-0.00015
20	-4.5E-05	-4.5E-05	-4.5E-05

Table 248. The z-component of the collision-induced dipole moment at an internuclear distance of 2.1 bohr for geometry 45-0-60-0

Intermolecular Distance (bohr)	μ_z (singlet)	μ_z (triplet)	μ_z (quintet)
5	0.021409	0.016003	0.002371
6	-0.00039	-0.00206	-0.00519
8	-0.00169	-0.00179	-0.00195
10	-0.00065	-0.00065	-0.00066
12	-0.00026	-0.0003	-0.00029
15	-0.00011	-0.00011	-0.00011
20	-3.4E-05	-3.4E-05	-3.4E-05

Table 249. The z-component of the collision-induced dipole moment at an internuclear distance of 2.2 bohr for geometry 45-0-60-0

Intermolecular Distance (bohr)	μ_z (singlet)	μ_z (triplet)	μ_z (quintet)
5	0.01148	0.010136	0.00197
6	-0.00097	-0.00155	-0.00419
8	-0.00129	-0.00132	-0.00145
10	-0.00048	-0.00048	-0.00046
12	-0.00021	-0.0002	-0.00019
15	-8.4E-05	-8.3E-05	-7.9E-05
20	-2.6E-05	-2.6E-05	-2.4E-05

Table 250. The z-component of the collision-induced dipole moment at an internuclear distance of 2.28187 bohr for geometry 45-0-60-0

Intermolecular Distance (bohr)	μ_z (singlet)	μ_z (triplet)	μ_z (quintet)
5	0.120412	0.001588	0.006317
6	0.005561	-0.00228	-0.00186
8	0.006482	-0.001	-0.001
10	0.002691	-0.00033	-0.00033
12	0.001256	-0.00013	-0.00013
15	0.000505	-6.4E-05	-6.2E-05
20	0.000159	-1.8E-05	-1.8E-05

Table 251. The z-component of the collision-induced dipole moment at an internuclear distance of 2.296 bohr for geometry 45-0-60-0

Intermolecular Distance (bohr)	μ_z (singlet)	μ_z (triplet)	μ_z (quintet)
5	-0.00224	0.000149	0.00629
6	-0.00274	-0.0024	-0.0017
8	-0.00095	-0.00094	-0.00094
10	-0.00029	-0.0003	-0.0003
12	-0.00012	-0.00012	-0.00012
15	-5.4E-05	-5.3E-05	-5.4E-05
20	-1.7E-05	-1.7E-05	-1.7E-05

Table 252. The z-component of the collision-induced dipole moment at an internuclear distance of 2.36 bohr for geometry 45-0-60-0

Intermolecular Distance (bohr)	μ_z (singlet)	μ_z (triplet)	μ_z (quintet)
5	-0.01092	-0.00627	0.006057
6	-0.00385	-0.00295	-0.00114
8	-0.00072	-0.0007	-0.00064
10	-0.00018	-0.00018	-0.00018
12	-7.3E-05	-6.7E-05	-6.6E-05
15	-3.4E-05	-3.4E-05	-3.4E-05
20	-1.1E-05	-1.1E-05	-1.1E-05

Table 253. The z-component of the collision-induced dipole moment at an internuclear distance of 2.457 bohr for geometry 45-0-60-0

Intermolecular Distance (bohr)	μ_z (singlet)	μ_z (triplet)	μ_z (quintet)
5	-0.02362	-0.01582	0.005392
6	-0.00547	-0.00378	-0.00039
8	-0.00038	-0.00033	-0.00021
10	-4.8E-06	2.95E-06	1.01E-06
12	5.79E-06	1.36E-05	1.28E-05
15	-4.7E-06	-4.5E-06	-4.8E-06
20	-2.4E-06	-2.4E-06	-2.4E-06

Table 254. The z-component of the collision-induced dipole moment at an internuclear distance of 2.646 bohr for geometry 45-0-60-0

Intermolecular Distance (bohr)	μ_z (singlet)	μ_z (triplet)	μ_z (quintet)
5	-0.04731	-0.03436	0.003167
6	-0.00847	-0.0054	0.000773
8	0.000227	0.000348	0.000571
10	0.000314	0.00032	0.000325
12	0.000155	0.000155	0.000155
15	4.86E-05	4.88E-05	4.88E-05
20	1.44E-05	1.44E-05	1.44E-05

Table 255. The z-component of the collision-induced dipole moment at an internuclear distance of 2.929 bohr for geometry 45-0-60-0

Intermolecular Distance (bohr)	μ_z (singlet)	μ_z (triplet)	μ_z (quintet)
5	-0.07883	-0.06107	-0.0016
6	-0.01231	-0.00751	0.002136
8	0.001022	0.001218	0.001582
10	0.00072	0.000728	0.000739
12	0.000335	0.000335	0.000334
15	0.000119	0.000122	0.000118
20	3.62E-05	3.63E-05	3.63E-05

Table 256. The z-component of the collision-induced dipole moment at an internuclear distance of 3.213 bohr for geometry 45-0-60-0

Intermolecular Distance (bohr)	μ_z (singlet)	μ_z (triplet)	μ_z (quintet)
5	-0.09669	-0.0764	-0.00414
6	-0.01406	-0.00835	0.003689
8	0.001636	0.001854	0.002384
10	0.001022	0.001029	0.001048
12	0.000475	0.000467	0.000466
15	0.000169	0.00017	0.000168
20	5.23E-05	5.24E-05	5.23E-05

Table 257. The z-component of the collision-induced dipole moment at an internuclear distance of 3.3 bohr for geometry 45-0-60-0

Intermolecular Distance (bohr)	μ_z (singlet)	μ_z (triplet)	μ_z (quintet)
5	-0.10003	-0.07939	-0.00226
6	-0.01347	-0.00779	0.004501
8	0.001793	0.002061	0.002567
10	0.00109	0.001094	0.001125
12	0.000494	0.000496	0.000494
15	0.00018	0.000181	0.000202
20	5.58E-05	5.64E-05	4E-05

Table 258. The z-component of the collision-induced dipole moment at an internuclear distance of 2 bohr for geometry 45-0-90-0

Intermolecular Distance (bohr)	μ_z (singlet)	μ_z (triplet)	μ_z (quintet)
5	0.003528	0.003724	0.009915
6	-0.00745	-0.00766	-0.00634
8	-0.00395	-0.00393	-0.00398
10	-0.00157	-0.00154	-0.00157
12	-0.0007	-0.00068	-0.0007
15	-0.00027	-0.00026	-0.00027
20	-8.5E-05	-8.3E-05	-8.5E-05

Table 259. The z-component of the collision-induced dipole moment at an internuclear distance of 2.1 bohr for geometry 45-0-90-0

Intermolecular Distance (bohr)	μ_z (singlet)	μ_z (triplet)	μ_z (quintet)
5	-0.00041	0.005118	0.011127
6	-0.00708	-0.00593	-0.00493
8	-0.00319	-0.00325	-0.00327
10	-0.0012	-0.00125	-0.00125
12	-0.00053	-0.00055	-0.00055
15	-0.00021	-0.00022	-0.00022
20	-6.6E-05	-6.9E-05	-6.9E-05

Table 260. The z-component of the collision-induced dipole moment at an internuclear distance of 2.2 bohr for geometry 45-0-90-0

Intermolecular Distance (bohr)	μ_z (singlet)	μ_z (triplet)	μ_z (quintet)
5	0.000574	0.004555	0.012104
6	-0.00549	-0.00488	-0.00363
8	-0.00256	-0.00257	-0.00258
10	-0.00092	-0.00093	-0.00094
12	-0.0004	-0.0004	-0.0004
15	-0.00017	-0.00017	-0.00017
20	-5.2E-05	-5.2E-05	-5.2E-05

Table 261. The z-component of the collision-induced dipole moment at an internuclear distance of 2.28187 bohr for geometry 45-0-90-0

Intermolecular Distance (bohr)	μ_z (singlet)	μ_z (triplet)	μ_z (quintet)
5	-0.0005	0.004082	0.012767
6	-0.0048	-0.00408	-0.00264
8	-0.00203	-0.00203	-0.00203
10	-0.00068	-0.00069	-0.00071
12	-0.00032	-0.00028	-0.0003
15	-0.00012	-0.00012	-0.00012
20	-3.9E-05	-4E-05	-3.8E-05

Table 262. The z-component of the collision-induced dipole moment at an internuclear distance of 2.296 bohr for geometry 45-0-90-0

Intermolecular Distance (bohr)	μ_z (singlet)	μ_z (triplet)	μ_z (quintet)
5	-0.00343	0.005967	0.015685
6	-0.00539	-0.00313	-0.00146
8	-0.00187	-0.00168	-0.0017
10	-0.00057	-0.00057	-0.00057
12	-0.00023	-0.00024	-0.00024
15	-0.0001	-0.00011	-0.00011
20	-3.2E-05	-3.2E-05	-3.2E-05

Table 263. The z-component of the collision-induced dipole moment at an internuclear distance of 2.36 bohr for geometry 45-0-90-0

Intermolecular Distance (bohr)	μ_z (singlet)	μ_z (triplet)	μ_z (quintet)
5	-0.00148	0.005693	0.013285
6	-0.00418	-0.00245	-0.00174
8	-0.00152	-0.00121	-0.00152
10	-0.00046	-0.00037	-0.00046
12	-0.00018	-0.00016	-0.00018
15	-8.4E-05	-7.2E-05	-8.4E-05
20	-2.6E-05	-2.1E-05	-2.6E-05

Table 264. The z-component of the collision-induced dipole moment at an internuclear distance of 2.457 bohr for geometry 45-0-90-0

Intermolecular Distance (bohr)	μ_z (singlet)	μ_z (triplet)	μ_z (quintet)
5	-0.0026	0.005238	0.013798
6	-0.00345	-0.00148	-0.00069
8	-0.00093	-0.00059	-0.00091
10	-0.00019	-7.7E-05	-0.00019
12	-5.8E-05	1.81E-05	-5.8E-05
15	-3.6E-05	-2.1E-05	-3.6E-05
20	-1E-05	-4.3E-06	-1E-05

Table 265. The z-component of the collision-induced dipole moment at an internuclear distance of 2.646 bohr for geometry 45-0-90-0

Intermolecular Distance (bohr)	μ_z (singlet)	μ_z (triplet)	μ_z (quintet)
5	-0.00455	0.004193	0.014332
6	-0.00217	0.000185	0.001144
8	0.000124	0.000598	0.00018
10	0.000299	0.000438	0.000297
12	0.000164	0.00022	0.000163
15	5.11E-05	7.52E-05	5.11E-05
20	1.83E-05	2.65E-05	1.83E-05

Table 266. The z-component of the collision-induced dipole moment at an internuclear distance of 2.929 bohr for geometry 45-0-90-0

Intermolecular Distance (bohr)	μ_z (singlet)	μ_z (triplet)	μ_z (quintet)
5	-0.00725	-	0.013789
6	-0.00063	-	0.003282
8	0.001419	-	0.001514
10	0.000888	-	0.000887
12	0.000433	-	0.000432
15	0.00016	-	0.00016
20	5.47E-05	-	5.47E-05

Table 267. The z-component of the collision-induced dipole moment at an internuclear distance of 3.213 bohr for geometry 45-0-90-0

Intermolecular Distance (bohr)	μ_z (singlet)	μ_z (triplet)	μ_z (quintet)
5	-0.00725	-	0.013789
6	-0.00063	-	0.003282
8	0.001419	-	0.001514
10	0.000888	-	0.000887
12	0.000433	-	0.000432
15	0.00016	-	0.00016
20	5.47E-05	-	5.47E-05

Table 268. The z-component of the collision-induced dipole moment at an internuclear distance of 3.3 bohr for geometry 45-0-90-0

Intermolecular Distance (bohr)	μ_z (singlet)	μ_z (triplet)	μ_z (quintet)
5	-0.00917	-0.00242	0.011359
6	0.000589	0.001995	0.004788
8	0.002479	0.002528	0.002628
10	0.001377	0.001377	0.001382
12	0.000661	0.000662	0.000656
15	0.000255	0.000255	0.000259
20	8.72E-05	8.73E-05	7.31E-05

Table 269. The z-component of the collision-induced dipole moment at an internuclear distance of 2 bohr for geometry 35-0-65-80

Intermolecular Distance (bohr)	μ_z (singlet)	μ_z (triplet)	μ_z (quintet)
5	0.083649	0.067614	0.000258
6	0.004315	0.00024	-0.00819
8	-0.00254	-0.00268	-0.00296
10	-0.00104	-0.00103	-0.00104
12	-0.00047	-0.00047	-0.00047
15	-0.00019	-0.00019	-0.00019
20	-5.9E-05	-5.9E-05	-5.9E-05

Table 270. The z-component of the collision-induced dipole moment at an internuclear distance of 2.1 bohr for geometry 35-0-65-80

Intermolecular Distance (bohr)	μ_z (singlet)	μ_z (triplet)	μ_z (quintet)
5	0.049108	0.040076	-0.00064
6	7.29E-05	-0.00227	-0.00714
8	-0.00225	-0.00231	-0.00247
10	-0.00084	-0.00083	-0.00084
12	-0.00037	-0.00037	-0.00037
15	0.067387	0.068387	0.068302
20	-5E-05	-5E-05	-5E-05

Table 271. The z-component of the collision-induced dipole moment at an internuclear distance of 2.2 bohr for geometry 35-0-65-80

Intermolecular Distance (bohr)	μ_z (singlet)	μ_z (triplet)	μ_z (quintet)
5	0.019086	0.01594	-0.00273
6	-0.00371	-0.00461	-0.00659
8	-0.00192	-0.00197	-0.00203
10	-0.00064	-0.00065	-0.00065
12	-0.00028	-0.00028	-0.00028
15	0.116809	0.117729	0.117653
20	-4.1E-05	-4.1E-05	-4.1E-05

Table 272. The z-component of the collision-induced dipole moment at an internuclear distance of 2.28187 bohr for geometry 35-0-65-80

Intermolecular Distance (bohr)	μ_z (singlet)	μ_z (triplet)	μ_z (quintet)
5	-0.00415	-0.00244	-0.00489
6	-0.00647	-0.00644	-0.00636
8	-0.0018	-0.0017	-0.0017
10	-0.00058	-0.0005	-0.0005
12	-0.00022	-0.00021	-0.00021
15	-0.0001	-0.0001	-0.0001
20	-3.3E-05	-3.3E-05	-3.3E-05

Table 273. The z-component of the collision-induced dipole moment at an internuclear distance of 2.296 bohr for geometry 35-0-65-80

Intermolecular Distance (bohr)	μ_z (singlet)	μ_z (triplet)	μ_z (quintet)
5	-0.00734	-0.00551	-0.00526
6	-0.00693	-0.00676	-0.00633
8	-0.00167	-0.00165	-0.00165
10	-0.00047	-0.00047	-0.00047
12	-0.00019	-0.00019	-0.0002
15	-9.7E-05	-9.5E-05	-9.7E-05
20	-3.2E-05	-3.2E-05	-3.2E-05

Table 274. The z-component of the collision-induced dipole moment at an internuclear distance of 2.36 bohr for geometry 35-0-65-80

Intermolecular Distance (bohr)	μ_z (singlet)	μ_z (triplet)	μ_z (quintet)
5	-0.0238	-0.01899	-0.0069
6	-0.00905	-0.0081	-0.00621
8	-0.00151	-0.00147	-0.00141
10	-0.00036	-0.00035	-0.00036
12	-0.00014	-0.00014	-0.00014
15	-7.8E-05	-7.8E-05	-7.8E-05
20	-2.6E-05	-2.6E-05	-2.6E-05

Table 275. The z-component of the collision-induced dipole moment at an internuclear distance of 2.457 bohr for geometry 35-0-65-80

Intermolecular Distance (bohr)	μ_z (singlet)	μ_z (triplet)	μ_z (quintet)
5	-0.04652	-0.03772	-0.00871
6	-0.01195	-0.00994	-0.00597
8	-0.00124	-0.00117	-0.00105
10	-0.0002	-0.0002	-0.00019
12	-6.7E-05	-6.9E-05	-6.7E-05
15	-5E-05	-5E-05	-5E-05
20	-1.8E-05	-1.8E-05	-1.8E-05

Table 276. The z-component of the collision-induced dipole moment at an internuclear distance of 2.646 bohr for geometry 35-0-65-80

Intermolecular Distance (bohr)	μ_z (singlet)	μ_z (triplet)	μ_z (quintet)
5	-0.07906	-0.06427	-0.00778
6	-0.01609	-0.01247	-0.00492
8	-0.00072	-0.0006	-0.00038
10	0.000102	0.000106	0.000114
12	7.13E-05	7.28E-05	7.14E-05
15	1.71E-06	8.34E-07	1.62E-06
20	-1.2E-06	-1.1E-06	-1.2E-06

Table 277. The z-component of the collision-induced dipole moment at an internuclear distance of 2.929 bohr for geometry 35-0-65-80

Intermolecular Distance (bohr)	μ_z (singlet)	μ_z (triplet)	μ_z (quintet)
5	-0.10555	-0.088	0.009087
6	-0.01812	-0.0129	-0.00157
8	-2.1E-05	0.000161	0.000531
10	0.00049	0.000494	0.000507
12	0.000247	0.000248	0.000247
15	6.8E-05	6.8E-05	6.79E-05
20	1.99E-05	2E-05	1.99E-05

Table 278. The z-component of the collision-induced dipole moment at an internuclear distance of 3.213 bohr for geometry 35-0-65-80

Intermolecular Distance (bohr)	μ_z (singlet)	μ_z (triplet)	μ_z (quintet)
5	-0.19626	-0.20172	-0.00353
6	-0.00428	0.001318	0.010245
8	0.000605	0.000781	0.001304
10	0.000778	0.000784	0.000802
12	0.000377	0.000376	0.000377
15	0.000117	0.000117	0.000116
20	3.52E-05	3.52E-05	3.53E-05

Table 279. The z-component of the collision-induced dipole moment at an internuclear distance of 3.3 bohr for geometry 35-0-65-80

Intermolecular Distance (bohr)	μ_z (singlet)	μ_z (triplet)	μ_z (quintet)
5	-0.22297	-0.22983	-0.0286
6	0.004919	0.013395	0.021606
8	0.000952	0.00119	0.00164
10	0.000855	0.000863	0.000881
12	0.00041	0.00041	0.000411
15	0.000129	0.000129	0.000129
20	3.88E-05	3.88E-05	3.89E-05

Table 280. The z-component of the collision-induced dipole moment at an internuclear distance of 2 bohr for geometry 60-0-80-65

Intermolecular Distance (bohr)	μ_z (singlet)	μ_z (triplet)	μ_z (quintet)
5	0.012921	0.01109923	0.006998589
6	-0.00299	-0.0033133	-0.003972012
8	-0.00265	-0.00267022	-0.002716727
10	-0.00109	-0.00109386	-0.001096505
12	-0.00048	-0.00047762	-0.000477698
15	-0.00019	0.03934983	-0.000185307
20	-5.8E-05	-5.802E-05	0.039376189

Table 281. The z-component of the collision-induced dipole moment at an internuclear distance of 2.1 bohr for geometry 60-0-80-65

Intermolecular Distance (bohr)	μ_z (singlet)	μ_z (triplet)	μ_z (quintet)
5	0.009577	0.00725665	0.00875939
6	-0.00238	-0.00086487	-0.002517901
8	-0.00203	-0.0009352	-0.002071723
10	-0.00081	-0.00032217	-0.000814438
12	-0.00035	-0.00011516	-0.000350025
15	0.067394	-5.549E-05	0.068313984
20	-4.3E-05	-1.6395E-05	-4.3416E-05

Table 282. The z-component of the collision-induced dipole moment at an internuclear distance of 2.2 bohr for geometry 60-0-80-65

Intermolecular Distance (bohr)	μ_z (singlet)	μ_z (triplet)	μ_z (quintet)
5	0.006935	0.00815793	0.010150585
6	-0.0017	-0.00154388	-0.001200851
8	-0.00142	-0.00142714	-0.00144361
10	-0.00054	-0.00053789	-0.000539831
12	-0.00023	-0.00022491	-0.000225481
15	-9.3E-05	-9.2511E-05	-9.25455E-05
20	-2.9E-05	-2.873E-05	-2.8732E-05

Table 283. The z-component of the collision-induced dipole moment at an internuclear distance of 2.28187 bohr for geometry 60-0-80-65

Intermolecular Distance (bohr)	μ_z (singlet)	μ_z (triplet)	μ_z (quintet)
5	0.005111	0.00724912	0.011086854
6	-0.0012	-0.00086487	-0.00020401
8	-0.00094	-0.0009352	-0.000943633
10	-0.00036	-0.00032217	-0.000320449
12	-0.00016	-0.00011516	-0.000125418
15	-0.00016	-5.549E-05	-5.3899E-05
20	-1.8E-05	-1.6395E-05	-1.6739E-05

Table 284. The z-component of the collision-induced dipole moment at an internuclear distance of 2.296 bohr for geometry 60-0-80-65

Intermolecular Distance (bohr)	μ_z (singlet)	μ_z (triplet)	μ_z (quintet)
5	0.004801	0.00710114	0.011234226
6	-0.00111	-0.00075009	-3.88715E-05
8	-0.00092	-0.00085364	-0.000859238
10	-0.00028	-0.00028493	-0.000284609
12	-0.00011	-0.00010785	-0.000109683
15	-4.8E-05	0.03179388	0.031584293
20	-1.5E-05	-1.4657E-05	-1.46725E-05

Table 285. The z-component of the collision-induced dipole moment at an internuclear distance of 2.36 bohr for geometry 60-0-80-65

Intermolecular Distance (bohr)	μ_z (singlet)	μ_z (triplet)	μ_z (quintet)
5	0.003531	0.00645223	0.011843887
6	-0.00073	-0.00024746	0.000684948
8	-0.0005	-0.00048389	-0.000482212
10	-0.00012	-0.00011862	-0.000120201
12	-3.7E-05	-3.4904E-05	-3.50305E-05
15	-1.9E-05	-1.9101E-05	-1.91715E-05
20	-5.4E-06	-5.4395E-06	-5.44699E-06

Table 286. The z-component of the collision-induced dipole moment at an internuclear distance of 2.457 bohr for geometry 60-0-80-65

Intermolecular Distance (bohr)	μ_z (singlet)	μ_z (triplet)	μ_z (quintet)
5	0.001745	0.0055251	0.012619918
6	-0.00016	0.00046692	0.001701971
8	2.75E-05	5.07E-05	6.31225E-05
10	0.000126	0.00011804	0.000117428
12	7.34E-05	7.307E-05	7.29785E-05
15	2.35E-05	2.3152E-05	2.3134E-05
20	8.15E-06	8.1515E-06	8.14501E-06

Table 287. The z-component of the collision-induced dipole moment at an internuclear distance of 2.646 bohr for geometry 60-0-80-65

Intermolecular Distance (bohr)	μ_z (singlet)	μ_z (triplet)	μ_z (quintet)
5	-0.00132	0.00378423	0.013595855
6	0.000755	0.00163809	0.003383198
8	0.000957	0.00097443	0.001008493
10	0.00053	0.00053038	0.000529546
12	0.000261	0.00025953	0.000260425
15	9.88E-05	9.2084E-05	9.80295E-05
20	3.24E-05	3.2419E-05	3.2422E-05

Table 288. The z-component of the collision-induced dipole moment at an internuclear distance of 2.929 bohr for geometry 60-0-80-65

Intermolecular Distance (bohr)	μ_z (singlet)	μ_z (triplet)	μ_z (quintet)
5	-0.00519	0.00100098	0.013536288
6	0.001588	0.00275463	0.005043228
8	0.001965	0.00199917	0.00206309
10	0.000993	0.0009936	0.000994514
12	0.000474	0.00047472	0.00047374
15	0.000185	0.00018418	0.000184059
20	6.11E-05	6.1087E-05	6.109E-05

Table 289. The z-component of the collision-induced dipole moment at an internuclear distance of 3.213 bohr for geometry 60-0-80-65

Intermolecular Distance (bohr)	μ_z (singlet)	μ_z (triplet)	μ_z (quintet)
5	-0.00591	-0.00071694	0.013008996
6	0.001893	0.00317577	0.005832928
8	0.002562	0.00260899	0.002703016
10	0.001284	0.00128675	0.001287576
12	0.000612	0.00061259	0.000611612
15	10.63491	0.00023988	0.000242234
20	8.02E-05	8.0188E-05	8.0214E-05

Table 290. The z-component of the collision-induced dipole moment at an internuclear distance of 3.3 bohr for geometry 60-0-80-65

Intermolecular Distance (bohr)	μ_z (singlet)	μ_z (triplet)	μ_z (quintet)
5	-0.00189	0.00117656	0.014529242
6	0.00208	0.00328943	0.006056219
8	0.002679	0.00273255	0.002831867
10	0.001346	0.00134915	0.001350375
12	0.000642	0.00064088	0.000642193
15	0.000256	0.00025568	0.000255522
20	8.45E-05	8.4509E-05	8.45285E-05

Table 291. The z-component of the collision-induced dipole moment at an internuclear distance of 2 bohr for geometry 70-0-65-75

Intermolecular Distance (bohr)	μ_z (singlet)	μ_z (triplet)	μ_z (quintet)
5	0.013083117	0.007991191	-0.003043383
6	0.000506736	-0.00042381	8.07945E-05
8	-0.000739704	-0.000762124	0.000264418
10	-0.000361784	-0.000362577	8.78825E-05
12	-0.000169355	-0.000169816	3.6397E-05
15	-5.74475E-05	-5.85785E-05	1.62235E-05
20	-1.72125E-05	-1.7206E-05	4.71749E-06

Table 292. The z-component of the collision-induced dipole moment at an internuclear distance of 2.1 bohr for geometry 70-0-65-75

Intermolecular Distance (bohr)	μ_z (singlet)	μ_z (triplet)	μ_z (quintet)
5	0.007529162	0.004351609	-0.002301459
6	0.00048671	-8.39445E-05	-0.001181748
8	-0.000376704	-0.000396524	-0.000415309
10	-0.000198354	-0.000198254	-0.000198463
12	-9.45115E-05	-9.4468E-05	-9.4583E-05
15	0.067497574	0.068496472	0.068413302
20	-9.61151E-06	-9.60549E-06	-9.611E-06

Table 293. The z-component of the collision-induced dipole moment at an internuclear distance of 2.2 bohr for geometry 70-0-65-75

Intermolecular Distance (bohr)	μ_z (singlet)	μ_z (triplet)	μ_z (quintet)
5	0.00248198	0.000844489	-0.002527649
6	0.000432141	0.000143281	-0.000414758
8	-1.6272E-05	-1.88995E-05	-3.5332E-05
10	-4.00295E-05	-3.53835E-05	-3.81875E-05
12	-2.1499E-05	-2.18605E-05	-2.21005E-05
15	0.116906251	0.117827644	0.117752222
20	-1.76499E-06	-1.76649E-06	-1.774E-06

Table 294. The z-component of the collision-induced dipole moment at an internuclear distance of 2.28187 bohr for geometry 70-0-65-75

Intermolecular Distance (bohr)	μ_z (singlet)	μ_z (triplet)	μ_z (quintet)
5	-0.00137783	0.007249122	-0.003043383
6	0.000351797	-0.000864873	8.0794E-05
8	0.000237922	-0.000935198	0.000264418
10	9.5842E-05	-0.00032217	8.7882E-05
12	4.45575E-05	-0.000115156	3.6397E-05
15	0.00018977	-5.54925E-05	1.6224E-05
20	-1.3537E-05	-1.63955E-05	4.718E-06

Table 295. The z-component of the collision-induced dipole moment at an internuclear distance of 2.296 bohr for geometry 70-0-65-75

Intermolecular Distance (bohr)	μ_z (singlet)	μ_z (triplet)	μ_z (quintet)
5	-0.002014441	-0.002448283	-0.003147054
6	0.000339687	0.000276341	0.000155198
8	0.000299545	0.000310868	0.000314701
10	0.00010312	0.000116626	0.000110535
12	4.84905E-05	4.25085E-05	4.4646E-05
15	1.8854E-05	0.031565533	0.031361766
20	5.83699E-06	5.84149E-06	5.83699E-06

Table 296. The z-component of the collision-induced dipole moment at an internuclear distance of 2.36 bohr for geometry 70-0-65-75

Intermolecular Distance (bohr)	μ_z (singlet)	μ_z (triplet)	μ_z (quintet)
5	-0.004871741	-0.004554106	-0.003650482
6	0.000259797	0.000336672	0.000479026
8	0.00052111	0.000529194	0.000538358
10	0.000208174	0.000193879	0.000205704
12	8.2854E-05	8.6665E-05	8.7185E-05
15	3.50035E-05	3.4984E-05	3.49945E-05
20	1.07975E-05	1.07995E-05	1.0801E-05

Table 297. The z-component of the collision-induced dipole moment at an internuclear distance of 2.457 bohr for geometry 70-0-65-75

Intermolecular Distance (bohr)	μ_z (singlet)	μ_z (triplet)	μ_z (quintet)
5	-0.008822006	-0.007482709	-0.004355787
6	0.000139774	0.00040702	0.000912761
8	0.000823628	0.000838882	0.000857546
10	0.000330497	0.000340626	0.000341441
12	0.000147486	0.000148496	0.000147607
15	5.81345E-05	5.8125E-05	5.80805E-05
20	1.8021E-05	1.8026E-05	1.802E-05

Table 298. The z-component of the collision-induced dipole moment at an internuclear distance of 2.646 bohr for geometry 70-0-65-75

Intermolecular Distance (bohr)	μ_z (singlet)	μ_z (triplet)	μ_z (quintet)
5	-0.014659778	-0.011735642	-0.004938887
6	-2.3832E-05	0.000561576	0.001672538
8	0.001328498	0.001351673	0.001395216
10	0.000566273	0.000565704	0.000568773
12	0.000247846	0.000249146	0.000247875
15	9.73135E-05	9.2468E-05	9.7262E-05
20	3.03035E-05	3.02085E-05	3.0305E-05

Table 299. The z-component of the collision-induced dipole moment at an internuclear distance of 2.929 bohr for geometry 70-0-65-75

Intermolecular Distance (bohr)	μ_z (singlet)	μ_z (triplet)	μ_z (quintet)
5	-0.017443569	-0.013832797	-0.003010278
6	-2.46945E-05	0.000880725	0.002673931
8	0.001872157	0.001890734	0.001984117
10	0.000812579	0.000812668	0.000816658
12	0.000356217	0.000357384	0.000356193
15	0.000141347	0.000138936	0.00014004
20	4.387E-05	4.38655E-05	4.3859E-05

Table 300. The z-component of the collision-induced dipole moment at an internuclear distance of 3.213 bohr for geometry 70-0-65-75

Intermolecular Distance (bohr)	μ_z (singlet)	μ_z (triplet)	μ_z (quintet)
5	-0.004200936	-0.003648094	0.010353625
6	0.001561565	0.002405413	0.004516636
8	0.00221801	0.0022705	0.002369121
10	0.000976945	0.000982136	0.000982964
12	0.000429469	0.000449846	0.000429416
15	0.000168266	0.000167092	0.000168397
20	5.2616E-05	5.2605E-05	5.2616E-05

Table 301. The z-component of the collision-induced dipole moment at an internuclear distance of 3.3 bohr for geometry 70-0-65-75

Intermolecular Distance (bohr)	μ_z (singlet)	μ_z (triplet)	μ_z (quintet)
5	-0.002078351	0.001341718	0.016234705
6	0.004296294	0.004771711	0.006783943
8	0.002289715	0.0023472	0.002450876
10	0.001013749	0.001014869	0.001020262
12	0.000446352	0.000436642	0.000446545
15	0.000174767	0.000173814	0.000174893
20	5.4558E-05	5.45635E-05	5.45845E-05

Table 302. The z-component of the collision-induced dipole moment at an internuclear distance of 2 bohr for geometry 50-0-95-55

Intermolecular Distance (bohr)	μ_z (singlet)	μ_z (triplet)	μ_z (quintet)
5	0.024205	0.02042	0.01064
6	-0.00303	-0.00374	-0.00515
8	-0.00336	-0.0034	-0.00348
10	-0.00136	-0.00136	-0.00137
12	-0.0006	-0.0006	-0.0006
15	-0.00024	-0.00024	-0.00024
20	-7.4E-05	-7.4E-05	-7.4E-05

Table 303. The z-component of the collision-induced dipole moment at an internuclear distance of 2.1 bohr for geometry 50-0-95-55

Intermolecular Distance (bohr)	μ_z (singlet)	μ_z (triplet)	μ_z (quintet)
5	0.015874	0.015132	0.012215
6	-0.00309	-0.00333	-0.00368
8	-0.00272	-0.00276	-0.0028
10	-0.00106	-0.00106	-0.00107
12	-0.00046	-0.00046	-0.00046
15	0.067352	-0.00019	-0.00019
20	-5.8E-05	-5.8E-05	-5.8E-05

Table 304. The z-component of the collision-induced dipole moment at an internuclear distance of 2.2 bohr for geometry 50-0-95-55

Intermolecular Distance (bohr)	μ_z (singlet)	μ_z (triplet)	μ_z (quintet)
5	0.008992	0.010718	0.01064
6	-0.00313	-0.00288	-0.00515
8	-0.00211	-0.00212	-0.00348
10	-0.00077	-0.00077	-0.00137
12	-0.00033	-0.00033	-0.0006
15	-0.00014	-0.00014	-0.00024
20	-4.3E-05	-4.3E-05	-7.4E-05

Table 305. The z-component of the collision-induced dipole moment at an internuclear distance of 2.28187 bohr for geometry 50-0-95-55

Intermolecular Distance (bohr)	μ_z (singlet)	μ_z (triplet)	μ_z (quintet)
5	0.003998	0.007475	0.014051
6	-0.0031	-0.00253	-0.00144
8	-0.00162	-0.00163	-0.00163
10	-0.00061	-0.00054	-0.00054
12	-0.00022	-0.00022	-0.00022
15	-0.00027	-9.8E-05	-9.5E-05
20	-3E-05	-3.6E-05	-3E-05

Table 306. The z-component of the collision-induced dipole moment at an internuclear distance of 2.296 bohr for geometry 50-0-95-55

Intermolecular Distance (bohr)	μ_z (singlet)	μ_z (triplet)	μ_z (quintet)
5	0.003177	0.00694	0.01416
6	-0.00311	-0.00247	-0.00128
8	-0.00154	-0.00154	-0.00155
10	-0.00049	-0.0005	-0.0005
12	-0.0002	-0.0002	-0.0002
15	0.031024	-9E-05	0.031496
20	-2.8E-05	-2.8E-05	-2.8E-05

Table 307. The z-component of the collision-induced dipole moment at an internuclear distance of 2.36 bohr for geometry 50-0-95-55

Intermolecular Distance (bohr)	μ_z (singlet)	μ_z (triplet)	μ_z (quintet)
5	-0.00039	0.004602	0.014598
6	-0.00302	-0.00221	-0.00059
8	-0.00118	-0.00117	-0.00116
10	-0.0003	-0.00033	-0.00033
12	-0.00012	-0.00012	-0.00012
15	-5.9E-05	-5.9E-05	-5.9E-05
20	-1.8E-05	-1.8E-05	-1.8E-05

Table 308. The z-component of the collision-induced dipole moment at an internuclear distance of 2.457 bohr for geometry 50-0-95-55

Intermolecular Distance (bohr)	μ_z (singlet)	μ_z (triplet)	μ_z (quintet)
5	-0.00536	0.001311	0.015168
6	-0.00293	-0.00181	0.000389
8	-0.00064	-0.00061	-0.00059
10	-6.2E-05	-7.2E-05	-7.3E-05
12	-3.9E-06	-3E-06	-4.4E-06
15	-1.4E-05	-1.4E-05	-1.4E-05
20	-3.4E-06	-3.4E-06	-3.4E-06

Table 309. The z-component of the collision-induced dipole moment at an internuclear distance of 2.646 bohr for geometry 50-0-95-55

Intermolecular Distance (bohr)	μ_z (singlet)	μ_z (triplet)	μ_z (quintet)
5	-0.01338	-0.00415	0.016108
6	-0.00272	-0.00111	0.00208
8	0.000315	0.000349	0.000414
10	0.000378	0.000378	0.000378
12	0.000202	0.000201	0.000202
15	6.77E-05	6.75E-05	6.76E-05
20	2.32E-05	2.32E-05	2.31E-05

Table 310. The z-component of the collision-induced dipole moment at an internuclear distance of 2.929 bohr for geometry 50-0-95-55

Intermolecular Distance (bohr)	μ_z (singlet)	μ_z (triplet)	μ_z (quintet)
5	-0.01802	-0.0074	0.017905
6	-0.00238	-0.00027	0.003984
8	0.001413	0.001474	0.001585
10	0.000903	0.000905	0.000906
12	0.000446	0.000446	0.000446
15	0.000166	0.000166	0.000166
20	5.56E-05	5.57E-05	5.56E-05

Table 311. The z-component of the collision-induced dipole moment at an internuclear distance of 3.213 bohr for geometry 50-0-95-55

Intermolecular Distance (bohr)	μ_z (singlet)	μ_z (triplet)	μ_z (quintet)
5	0.009469	0.009469	0.030927
6	0.001672	0.001672	0.005971
8	0.002175	0.002175	0.002341
10	0.001245	0.001245	0.001249
12	0.000606	0.000606	0.000607
15	0.000232	0.000232	0.000232
20	7.78E-05	7.78E-05	7.78E-05

Table 312. The z-component of the collision-induced dipole moment at an internuclear distance of 3.3 bohr for geometry 50-0-95-55

Intermolecular Distance (bohr)	μ_z (singlet)	μ_z (triplet)	μ_z (quintet)
5	-0.01783	0.00287	0.039205
6	0.003059	0.004356	0.007796
8	0.002278	0.002357	0.002529
10	0.001319	0.001321	0.001326
12	0.000643	0.000642	0.000643
15	0.000243	0.000249	0.000247
20	8.28E-05	8.28E-05	8.29E-05

REFERENCES

REFERENCES

[1] L. Frommhold, *Collision-Induced Absorption in Gases*, (Cambridge University Press, New York, 2006).

[2] J. Wildt, E.H. Fink, P. Biggs, and R.P. Wayne, and A.F. Vilesov, *Chemical Physics* **159**, 127 (1992).

[3] M.F.Crawford, H.L.Welsh, and J.L.Locke, *Phys Rev* **80**, 1607 (1949).

[4] G.C. Tabisz, E.J. Allin, and H.L. Welsh, *Canadian Journal of Physics* 47, 2859 (1969).

[5] H.L. Welsh, M.F. Crawford, J.C.F. MacDonald and D.A. Chrisholm *Phys. Rev.* **83**, 1264 (1951).

[6] M.M. Shapiro and H.P. Gush, *Canadian Journal of Physics* **44,** (1966).

[7] M.M. Shapiro, M.A. Thesis, University of Toronto, Toronto, Ont. (1961).

[8] J. Van Kranendonk, *Physica* **23,** 825 (1957); *Physica* **24**, 347 (1958).

[9] R.P.H. Rettschnick and G.J. Hoytink, *Chem. Phys. Lett.* **1,** 145-148 (1967).

[10] L. Herzberg and G. Herzberg, *Astrophys*. **105,** 353 (1947) .

[11] G. Herzberg, *Molecular spectra and molecular structure, Vol. I, Diatomic molecules*, (D. Van Nostrand, Princeton, N.J. , 1950).

[12] J.A.A. Ketelaar, *Nuovo Cimento Suppl*. **2 ,** set. X, 763-765 (1955).

[13] V.I. Dianov-Klokov, *Opt. Spectros. Engl. Transl.* **16**, 224-227 (1964).

[14] C.W. Cho, E. J. Allin, and H. L. Welsh, *Can J. Phys*. **41**, 1991-2002 (1963).

[15] R.M. Badger, A. C. Wright, and R. F. Witlock, *J. Chem. Phys*. **43**, 4345-4350 (1965).

[16] D. Babcock and L. Herzberg, *Astrophys. J.* **108**, 167 (1946).

[17] G. Herzberg, *Can. J.Phys.* **31,** 657 (1953).

[18] G.Herzberg, *Can. J. Phys*. **30,** 185 (1952).

[19] K.Watanabe, E.C.Y.Inn and M.ZeIikoff, *J.Chem. Phys.* **21**, 1026 (1953).

[20] V.I. Dianov-Klokov, *Opt. Spectrosc.* **20**, 530 (1966).

[21] H. Naus and W. Ubachs, *J. Mol. Spectrosc.***193**, 442 (1999).

[22] R.P. Blickensderfer and G.E. Ewing, *The Journal of Chemical Physics* **51**, 873 (1969).

[23] A.R.W. McKellar, N.H. Rich, and H.L. Welsh, *Can. J. Phys*. **50**, (1972).

[24] D. Perner and U. Platt, *Geophys. Res. Lett.* **7**, 1053-1056 (1980).

[25] J.J. Orlando, G. S. Tyndall, K. E. Nickerson, and J. G. Calvert *J .Geophys. Res.* **96**,755-760 (1991).

[26] F. Thibault, V. Menoux, R. Le Doucen, L. Rosenmann, J.-M. Hartmann, and Ch. Boulet, *Appl. Opt.* **36**, 563 (1997).

[27] C.P. Rinsland, M.A.H. Smith and R.K. Seals, Jr., A. Goldman, F.J. Murcray and D.G. Murcray, and J.C. Larsen and P.L. Rarig, *J .Geophys. Res.* **87**, 3119-3122 (1982).

[28] J.M. Russell and J. C. Gille, *The Nimbus 7 Users' Guide*, edited by C. Madrid, pp. 71-103, (Goddard Space Flight Center, Greenbelt, Md., 1978).

[29] K. Pfeilsticker, F. Erle, and U. Platt, *J. Atmos. Sci*. **54,** 933(1997).

[30] J.T. Houghton, L. G. Meira Filho, J. Bruce, H. Lee, B. A. Callander, E. Haites, N. Harris, and K. Maskell, *Radiative Forcing of Climate Change and an Evaluation of the IPCC IS92 Emission Scenarios* (Cambridge University Press, New York, 1994).

[31] R.A. Kerr, *Science* **267,** 454 (1995).

[32] F. Erle, K. Pfeilsticker, and U. Platt, *Geophys. Res. Lett.* **22,** 2725–2728 (1995).

[33] U. Platt, *Chemical Analysis Series* **127,** 27-84, (John Wiley and Sons, Hoboken, New Jersey 1994).

[34] S. Solomon, R.W. Portmann, R.W. Sanders, and J.S. Daniels, *J. Geophys. Res.* **103**,3847-3858 (1998).

[35] G. D. Greenblatt, J.J Orlando, J.B. Burkholder, and A.R. Ravishankara, *J. Geophys. Res.* **95,** 18557–18582 (1990).

[36] J. C. S. Chagas, D. A. Newnham, K. M. Smith and K. P. Shine, *Q. J. R. Meteorol. Soc.* **128**, 2377–2396 (2002).

[37] R. L. Miller, A. G. Suits, P. L. Houston, R. Toumi, J. A. Mack and A. M. Wodtke, *Science* **265,** 1831-1838 (1994).

[38] H. Park and T.G. Slanger, *J. Chem. Phys.* **100**, (1994).

[39] D. Stranges, X. Yang, J. D. Chesko, and A. G. Suits, *J. Chem. Phys.* **102**, 6067 (1995).

[40] R. Toumi, P.L. Houston, and A. M. Wodtke, *J. Chem. Phys.* **104,** 775 (1996).

[41] R. Hernández, R. Toumi, and D. C. Clary, *J. Chem. Phys.* **102**, 9544 (1995).

[42] D. Lauvergnat and D. C. Clary, *J. Chem. Phys.* **108**, 3566 (1998).

[43] C. E. Fairchild, E. J. Stone, and G. M. Lawrence, *J. Chem. Phys.* **69**, 3632 (1978).

[44] R. K. Sparks, L. R. Carlson, J. Shobatake, M. L. Kowalczyk, and Y. T.Lee, *J. Chem. Phys.* **72**, 1401 (1980).

[45] C. A. Rogaski, J. M. Price, J. A. Mack, and A. M. Wodtke, *Geophys. Res. Lett*. **20**, 2885 (1993).

[46] J. M. Price, J. A. Mack, C. A. Rogaski, and A. M. Wodtke, *Chem. Phys*. **175**, 83 (1993).

[47] J. Eluszkiewicz and M. Allen, *J. Geophys. Res.* **98**, 1069 (1993).

[48] M. Allen, *J. Geophys. Res.* **91**, 2844 (1986).

[49] J. A. Syage, *J. Phys. Chem.* **99**, 16530 (1995).

[50] J. A. Syage, *J. Chem. Phys*. **105**, 1007 (1996).

[51] J. A. Syage, *J. Phys. Chem*. **100**, 13885 (1996).

[52] P. L. Houston, A. G. Suits, and R. Toumi, *J. Geophys. Res*. **101**, 18829 (1996).

[53] T. G. Slanger, L. E. Jusinski, G. Black, and G. E. Gadd, *Science* **241**, 945 (1988).

[54] R. Toumi, *J. Atm. Chem*. **15**, 69 (1992).

[55] J. D. Geiser, S. M. Dylewski, J. A. Mueller, R. J. Wilson, R. Toumi, and P. L. Houston, *J. Chem. Phys.* **112**, 1279 (2000).

[56] A. J. C. Varandas and A. A. C. C. Pais, *Theoretical and Computational Models for Organic Chemistry*,(Kluwer Academic Publishers, Dordrecht, The Netherlands, p. 55 (1991)).

[57] H. Szichman, A. J. C. Varandas, and M. Baer, *Chem. Phys. Lett.* **231**, 253 (1994).

[58] H. Szichman, A. J. C. Varandas, and M. Baer, *J. Chem. Phys*. **102**, 3474 (1995).

[59] N. Balakrishnan and G. D. Billing, *Chem. Phys. Lett.* **242**, 68 (1995).

[60] N. Balakrishnan and G. D. Billing, *J. Chem. Phys*. **104**, 9482 (1996).

[61] J. A. Mack, Y. Huang, A. M. Wodtke, and G. C. Schatz, *J. Chem. Phys.***105**, 7495 (1996)

[62] R. Hernández-Lamoneda, M. I. Hernández, E. Carmona-Novillo, J. Campos-Martínez, J. Echave, and D. C. Clary, *Chem. Phys. Lett*. **276**, 152 (1997).

[63] N. Balakrishnan, A. Dalgarno, and G. D. Billing, *Chem. Phys. Lett.* **288**, 657 (1998).

[64] A. J. C. Varandas and W. Wang, *Chem. Phys*. **215**, 167 (1997).

[65] W. Wang and A. J. C. Varandas, *Chem. Phys*. **236**, 181 (1998).

[66] J. Campos-Martinínez, E. Carmona-Novillo, J. Echave, M. I. Hernández, R. Hernández-Lamoneda, and J. Palma, *Chem. Phys. Lett*. **289**, 150 (1998).

[67] J. L. Hunt and J.D. Poll, *Can. J. Phys*. **56**, 950 (1978).

[68] J.D. Poll and J.L. Hunt, *Can J. Phys.* **54**,461 (1976).

[69] J. E. Bohr and K. L. C. Hunt, *J.Chem. Phys*. **87**, 3821 (1987).

[70] J. Boissoles, C. Boulet, R.H. Tipping, Alex Brown, Q. Ma, *J. Quant. Spectrosc. Radiat. Transfer* **82**,505–516(2003).

[71] T. G. Slanger and R. A. Copeland, *Chem. Rev.* **103,** 4731 (2003).

[72] A. A. Vigasin and Z. Slanina, *Molecular Complexes in the Earth's, Planetary, Cometary and Interstellar Atmospheres* (World Scientific, Singapore, 1998).

[73] J. Liu and K. Morokuma, *J. Chem. Phys.* **123**, (2005).

[74] A. V. Avdeenkov and J. L. Bohn, *Phys. Rev. A* **64**, 52703 (2001).

[75] Y. A. Freiman and H. J. Jodl, *Phys. Rep*. **401**, (2004).

[76] T.H. Dunning, *J. Chem. Phys.* **90,** 1007 (1989).

[77] K. Andersson, P. A. Malmqvist, B. O. Roos, A. J. Sadlej, and K. Wolinski, *J. Phys. Chem.* **94**, 5483 (1990).

[78] K. Andersson, P.A. Malmqvist, and B.O. Roos, *J. Chem. Phys.* **96,** 1218 (1992).

[79] MOLPRO, version 2010.1, a package of *ab initio* programs, H.-J. Werner, P.J. Knowles, G. Knizia, F.R. Manby, and others, see http://www.molpro.net

[80] V. Aquilanti, D. Ascenzi, M. Bartolomei, D. Cappelleti, S. Cavalli, M. Vitores, and F. Pirani *J. Am. Chem. Society* **121**, 10794 (1999).

[81] S.F. Boys and F. Bernardi, *Mol. Phys.* **19,** 553 (1970).

[82] A.J. Stone, *The Theory of Intermolecular Forces* (Clarendon Press, Oxford, 1996).

[83] (a) P. E. S. Wormer and A. van der Avoird, *J. Chem. Phys.***81**, 1929 (1984); (b) M. C. van Hemert, P. E. S. Wormer and A. van der Avoird, *Phys. Rev. Lett.* **51**, 1167 (1983).

[84] V. Adamantides, *Chem. Phys.* **48,** 221-225(1980).

[85] V. Adamantides, D. Neisius, and G. Verhaegen, *Chem. Phys.* **48,** 215-220 (1980).

[86] A.C. Pavão, G.M. Seabra, and C.A Taft, *J. Mol. Struct. (Theochem)* **335**, 59-61 (1995).

[87] G.D. Billing and R.E. Kolesnick, *Chem. Phys. Lett.* **200**, (1992).

[88] H. Hettema, P.E.S. Wormer, P. Jørgensen, H.J.Aa. Jensen, and T.Helgaker, *J. Chem. Phys.* **100**, 1297 (1994).

[89]B.F. Minaev, V.D. Nikolaev, H. Agren, *Spec. Lett.* **29**, 677-695 (1996).

[90] D. Lauvergnat and D. C. Clary, *J. Chem. Phys.* **108**,(1997).

[91] A.J.C. Varandas, A.A.C.C. Pais, in: S.J. Formosinho, I.G.Czismadia, L.C. Arnaut Eds., *Theoretical and Computational Models for Organic Chemistry, Nato ASI Series C*,(Kluwer, Dordrecht, 1991).

[92] B. Bussery, P. E. S. Wormer, *J. Chem. Phys*. **99**, 1230 (1993).

[93] B. Bussery-Honvault and V. Veyret, *Phys. Chem. Chem. Phys*. **1**, 3387-3393 (1999).

[94] A. van der Avoird and G. Brocks, *J. Chem. Phys.,* **87,** 5346 (1987).

[95] F. Uhlik, Z. Slanina and A. Hinchlie, *J. Mol. Struct. (Theochem),***285**, 273 (1993).

[96] Cecilia Coletti and Gert D. Billing *Chem Phys. Lett.* **356**, 14–22 (2002) .

[97] R. Hernández-Lamoneda, M. Bartolomei, M. I. Hernández and J. Campos-Martínez, and F. Dayou *J. Phys. Chem. A* **109**,11587-11595 (2005).

[98] F. Dayou, M. I. Hernández and J. Campos-Martínez, and R. Hernández-Lamoneda *J. Chem. Phys.* **123**, 074311 (2005).

[99] M. Bartolomei, E. Carmona-Novillo, M.I. Hernández, J. Campos-Martínez, R. Hernandez-Lamoneda *J. Chem. Phys.* **128**, 214304 (2008).

[100] M. Bartolomei, M.I. Hernández, J. Campos-Martínez, E. Carmona-Novillo, and R. Hernandez-Lamoneda, *Phys. Chem. Chem. Phys*. **10**, 5374–5380 (2008).

[101] T.V. Nguyen, Q. K. Timerghazin, H. Vach, and G. H. Peslherbe, *J. Chem. Phys.* **134**, 064305 (2011).

[102] R. Cambi, D. Cappelletti, G. Liuti, and F. Pirani, *J. Chem. Phys.* **95**, 1852 (1991).

[103] G. C. Fotis, *Phys. Rev. B* **23**, 4714 (1981).

[104] B. Brunetti, G. Liuti, F. Pirani, and F. Vecchiocattivi, *J. Chem. Phys.***74,** 6734-6741 (1981).

[105] J. Goodman and L. E. Brus, *J. Chem. Phys.* **67,** 4398 (1977).

[106] V. Aquilanti, D. Ascenzi, D. Cappelletti, F. Pirani, *J. Phys. Chem.* **99**, 13620-13626 (1995).

[107] R.B. Bernstein and T.J.P. O'Brien, *Discuss. Faraday Soc.* **40,** 35-44 (1965); *J. Chem. Phys.* **46,** 1208-1209 (1967).

[108] F. Pirani, and F. Vecchiocattivi. *Mol. Phys.* **45,** 1003-1013 (1982).

[109] P. C. Hariharan and J. A. Pople, *Chem. Phys. Lett.* **66**, 217 (1972).

[110] J. D. Watts, J. Gauss and R. J. Bartlett, *J. Chem. Phys*. **98**, 8718 (1993).

[111] H.-J. Werner and P. J. Knowles, *J. Chem*. *Phys*. **89,** 5803 (1988).

[112] J. Campos-Martínez, M. I. Hernández, M. Bartolomei, E. Carmona-Novillo, R. Hernández-Lamoneda, and F. Dayou, *Frontiers in Quantum Systems in Chemistry and Physics, Prog. Theor. Chem. Phys.* **18**, pp. 387-401, edited by S. Wilson, P. J. Grout, J. Marauni, G. Delgado-Barrio, and P. Piecuch (Springer Publishing, the Netherlands, 2008).

[113] Y. N. Kalugina and V. N. Cherepanov, *Atmos. Oceanic Opt.* **28**, 406 (2015).

[114] M. Bartolomei, E. Carmona-Novillo, M. I. Hernández, J. Campos-Martínez, and R. Hernández-Lamoneda, *J. Comp*. *Chem*. **32,** 279 (2011).

[115] Y. Luo, H. Ågren, B. Minaev, and P. Jørgensen, *Journal of Molecular Structure (Theochem),***336**, 61(1995).

[116] T. D. Poulsen, P. R Ogilby, and K. V. Mikkelsen, *J. Phys. Chem,* **102**, 8970-8973 (1998).

[117] M. Lepers, B. Bussery-Honvault, and Olivier Dulieu, *J. Chem. Phys.,* **137**, 234305 (2012)

[118] P. Neogràdy, M. Medved, I. Černusak, and M. Urban, *Mol. Phys.* **100**, 541-560 (2002).

[119] G.D. Purvis and R.J. Bartlett, *J. Chem. Phys.***76,** 1910 (1982).

[120] A. Zen, B. L. Trout, and Leonardo Guidoni, *J. Chem. Phys.* **141**, 014305 (2014).

[121] J.P. Coe and M.J. Paterson, arXiv:1409.7276v1 25 Sep 2014.

[122] F. Bielsa, R. Tattesti, C. Robilliard G. Bialolenker, G. Bailly, G. Trenec, A. Rizzo, and C. Rizzo, *Eur. Phys. J. D,* **36**, 261 (2005).

[123] V. W. Couling and S. S. Ntombela, *Chem. Phys. Lett.* **41**, 614 (2014).

[124] B. Minaev, *Spectrochimica Acta Part A* **60,** 1027 (2004).

[125] E. F. May, M. R. Moldover, and J. W. Schmidt, *Phys. Rev. A* **78**, 032522 (2008).

[126] D. Spelsberg and W. Meyer, *J. Chem. Phys.* **109,** 9802 (1998).

[127] T. Slanger and R. Copeland, *Chem. Rev.* **103,** 4731-4765 (2003).

[128] J. W. Cooley, *Math. Comput*. **15**, 363 (1961).

[129] I. N. Levine, *Quantum Chemistry*, *5th ed*.(Prentice-Hall, USA).

[130] A. D. McLean and M. Yoshimine, *J. Chem. Phys*. **47**, 1927 (1967).

[131] E. Miliordos and Katharine L.C. Hunt, manuscript prepared.

[132] Yi Luo, O. Vahtras, H. Ågren, and P. Jørgensen, *Chem. Phys. Lett.,* **205**, 555 (1993)

[133] J. Borysow, L. Trafton, L. Frommhold, and G. Birnbaum, Astrophys. J. **296,** 644(1985)

[134] W. Meyer and L. Frommhold, *Phys. Rev. A,* **34**, 2771, 2936 (1986).

[135] L. Frommhold and A. Borysow, *Astrophys. J.* **303**, 495 (1986).

[136, 137] J. Van Kranendonk, Physica **24,** 347 (1958); J. Van Kranendonk and Z.J. Kiss, *Can. J. Phys.* **37,** 1187 (1959).

[138] J.D. Poll and J. Van Kranendonk, *Can. J. Phys.* **39,** 189 (1961).

[139] J.D. Poll and J.L. Hunt, *Can. J. Phys*. **59** 1448 (1981).

[140] J.P. Colpa and J.A.A. Ketelaar, *Mol. Phys*. **1**, 343 (1958).

[141] C.G. Gray, *J Phys. B* **4**, 1661 (1971).

[142] G. Birnbaum and E.R. Cohen, *Mol. Phys.* **32,** 161 (1976); *Can. J. Phys*. **54**, 593 (1976).

[143] E.R Cohen and G. Birnbaum, *J. Chem. Phys*. **66,** 2443 (1977).

[144] A.D. Buckingham and A.J. C. Ladd, *Can. J. Phys*. **54**, 611 (1976).

[145] M. Moon and D.W. Oxtoby, *J. Chem. Phys.* **75** (1981).

[146] M. Moon and D.W. Oxtoby, *J. Chem. Phys*. **84**, 3830 (1986).

[147] A.D. Buckingham and G.C. Tabisz, *Opt. Lett*. **1**, 220 (1977); Mol. Phys. **36,** 583 (1978).

[148] A.D. Buckingham, in *Proprietes Optiques et Acoustiques des Fluids Comprimeset Actions Intermoleculaires*,p. 57 (Centre National de la Recherche Scientifique, Paris, 1959).

[149] J.E. Bohr and K.L.C. Hunt, J. Chem. Phys. **86**, 5441 (1987).

[150] P.W. Fowler and A.D. Buckingham, *Mol. Phys*. **50**, 1349 (1983).

[151] H.-J Werner and P.J. Knowles, *J. Chem. Phys.* **82**, 5053 (1982).

[152] P.J. Knowles and H.-J. Werner, *Chem. Phys. Lett*. **115**, 259 (1985).